LASER-PLASMA LIGHTSOURCES:

RESEARCH AND DEVELOPMENTS FOR INCREASED CONTROL,
STABILITY, GAIN AND BRIGHTNESS

ANDREAS STEFAN DÖPP

A thesis submitted for the degree of

DOCTEUR DE L'ÉCOLE POLYTECHNIQUE
DOCTOR EN FÍSICA POR LA UNIVERSIDAD DE SALAMANCA

Kim TA PHUOC, Investigador del CNRS en el Laboratoire d'Optique Appliquée de ENSTA-ParisTech/CNRS/Ecole Polytechnique/Université Paris-Saclay, Camilo RUIZ MÉNDEZ, Profesor en el departamento de didáctica de matemáticas y ciencias en la Universidad de Salamanca, y Enrique CONEJERO JARQUE, Profesor Titular del Área de Óptica del Departamente de Física Aplicada en la Universidad de Salamanca certifican que la presente memoria,

LASER-PLASMA LIGHTSOURCES: RESEARCH AND DEVELOPMENTS FOR INCREASED CONTROL, STABILITY, GAIN AND BRIGHTNESS

ha sido realizada bajo su dirección y turoría en el Laboratoire d'Optique Appliquée y en el Área de Óptica del Departamento de Física Aplicada de la Universidad de Salamanca por Don Andreas Stefan DÖPP y constituye su Tesis Doctoral para optar a los grados de Docteur de l'École Polytechnique y de Doctor en Física por la Universidad de Salamanca.

Kim TA PHUOC, Director	Camilo RUIZ MÉNDEZ, Co-Director	Enrique CONEJERO JARQUE, Tutor

Palaiseau / Salamanca, 20 de octubre de 2015.

Abstract

Laser-plasma technology has the potential to provide compact sources of bright femtosecond X-ray, which may soon serve as an alternative to their conventional counterparts. Proof-of-principle experiments have impressively demonstrated the sources' prospects, yet the poor stability and tunability drastically limit their scope of applicability.

Conventional systems have achieved their remarkable control over the source by progressive improvement of the discrete stages of injection, acceleration, beam transport and radiation generation. In this work we have adapted this approach for laser-plasma sources and made advances on all individual parts of the source.

The manuscript is organized in the same, successive way. The first part of the thesis discusses new injection methods which permit to create either stable, tunable, mono-energetic electrons or beams of elevated charge and bandwidth. In the second part we use tailored density profiles to adapt the plasma cavity size. This rephasing allows us to accelerate electrons beyond the conventional limits of wakefield accelerators. We also demonstrate for the first time focusing of ultrashort electron beams in an all-optical laser-plasma lens. The last part of the manuscript is dedicated to radiation sources. In particular we made significant improvements to the laser-driven betatron source, namely the production of stable, polarized X-ray from ionization injected electron beams and increased X-ray yield in density tailored plasma channels. Furthermore we have studied bremsstrahlung conversion and Compton backscattering, with emphasis on imaging applications.

Résumé

Les progrès réalisés dans le domaine de l'interaction laser-plasma au cours des dix dernières années ont permis de produire de nouvelles sources de rayonnement X pouvant rivaliser avec les conventionnels synchrotron et tubes X. Ces nouvelles sources ont un fort potentiel mais leur domaine d'applications reste très limitées en raison d'importantes fluctuations et du peu de contrôle de leurs propriétés.

Ces sources sont basées sur le même principe qu'un Synchroton. Il n'agit d'accélérer des électrons jusqu'à des vitesses relativistes et de les faire osciller de manière à ce qu'ils émettent efficacement du rayonnement X. Afin de obtenir un meilleur contrôle de la source nous avons étudié les différentes étapes conduisant à la production de rayonnement : l'injection d'électrons dans l'onde plasma créée dans le sillage du laser, l'accélération et le transport de ces électrons puis les méthodes permettant de les faire osciller. Le manuscrit présente les progrès réalisés dans ces domaines.

La première partie est consacrée aux nouvelles méthodes d'injection d'électrons permettant de produire des faisceaux d'électrons stables, mono-énergétiques et accordables ou de forte charge à spectre large. Dans la seconde partie nous montrons comment accélérer des faisceaux d'électrons au delà des limites conventionnelles des accélérateurs laser-plasma. Nous démontrons ensuite une méthode innovante et entièrement optique permettant de focaliser un faisceau d'électrons. Enfin, nous présentons les progrès réalisés dans le domaines des sources X femtoseconde utilisant ces électrons relativistes, c'est à dire les sources Betatron et Compton. Nous avons considérablement amélioré les propriétés de la source Betatron en produisant des faisceaux de rayonnement X stables et polarisés. Nous avons également développer un schéma permettant de découpler les étapes d'accélération et de production de rayonnement. Concernant la source Compton, nous l'avons caractérisée et utilisée pour des applications en imagerie X à haute résolution spatiale.

Resumen

La tecnología de la interacción láser-plasma tiene el potencial de producir nuevas fuentes de rayos X, brillantes, compactas y ultracortas que reemplacen o sean una alternativa viable a las fuentes convencionales existentes. Experimentos recientes han demostrado los principios básicos de estas fuentes y su increíble potencial, pero también su pobre estabilidad y poco control, lo que limita el alcance de sus aplicaciones.

La tecnología de aceleradores convencionales ha logrado un alto grado de control en las características de las fuentes de radiación ionizante mejorando progresivamente cada uno de sus elementos como la inyección, la aceleración el transporte del haz y la generación de radiación. En este trabajo utilizamos esta metodología de optimización individual para las fuentes láser-plasma y reportamos avances en cada uno de estos elementos.

El manuscrito está organizado de la siguiente forma: Empezamos con un discurso sobre nuevos métodos de inyección controlada para crear haces de electrones, explorando en particular la inyección por choque y la inyección por ionización. En la segunda parte presentamos los primeros resultados experimentales acerca de la evolución de la energía de un haz de electrones en un acelerador con un perfil de densidad previamente diseñado. Se demuestra también la posibilidad de focalizar un haz de electrones ultracorto en una lente completamente óptica, utilizando la estela lineal del pulso en un plasma de baja densidad.
La última parte del texto está dedicada a la generación de radiación. En particular reportamos avances significativos en una fuente betatrón. Demostramos la producción de una fuente estable y polarizada de rayos X producida por electrones inyectados por medio de ionización retrasada. Finalmente reportamos la producción optimizada de rayos X en canales de plasma sobre perfiles de plasma diseñados. Además, hemos estudiado la radiación de frenado y la retrodispersión Compton, centrándonos en sus aplicaciones en imagen de rayos X.

Contents

1 Introduction

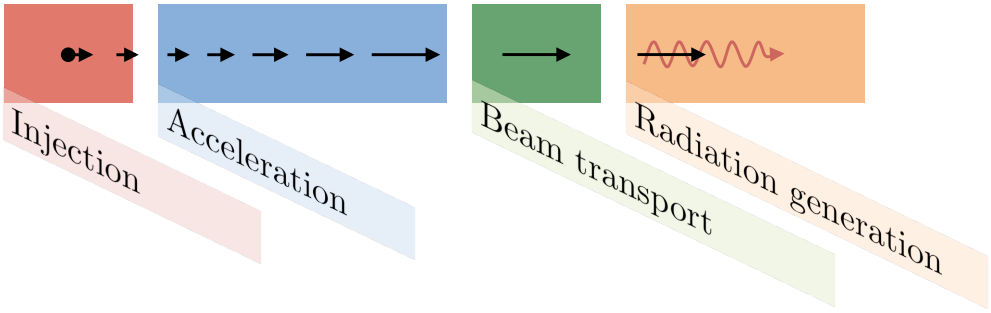

From the earliest X-ray tubes to free-electron lasers the development of lightsources has been linked to the control of four different stages: Electron generation, acceleration, beam transport and finally radiation generation. The aim of this work is to apply the same staging philosophy to the emerging technology of laser-plasma lightsources, ameliorating the source by individual improvement of each element.

After an introduction to conventional accelerators and lightsources we will review qualitatively plasma-wakefield generation and radiation generation. Subsequently we briefly introduce some basic concepts of laser-plasma interactions in order to establish a foundation for the main chapters.

Contents

The discovery of the Higgs boson in 2014 is undoubtedly one of the greatest achievements in modern science. It was only made possible by the large hadron collider (LHC), a 26.7 kilometer long synchrotron, capable of accelerating particles to never preceded energies. The LHC is one of very few large accelerators in the public spotlight, yet particle accelerators and X-ray sources are nowadays ubiquitous in industrial, scientific and medical environments. Most of these small sources still rely on technology developed in the first half of the 20th century, when the development of industrial and scientific accelerators was still closely linked. This situation changed when scientific accelerators started to outgrow the size of university laboratories, needing own dedicated accelerator centers like CERN in Switzerland or DESY in Germany. This concentration to a few accelerator centers per country has drastically limited the accessibility to modern particle- and lightsources, despite their indisputable advantages for society. One of the central aims of laser-plasma technology is to fill this gap between large-scale facilities and common X-ray tubes.

1.1 X-ray sources: from discharge tubes to free-electron-lasers

The discovery of X-ray by Wilhelm Conrad Röntgen in 1895 [1] can be seen as the beginning of a new era in science. Yet from a technological point of view, the era of modern X-ray and particle sources commenced some years later, in the 1900s and 1910s. In fact, these two decades mark the timeframe that was needed to go from a machine that 'accidentally' created X-ray to a device that was designed to do so.

The Crookes tube Röntgen used for his work creates electrons via field ionization of residual gas in a discharge. The freed electrons are then attracted by the anode where they emit radiation in form of bremsstrahlung and line excitation. Meanwhile the ions drift towards the cathode, where they free electrons via collision ionization. Electrons originating from the cathode can be accelerated to higher energies than the gas electrons and therefore radiate more when they eventually hit the anode. These early X-ray tubes (also called ion X-ray tubes or cold cathode Tubes) were not very efficient, hardly tunable and would stop working once the residual gas in the bulb was exhausted.

The modern X-ray tube design, which operates at higher vacuum and wherefore all electrons originate at the cathode, was developed later by Julius E. Lilienfeld in Germany [2] and William D. Coolidge in the United States [3]. In Coolidge's X-ray tube [4] electrons are created by thermionic emission, heating a tungsten cathode to ~ 2000°C. The thermionic emitter itself was already studied before, yet Coolidge was the first to achieve a vacuum good enough to reduce the effect of positive ions. Figure 1.1 shows Coolidge's focusing X-ray tube No.147, which remarkably incorporates all main components of a modern X-ray source.

The principal component is the **electron source**, a closely wound tungsten spiral, the *filament*, which is heated by a current of 3 to 5 Amperes to temperatures of 1890 to 2540 Kelvin. Electrons are emitted from this spiral via thermionic emission, which is still the most common cathode type for this application. Then there is a **focusing device**, consisting of a cylindrical

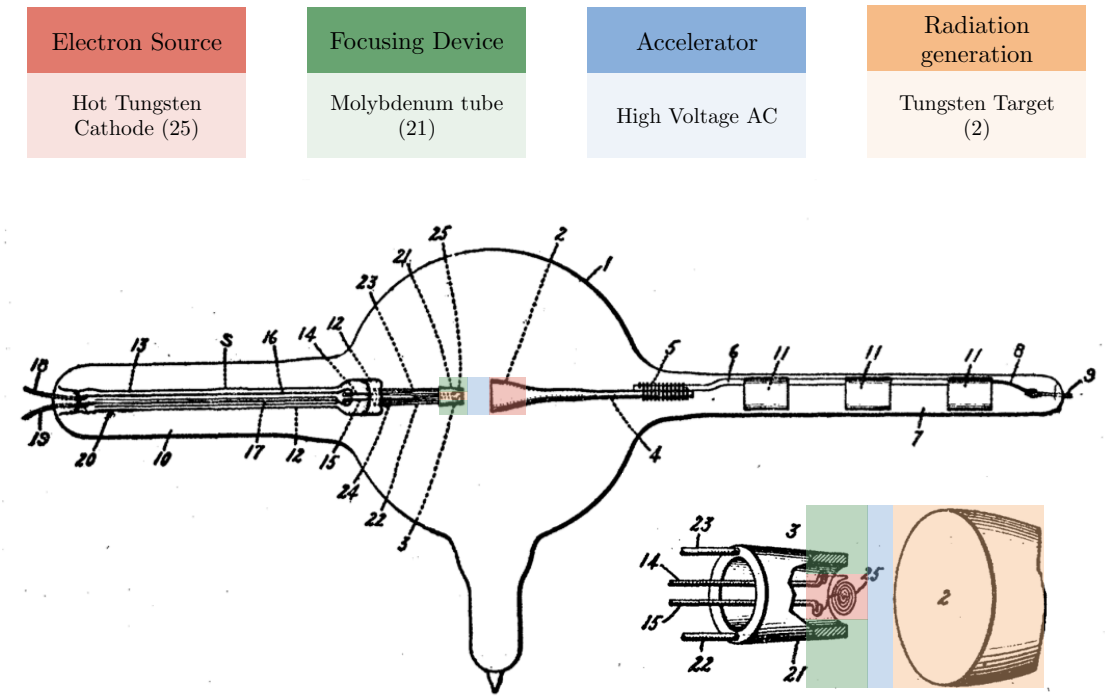

Figure 1.1 – Schematic layout of Coolidge's X-ray tube from the original publication in 1913. The different parts of the tube are colored according to their function.

molybdenum tube that serves as electrostatic lens. Today this part is called the *focusing cup*; it is used to control the way the electrons hit the target anode. The gap between cathode and anode forms the **accelerator**, where a high voltage is applied to accelerate electrons in an electrostatic field. In Coolidge's case up to 100 kV were reached, which is within the range of modern diagnostic X-ray generators ($\sim 20-150$ kV). Once electrons are accelerated, their energy is converted into **radiation** when they hit the anode, which is tilted so X-rays are emitted outwards the bulb. The target is made of tungsten which produces, as a heavy element, more bremsstrahlung and provides good heat resistance. Nowadays tungsten remains most widely used, though sometimes alloys with better resistance to surface damage (e.g. 10% rhenium and 90% tungsten) or materials with specific emission lines (e.g. molybdenum or rhodium) are employed.

While the hot cathode tube was (and still is) perfectly adequate for most medical applications, scientists were interested in producing even harder X-ray. To do so, electrons had to be accelerated to higher energies, thus requiring field strength enhancement. Such could be

provided using Van-de-Graaff (1929) and Cockcroft-Walton (1932) generators, which allowed the acceleration of electrons to MeV level, yet at even higher field strength sparks would form.[1]

A major breakthrough in accelerator history was when Ising conceived (1925) and Wideroe demonstrated (1928) the principle of *resonance acceleration*. In lieu of electrostatic acceleration, these machines operate with a time-dependent electric field and increase particle energies successively in several accelerating structures. With this principle Wideroe's first 1 MHz radio-frequency linear accelerator (*RF linac*) managed to accelerate particles to twice the AC voltage using a drift tube and two grounded electrodes. His work inspired Ernest Lawrence in the United States to apply the resonance principle to a cyclic accelerating structure, thus increasing the particle energy during each revolution. However his *cyclotron*, which remains a widespread ion source nowadays, is limited to non-relativistic particle velocities in order to maintain synchronization and is therefore inadequate for electron acceleration. Instead, two other cyclic accelerator concepts were conceived and implemented shortly after: The *betatron* and the *synchrotron* [5].

The concept of a betatron is to accelerate electrons in a tangential electric field that is produced by a changing magnetic flux. In contrast to the cyclotron such a configuration can achieve relativistic energies. But, as Iwanenko and Pomeranchuk pointed out in 1944 [6], it will be ultimately limited by radiation losses, because particles are continuously accelerated in perpendicular direction in order to keep them on a circular orbit. At the same time Julian Schwinger also developed a theory for the radiation in a betatron [7], indicating that the radiation emission of a 100 MeV betatron should be peaked in the near infrared or visible part of the spectrum. In 1945 McMillan proposed the synchroton [8], which is in many ways a combination of Wideroe's RF linac and Lawrence's cyclotron. A crucial difference to preceding cyclic accelerator concepts is that the synchrotron cannot accelerate particles initially at rest, but instead needs an *injector* to provide electrons at already relativistic velocities. Shortly after the first demonstration of a synchrotron by Goward and Barnes [9], a more powerful 70 MeV machine was realized under the direction of Pollock [10]. It was his team that discovered the visible signal Schwinger predicted [11], now known as *synchroton radiation*.

The consecutive development of this 1st generation of synchrotons concentrated initially on reaching higher (over 1 GeV at ElettroSincrotrone in Frascati) and higher (6 GeV at DESY, etc.) beam energies. Later the development of storage rings provided higher beam currents and greater stability. However all these facilities were hybrid sources for high energy particles and radiation. The construction of facilities exclusively dedicated to the production of synchrotron radiation, like the SRS in Daresbury (UK) [12], marks the beginning of what is called 2nd generation facilities.

Though synchrotron radiation was discovered in cyclic accelerators, it was soon realized that also magnetic fields that alternate in the direction of motion could provoke transverse

[1] For high electric fields, field emission causes a local surface heating, which will then release particles into the cavity. The gas is then ionized and as soon as the density rises sufficiently an arc form from the cathode to anode, leading to what is called vacuum breakdown.

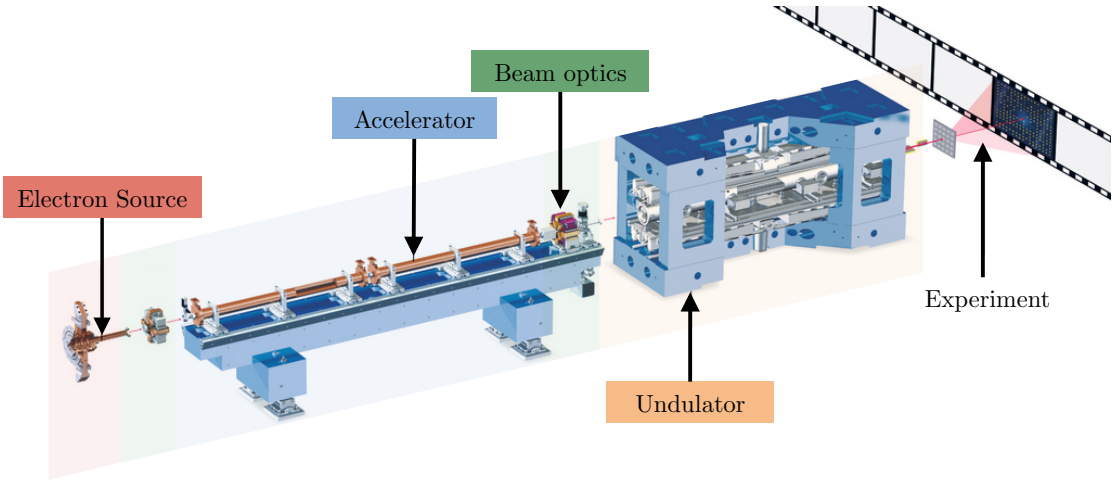

Figure 1.2 – Artistic view of a typical modern lightsource. The different parts responsible for electron generation and injection, acceleration, collimation and radiation generation are marked accordingly.

oscillation of electrons and therefore create radiation. For large oscillation amplitudes an observer will measure short flashes of radiation, whose Fourier transform corresponds to a wide radiation spectrum. With the same qualitative argument we see that the low amplitude undulator case will have a very narrow energy spectrum peaked around a fundamental frequency. This search-light model was introduced by Motz [13], who built the first undulator at the Stanford 100 MeV linac in 1953, producing 400 nm radiation [14]. Undulator radiation has a much better spatial and temporal coherence than Wiggler radiation, which is why modern synchrotrons are using mostly undulator configurations.

The high spatial coherence of synchrotron radiation also gave birth to a new generation of X-ray imaging techniques. For example, X-ray imaging using *phase contrast* has many advantages over conventional absorption contrast imaging [15].

In 1971 Madey proposed the free-electron-laser (FEL) [16], which was shortly later experimentally realized at Stanford [17]. The FELs mimics the concept of conventional lasers [18], but replaces the lasing medium with a relativistic electron beam. As operated in the IR or visible (3.4µm for [17]) an optical cavity can be set up using mirrors, with the light intensity growing by a few percent each passage.

However, in the extreme ultraviolet and X-ray regime it is not possible to set up a multi-pass cavity using mirrors. Instead an effect called microbunching becomes important. Mircobunching means that the normally more or less equally distributed electrons, due to interactions with the radiation, drift into small bunches at a distance of one radiation wavelength each. This effect leads to coherent emission of all electron states and thus, laser-like properties.

Providing much higher gain than the conventional technique, spontaneous emission can be self-amplified within a single pass [19, 20].

First lasing in this SASE configuration was demonstrated in 2001 at the Advanced Photon Source, located at Argonne National Laboratory, [21] and emission in the Ångstrom regime was reached in 2011 at the SLAC Linear Coherent Light source [22]. Currently many projects are underway to built X-Ray FELs around the world, providing light at unprecedented intensities [23]. Also many facilities aim to replace the amplification of spontaneous emission by a seeded operation [24], which would provide even better temporal coherence. There are many ways such a seed can be implemented, e.g. by self-seeding [25], HHG seeding [26] or echo-enabled harmonic generation [27]. The typical layout of an FEL is shown in Fig. 1.2.

X-FELs are the pinnacle of accelerator and lightsource development, but even more, they are the result of a century of research and development around the same basic elements as Coolidge's X-ray tube from 1913: electron source, accelerator, beam transport and radiation generation.

1.2 Merits of laser-plasma technology

Modern lightsources are not only extraordinary by means of their scientific value, but also due to their enormous scale. For example, the european XFEL consists of a 1.7 kilometer long accelerator and undulators of over 100 meter length [28]. And a typical 3rd generation synchrotron has a circumference of some hundred meters, with beam lines extending up to some tens of meters [29]. These large dimensions are dictated by technological limitations: First, the accelerating gradient in conventional accelerators cannot exceed ~ 150 MV/m due to the vacuum breakdown limit. Second, the magnet arrays used in undulators cannot be made arbitrarily small, but have a minimal period of some millimeters.

So it is obvious that the spread of any technology based on synchrotron radiation, regardless its advantages, will be hindered by the limited accessibility of synchrotron sources itself. Laser-plasma lightsources may be able to surpass these limitations.

As an example, Figure 1.3 shows the results from an experiment on laser-driven electron acceleration with the ASTRA GEMINI Laser in 2011 [30]. During the experimental campaign, electrons were accelerated over ~ 10 millimeters to GeV-energies and emitted synchrotron-like hard X-ray. The spatial coherence of these X-ray was indeed sufficient to acquire phase contrast radiographies of a specimen.

This experiment is representative for the state-of-the-art of laser-plasma lightsources at the beginning of this work. In the following we will therefore discuss qualitatively how this experiment worked and what particular challenges the technology still faces.

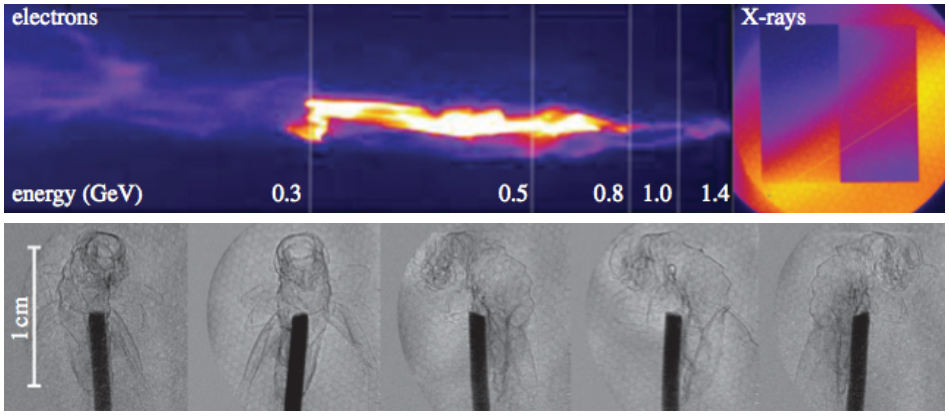

Figure 1.3 – Top: Electron beam spectrum and X-ray signal observed in 2011 at the ASTRA GEMINI Laser. The laser plasma accelerator is operated in the transverse self-injection regime and therefore the beam energy spread and divergence are elevated. Bottom: Propagation-based phase contrast images of a specimen at different angles from the same experiment.

1.2.1 The self-guiding, self-injecting and self-radiating regime

The main advantage of laser-plasma accelerators to conventional RF accelerator technology is that the plasma can sustain substantially higher fields, reaching TV/m. A laser-plasma accelerator (LPA) can boost electrons to GeV level energies over a centimeter, within a plasma cavity of some tens of micrometers. Also, due to the small dimensions of the cavity the accelerated electron bunches have a much shorter duration than in conventional facilities, usually in the femtosecond regime. In addition, the source size is in the micrometer range, hence the phase space volume of the beam is very small. Most early experiments on laser wakefield acceleration share on a fairly simple setup, relying in laser self-focussing and self-injection of electrons.

In this scheme a high power laser is focused onto a helium target, which is immediately ionized by the leading edge of the pulse. The intensity gradient of the focused laser leads to a net acceleration of particles away from high intensity regions. This so-called ponderomotive force scales as $F_p \propto \langle \vec{A}^2 \rangle / \gamma$, so the force is proportional to the mean square of the vector potential $\langle \vec{A}^2 \rangle$ and thus acts in the same direction for both electrons and ions. Yet the widely different inertia of both species lead to disparate acceleration rates $\ddot{x}_{ion} = \frac{m_e}{m_{ion}} \ddot{x}_e \ll \ddot{x}_e$, wherefore charge separation is induced. Depending on the laser intensity this can range from a weak density perturbation up to a complete electron blowout, cf. Fig.1.4.

The transverse extension of the electron rarefaction is usually of the order of the laser spot size, while its length is restricted by the fact that electrons feel a restoring force from the ion background. The longitudinal extension is therefore limited by the (relativistic) plasma wavelength $\lambda_p \propto \sqrt{\gamma_e / n_e}$. The relativistic regime is reached if the laser potential is sufficient

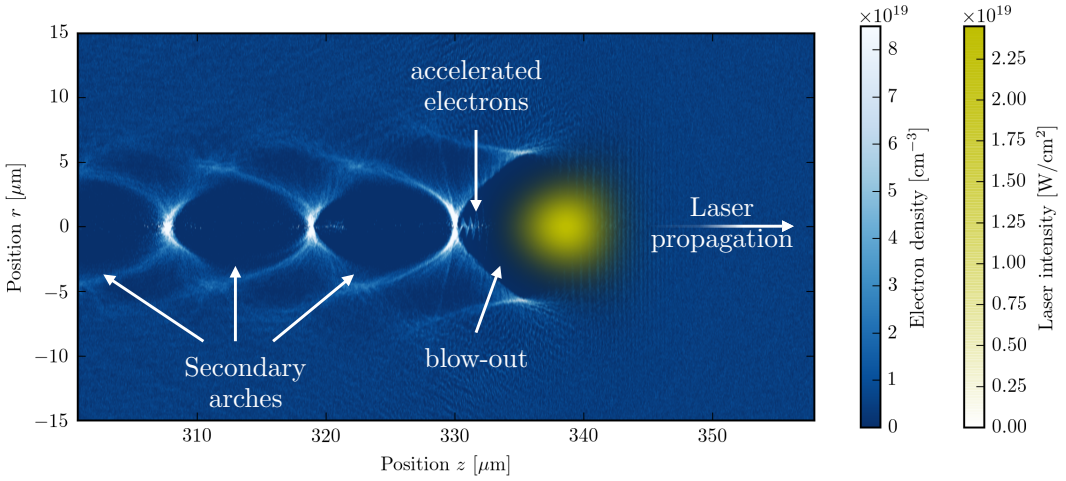

Figure 1.4 – Snapshot from a simulation of laser wakefield acceleration. Electrons are injected in the back of the ion cavity formed behind the laser pulse (yellow). Due to initial transverse momentum during the injection the electrons perform betatron oscillations within the cavity, which leads to the emission of synchrotron radiation in direction of propagation.

to accelerate electrons to relativistic velocities, i.e. the normalized peak vector potential $a_0 = eA_0/m_ec^2 > 1$.

The ponderomotive expulsion and relativistic mass increase will also modify the dispersion relation, leading to relativistic self-focusing of the laser pulse [31]. As discussed in the preceding paragraph, fluctuation of the laser intensity due to this effect and variations of the local ion density will affect the cavity size. This alters the wake velocity and facilitates injection of background electrons into accelerating part of the cavity, a process known as self-injection.

Once injected, electrons will gain energy from the potential inside the plasma cavity, which is close to parabolic in both longitudinal and transverse direction. Electrons with non-zero transverse momentum perform so-called betatron oscillations and emit broadband synchrotron radiation.

Apart from its poor shot-to-shot stability, the main disadvantage of this setup is that it is impossible to tune parameters like electron energy, charge, divergence and X-ray yield independently. For example, best X-ray results are achieved with electron beams of worst emittance, whereas mono-energetic, well-confined electron beams emit weak up to non-measurable betatron radiation. Ergo, there is a need for more sophisticated solutions which allow to control different parameters of the laser-plasma source independently over a wide range. As in conventional lightsources this involves individual improvement of the stages of injection, acceleration, beam transport and radiation generation.

1.2.2 Stages of laser-plasma lightsources and thesis outline

As laser-plasma accelerators operate in an already ionized medium, there is no need for a cathode to provide free electrons. Instead the challenge of the injection stage is to couple non-relativistc plasma background electrons to a plasma wave that propagates at a velocity close to the speed of light. The first experiment to achieve this in a controlled manner was presented in 2006 [32], and since then many different schemes have been proposed controlled particle injection. **Chapter 2: Injection** of this work focuses on experimental results on two injection mechanisms: injection due to cavity expansion in sharp density gradients and injection triggered by late ionization of higher charge states.

Once an electron is injected, it will be accelerated until either the laser-driver cannot sustain the wake anymore, or until the different velocities of electrons and driver let the electrons go off resonance, resulting in deceleration. In order to mitigate the effects of such *dephasing*, it has been proposed control the wake velocity via density tailoring. In **Chapter 3: Acceleration** we present analytical, numerical and experimental results on electron rephasing in the blowout regime using sharp density gradients. Also, we present experimental data that suggest electron acceleration beyond laser depletion due to wakefields driven by the electron bunch itself.

A central drawback of laser-accelerated beams is their large divergence compared to conventional accelerators. If not collimated close to the accelerator exit, this can lead to severe degradation of the beam quality. Yet conventional beam optics are not powerful enough to achieve collimation on a millimeter scale. In **Chapter 4: Beam Transport** we will discuss how transverse wakefields can be used instead. Following a theoretical comparison of such plasma lenses to conventional beam optics, we present experimental results on electron beam focusing in a laser-driven wakefield lens. Furthermore we introduce the concept of electron defocusing via density tailoring, which can possibly amplify betatron radiation.

Speaking of which we come to the last stage: **Chapter 5: Radiation Generation**. Here we are going to discuss several methods to produce energetic photon beams with laser-accelerated electron beams. First we use bremsstrahlung conversion, similar to a conventional X-ray tube, to create MeV level radiation. This techniques has been demonstrated before, however the combination with ionization injection allows the - to our knowledge - first stable operation of such a source over hundreds of shots. Then we present results on synchrotron sources. First we investigate radiation generation via Compton backscattering. This section comprises a numerical investigation of different scattering geometries and experimental results using an all-optical scheme presented a few years ago. Finalizing the work, a larger part is dedicated to the improvement of betatron radiation, showing significant signal enhancement in density tailored plasmas and increased stability and polarization for ionization injected beams.

1.3 Basic laser-plasma interaction and acceleration

In this section we will establish a theoretical basis of laser-plasma interactions that we are going to build up on in the following chapters. Principal findings and definitions are also reviewed in the formulary.

1.3.1 Vlasov-Maxwell system

Most generally we are interested in the evolution of a particle distribution in space, velocity and time $f(\vec{x},\vec{v},t)$. In a collisionless system, were particles are neither created or destroyed, the continuity equation is valid

$$\frac{df}{dt} = \frac{\partial f}{\partial t} + \nabla_x \cdot \left(\frac{\partial \vec{x}}{\partial t} f\right) + \nabla_p \cdot \left(\frac{\partial \vec{v}}{\partial t} f\right) = 0. \tag{1.1}$$

In a electron-ion plasma, where the term $\partial_t \vec{v}$ is associated to the Lorentz force, we find that evolution of the distribution function is given by the Vlasov equations

$$\frac{\partial f_e}{\partial t} + \vec{v}_e \cdot \nabla_x f_e - e\left(\vec{E} + \frac{\vec{v_e}}{c} \times \vec{B}\right) \cdot \nabla_p f_e = 0 \tag{1.2a}$$

$$\frac{\partial f_i}{\partial t} + \vec{v}_i \cdot \nabla_x f_i + Z_i e\left(\vec{E} + \frac{\vec{v_i}}{c} \times \vec{B}\right) \cdot \nabla_p f_i = 0 \tag{1.2b}$$

coupled to the Maxwell-equations (cgs-units)

$$\nabla \times \vec{B} = \frac{4\pi \vec{j}}{c} + \frac{1}{c}\frac{\partial \vec{E}}{\partial t} \qquad \nabla \cdot \vec{B} = 0 \tag{1.3a}$$

$$\nabla \times \vec{E} = -\frac{1}{c}\frac{\partial \vec{B}}{\partial t} \qquad \nabla \cdot \vec{E} = 4\pi\rho \tag{1.3b}$$

where

$$\rho = e\int (Z_i f_i - f_e) d^3p, \quad \vec{j} = e\int (Z_i f_i \vec{v}_i - f_e \vec{v}_e) d^3p. \tag{1.4}$$

This set of equations completely describes the behavior of a collisionless plasma. However, in order to extract useful information from it we need a way to solve these equations in some way. In particle-in-cell (PIC) codes the Maxwell equations are solved on a numerical grid. Meanwhile the Vlasov equation is solved continuously using a set of macroparticles, each usually representing ~ fC of charge, to probe the density function. PIC codes are the most popular numerical solver for this problem and were used throughout this work, for example to obtain Fig.1.4. Yet they are numerically demanding and to get first intuition how the laser-plasma interaction works we will pursue a reduced analytical approach.

1.3.2 One-dimensional plasma waves

Let us now consider a simplified set of equations, treating the plasma like a fluid. For the moment we are not interested in the velocity but the density distribution, which can be obtained by integrating Vlasov equation over velocity space $\mathrm{d}^3 v$, i.e. $\int \frac{\mathrm{d}}{\mathrm{d}t} f(x,v,t)\mathrm{d}^3 v = 0$. This leads to the continuity equation of particle density, whose unidimensional form is written as

$$\partial_t n_e(z,t) + \partial_z j(z,t) = 0. \tag{1.5}$$

It is common to describe the interaction in a frame moving at the phase velocity v_ϕ along the z-axis

$$\xi = z - v_\phi t \qquad \text{and} \qquad \tau = t \tag{1.6}$$

where the laser pulse appears only slowly varying in proper time τ and is nearly stationary. This quasi-static approximation allows us to express the differentials ∂_ξ and ∂_τ in terms of the phase velocity of the pulse. Also, the electrodynamic Maxwell equations can be reduced to the electrostatic Poisson equation. As shown in [33] this leads to the reduced system

$$\frac{d^2\Phi(\xi,\tau)}{d\xi^2} = -k_p^2\,(n_0(\tau) - n_e(\xi,\tau)) = k_p^2 \delta n(\xi,\tau) \tag{1.7}$$

$$\delta n = n_e - n_0 = \left(\frac{1}{1 - v_z/v_\phi} - 1\right) n_0, \tag{1.8}$$

where we have expressed the current $j = -e n_e v_z$ in terms of electron density n_e and fluid velocity v_z. In the limit $\beta_\phi \to 1$ we get then

$$\frac{1}{k_p^2}\frac{\partial^2}{\partial\xi^2}\Phi = \frac{n_e}{n_0} - 1 = \frac{\beta}{1-\beta} = \frac{\beta}{1-\beta}\frac{\gamma}{\gamma} = \frac{p_z}{\gamma - p_z}. \tag{1.9}$$

What is missing now is an expression for the particle momentum evolution p_z in terms of the potential. Such can be found from the relativistic Lagrangian for an electron in an external field $\Phi(\xi)$ [34]

$$\mathscr{L} = -\sqrt{1-\beta_z^2} + \Phi(\xi), \tag{1.10}$$

which via Legendre transformation leads to the Hamiltonian [2]

$$\mathscr{H} = \gamma(1 - \beta_z\beta_\phi) - \Phi(\xi). \tag{1.11}$$

As there is no explicit time dependence, the Hamiltonian is conserved $\mathscr{H}(t) = \text{const.}$, where the constant is defined by the initial conditions. For a particle initially at rest ($p_z(t=0) = 0$

[2] $\mathscr{H} = P\cdot\dot{\xi} - \mathscr{L} = p_z(\beta_z - \beta_\phi) - \mathscr{L} = -\frac{p_z}{\beta_z}(\beta_z^2 - \beta_z\beta_\phi) + \gamma^{-1} - \Phi(\xi) = -\gamma((1-\beta_z^2) + (1-\beta_\phi\beta_z)) + \gamma^{-1} - \Phi(\xi) = \gamma(1-\beta_z\beta_\phi) - \Phi(\xi)$.

and $\gamma(t=0)=1$) we find

$$\gamma = 1 + \Phi + p_z. \tag{1.12}$$

It can be shown [33] that the transverse particle momentum $p_\perp$ follows the vector potential a and as the energy of a relativistic particle is given by $\gamma = \sqrt{1+p_\perp^2+p_\parallel^2}$, we find

$$\gamma = 1 + p_z \rightarrow \gamma^2 = 1 + 2p_z + p_z^2 = 1 + p_\perp^2 + p_z^2 = 1 + a^2 + p_z^2 \tag{1.13}$$

and therefore we find an equation for the longitudinal momentum

$$p_z = \frac{1+\Phi}{2}\left(\frac{1+a^2}{(1+\Phi)^2} - 1\right) \tag{1.14}$$

From (1.12) we know that $1+\Phi = \gamma - p_z$ and so we can combine (1.9) and (1.14) to the non-linear one-dimensional plasma wave equation

$$\frac{\partial^2}{\partial\xi^2}\Phi = \frac{1}{2}\left(\frac{1+a^2}{(1+\Phi)^2} - 1\right)k_p^2. \tag{1.15}$$

In the upper frame of Fig.1.5 solutions for the potential Φ, the electric field E and the density perturbation δn based on (1.15) are shown. The plasma wave is excited by a $\sin^2$-envelope laser pulse with a duration of $\tau_0 = \lambda_p/2c_0$. The field strength is expressed in units of the electron rest mass $m_e c^2$, which is convenient to distinguish between the linear non-relativistic regime and the non-linear relativistic regime. In this case the normalized peak vector potential $a_0 = e\vec{A}_0/m_e c$ has a value $a_0 = 0.2$, i.e. the laser pulse induces only weak density perturbations and the transverse electron motion remains non-relativistic ($p_\perp \ll m_e c^2$).

1.3.3 Linear wakefields and particle acceleration

We have seen in Fig.1.5 that the electric field in the wake of the pulse seems close to sinusoidal. Assuming a weak excitation ($a \ll 1$ and $\Phi \ll 1$) the wave equation (1.15) reduces to

$$\left(\frac{\partial^2}{\partial\zeta^2} + k_p^2\right)\Phi = k_p^2\frac{\langle a^2\rangle}{2}. \tag{1.16}$$

Here $\langle a^2\rangle/2$ is the ponderomotive potential of the pulse, which represents the average effect of the field integrated over a laser cycle. In a similar way one defines the one-dimensional ponderomotive force $F_p = \partial_\xi\langle a^2\rangle/2$ as the net effect of the Lorentz force over one laser period.

Equation (1.16) is an inhomogeneous Helmholtz equation and it can be shown [35] that for a laser pulse at position ξ_0

$$\Phi = \frac{a_0^2}{4}c_{\text{env}}\sin[k_p(\xi-\xi_0)]. \tag{1.17}$$

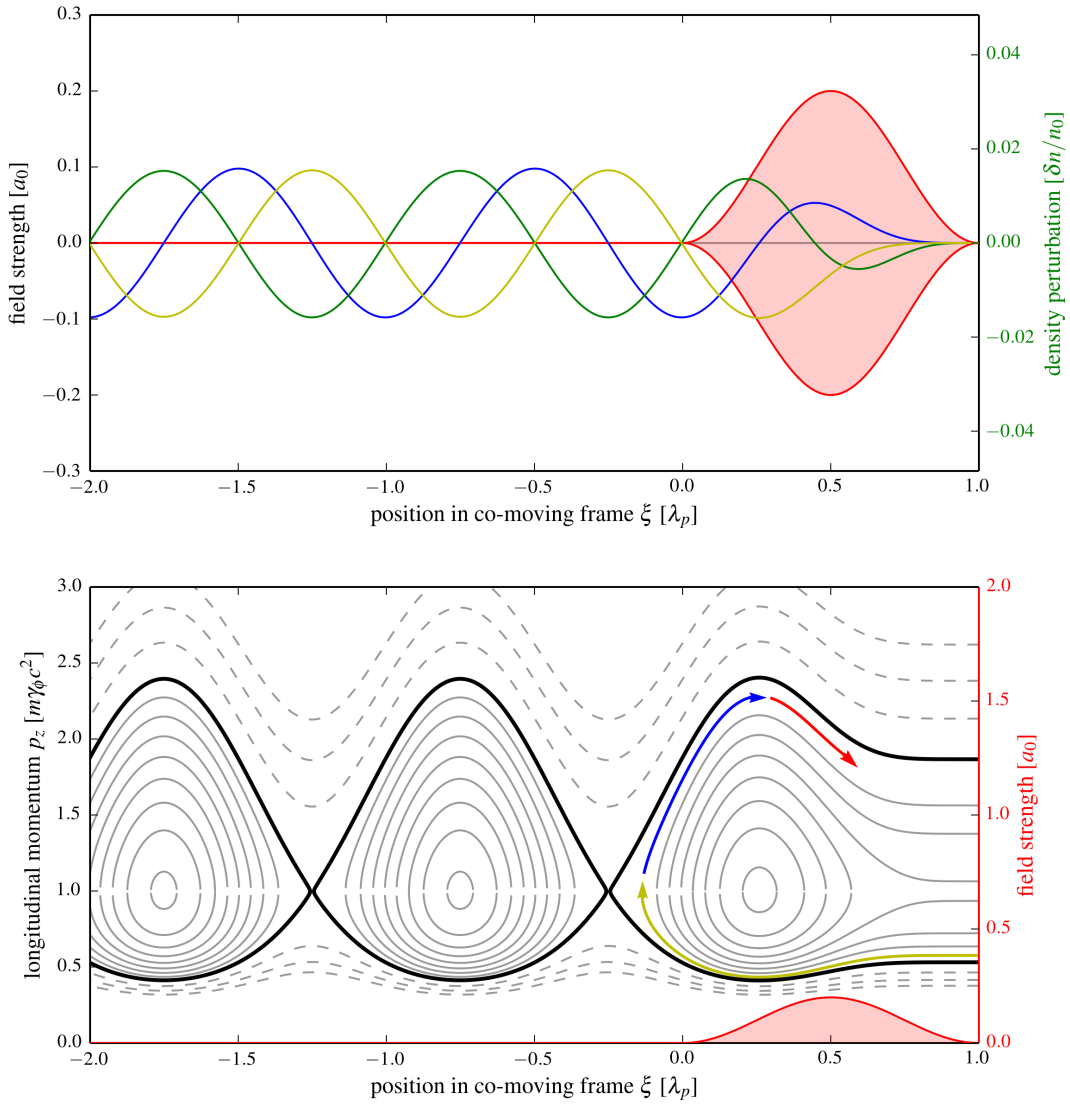

Figure 1.5 – Upper frame: Solution of the one-dimensional wakefield equation for a pump pulse with a peak field strength $a_0 = 0.2$ and a $\sin^2$-shaped envelope with FWHM of $\lambda_p/2$. The laser induced density perturbation (linear plasma wave) is marked in green, while the longitudinal electric fields are in blue and the potential is plotted in yellow. For visualization purposes the sign of δn is flipped and both E_z and Φ are plotted in arbitrary units.
Lower frame: Solution of the hamiltonian for the above potential. The injection (discussed in Ch.2) is marked in yellow. We define an electron as injected into the wake as soon as it co-propagates with the wake, i.e. $p_z = m\gamma_\phi c^2$. During the acceleration process (shown in blue), the electrons gains significantly in energy, until it has advanced over half a plasma wavelength (linear dephasing length), when it starts to experience decelerating longitudinal fields (red). Note that the above solution is normalized in terms of the plasma density, meaning that it is just dependent on the pump pulse and not on the density anymore.

Here c_{env} is a coefficient that reflects how well the pulse envelope couples to the wakefield.[3] From (1.17) we see that the electric field $E_z = -\partial_z \Phi$ evolves according to

$$E_z = \frac{a_0^2}{4} \frac{mc\omega_p}{e} c_{\text{env}} \cos[k_p(\xi - \xi_0)], \tag{1.18}$$

which is indeed sinusoidal. Assuming a resonant pulse ($c_{\text{env}} \sim 1.5$), we find that the maximum field strength is of the order of

$$|E_{z,max}| \sim \frac{a_0^2}{3} \times 96 \sqrt{n_0 [10^{18}\text{cm}^{-3}]} \text{ GV/m}. \tag{1.19}$$

This means that in the above scenario with $a_0 = 0.2$ and assuming a plasma density of $n_0 = 10^{18}\text{cm}^{-3}$ the electric fields reach over 1 GV/m. This is an order of magnitude higher than the strongest fields achievable in conventional RF cavities, whence the attractiveness of plasma waves for acceleration. As we will discuss in Sec.3.2 the fields can reach even beyond TV/m in the highly non-linear regime.

As we have already derived an equation for the Hamiltonian and the wake potential, we can use classical mechanics to calculate the energy gain of a particle with a given initial momentum $p_z = \gamma\beta_z$. The solutions are plotted in the lower frame of Fig.1.5.

If $\beta_z \ll \beta_\phi$ the electron gets periodically accelerated and decelerated. In the co-moving frame the electron travels in opposite direction to the laser (i.e. right-to-left) and so the interaction length in the laboratory frame is of the order of some plasma wavelength λ_p. In contrast an electron with a much greater momentum $p_z > m\gamma_\phi c^2$ would catch up, co-propagate and then eventually outrun the plasma wave. As the electrons move into the same direction, the interaction length is of the order $\lambda_p/(\beta_z - \beta_\phi) \gg \lambda_p$. This allows the particle to gain significant energy from the plasma wave. However, in this case we only accelerate particles that are already relativistic.

A special case is the regime in between, within the separatrix. Here particles are originally slower than the driver, but once they experience the wakefield, they are accelerated and catch up, i.e. $\beta_z > \beta_\phi$.[4] In the following **Chapter 2: Injection** we are going to discuss in detail how this is realized experimentally. Once injected, electrons are co-propagating, which means that the interaction length - and therefore the acceleration length - is substantially increased. However, $\beta_z > \beta_\phi$ implies that the electron advances with respect to the driver and it will ultimately reach a region of inverse, decelerating electric field. Such dephasing is the limiting

[3] Depending on the pulse shape the coefficient is

$c_{\text{env}} = [1 - (k_p\sigma_z/\pi)^2]^{-1} \sin(k_p\sigma_z)$ ($\sin^2$ pulse)

$c_{\text{env}} = \sqrt{\pi/4\log(2)}(\omega_p\tau) \exp[-(\omega_p\tau)^2/16\log(2)]$ (gaussian pulse)

[4] In the co-moving frame this just means that they turn.

factor of most laser-plasma accelerators and in **Chapter 3: Acceleration** we will discuss how to mitigate phase detuning by changing the driver velocity.

1.3.4 Laser pulse propagation

Both the injection and the acceleration processes are closely linked to the phase velocity of the plasma wave v_ϕ. At a constant plasma density v_ϕ is entirely determined by the laser driver and it will therefore be useful for the following chapters to introduce some concepts of laser pulse propagation in cold collisionless plasmas.

In such a plasma the phase and group velocity are given by

$$v_{ph} = \frac{\omega_0}{k} = \frac{c_0}{\eta} \qquad \text{and} \qquad v_g = \frac{d\omega_0}{dk} = \eta c_0, \tag{1.20}$$

where $\eta = \sqrt{1-\omega_p^2/\omega_0^2}$ is the refractive index. If the plasma frequency ω_p is equal or higher than the laser frequency ω_0, the plasma is called overdense and the laser gets reflected. The density at which this transition occurs is called the critical density n_c. In contrast, for an underdense plamsa ($n_e \ll n_c$) we can approximate $\eta \simeq 1-\omega_p^2/2\omega_0^2$. While this relationship is quite accurate for linear wakefield generation, intense laser pulses enter the regime of relativistic optics ($a_0 > 1$). As we have mentioned in the previous section, the plasma frequency changes at relativistic intensities. This modifies the refractive index to $\eta \simeq 1-\omega_p^2/2\gamma\omega_0^2$. The average momentum gain comes mostly from transverse acceleration $a_0 = p_\perp$, so $\gamma \simeq \gamma_\perp\sqrt{1+\langle a_0^2\rangle}$.

The laser induced particle motion will also locally modifying the plasma density as $n = n_0 + \delta n$, which is the ponderomotive blowout. Including both effects we find [36]

$$\eta \simeq 1 - \frac{1}{2}\frac{\omega_p^2}{\omega_0^2}\left(1 + \frac{\delta n}{n_0} - \frac{\langle a_0^2\rangle}{2}\right), \tag{1.21}$$

where we assumed again weak perturbations ($\delta n \ll n_0$) and field strength ($a_0 < 1$).

The change of the refractive index creates a lensing effect, leading to self-focussing of the laser pulse. According to its physical origin the δn component is also called ponderomotive self-focusing [37, 38], while the a_0^2 term is called relativistic self-focusing [39, 40]. The latter is predominant for weak drivers. For a gaussian beam of waist w_0 we can equate the beam diffraction near focus ($\partial^2 w/\partial z^2 \approx 4/\omega_0^2 w_0^3$) with the relativistic self-focusing term ($\partial^2 w/\partial z^2 \simeq -(a_0\omega_p/\omega_0)^2/8w$) and find that the spot size evolves according to [36]

$$\frac{\partial^2 w}{\partial z^2} = \frac{4c_0^2}{k_0^2 w_0^3}\left(1 - \frac{1}{32}a_0^2 w_0^2 \omega_p^2\right). \tag{1.22}$$

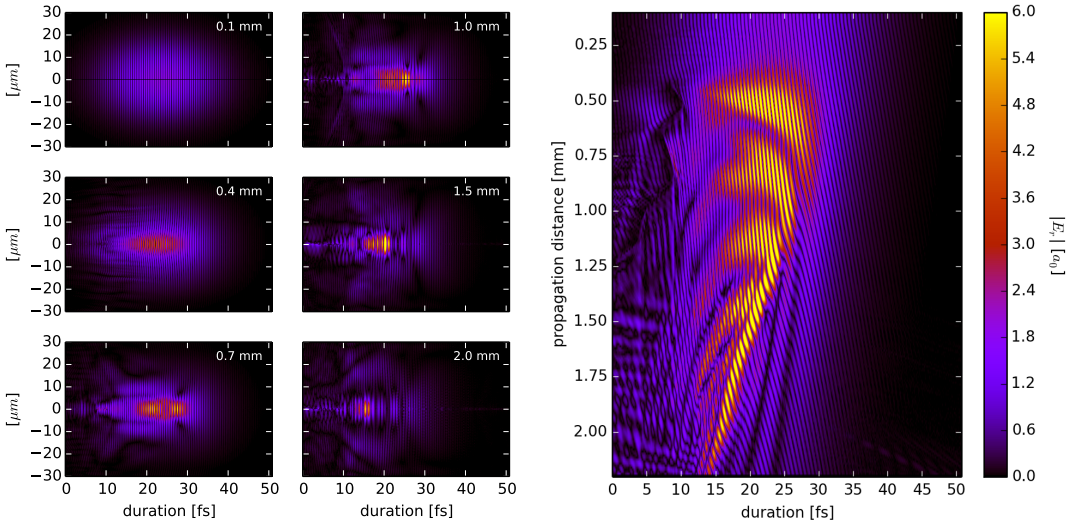

Figure 1.6 – Particle-In-Cell simulation of the evolution of a laser pulse of 800 nm wavelength (no chirp) in a plasma. The pulse is focused to 18 μm waist ($\sim$ f/18), which corresponds to a Rayleigh length $L_R \sim 1.26$ mm in vacuum. The focus is at the entrance of a gas cell at $z = 0.1$mm. From this point the plasma density rises linearly from zero to 8.0×10^{18}cm^{-3} at $z = 1.0$ mm and remains constant beyond this point.
The left side shows the beam waist and duration for different propagation distances, while the plot on the right side shows the evolution of the on-axis field strength. As the simulation window advances at c_0 the laser velocity can be measured as an angle. In this representation the different velocities of the pulse front and the etching are clearly visible.

This equation indicates that the spot size will diminish if the right-hand side is negative, i.e. $a_0^2 w^2 > 32/\omega_p^2$. The term $a_0^2 w^2$ is proportional to the laser power and we can therefore define a critical power

$$P_c = \frac{m_e c_0^5}{e^2} \frac{\omega_0^2}{\omega_p^2} \simeq 17 \frac{\omega_0^2}{\omega_p^2} \text{ GW} \tag{1.23}$$

for which the laser will undergo self-focusing [40]. Importantly the critical power is inversely proportional to the plasma density.

Self-focusing as described above would be, in principle, a self-amplifying instability. But in reality self-focusing only grows until the ponderomotive self-focusing term takes over in the non-linear regime. This term is then ultimately counteracted by the recoiling force of the ion background. Many experiments operate in this regime, where a quasi-stable equilibrium exists. Once the laser has reached this *matched* spot size, it can be guided over several Rayleigh lengths at relatively stable intensity [41].

To illustrate the complex pulse evolution, Fig.1.6 shows the results of a Particle-In-Cell simulation of the propagation of a laser pulse in a plasma. Up to $z = 1$mm we observe how the

laser self-focuses. At the same time the pulse length reduces. This is a consequence of the ponderomotive $\delta n/n_0$ term, which leads to a reduction of the plasma density in the rear part of the pulse. Accordingly the rear part propagates faster than the front, compressing the pulse (cf. for example $z = 0.7$mm and $z = 1.0$mm).

But we also observe that from $z = 1$mm to $z = 1.5$mm the peak intensity shifts backwards. This so-called etching is the typical signature of pump depletion. This term is important to ensure energy transfer to the wake and it also antagonizes the defocusing effect of the longitudinal ponderomotive force at the pulse front. An analysis based on the one-dimensional wave model (1.15) finds that the etching velocity is given by

$$v_{etch} \simeq \frac{\omega_p^2}{\omega_0^2} c_0. \tag{1.24}$$

Interestingly this value is independent of the wake excitation term a_0 and amplitude ∂n, which cancels out in the derivation [42]. Even this velocity is derived for the non-linear 1D wave model, 3D Particle-In-Cell simulations [41] and experiments [43] find that the estimations from the Decker model are quite accurate, even beyond its initial validity region.

The phase velocity of the plasma wake, given by the propagation velocity of the plasma wave excitation is therefore of the order of the laser group velocity minus the etching term, i.e.

$$v_\phi \simeq v_g - v_{etch} \simeq \left(1 - \frac{3}{2}\frac{\omega_p^2}{\omega_0^2}\right) c_0. \tag{1.25}$$

2 Injection

This chapter concentrates on the problem of particle injection into a propagating accelerating field. First we discuss conventional solutions and their performance, followed by a qualitative overview of laser-plasma injection techniques.

All experiments performed for this work relied on three main injection schemes, namely self-injection, density downramp injection and ionization injection. We will discuss these methods and give examples for beam quality obtained using injection in sharp density transitions and ionization injection.

Contents

As discussed in the introductory chapter linacs, cyclotrons, synchrotrons and also laser wakefield accelerators are types of what is called *resonance accelerators*. In such an accelerator the accelerating field is time-dependent and particles need to stay in phase for sustained energy gain. As a consequence it is necessary that particles are injected into the accelerator stage with a propagation velocity v_e close to the phase velocity v_ϕ of the field.

In conventional accelerator facilities the creation and pre-acceleration of the electron beam is done using a separate device, called the electron gun. An electron gun consists of a cathode that emits electrons, which is coupled to a DC or RF field. In this field, electrons are accelerated to mildly relativistic energies, from whereon they can be injected into the accelerator. While this works well for conventional accelerators, injection into the a plasma wakefield is challenging due to the small cavity size ($\lambda_p \sim 10^{-5}$ m) [44, 45, 46].

Instead, laser-wakefield accelerators rely on the injection of electrons from the plasma itself. Numerous variants of such injection schemes exist, but in an illustrative way we can divide them into two main approaches. The first one is analogous to the electron gun in conventional accelerators, i.e. to accelerate the plasma electrons to relativistic energies. An example of this is optical colliding pulse injection [32]. The second method is to slow down the wake by inducing an expansion of the cavity. As the wake size depends on the plasma density n_e and the laser intensity a_0, variations of these can therefore induce injection. Such variations can happen within the plasma itself, e.g. from self-focussing of the laser pulse. Or can be created intentionally e.g. with a density downramp.[1]

2.1 Conventional injectors

As we have seen before, the main task of the injector is to provide electrons and manage to inject them in phase into a resonance accelerator. In a plasma accelerator the first task this is straightforward as the plasma itself serves as supply of free electrons. However in solids the situation is different, as electrons are still bound and first have to be freed. In fact, the electron extraction at the cathode already defines many beam parameters for the subsequent acceleration.

2.1.1 Cathodes and electron guns

In solids there are three main approaches to free electrons, cf. Fig.2.1. One is to heat the solid so the electron energy distribution extents beyond the binding potential, known as thermionic emission [47, 48]. Another way is to apply a strong electric field and therefore increase the

[1] The central aim of this chapter is to familiarize the reader with different injection methods and to evaluate their performance for coupling them to subsequent stages of a laser-plasma lightsource. An extensive discussion of our results on controlled injection schemes will be published in E.GUILLAUME, **Control of electron injection and acceleration in Laser-Wakefield Accelerators**, Ph.D. thesis (2015) [89].

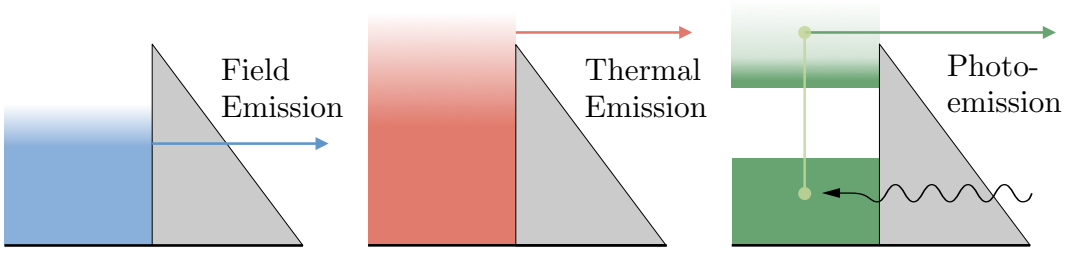

Figure 2.1 – Illustration of the principle of the three main cathode types: Field emitters, thermionic emitters and photocathodes.

tunneling probability of electrons to escape. This process is known as field emission [49, 50].[2] Third, electrons can gain energy to escape from photoelectric absorption [51, 52].

Thermionic and field emitters are widespread due to the simplicity and robustness of the setup. However, the electron bunches created in such devices have a long duration (>100 ps) and are difficult to control. On the contrary, in photoemitters the electron properties are determined by the exciting laser [53], which means that very short pulses with low emittance can be created.

The two main families are semiconductor and metal photocathodes. Semiconductor cathodes can provide high current beams and usually have a good quantum efficiency in the visible, thus allowing the usage of standard (green) lasers. In contrast they require a very good vacuum quality for operation and have the shortest lifetime among all cathode types. Metal photocathodes are much more durable and due to their faster response time (femtoseconds vs picoseconds) they can be used to produce ultrashort electron bunches. Their principal drawback is that metals have a work function of some eV (e.g. 4.65 eV for copper), which requires UV light to free the electrons.

Once electrons are freed they have to be boosted to relativistic velocities. Note that at the moment of emission they are still non-relativistic, so space charge effects are much more important than in any other part of the accelerator. Therefore beam optics are used to shape the beam, while either DC or RF fields are used to accelerate it towards subsequent accelerating sections.

For lightsources the whole range of electron gun types is employed, depending on the specific needs of the facility. For example, at ESRF a thermionic gun produces either 1ns-1nC or 1μs-10nC bunches at an emittance of 35 and 15 mm.mrad, respectively. The bunch is then accelerated to 85 keV in a DC field and coupled to RF cavities [54]. In contrast, the LCLS free electron laser requires short low-emittance beams. It therefore uses a copper photocathode that is illuminated with a 255 nm UV laser. This cathode is capable of producing up to 1nC

[2] Field emission is conceptually related to field ionization we will discuss later in this Chapter. Also, it is one of the primary causes of vacuum breakdown which limits conventional accelerator field strengths, cf. Ch.3.

bunches at 10ps duration with an emittance of 1.2 mm.mrad, which are pre-accelerated in a 115 MV/m RF cavity [55].

2.1.2 Conventional linac as injector of LPAs

Laser-plasma acceleration was demonstrated for the first time in the early 1990s using external injection of electrons into a laser-plasma beat wave. For example the UCLA group showed trapping of 2 MeV electrons inside a wake with $\gamma_\phi = 33$. In these experiments electrons were accelerated in a gradient of ~ 2.8 GeV/m up to 30 MeV. Such plasma beat wave experiments used picosecond laser pulses, with injection electron beams of ~ 10 ps in the case of [56]. Additionally there was a jitter of ±50 ps between both laser and electron beam, leading to an unstable operation with strong energy variations.

However, since the early 2000s another acceleration scheme, resonant laser wakefield acceleration prevails the field of laser-plasma acceleration. In this scheme it is even more difficult to inject the beam as one needs femtosecond bunches and very low jitter.

Due to the short pulse duration, photocathode based injectors are best suited to be coupled to a laser wakefield accelerator. This is for example one of the goals of REGAE (Relativistic Electron Gun for Atomic Exploration) at DESY. Here a Cs_2Te p-type semiconductor photocathode is used as source for low charge (~ 1 pC) electron bunches. Including a section for beam compression, this gun should provide 10-15 fs beams at 3-5 μm RMS width and 0.3 mm.mrad emittance. With a final energy of up to 5 MeV, such an accelerator could be used for external injection in wakefields. However, due to the very low charge produced, RAGAE and similar facilities are principally intended for basic research on wakefield acceleration rather than for applications.

2.2 Laser-plasma injection schemes

As we have seen in the preceding section it is challenging to use conventional electron sources as injector for a wakefield accelerator. An easier way is to use electrons from the plasma itself. As discussed previously the main requirement for injection into a wakefield is that the electrons can maintain phase, which basically reduces to the simple condition that $v_z > v_\phi$ at the rear part of the wake.

For the fluid model that we introduced in the first chapter the condition $v_z > v_\phi$ means that part of the fluid elements is moving faster than the wave, i.e. the wave brakes. Earlier we have seen that the static Hamiltonian for this system is $\mathcal{H} = \gamma(1 - \beta_z\beta_\phi) - \phi$. In the moment of injection ($v_z = v_\phi$), hence $\mathcal{H} = 1 - \phi_{inj}$. Momentum is conserved, so to trap a particle initially at rest, the potential difference needs to be $\phi_{inj} \gtrsim 1$. Using Poisson's equation we find the

non-relativistic *wavebreaking* threshold in a cold plasma [57]

$$E_0 \simeq \frac{m_e c \omega_p}{e} = 96\ \mathrm{GV/m} \times \sqrt{n_0\,[10^{18}\ \mathrm{cm}^{-3}]}. \tag{2.1}$$

The above expression is only a rough estimation, as electrons are moving at a speed close to the phase velocity during injection, so a relativistic treatment is unavoidable. This effect becomes more important the faster the wave moves and increases the cold wavebreaking limit by a factor $\sqrt{2(\gamma_\phi - 1)}$.[58]

Earlier we derived the maximum field strength in the linear wakefield regime (1.19), which we can now be rewritten as $|E_{z,max}| \sim (c_{\mathrm{env}} a_0^2/4) \times E_0$. The linear regime is only valid for non-relativistic field strength ($a_0 \ll 1$), so it is apparent that $|E_{z,max}| < E_0$, i.e. wavebreaking cannot occur in the linear wakefield regime.

Self-injection

Instead non-linear plasma waves have to be excited in order to achieve electron injection via wavebreaking. This was first demonstrated in 1995 [59] at the VULCAN laser which delivered 0.8 ps laser pulses at peak intensities of up to $a_0 \sim 1.9$. In this experiment plasmas with densities $n_e > 10^{19}$ cm^{-3} were used. As the pulse is much longer than the plasma wavelength $c\tau_0 \gg \lambda_p$, it is self-modulated and excites a non-linear plasma wave. Wavebreaking lead to continuous *self-injection* of electrons into the wake and the acceleration resulted in Maxwellian electron spectra extending up to 44 MeV.

The advent of high power Ti:Sapphire systems with durations below 100 fs allowed for the first time to operate in a regime of resonant wake excitation ($c\tau_0 \sim \lambda_p$) while guiding the pulse beyond the Rayleigh length via self-focusing ($P > P_c = 17\omega_0^2/\omega_p^2$ GW). This permitted to accelerate electrons up to ~ 200 MeV [60], yet the spectrum was still Maxwellian.

In 2002 it was theoretically predicted that acceleration in the highly non-linear broken-wave regime could lead to beams with monoenergetic features [61]. The publication raised a lot of attention and became widely known as bubble regime. Even the simulated laser parameters ($a_0 = 10$, 33 fs) were beyond the experimental means of the time, first narrow energy spread beams were demonstrated experimentally shortly later [62, 63, 64]. Three different mechanisms were suggested to explain the low energy spread in these experiments: (a) Temporally cavity expansion induced by self-focusing of the laser pulse, (b) inhibited continuous injection due to beam loading and (c) dephasing induced energy spread reduction. In most experimental conditions a combination of all three effects will occur. We will discuss (c) in **Chapter 3: Acceleration** and concentrate for the moment on (a) and (b).

We have stated earlier that the wake that forms behind the laser scales with $\sqrt{a_0/n_e}$. So self-focusing of the laser will increase the wave period. This expansion has two effects. Firstly, it will reduce the phase velocity of the wake as function of the phase ϕ within the wakefield.

Secondly, for a rapid expansion the symmetry between accelerating and decelerating field is temporarily broken, meaning that an electron with proper timing can gain net energy from the wake due to the expansion and gets injected. However, this requires proper timing and hence results in a short injection length. Also, once particles are injected into the wake they shield the ions and reduce locally the wakefield, a process also known as beam-loading.

We distinguish two regimes of such self-focusing driven self-injection [65]. If the initial laser intensity is highly relativistic ($a_0 \gtrsim 3-4$), ponderomotive expulsion leads to a formation of an ion cavity behind the laser pulse. In this case electrons can only get trapped transversely, traveling along the sheaths. To date this *transverse self-injection* is the most common injection mechanism in laser wakefield acceleration. At lower weakly relativistic intensities ($a_0 \sim 1-3$) there remains charge on axis, which can then get injected via *longitudinal self-injection*.

Controlled injection schemes

Self-injection into the wake provides a simple method to trap electrons in a laser-wakefield, however it is not directly controllable and subject to strong shot-to-shot fluctuations. During the last years a number of controlled injection schemes have been proposed or demonstrated that extent the reliability and tunability of the source.[66]

As the wake scales also with the plasma density, alternatively to increasing the laser intensity a cavity expansion can be induced by a reduction of the plasma density. Again, for a weak long gradient the main effect is the reduced phase velocity, leading continuous *down-ramp injection* [67, 68]. In contrast, for a sharp transition, as for example possible to create with shocks, the asymmetric acceleration leads to a short well-located injection [69, 70, 71].

Another way to gain net energy from the wakefield and facilitate injection is via late ionization. To do so a high-Z gas (usually nitrogen or argon) is used to create the plasma. While the outer shells are ionized by the pulse front, the deeper ionization states are only reached close to the peak of the pulse. Electrons are therefore born late into the wake and ideally experience only the accelerating part of the wake [72, 73, 74]. This *ionization injection* leads to continuous injection along the axis, so the beams have a high charge but also large energy spread, as demonstrated for example in [75, 76].

A conceptually similar proposed injection scheme is *cold-optical injection* [77]. Here a second laser pulse leads to a spatially periodic and time-independent beatforce. This force would then freeze the longitudinal electron motion during the decelerating phase of the wake, which again allows the electron to gain net energy from the wake and get trapped.

Alternatively a beat can be used to increase a particles momentum, thus speeding up the particle to facilitate injection. This *colliding pulse injection* has been demonstrated in 2006 [32] and it was shown that the method not only allows to produce monoenergetic particle beams, but furthermore the energy could be tuned by varying the injection position. Also, the

phase-space volume occupied by injected electrons can be varied by changing the scattering pulse energy [78].

Let us now enlarge upon those injection schemes that we used for this work, i.e. self-injection (Sec.2.3), density downramp injection (Sec.2.4) and ionization injection (Sec.2.5).

2.3 Self-injection

To date, self-injection remains probably the most common type of injector used in laser-wakefield acceleration, as it requires no additional external measures. But even self-injection is the simplest type of injection to be set up in an experiment, it is a physically complex phenomenon which can occur under many different circumstances, e.g. in the quasi-linear and the non-linear regime, for both evolving [79, 80, 81] and non-evolving bubbles [82].

To illustrate this, Figures 2.3 and 2.4 show the results of different Particle-in-Cell simulations. The only changing parameter is the plasma density profile, which as we observe, greatly changes the simulations' outcome.[3]

All simulations have in common that the laser pulse evolves during propagation and after ~ 1 mm it reaches a stable spot size. This matched field strength is found to scale about linearly with the plateau density. At high plasma densities the wakefields that build up behind the laser exceed the wavebreaking threshold. In this case electrons gain longitudinal momentum that exceeds the phase velocity (cf. Fig.2.2) and continuous electron injection begins.

The lower the plasma density, the later this wavebreaking initiates. At $n_e = 1.5 \times 10^{19}\text{cm}^{-3}$ injection starts around 0.7 mm into the jet, while at $1.0 \times 10^{19}\text{cm}^{-3}$ it is delayed to ~ 1.5 mm (not shown here) and at $0.8 \times 10^{19}\text{cm}^{-3}$ no electrons are injected at all. This changes however as we modify the density ramp. If the density increases much faster than self-focusing can react, the bubble undergoes important laser-induced fluctuations. An expanding cavity will facilitate injection and via this mechanism electrons can still get injected into the wake. However, in this case injection occurs only over a short distance, leading to a quasi-monoenergetic electron beam, cf. Fig.2.4. Also depending on the laser intensity, electrons can be either injected transversely or longitudinally.

So we have seen that self-injection heavily depends on the laser and plasma evolution. Some regimes are more sensible to fluctuations than others, e.g. low charged injection close to injection threshold is usually more stable in terms of accelerated charge, energy, divergence and pointing, than high density operation, see e.g. [83, 84]. For the aforementioned reasons it is difficult to define a 'typical shot' for self-injection as a whole. Instead we will give some examples of experimentally observed spectra in the following.

[3] The other simulation parameters are as follows: Simulations are performed using CALDER-CIRC at a resolution $\Delta z = 0.3k_0^{-1}$, $\Delta r = 1.5k_0^{-1}$ and $\Delta t = 0.96\Delta z$, with a simulation mesh size $n_z \times n_r = 1500 \times 250$. The laser pulse is identically initiated as well, with parameters similar to SALLE JAUNE (duration of 30 fs, waist of 11.5 microns and peak potential $a_0 = 2.5$).

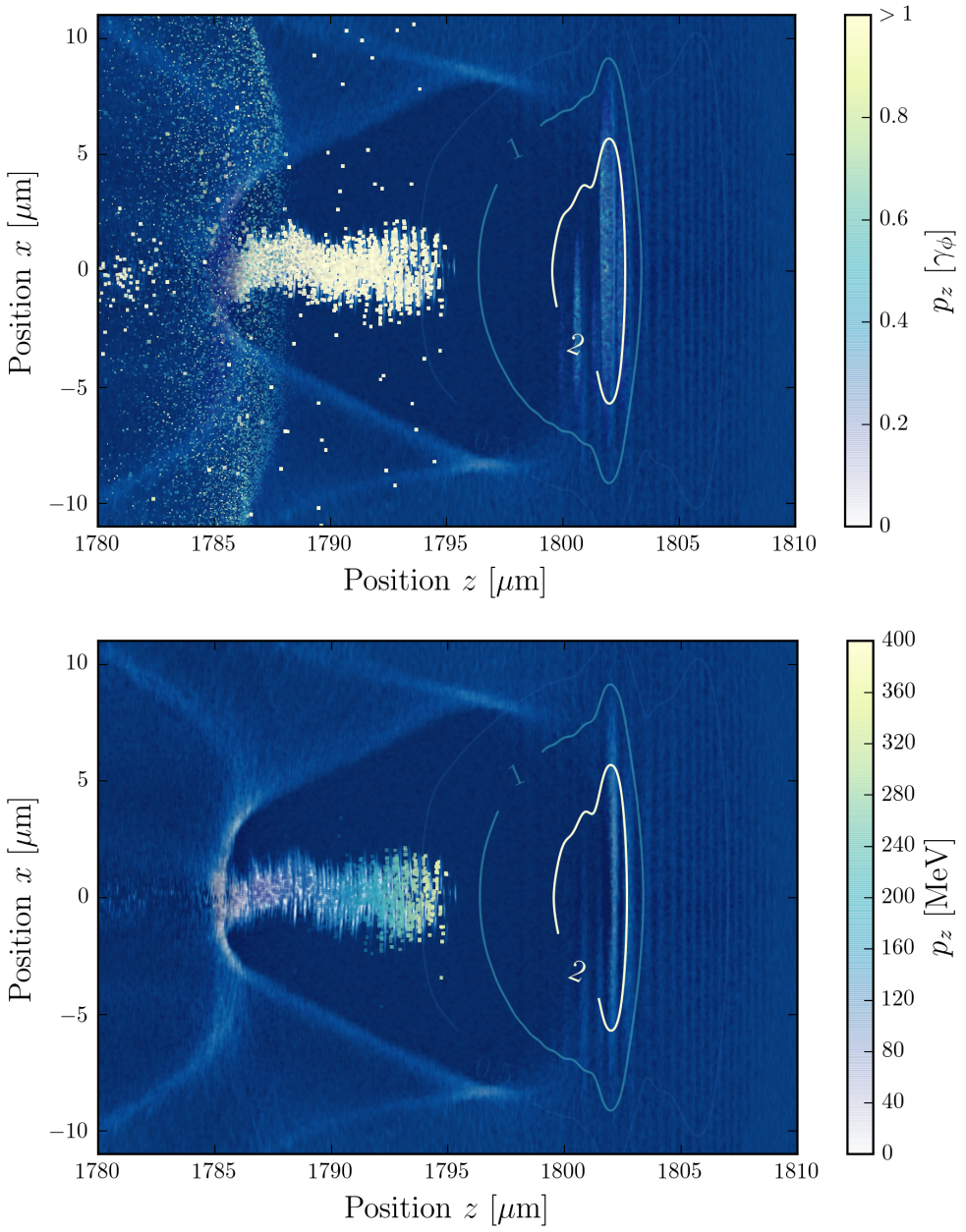

Figure 2.2 – Particle-In-Cell simulation with CALDER-CIRC of self-injection, with macro particles projected onto the density map. The upper frame is normalized to the wake phase velocity $\gamma_\phi = \omega_0/\omega_p$. In this representation it is clear that injected particles are faster than the wake and we can see those which are going to be injected soon in the back of the bubble. In the lower frame the momentum is color-coded in MeV. This illustrates the broadband nature of the electron spectrum, with highest energies at the head of the beam. Pixel area corresponds to the weight, color and transparency to the momentum.

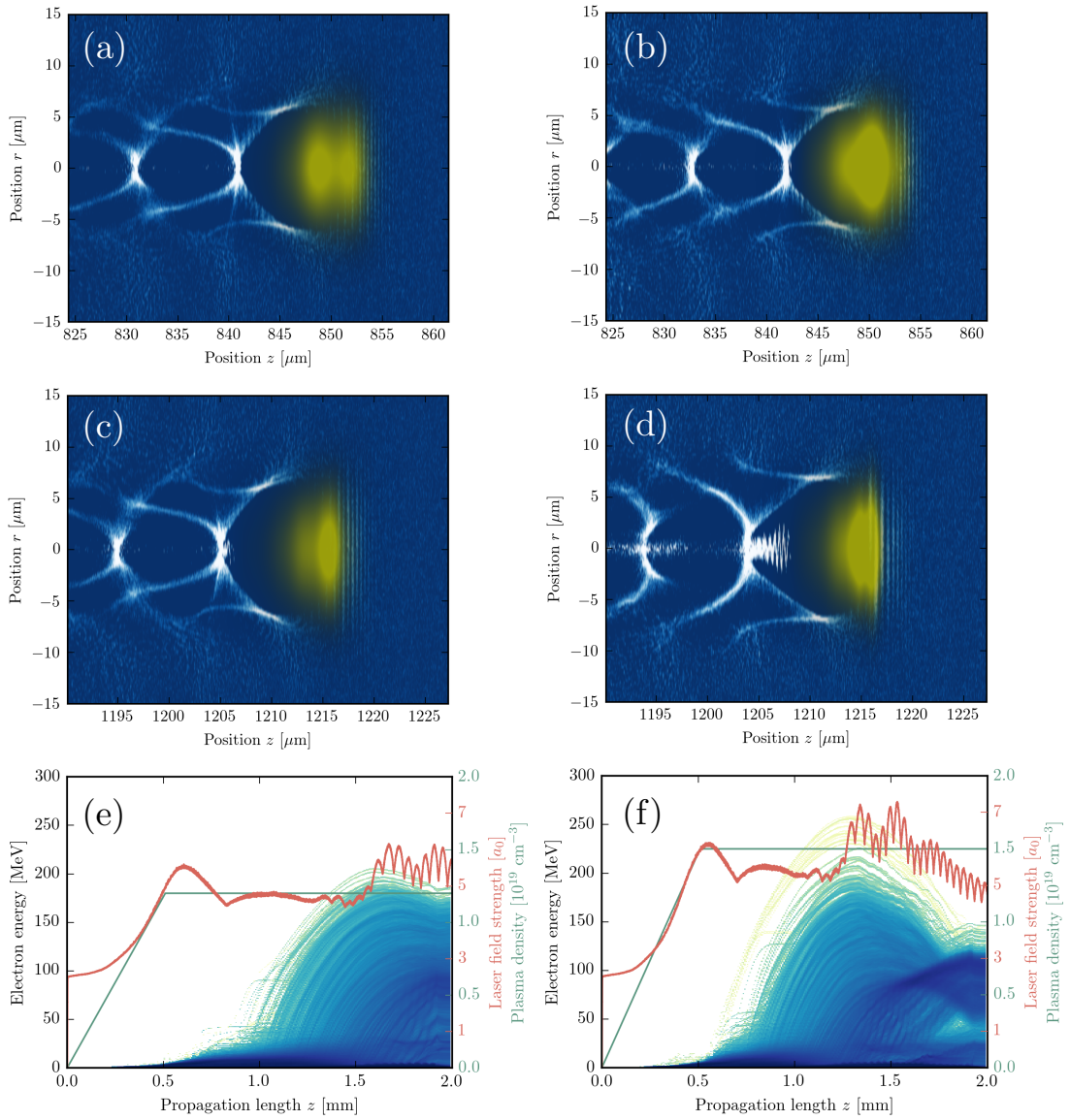

Figure 2.3 – Particle-In-Cell simulation with CALDER-CIRC of self-injection for two different densities, $1.2 \times 10^{19}\text{cm}^{-3}$ on the left and $1.5 \times 10^{19}\text{cm}^{-3}$ on the right. Figures (e) and (f) show the density profiles (solid green) and the corresponding laser pulse evolution (red). The beam spectrum is represented with a logarithmic colorscale, with a charge difference of 10^6 between yellow and dark blue. We see that increasing the plasma density anticipates injection. (a-b) shows the electron density and laser pulse just before injection begins. In (c-d) we see how electrons have been continuously injected into the cavity.

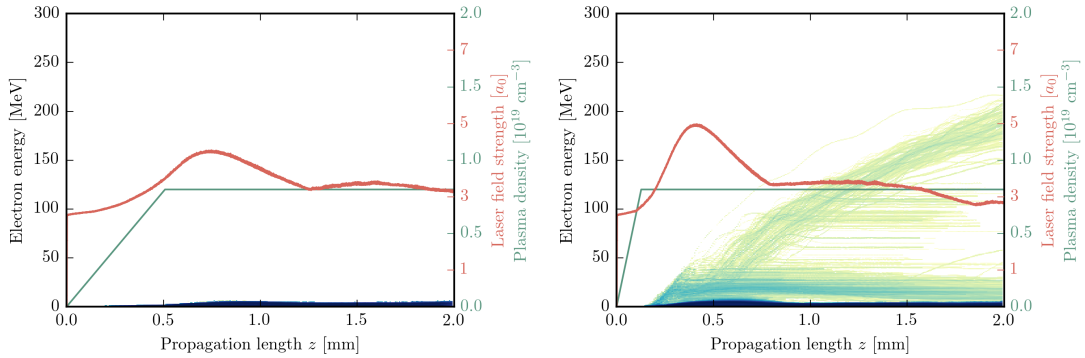

Figure 2.4 – Particle-In-Cell simulation with CALDER-CIRC of self-injection at $0.8 \times 10^{19}\text{cm}^{-3}$. On the left the density ramp is 0.5 mm long, as in Fig.2.3. Clearly this density is below the self-injection threshold and no electrons are accelerated. But for a steeper density ramp (0.125 mm) we observe injection at around $z \sim 0.5$ mm.

Longitudinal self-injection

Longitudinal self-injection occurs at moderately high laser intensities ($a_0 \sim 1-3$), when the laser forms a wake, yet not all electrons are ponderomotively blown out. In this case it is possible for electrons to get injected on axis, usually during laser self-focusing, when cavity expansion facilitates injection. Longitudinal self-injection is limited to the quasi-linear regime and thus only happens early during the laser propagation. It therefore leads to higher energies than transverse self-injection. In contrast the injected charge is much less, typically some pC. Longitudinally injected beams have usually a divergence of some millirad and a reasonable shot-to-shot stability. Longitudinal self-injection will be used in Sec.4.4.3, cf. Fig.4.11.

Transverse self-injection

In contrast, transverse self-injection takes place in the blow-out regime, when sheaths electrons get trapped during an expansion phase or when the wakefields exceed the wavebreaking threshold. Most experiments that use self-injection operate in this regime and it is characteristic that electrons that originate from this mechanism have higher transverse momentum.

The transition between both self-induced self-injection processes is related to the laser field strength, which is usually defined by self-focusing and therefore density dependent. At lower densities, below the transverse self-injection threshold, only longitudinal injection takes place. However, at higher densities (or longer propagation lengths) transverse self-injection will dominate by far, as this regime allows injection of some hundred pC into the wake. It has been shown that when operated close to the injection threshold transverse self-injection can lead to quasi-monoenergetic beams. Experiments relying on transverse self-injection are discussed in sections 3.4.4, 5.4.2 and 5.5.3.

2.4 Density transition injection

Injection in a density transition is conceptually related to self-injection, with the difference that the cavity expansion is triggered by a rapid reduction of the plasma density. [69, 85, 86]

To illustrate the effect we simulate the propagation of a laser with intensity $a_0 = 2.5$ in a plasma using CALDER-CIRC.[4] The density of the plasma is chosen relatively low ($n_e < 10^{19}$ cm^{-3}) in order to avoid self-injection, as shown in Fig.2.5c. Also, there is an initial density upramp which prevents injection before the jump. Fig.2.5a shows the wake just before the density transition and (b) behind the 50 µm long transition from $n_e = 1 \times 10^{19}$ cm^{-3} to 0.6×10^{19} cm^{-3}. In Fig.2.5b we observe that there is now a short electron bunch where the trajectory crossing occurred before the cavity expansion. The length of this bunch is less than a micrometer, corresponding to a duration of $\lesssim 3$ fs. We will come back to the subsequent acceleration of the bunch (Fig.2.5c) in Chapter 3. Let us now discuss how density profiles, such as used for this simulation, can be realized in an experiment.

Creating sharp density transitions

It has been shown that sharp density transitions in a plasma can be created by either controlling the gas flow [70] or by means of a second laser pulse [87]. For this work we have chosen the former scheme, where an obstacle is placed within the path of a supersonic gas flow, leading to the formation of a shock front.

The sharpness of the density transition created through this process depends on ratio between the fluid velocity v and the velocity of sound c at the location of the obstacle, which is given by the Mach-number $M = v/c$. In subsonic gas flows the information about the obstacle in the path can travel upstream, thus forming a smooth density profile. In contrast when the flow is faster than the speed of sound a shock front, a sharp density and pressure transition forms.

In case of a thin object (e.g. as a wire) the shock propagates downstream in both directions, forming an 'M'-like density profile [88]. On contrast, if a larger object is moved from outside into the stream (for instance a razor blade), the shock can only propagate inwards of the jet, cf. Fig.2.6a. The density profile changes downstream, with the transition becoming smoother. In order to provide sharpest transitions, the laser is therefore focused just above the blade.

As stated before, sharpness and ratio of the density transition critically depend on the Mach number. The Mach number increases with distance to the nozzle exit, so the shock becomes sharper and more pronounced the further away the blade is placed from the jet. Also the shock should occur early during the laser propagation in order to minimize laser depletion and maximize the remaining propagation distance. For this the blade should be placed close to the entrance of the jet.

[4] All simulation parameters except the density profile are the same as in Sec.2.3.

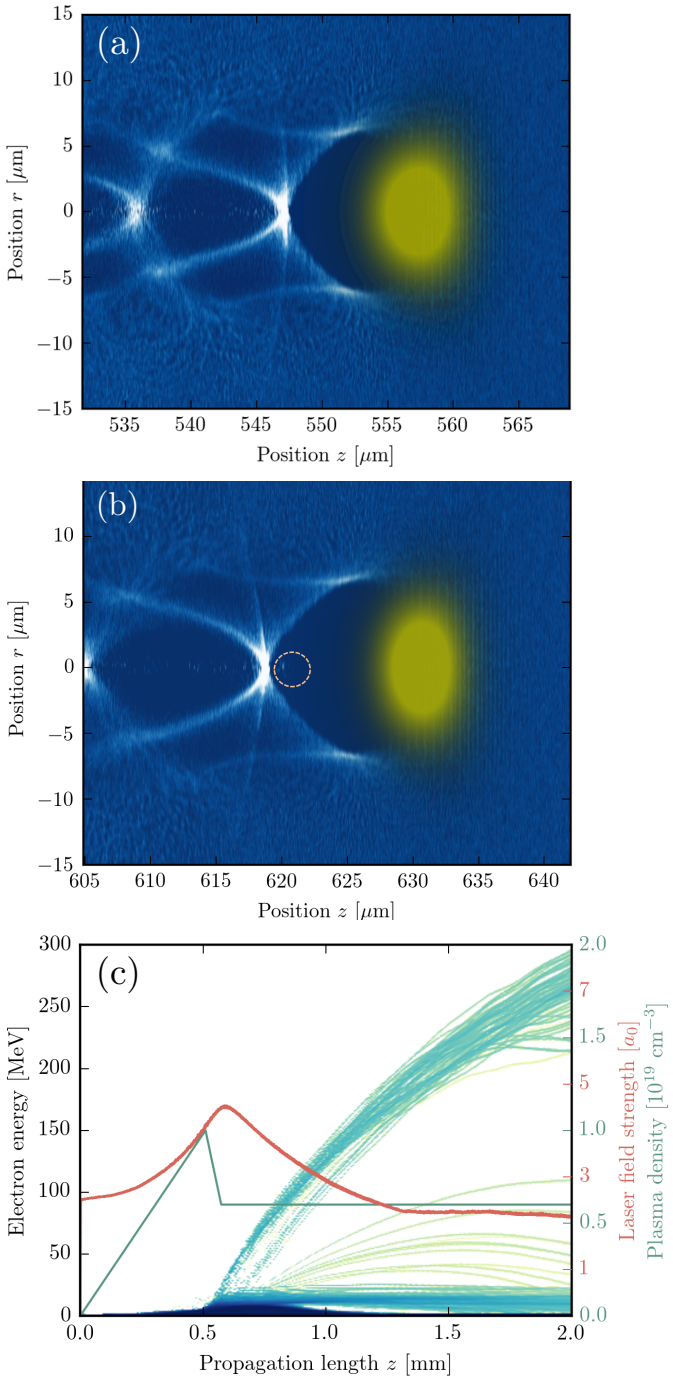

Figure 2.5 – Particle-In-Cell simulation with CALDER-CIRC of shock injection. (a) shows the electron density and laser pulse just before the density transition. After the transition (b) an electron bunch has been injected into the wakefield. (c) shows the plasma density profile used in the simulation (green line) and the evolution of the beam spectrum for along the jet. All parameters are the same as in Fig.2.3, except the density profile.

In previous experiment metallic razor blades were used to create the shock. However, after extensive tests, we found that using cut silicon wafers lead to better results.

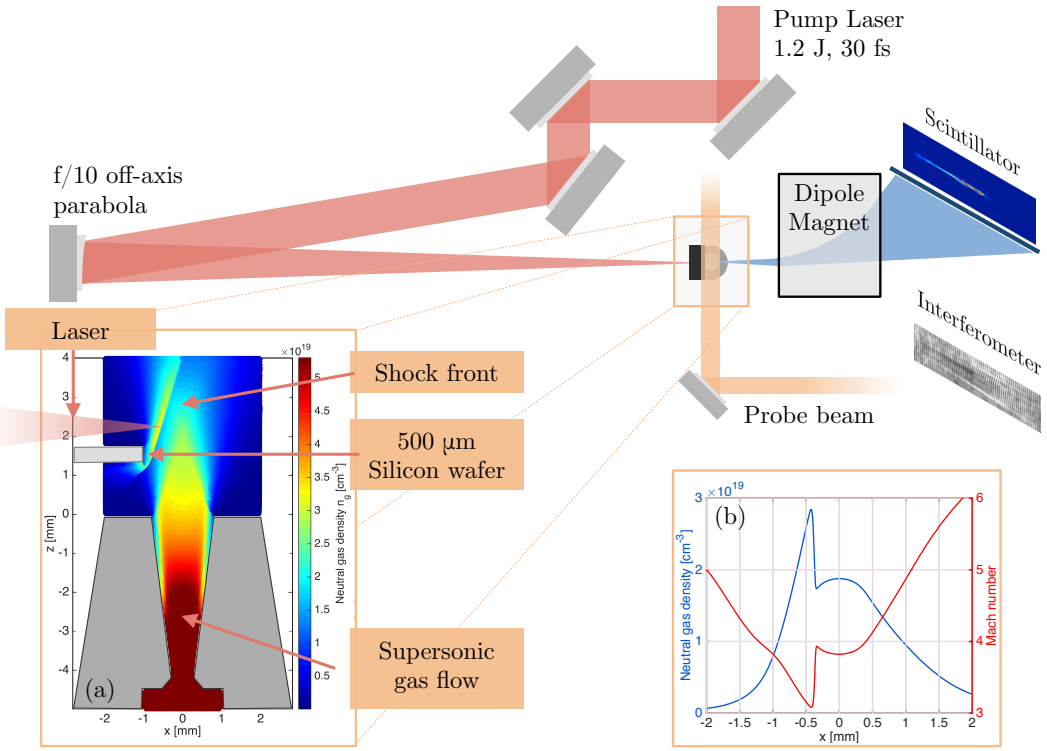

Figure 2.6 – Experimental setup for electron injection in sharp density transitions. (a) ANSYS FLUENT simulation of shock generation in a supersonic gas flow. (b) Density and Mach number transverse line-outs of the gas flow at z = 3 mm.

Experimental results

The experiment is performed at a background density below the self-injection threshold, in this case $n_e \sim 1.2 \times 10^{19}\text{cm}^{-3}$. This ensures that the results are not disturbed by additional self-injection.

We find that shock injected beams are much more stable than self-injection. Typical angularly resolved spectra are shown in Fig.2.7, where the peak varies within 121 ± 5 MeV, corresponding to 4.5% variation. In some experiments we observe a double energy peak structure, with two beams separated by about 10 MeV.

We find that by moving the blade over a distance 0.6 mm to 1.3 mm (measured from the center of the jet and $x = 1.5$ mm is outside the gas flow) the beam energy could be tuned from 75 to 250 MeV. The injected charge ranges from 3 to 15 pC, while the divergence is typically

between 2-4 mrad. The variation in charge can be explaineded by the width of the shock, which changes with the blade position. The closer the blade is placed to the center the wider the shock becomes, and so does the injection region.

More results on shock injection will be presented in [89]. In the context of this project we have employed shock injected beams for rephasing experiments in Sec.3.4.6.

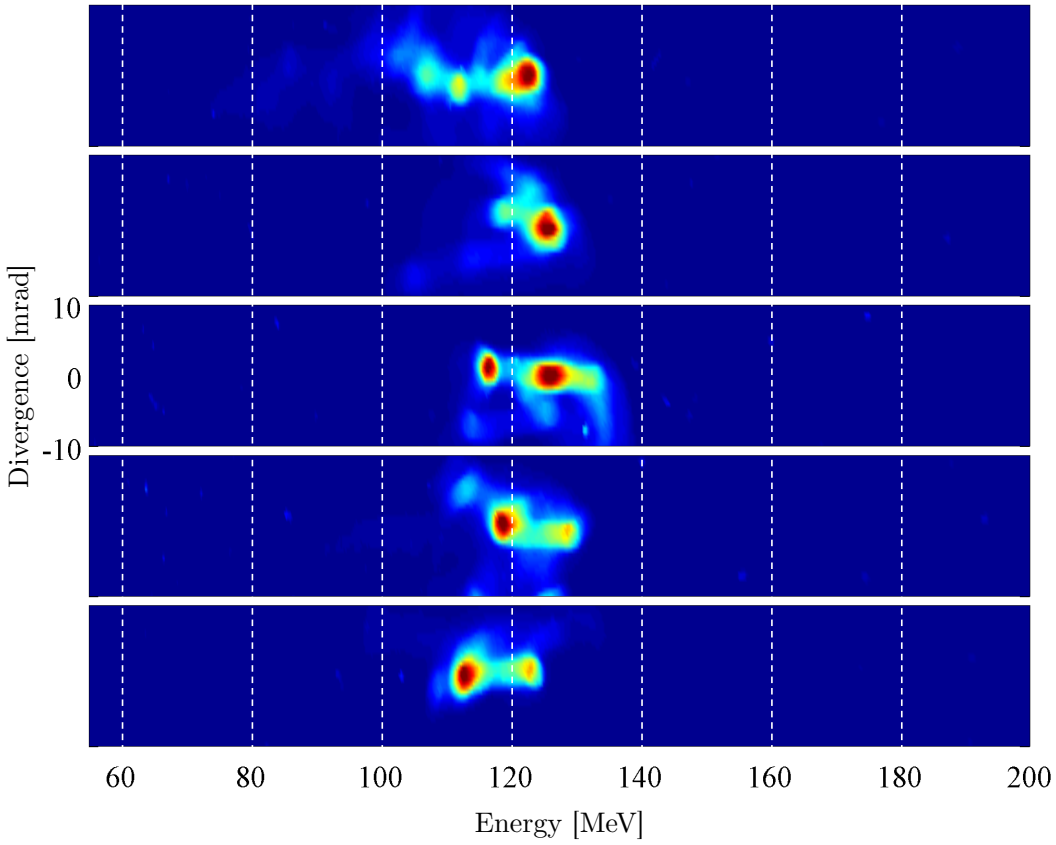

Figure 2.7 – Example for stability of typical electron spectra from shock injection.

2.5 Ionization injection

Ionization injection is a type of longitudinal injection that relies on delayed ionization of electron states with an elevated ionization potential. For better understanding of the underlying physics we will first discuss strong field ionization mechanisms as we encounter them in the conditions of laser wakefield acceleration and then introduce in more detail the concept of this injection scheme.

2.5.1 Strong field ionization

The binding energy of outer shell electrons is typically $\sim 5-15$ eV, which means that direct classical photo-ionization of these electrons would require ultraviolet light. However, if the photon density is high enough, there is a finite probability of ionzation via absorption of several low energy photons, a process which is accordingly called *multi-photon ionization* (MPI). In MPI the electron is ionized via passing through a number of unstable meta-states, as depicted in Fig.2.8. In order to be ionized the electron therefore needs to absorb a subsequent photon within the lifetime of these meta-states. This decay time is related to the uncertainty relation, so it is shorter the stronger an electron is bound and therefore the probability of multi-photon ionization to happen decreases rapidly.

At even higher intensities, the laser field can perturb the atomic potential, thus increasing the electron's tunneling probability. The threshold between multi-photon ionization and field ionization is estimated using the ponderomotive potential that we have introduced in **Chapter 1: Introduction** , which describes the average energy a free electron acquires during a laser cycle:

$$U_p = \frac{a_0^2}{4} \simeq 0.93\ \text{keV} \times \frac{I_0[10^{16}\ \text{W/cm}^2]}{(\lambda_0[\mu\text{m}])^2}. \tag{2.2}$$

According to Keldysh, the ionization is governed by MPI if the adiabatic parameter

$$\gamma_k = \sqrt{\frac{\zeta}{2U_p}} \tag{2.3}$$

is larger than unity. Here ζ denotes the ionization potential. In contrast, for $\gamma_k \ll 1$, field ionization dominates. For field ionization itself we distinguish two regimes: the *tunneling ionization* (TI) regime, where the potential barrier remains above the electron ground state, and the *barrier suppression ionization* (BSI), when the electron state is above the potential, leaving it essentially unbound. The threshold for barrier suppression to occur is estimated assuming a coulomb potential of a hydrogen-like atom, disturbed by an electric field: $V(x) = Ze^2/|x| - eE_0x$. For this potential we can estimate a critical field strength $E_{\text{BSI}} = \zeta^2/4Ze^3$ at which the potential is suppressed below the ground state. From this we find that BSI occurs

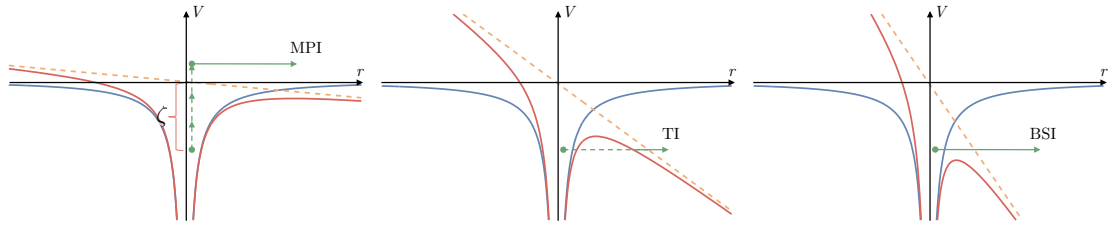

Figure 2.8 – Illustration of multi-photon ionization (MPI), tunneling ionization (TI) and barrier suppression ionization (BSI).

for intensities

$$I_{\mathrm{BSI}}[\mathrm{GW.cm^{-2}}] \sim \frac{4\zeta_i^4[\mathrm{eV}]}{Z^2}. \tag{2.4}$$

Once the field intensity I_0 exceeds I_{BSI}, an electron state will be rapidly ionized.[5] From (2.4) we find that the BSI threshold is of the order of $\sim 10^{16}$ W/cm^2 for He^{2+} and N^{5+}, whereas ionization of Nitrogen's K-shell (N^{6+} and N^{7+}) requires $\sim 10^{19}$ W/cm^2. For Argon there is a similar gap between the L-shell and the M-shell.

Between those two regimes ($\gamma \ll 1$ and $I_0 < I_{BSI}$), tunnel ionization models are used to estimate ionization rates [90]. First models for DC fields were established by Landau and Keldysh. A popular model for AC fieds was introduced by Ammosov, Delone and Kranov (ADK). In CALDER-CIRC the both Landau and ADK models are implemented. For estimations we have used ADK according to the formulation used in [91]

$$\mathrm{W_{ADK}}[\mathrm{fs^{-1}}] \approx 1.52 \frac{4^{n*}\zeta_i[\mathrm{eV}]}{n^*\Gamma(2n*)} \left(8.23\times10^4 \frac{\zeta_i^{3/2}[\mathrm{eV}]}{E[\mathrm{a_0}]}\right)^{2n*-1} \exp\left(-2.74\times10^4 \frac{\zeta^{3/2}[\mathrm{eV}]}{E[\mathrm{a_0}]}\right) \tag{2.5}$$

where $n^* \approx 3.69\, Z\zeta_i^{-1/2}$ is the effective principle quantum number and Z denotes the ionization state. ADK overestimates ionization close to barrier suppression [92], so there have be various proposals to extent the ionization rates towards and beyond the BSI threshold, e.g. by Krainov [93] or Tong and Lin [94]. Solving the time-dependent Schrödinger equation (TDSE) instead would provide better predictions, yet such calculations are too cumbersome to be performed in the context of Particle-In-Cell codes. In fact, it is still debated which implementation of ionization in a laser wakefield environment is most accurate, see e.g. [95], and simulation results in this context may be rather qualitative than quantitative.

[5] There will also be some back-reflection from the potential barrier, but for our purposes we can assume that this is essentially the threshold for complete ionization.

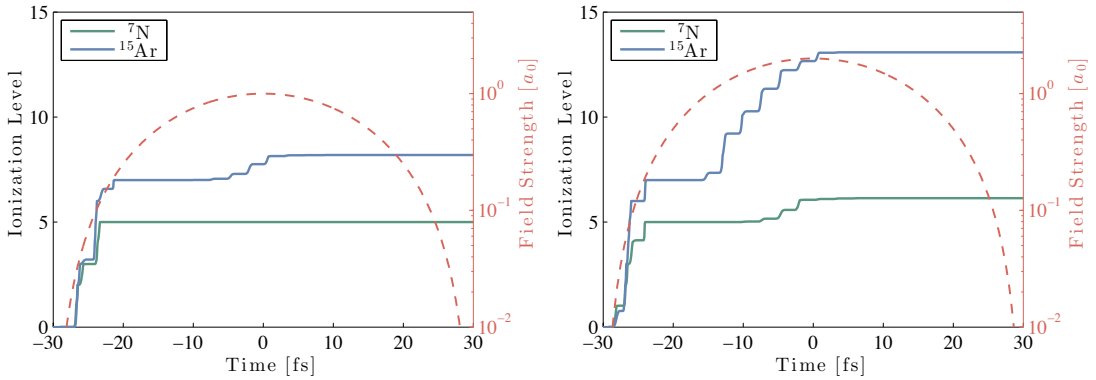

Figure 2.9 – Estimation of ionization rates using the ADK model for a 30 fs FWHM $\sin^2$ pulse with peak amplitudes $a_0 = 1.0$ (left) and $a_0 = 2.0$ (right).

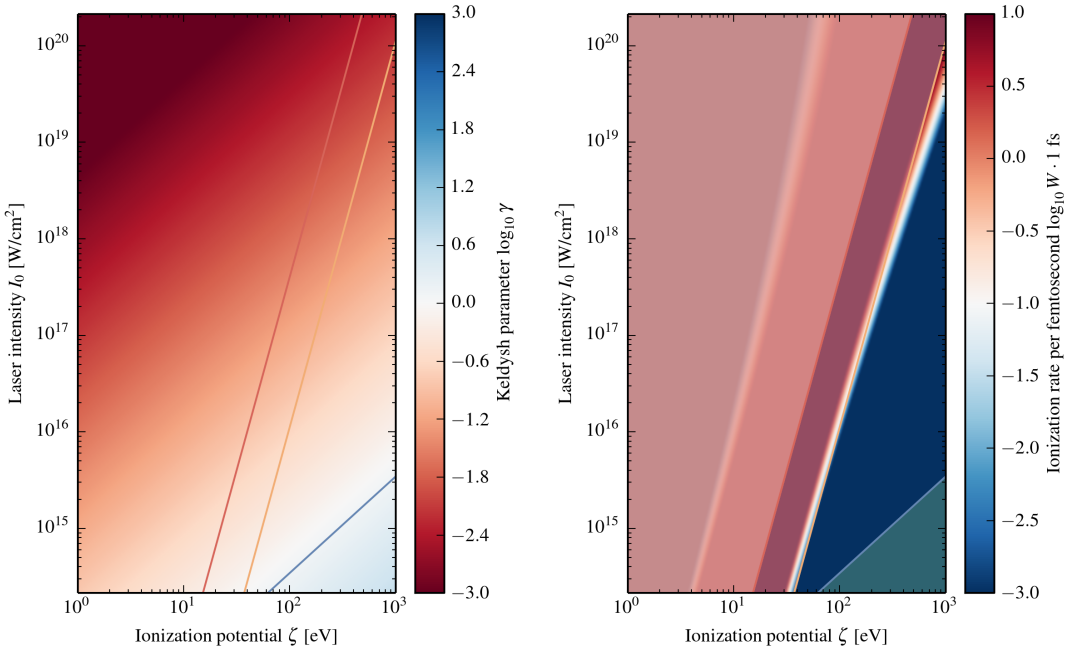

Figure 2.10 – Left: Keldysh parameter γ for different ionization potentials ζ and laser intensities at 800 nm wavelength. The blue line corresponds to $\gamma = 1$, i.e. below it multi-photon ionization dominates, whereas for $\gamma \ll 1$ field ionization processes occur. The barrier suppression thresholds for 1st and 6th ionization state are also plotted as function of the ionization potential. Above MPI and well below BSI the ADK model is valid to calculate ionization rates. Those are calculated for the $Z = 6$th ionization state on the right side. Here the areas governed by MPI and BSI are shaded.

Species	Ionization Potential ζ_i [eV]							
$_2$**He**	24.58	54.42						
$_7$**N**	14.53	26.60	47.45	77.47	97.89	552.07	667.05	
$_{18}$**Ar**	15.76	27.63	40.74	59.81	75.02	91.01	124.32	422.45
	478.69	538.96	618.26	686.10	755.74	854.77	918.03	

Table 2.1 – Ionization potentials below 1 keV for the three gases used in the experiment: Helium, Nitrogen and Argon.

2.5.2 Conceptual idea

Ionization injection is a longitudinal injection technique which is based on tunnel ionization of higher ionization states. While weakly bound electrons are usually ionized at the pulse front, the deeper shells are ionized later, close to the peak field. Figure 2.11 illustrates this for the case of argon, ionized by a laser pulse with peak intensity $a_0 = 1$. The lately ionized electrons skip a part of the decelerating phase, which allows them to gain more net energy from the wake than early ionized electrons. This is why the separatrix - and therefore the injection threshold - is lower behind the laser pulse, cf. Fig.2.11.

An additional three-dimensional effect is that electrons can be injected longitudinally, which further lowers the injection threshold as they can take advantage of stronger on-axis fields. This is even possible in the blowout regime (cf. Chapter 3), because their parent nuclei remain mostly unaffected by the ponderomotive force.

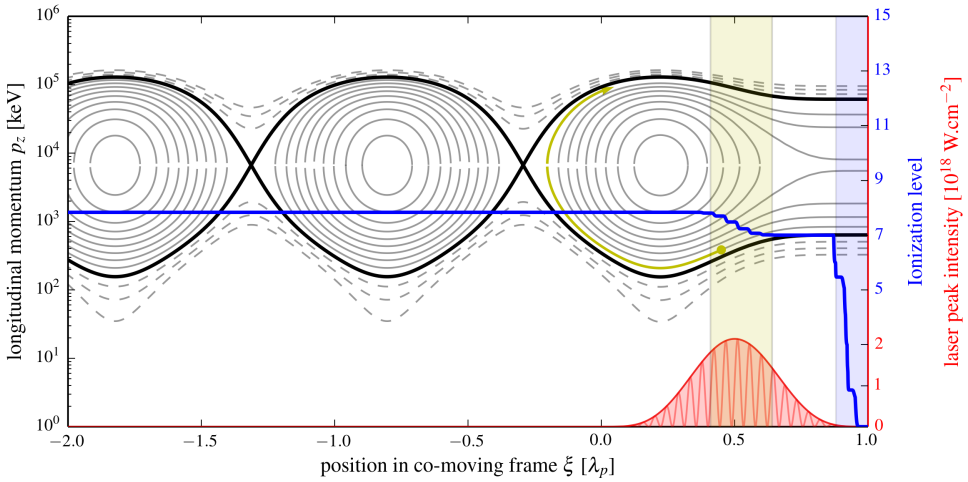

Figure 2.11 – Ionization injection of argon inner shell electrons into a plasma wake. The blue region corresponds to ionization of lower ionization states, while the yellow region is where ionization beyond Ar^{7+} occurs. Such electrons experience a reduced potential and are therefore easier trapped, as indicated by the yellow line.

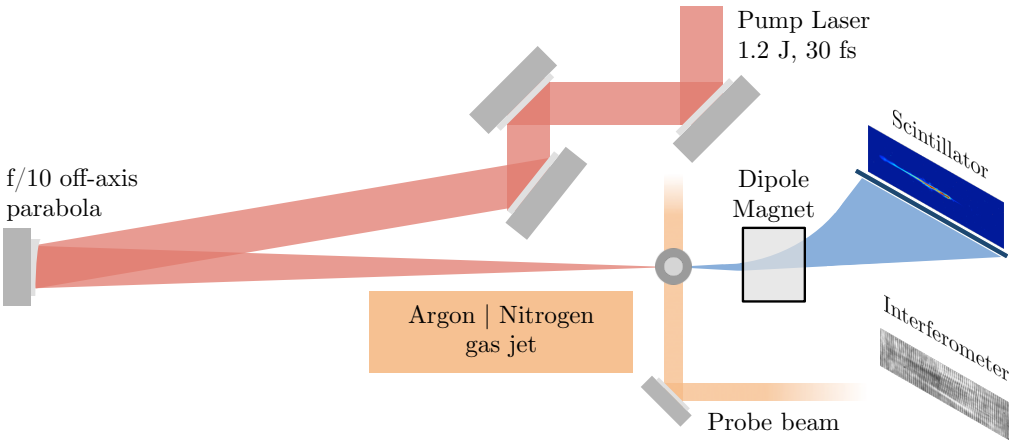

Figure 2.12 – Sketch of the setup for ionization injection in pure high-Z gases.

When using high-Z gases we have to take into account that inhomogeneous ionization does affect the laser propagation. As the laser intensity profile is usually centered around the propagation axis, ionization leads to an augmented electron population on-axis. Hence ionization creates a *defocusing* effect, inversely to ponderomotive self-focusing, which leads to a density reduction. In most ionization injection experiments high-Z gases are therefore only used as dopants in a helium-dominated gas, which evades ionization induced defocusing.

Yet in some cases the usage of high-Z gases can lead to desirable results. As defocusing limits the acceleration length, such a configuration should be suitable for applications requiring low beam energies. We have studied this regime using pure Argon and Nitrogen, as discussed in the following.

2.5.3 Ionization injection in pure high-Z gases

The experiment was performed at LOA using the Salle Jaune Laser System which at the time of the campaign delivered pulses with 28 fs duration (FWHM) and 2.1 J energy per pulse. The beam is focused with an f/10 off-axis parabola to a waist of 22 µm, within which 52 percent of the total energy are contained. This results in a peak intensity of 8.9×10^{18} W/cm^2, i.e. $a_0 \simeq 2.0$.

As target a 700 µm sonic gas nozzle is used. Shot at 1 mm above the nozzle exit, the resulting plasma channel length is ~ 1.5 mm with a gaussian-like profile. Producing relatively low energies, a smaller magnet spectrometer was used in this experiment. Using a permanent magnet of 20 mm length and 760 mT strength, electron energies between 7 and 50 MeV were detected, with a transverse acceptance angle of 110 mrad.

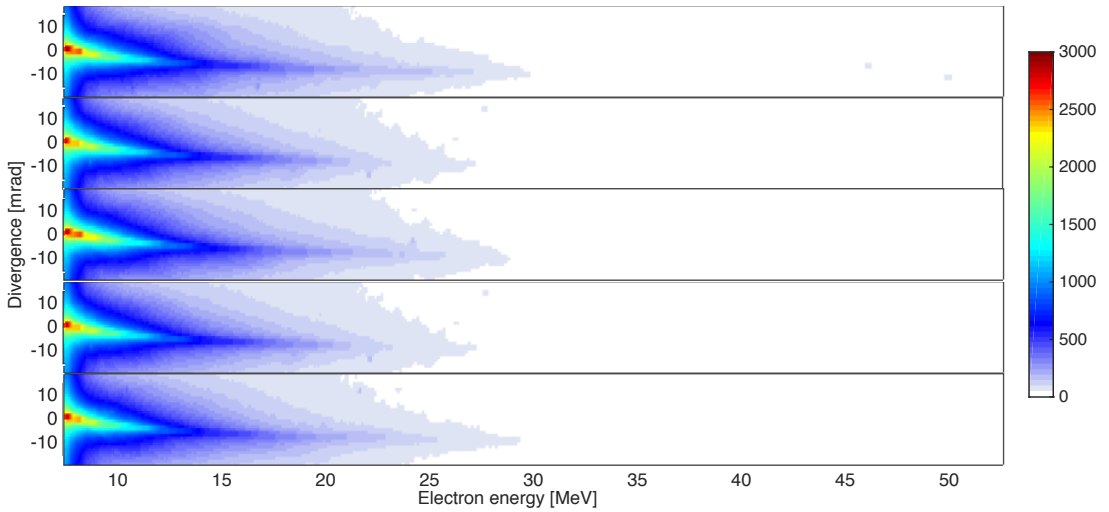

Figure 2.13 – Electron spectra for five consecutive shots in argon with $n_e = 1.9 \times 10^{19}$ cm^{-3} and 1.1 Joule pulse energy.

Experimental results

Electron acceleration in pure nitrogen and argon shows to be remarkably stable, both spectrally as well as in terms of charge, cf. Fig.2.13.[6] As expected from ionization injection the accelerated charge is quite high, almost reaching 1 nC per shot, however the continuous injection leads to a broad maxwellian-like spectrum. Below 10 MeV the distribution has a temperature of ~ 2 MeV, while the temperature between 10 and 30 MeV is ~ 4 MeV. The beam divergence is energy dependent. For the 'cold' part of the spectrum the divergence reaches up to 20 mrad, while the divergence above 10 MeV is about 10 mrad (FWHM).

In order to find the injection threshold of this regime, we varied the laser energy on target using a rotating half-wave plate and a polarizer. We measure an injection threshold energy of 200 mJ, corresponding to 1.6×10^{18} W/cm^2 or $a_0 \simeq 0.9$. Above this threshold the charge increases close to linearly with the laser energy, at a rate of ~ 110 pC per 100 mJ, cf. Fig.2.14. The highest charge measured is 910 pC at the maximum energy of 1.1 Joule. The shot-to-shot fluctuations are very small at maximum energy (percent level) and the strongest fluctuations were measured at 0.36 Joule (23 percent). Furthermore we find that neither the electron temperature changes significantly as we vary the beam energy. This is an unexpected finding, as the wakefield amplitude strongly depends on the laser intensity.

Interpretation and numerical studies

In order to explain this behavior we have performed Particle-In-Cell simulations with CALDER-CIRC. The grid resolution is $\Delta x = 0.2 k_0^{-1}$ and $\Delta r = 1.5 k_0^{-1}$. The number of neutral nitrogen

[6] In the following we only present experimental data for acceleration in Argon, however the results in Nitrogen are very similar.

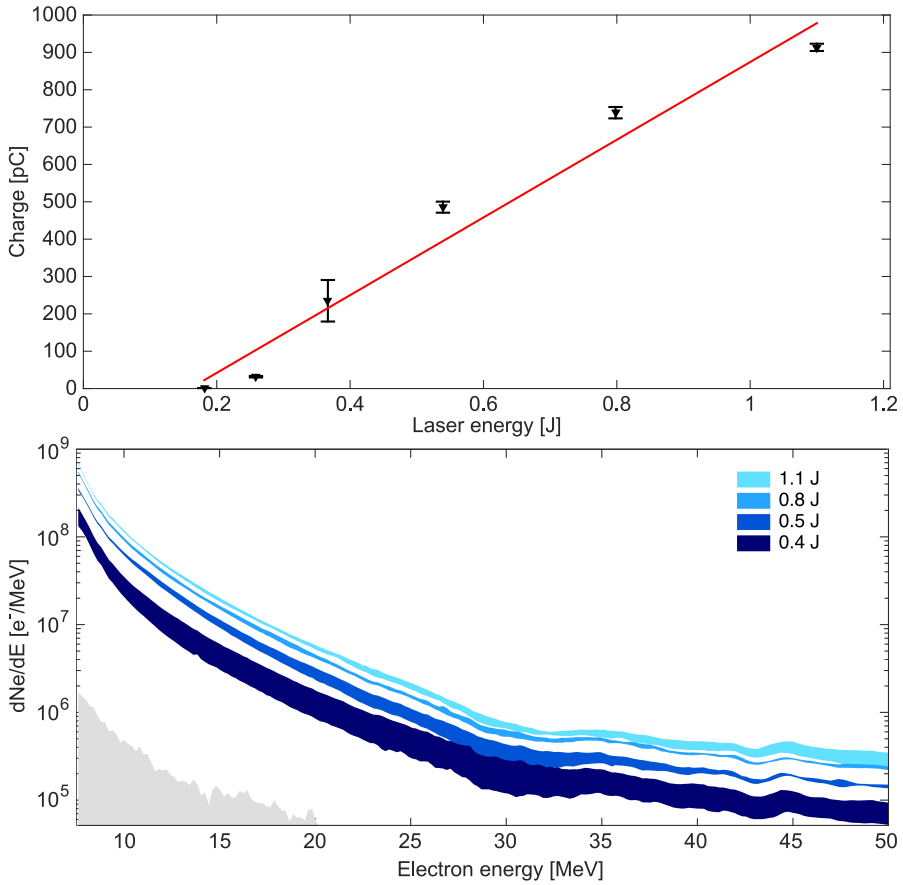

Figure 2.14 – Upper frame: Total integrated charge for different energy on target. Bottom: Electron spectra for the different energies. The line width corresponds to the error, showing the high stability of the source.

macro-particles per cell is 100, which results in 500 macro-particles per cell after ionization of the L-shell by the pulse front.

In the simulations we could reproduce that the electron temperature and divergence is almost independent of the laser energy. As found experimentally, changing the pulse energy primarily affects the total injected charge, cf. Fig.2.15. The absolute value of 1 nC in the simulations is close to the experimental results as well. Note that in contrast the electron temperature above 10 MeV is overestimated to lie between 15-20 MeV.

More physical insight on this behavior is gained when we look at the wake structure for different beam energies, as shown in Fig.2.16. For a driver with initial intensity $a_0 = 1.2$ only the primary wake and second arch are excited. However, the stronger the driver, the more wake periods are sustained. The maximum charge that can be accelerated in each of these wake cavities is limited by beam-loading, i.e. the fact that the space-charge of the beam counteracts the wakefield. Beam loading is roughly proportional to the background plasma density and the wake amplitude. As both of these are similar in all secondary arches, the

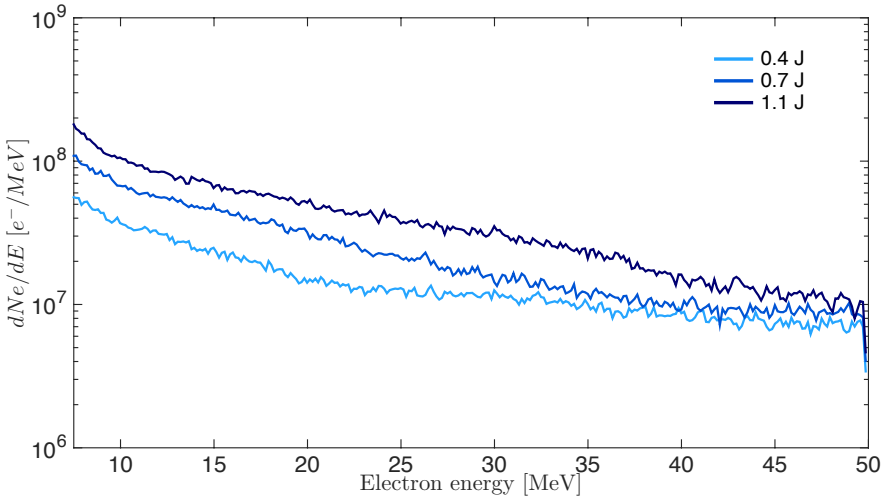

Figure 2.15 – Simulated electron spectra for different initial beam energies.

maximum charge of a fully loaded wake is expected to scale with the number of wake periods. While this argumentation explains the scaling of the accelerated charge, it does not provide an explanation for the similar spectra at different energies. We find that this is a consequence of the particular density profile used in the experiment.

During the first half of the jet there is a density upramp, which acts opposite to the downramps we have discussed before: Here the plasma wavelength diminishes, resulting in an effective speed-up of the phase velocity. Being a phase velocity, the value can even be superluminal, thus preventing any injection at all. As a consequence, electrons ionized early during propagation cannot be injected initially. Yet still they are almost trapped, meaning that they do co-propagate, yet dephase and slip backwards from cavity to cavity. Once the density profile flattens the wake slows down and the electrons get trapped, in a secondary arch. This process occurs almost simultaneously through the whole wake structure, i.e. electrons in all arches are injected at the same time and therefore reach similar final energies. This is depicted in Fig.2.16 (d) which shows the $x-\gamma$ phase space. Injection only continues until beam loading has reduced the longitudinal wakefields below the threshold field, which we estimate to be $E_{crit} \simeq 0.47 E_0$. Indeed, the wake amplitude after injection has terminated is very close to this value in all arches.

In conclusion we find that electron acceleration in high-Z gases has the potential to provide electron beams with very high charge (~ nC) and extraordinary shot-to-shot stability. The spectrum is maxwellian with temperature below 5 MeV and around 10 mrad divergence. In Section 5.1.2 we will use this injection method in combination with bremsstrahlung converters to create γ radiation.

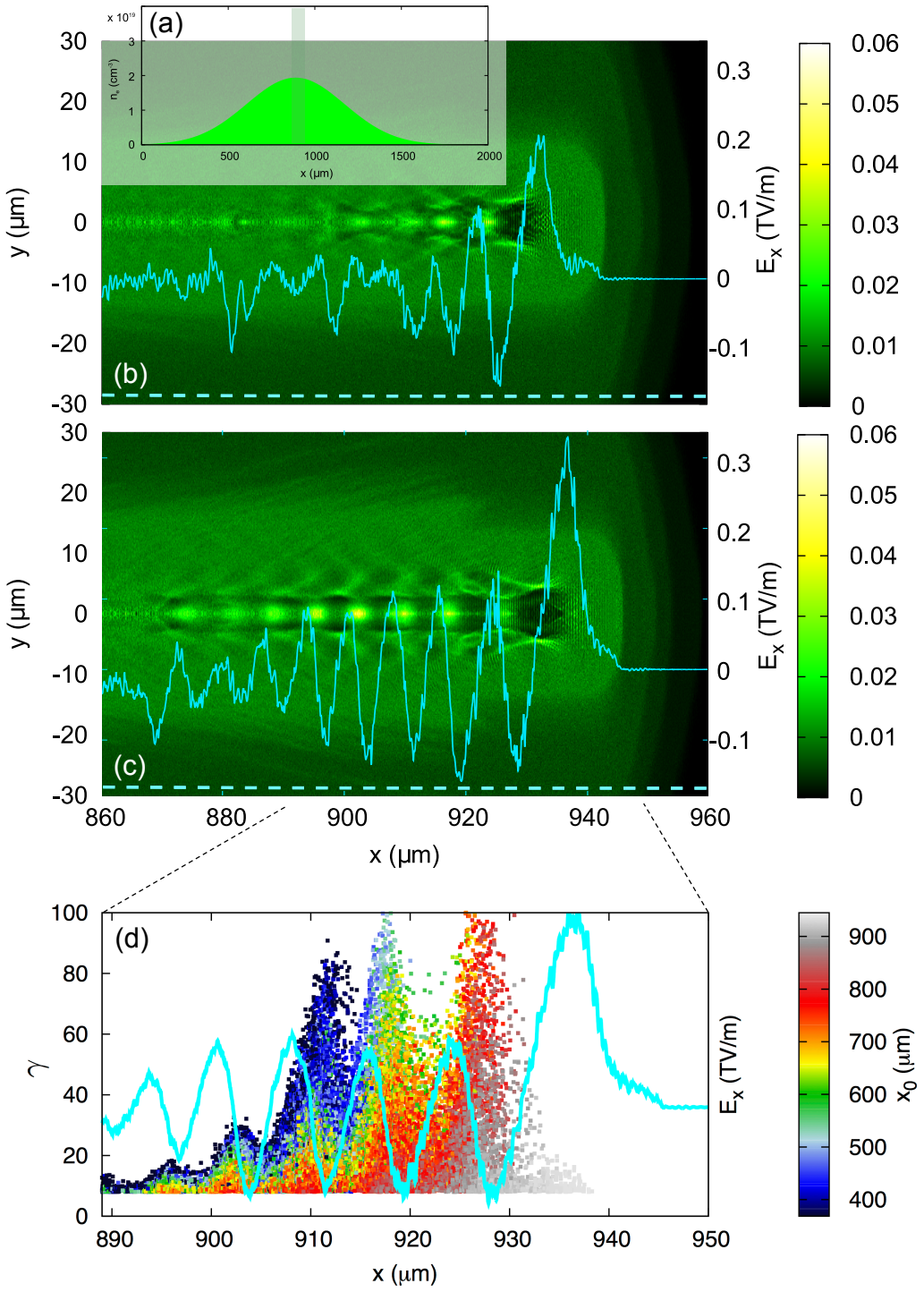

Figure 2.16 – Result from Particle-In-Cell simulations with CALDER-CIRC for the density profile shown in inlet (a), with peak density $n_e = 1.9 \times 10^{19}$ cm^{-3}. (b) and (c) show the electron density distribution close to the center of the jet for 0.4 J ($a_0 = 1.2$) and 1.1 J ($a_0 = 2.0$) laser energy (peak intensity), respectively. Also shown are the longitudinal wakefields on axis (light blue). (d) shows the phase space of electrons from the Nitrogen K-shell for 1.1 J beam energy, with color-coded ionization position.

2.5.4 Ionization injection in gas mixtures

When using high Z gases only as dopant the laser can propagate over longer distances, thus allowing to reach higher beam energies. We have studied various gas mixtures, among whose 98:2 Helium-Nitrogen produced the most stable results.

As for self-injection there are many different regimes and it is not possible to present a 'typical' ionization injection spectrum. But compared to self-injection in pure helium the beams from ionization injection have usually a larger divergence, while maintaining a better pointing stability. Beam charges vary as well, but tend to be higher than in self-injection.

A problem of ionization injection is the continuous injection which leads to large energy spread. To avoid this we have tried to combine ionization injection with injection in sharp density transitions. For this we used a gas mixture and the shock injector setup from Sec.2.4. Sample results from a 95:5 mixture are shown in Fig.2.18. We observe beam energies of 148±7.5 MeV. Such 5 percent peak energy variation is very comparable to what we have observed in Helium. Still, with 5% high Z gas contribution we still observe dark current. This is slightly improves when using only 2% nitrogen.

We have used ionization injection in gas mixtures for several experiments, cf. sections 4.5.2, 5.5.2 and 5.5.3.

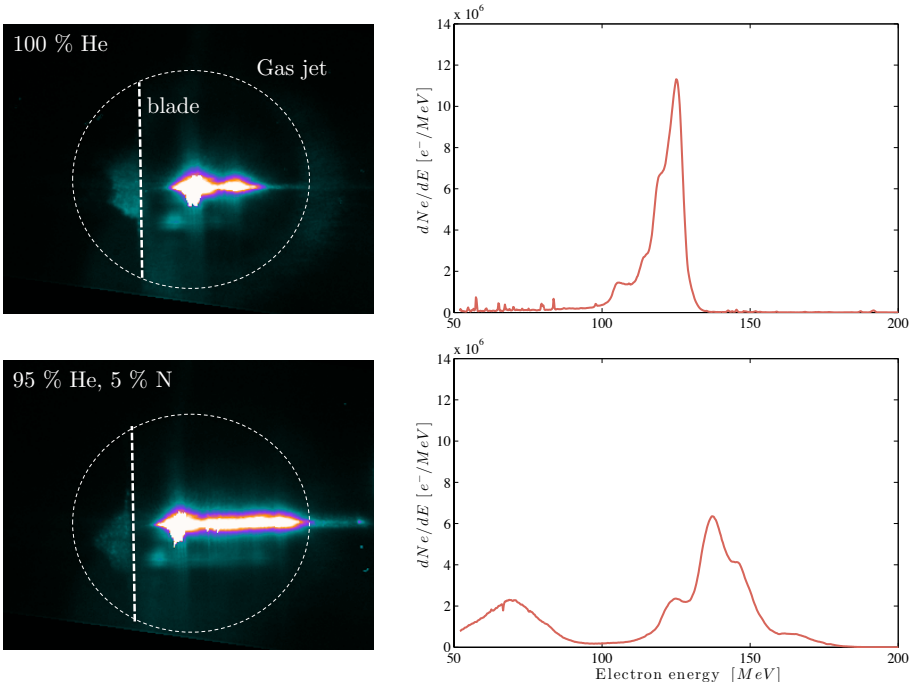

Figure 2.17 – Comparison of the top view plasma emission image for shock injection with pure Helium and with a mixture. We observe a longer emission tail for ionization injection, which we relate to continuous injection.

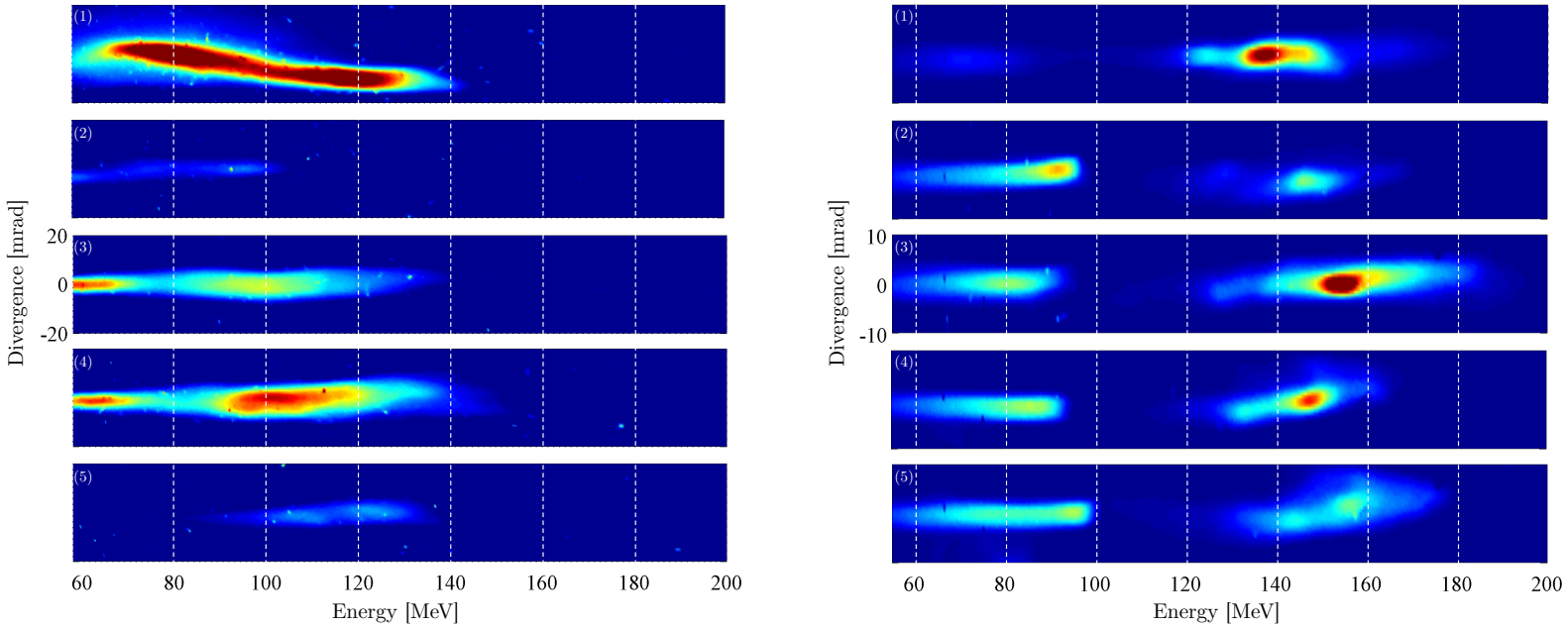

Figure 2.18 – Two examples for ionization injection in a 95:5 Helium-Nitrogen mixture. Left: Five consecutive shots for ionization injection, here the charge fluctuates significantly with 54 ± 36 pC. Right: Five consecutive shots for shock-assisted ionization injection in a 95:5 Helium-Nitrogen mixture. The charge in the quasi-monoenergetic peak fluctuates significantly from shot to shot, whereas the continuously injected dark current remains quite stable. Shots (2-5) have the same color scale, shot (1) has $\sim 3\times$ as much charge in the peak.

2.6 Conclusions

In this chapter we have seen that injection schemes have a similar function as electron guns in conventional accelerators. In particular the injection process determines many beam parameters like charge, energy spread and divergence.

Here we have studied several difference injection regimes: Longitudinal and transverse self-injection, shock injection, ionization assisted shock injection, ionization injection in mixtures and ionization injection in pure high-Z gases. We can therefore select among a wide range of laser-plasma injectors for different applications. The following summarizes our findings:

Highest beam charges (up to some hundred pC) are achieved with transverse self-injection and ionization injection in mixtures and pure gases, while longitudinal self-injection and shock injection usually lead to some pC beam charge.

The beam divergence is lowest in longitudinal injection techniques and for shock injection, in contrast transverse self-injection results in the strongest initial transverse momentum. The divergence of ionization injection depends on the ionization region, which itself depends on the laser energy.

The earliest injection occurs in longitudinal self-injection and ionization injection in gas mixtures, so they are potentially the most energetic. However, ionization induced defocusing can reduce the driver strength during propagation, leading to lower beam energies.

The lowest energy spread is achieved with shock injectors and close to the injection threshold of transverse self-injection. Continuous ionization injection usually results in a very large, maxwellian energy spread. The energy spread is also linked to the pulse duration. In the case of ionization injection and self-injection electrons can get trapped in several wake arches, which results in a pulse train with a total length of some tens of femtoseconds. Shock injected beams are expected to have a duration similar to optical injected pulses, reaching down to a femtosecond.

In terms of stability ionization injection techniques are the most reliable, followed by longitudinal injection and shock injection. Transverse self-injection, especially at high plasma density leads to strong fluctuations of all beam parameters. From an experimentalists point of view, both ionization injection schemes and self-injection are relatively easy to implement, whereas shock injection requires additional motorization, space and experience to align the blade.

3 Acceleration

In this chapter we will discuss the dynamics of the acceleration process itself, with emphasis on the non-linear blowout regime. Notably we present results for acceleration beyond laser depletion for highly charged beams from ionization injection. We also discuss how dephasing between electrons and the laser driver can be mitigated by manipulation of the plasma density. We quantify this using analytical and numerical models, with emphasis on phase-reset in density profiles with a sharp upramps. Such profiles can be created in experiment using shocks. We demonstrate that these tailored profiles can be used to increase the final electron energy or to shape the electron spectrum.

Contents

Plasma wakefield acceleration can be seen as a special type of resonance acceleration, whose accelerating structure is a wave. In this kind of accelerator a particle first goes through an injection process (cf. preceding chapter), whereupon it has to maintain a synchronous phase ϕ. Any phase miss-match can result in deceleration instead of acceleration. In order to provide continuous energy gain the accelerator has therefore to (i) sustain the wave structure and (ii) match electron velocity and phase velocity.

We start this chapter with an introduction to conventional traveling wave accelerators and subsequently discuss in detail plasma wakefield acceleration.

3.1 Conventional accelerators

As we have seen in **Chapter 1: Introduction** there exists a great variety of conventional accelerators. The type which is most important for electron acceleration is the traveling wave linac. This accelerator is conceptually similar to wakefield acceleration, but uses a microwave instead of a plasma wave for acceleration.

Belonging to the family of resonance accelerators, synchronicity between the field and the accelerated particles has to be maintained. In ion accelerators this condition means that phase velocities over a wide range from $0.1 - 1 c_0$ have to be covered, while an electron gun usually delivers already relativistic electron beams, i.e. the condition reduces to $v_\phi \approx c_0(1 - 1/2\gamma^2)$.

As we are directly using an electromagnetic wave to accelerate particles, a wave mode with non-zero axial electric field is required. This is the case for transverse magnetic (TM) modes, with TM_{01} being the simplest solution. In contrast to laser wakefield accelerators, where the phase velocity is basically the group velocity of the laser and therefore subluminal, the phase velocity of the accelerating TM_{01} exceeds the speed of light. In consequence, synchronicity cannot be achieved in this configuration.

In order to still accelerate particles, the wave needs to be slowed down. This is done by placing obstacles in the wave-guide, typically in form of irises. It can be shown that in such a disk-loaded cavity the phase velocity is less than the speed of light, decreasing with increasing volume enclosed between the irises.

Obviously the dispersion relation will depend on the radiofrequency chosen to operate the accelerator. For a practical resonator size of a meter or less typically frequencies > 300 MHz are used. So since the RF pulses in travelling wave structures are very short, the technology also permits to operate close to breakdown at highest acceleration gradients (e.g. $\sim$ 100 MV/m for the Compact Linear Collider study [96]).

However, the exact conditions for breakdown are still not completely clear. In particular, surface defects can increase the probability of field emission. This is described by the Fowler-Nordheim equation, which relates the emission to the local field and the material's work function. For a copper cavity the field emitted dark current is I_F [A/m^2] $\sim$

$0.4(\beta E\ [\mathrm{MV/m}])^2 \exp(-6.5\times10^4/(\beta E\ [\mathrm{MV/m}]))$, so the emission increases exponentially close to breakdown. Here β describes the enhancement of emission depending on the defect geometry (typically $\beta \sim 10-100$), which can abet field emission significantly [97]. Not included in this model is that empirical tests also show an RF frequency dependency. For example, according to the first investigation by Kilpatrick in the 1950s [98], the breakdown surface field scales as $E\ [\mathrm{MV/m}]\exp(-4.25/E\ [\mathrm{MV/m}]) = 24.7(f\ [\mathrm{GHz}])^{1/2}$. Later studies found that the Kilpatrick criterion underestimates the breakdown threshold, which might be due to large defect enhancement in early accelerators, yet they still find a frequency dependence [99].

In any case, breakdown remains an issue at conventional facilities, which can lead to serious damage of the accelerator structure. In order to reduce dark current and the risk of breakdown, conventional accelerator facilities have to go through long conditioning periods on startup and operate well below the breakdown limit.

3.2 Plasma accelerators

The particle colliders mentioned in the last section are intended to accelerate electrons and positrons to TeV energies, which given their breakdown limited field gradients requires kilometer-long linacs. The main idea of plasma accelerators is to create much higher fields by charge separation in a plasma.

Normally a plasma behaves quasi-neutral on a scale of the Debye screening length

$$\lambda_D = \sqrt{\frac{\epsilon_0 k_B T_e}{n_e e^2}}, \tag{3.1}$$

which is typically sub-micron scale for the plasmas concerned in this work. However, the quasi-neutrality is the equilibrium situation without additional external fields. It is possible to force a charge separation using e.g. the space-charge force of a particle beam (beam driver) or the radiation pressure of laser beam (laser driver). Charge separation is facilitated in an electron-ion plasma, where the two species have very different inertia and therefore eigenfrequencies. In this case the plasma dynamics are governed by the electron motion, while the ions are usually considered quasi-static. Once a density perturbation δn is introduced, the plasma will react to it on the scale of a plasma wavelength

$$\lambda_p = 2\pi\sqrt{\frac{\epsilon_0 m_e c_0^2}{n_e e^2}}. \tag{3.2}$$

Here we see that the plasma wavelength is of the order $k_B T_e/m_e c_0^2$ larger than the Debye length, usually some tens of microns. We have already shown that the plasma responds to small perturbations with a linear electron acoustic wave or Langmuir wave

$$\left(\frac{\partial^2}{\partial\zeta^2} + k_p^2\right)\Phi = k_p^2\left(\frac{\langle a^2\rangle}{2} + \frac{n_b}{n_0}\right). \tag{3.3}$$

where $\langle a^2 \rangle / 2$ is again the ponderomotive potential. Additionally we have now included beam space-charge effects with the term n_b / n_0, where n_b denotes the bunch density. Electron motion in this regime is laminar, so we can extend the model to cylindrical symmetry by simple multiplication with the radial driver profile. For either driver type the corresponding potential is then of the form

$$\Phi(\xi, r) = \kappa(\xi, r) \ \sin[k_p(\xi - \xi_0)]. \tag{3.4}$$

where $\kappa(\xi, r) < 1$ is a function depending on the driver strength and its longitudinal and radial shape. For example, the explicit solution of κ for a laser pulse with gaussian shape in both longitudinal and radial direction is $\kappa \simeq 0.266 a_0^2 (k_p \sigma_z) \exp[-0.09 k_p^2 \sigma_z^2] \exp[-2 r^2 \sigma_r^{-2}]$. Note that κ does not affect the phase in this regime, as depicted in Fig.3.1a/b, which shows longitudinal wakefields and density perturbation for a driver with $a_0 = 0.5$.

3.2.1 Nonlinear regime

The plasma wave equation in the last section was just an approximation of the one-dimensional plasma wave equation we derived in Chapter 1:

$$\frac{\partial^2}{\partial \zeta^2} \Phi = \frac{1}{2} \left(\frac{1 + a^2}{(1 + \Phi)^2} - 1 \right) k_p^2. \tag{3.5}$$

Figure 3.1c/d shows the solution of this equation for an increased driver strength ($a_0 = 2.0$). Recalling that the electron momentum follows the vector potential and that a normalized potential $a_0 = 1$ corresponds electron rest energy, it is evident that relativistic effects become important in this regime. A direct consequence is that the plasma frequency is intensity dependent and will diminish towards the laser axis by $\gamma^{-1/2}$. In the quasi-linear regime ($a_0 = 2.0$) this imbalance becomes noticeable and at high driver intensities we observe that the wake is horseshoe shaped, cf. Fig.3.1e/f for $a_0 = 8$.

A second characteristic of the non-linear regime is that the longitudinal wakefields are sawtooth-like. This effect is better visible in an on-axis lineout, cf. Fig.3.2. This quasi-linear shape of the electric field follows from the fact that the laser expels all electrons from axis, leaving a constant ion background.

The last statement would be true in reality, but when we look carefully at the density profiles, we observe that the electron density never drops below $-n_0/2$, which seems counterintuitive. In fact, for strong perturbations ($a_0 \gg 1$) we rapidly reach the limits of the fluid model. These limitations become obvious when we consider the velocity v_z of an electron fluid element (1.8)

$$v_z = v_\phi \left(1 - \frac{n_0}{n_e(z)} \right) \tag{3.6}$$

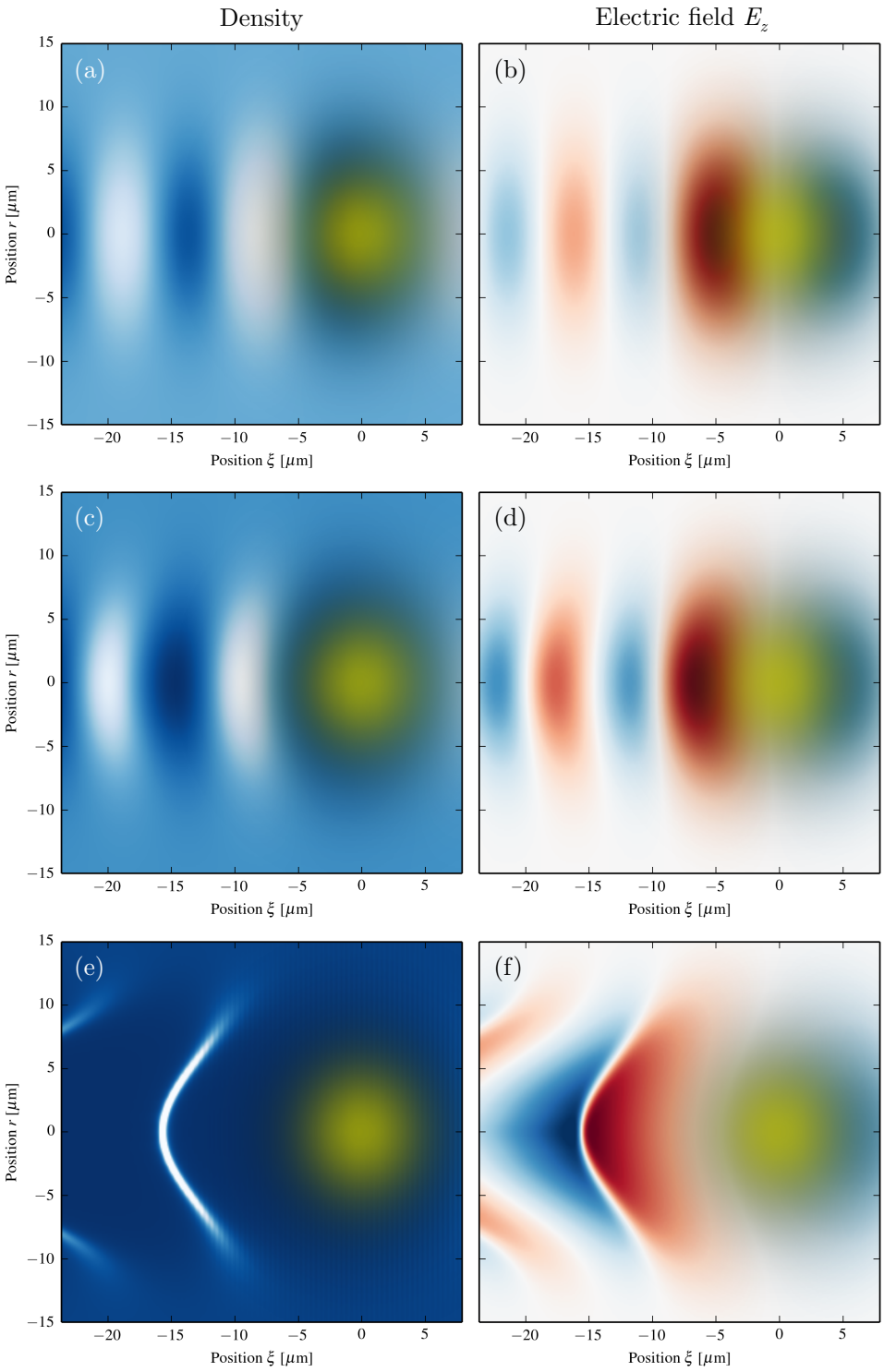

Figure 3.1 – Solutions of the fluid model for drivers with $w = 10\mu$m, $\tau = 30$ fs and $a_0 = 0.5$, 2 and 8 in a plasma with density 10^{19}cm^{-3}. It is clearly visible how the wave structures shifts from regular oscillations at the plasma wavelength to a horseshoe-like structure. At highest intensities the electrons (white) form a peak. Colormaps in each plot are normalized to the peak density and fields.

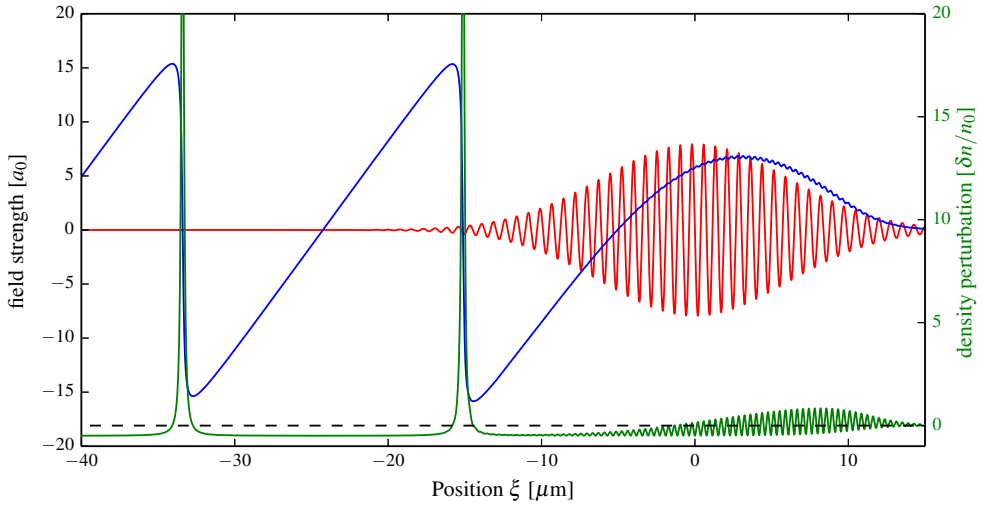

Figure 3.2 – On axis fields and density for a pulse with $a_0 = 8.0$.

As the phase velocity is close to $v_\phi \sim c_0$ we see that a density $n_e < n_0/2$ would imply that $v_z < -c_0$, i.e. a super-luminal return flow. This is obviously unphysical and for a better understanding we need to move beyond the cold fluid model and in particular of the laminar solution.

Instead, we use the three-dimensional particle-in-cell code CALDER-CIRC to order to solve the Vlasov-Maxwell system for the same driver and plasma density as in our last example ($a_0 = 8, w = 10\mu$m, $\tau = 30$ fs and $n_e = 1.0 \times 10^{19}$cm^{-3}). The resulting density and wakefield maps are shown in Figure 3.3. The result are similar, but especially the longitudinal fields are much weaker (shown later in Fig.3.13). Also, the electron density in this solution approaches zero behind the laser pulse, creating an ion cavity. Because of this, the regime is called *blow-out* regime, or in reference to the spherical shape *bubble* regime.

Fig.3.4 shows the momenta p_z, p_x and p_y for the same simulation. As seen in **Chapter 2: Injection** the electrons rapidly gain longitudinal momentum towards the end of the bubble. In addition we see clearly how the momentum along polarization x follows the laser field strength. In the y the laser does not drive oscillations, instead electrons gain momentum by the ponderomotive blowout. It is this quasi-isotropic ponderomotive momentum gain that is responsible for the shape and extension of the ion cavity. If we assume the cavity to have a spherical shape of radius r_B, the potential inside is

$$\Phi = \frac{k_p^2}{4}\left(r_B^2 - r^2\right) \tag{3.7}$$

and it immediately follows that the associated longitudinal fields are linear

$$E_z = -\frac{m_e\omega_p^2}{2e}(1-\phi)r_B \tag{3.8}$$

where ϕ describes the phase inside the wake. As mentioned before, the size of the blowout depends on the driver. Via simulations it was found that for a laser, which is self-focused to the matched spot size, the condition $k_p r_B \simeq k_p w_0 = 2\sqrt{a_0}$ holds [41]. In this case the maximal field strength is estimated to be of the order of

$$E_z^{\max} \sim \frac{m_e c \omega_p}{e}\sqrt{a_0} = E_0\sqrt{a_0} = 96\ \mathrm{GV/m} \times \sqrt{n_0[10^{18}\ \mathrm{cm}^{-3}]} \times \sqrt{a_0}. \tag{3.9}$$

However, the above condition is only a rough estimation and simulations show that the longitudinal field behaves sometimes highly non-linear at the back of the cavity, cf. Fig.3.13.

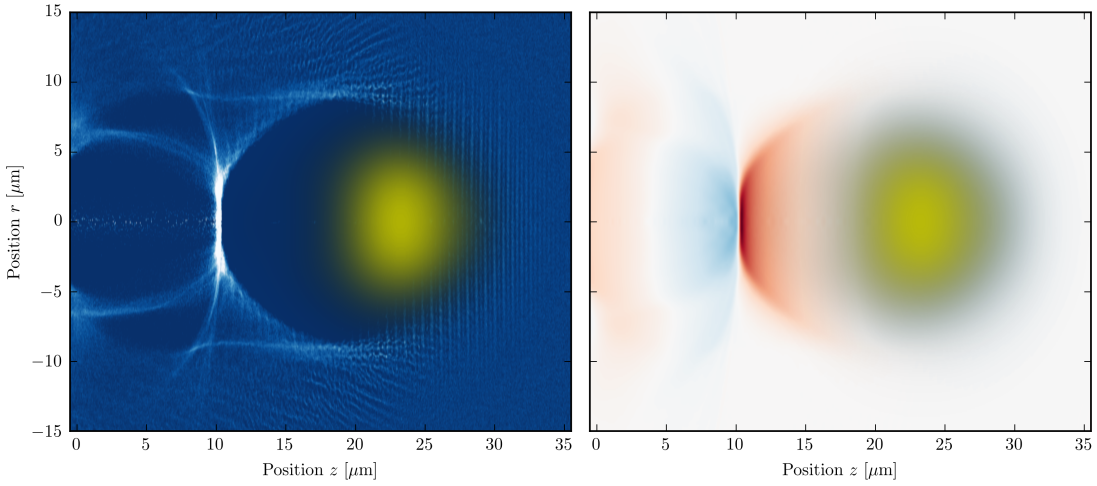

Figure 3.3 – Particle-in-Cell simulation of the same laser pulse as in Fig.3.1e/f. We see that in this more accurate simulation a bubble-shaped blowout region forms instead of the horseshoe-shape of the fluid model.

3.2.2 Energy gain and limitations

In the preceding section we have seen that driving a non-linear plasma wake can lead to even higher longitudinal fields than in the linear regime. But even field strength in an ion cavity can exceed a TV/m, this does not mean that we can (yet) create a tabletop TeV accelerator. As stated in the introduction, there are two types of limitations for the energy gain attainable in wakefield accelerators.

Plasma accelerator length

One limiting factor is obviously the length of the plasma channel itself. In beam-driven accelerators Lithium plasma channels of over a meter length are used, whereas laser wakefield accelerators typically use millimeter to centimeter long plasmas.

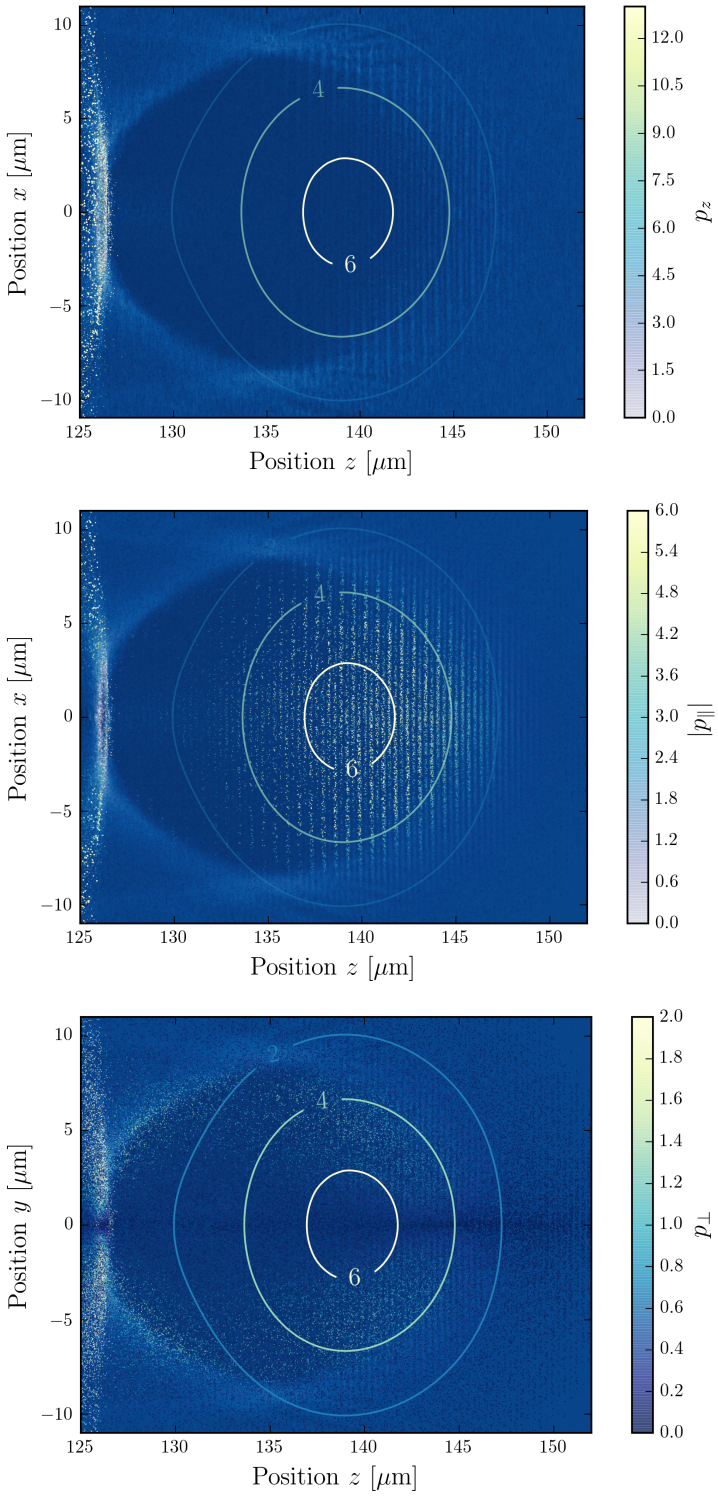

Figure 3.4 – Momentum distributions for the bubble shown in Fig.3.3. Significant longitudinal gain occurs at the back of the cavity. We clearly see that the transverse momentum parallel to the laser polarization follows the normalized field strength, which is indicated by the contour plot. Perpendicular to the polarization the momentum gain is due to the ponderomotive force.

But it is also clear that particles can only be accelerated in a plasma as long as the driver can sustain the wake responsible for acceleration inside the plasma. In the previous section we have discussed the plasma wave excitation and we found that it essentially depends on the driver intensity, i.e. the bunch charge density and the photon density (given by the normalized vector potential a).

A first limit on the acceleration length is then given by defocusing of the beam. As we will discuss later, defocusing effects primarily the head of the driver. Operating a plasma accelerator in this guiding limited regime or the propagation length limited case is the most inefficient, because it means that a significant amount of pulse energy is not used to drive the plasma wave. In contrast, the most efficient mode of operation in terms of energy transfer is the depletion limit. In this regime the driver energy is completely used for wake excitation. Depletion-limited accelerators are also very efficient for electron acceleration, because they operate at higher accelerating fields (cf. dephasing below).

Dephasing

Laser-driven plasma waves are subject to a particular phenomenon called dephasing. In beam-driven accelerators, both drive-bunch and witness bunch are highly relativistic and therefore both of them travel essentially at the speed of light in vacuum c_0. In contrast we have seen in **Chapter 1: Introduction** that the phase velocity of a laser-driven wake is approximately

$$\beta_\phi \simeq 1 - \frac{3}{2}\frac{\omega_p^2}{\omega_0^2} = 1 - \frac{3}{2}\frac{n_e}{n_c} \tag{3.10}$$

which is the group velocity of the laser in a cold underdense plasma minus the etching velocity. This means that once injected, electrons advance with respect to the wake and will eventually outrun the accelerating phase. Injected into the back of the wake, electrons will typically encounter decelerating fields once they have advanced half a wake period r_B. The corresponding distance in the laboratory frame

$$L_d = \frac{r_B}{1-\beta_\phi} \simeq \frac{3}{2} r_B \frac{n_c}{n_e} = \frac{2}{3} r_B \gamma_\phi^2 \tag{3.11}$$

is called the dephasing length. Operating the accelerator in the dephasing limited regime is desirable for the production of high quality beams, because the field gradient leads to a reduction of the longitudinal momentum spread, as illustrated in Fig.3.5. The lowest energy spread is reached close to the dephasing length where the bunch changes from a negative to a positive chirp [100]. From (3.11) we also find that the dephasing length scales inversely with the plasma density. Reducing the plasma density also effects the maximum accelerating fields, but only at $n_e^{1/2}$, so the dephasing limited energy gain scales as $\Delta\gamma \propto n_e^{-1/2}$.

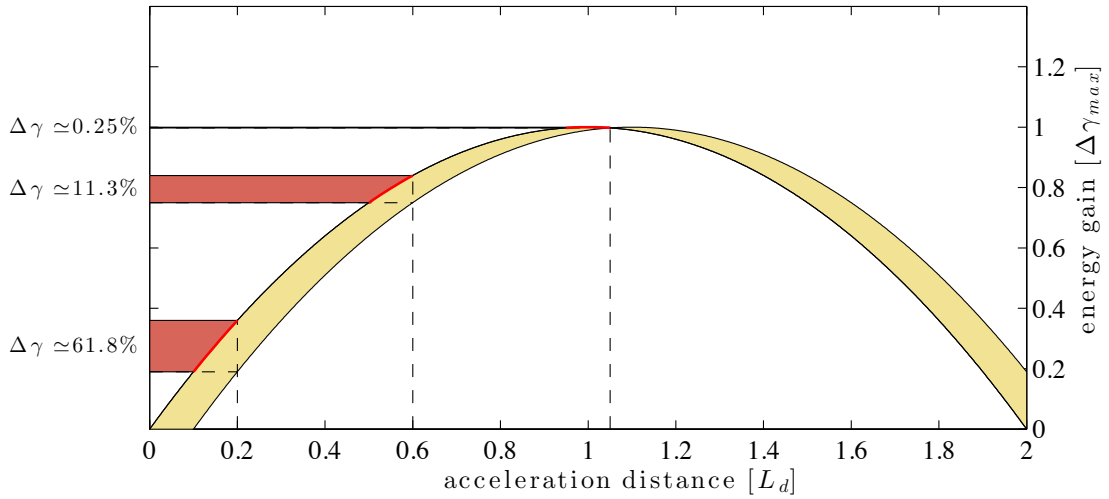

Figure 3.5 – Example for the evolution of electron energy and spread for an electron bunch injected over a distance $L_i = 0.1L_d$. The decreasing field strength leads to a rotation in the z/p_z phase space (indicated in red), reducing the energy spread significantly.

Energy gain in a constant density profile

Let us now quantify the energy gain in a laser-plasma accelerator. The energy gain of a particle accelerated in an electric field is given by

$$\Delta\gamma(z) = \frac{q}{m_e c_0^2}\int_0^z E_z(z')dz'. \tag{3.12}$$

where the field strength depends on phase and cavity size r_B. It is reasonable to assume that the electron is already highly relativistic at the moment of injection and therefore constantly advancing in the cavity at the velocity $c_0 - v_\phi$. If we furthermore approximate that both laser intensity and plasma density remain constant, we can express the energy gain as

$$\Delta\gamma(z) = \frac{q}{m_e c_0^2}\int_0^z E_z(n_0, a_0, z')dz'. \tag{3.13}$$

The maximum energy gain $\Delta\gamma_{\max} = \frac{q}{m_e c_0^2} < E_z > L_d$ is limited by the dephasing length L_d and the mean field strength $< E_z >$ experienced by the electron. We already mentioned that in the regime of complete electron blowout and matched laser spot size, a cavity of approximately $r_B \sim 2\sqrt{a_0}\lambda_p$ is formed [41]. According to (3.11) this yields to a dephasing length

$$L_d \simeq \frac{4\lambda_p}{3}\left(\frac{n_c}{n_e}\right)^{3/2}\sqrt{a_0}. \tag{3.14}$$

We have also discussed that the fields in this regime are sawtooth-like (3.8), so the average accelerating field is simply given by half the peak field strength $\langle E_z\rangle = E_z^{\max}/2$. The maximum

energy gain is then

$$\Delta\gamma_{\max} = \frac{2}{3}\frac{n_c}{n_e}a_0 \tag{3.15}$$

while the electron energy gain after at a distance z after injection is approximately

$$\begin{aligned}\Delta\gamma(z) &= \frac{q}{m_e c_0^2} \times E_z^{\max} \times \int_0^z (1 - z'/L_d)dz' \\ &= \Delta\gamma_{\max}\left(2\frac{z}{L_d} - \frac{z^2}{L_d^2}\right)\end{aligned} \quad . \tag{3.16}$$

which is the gain curve illustrated in Fig.3.5. Alternatively we can write this expression in the comoving frame in terms of the phase $\phi = z/2L_d$ and obtain $\Delta\gamma(\phi) = 4\Delta\gamma_{\max}(\phi - \phi^2)$.

3.3 Reacceleration in beam-driven wakefields

As discussed in the previous section, the energy gain in laser wakefield accelerators is mainly limited by the dephasing between the electron bunch and the optical driver, and intensity reduction of the laser driver due to depletion and defocusing. In this section we are going to discuss how the laser-accelerated electron bunch can excite its own wakefield and therefore drive acceleration beyond laser depletion and unaffected by dephasing.

3.3.1 Beam-driven plasma wakefield acceleration

In the introductory part we have seen that a plasma wake can be excited either by a laser pulse or by the space charge force of a beam. The latter is called the beam-driven regime. Its amplitude depends crucially on the charge density n_b, conventionally defined as the electron number N_e within a gaussian beam with σ_z rms length and σ_r rms radius, i.e.

$$n_b = \frac{N_e}{(2\pi)^{3/2}\sigma_z\sigma_r^2}. \tag{3.17}$$

In order to drive a wake this value should be of the order of the plasma density. For example, in a proof-of-principle experiments at SLAC in 2007 [101] it was shown that the energy of a 42 GeV electron beam could be doubled by plasma wakefield acceleration inside a 85 cm long plasma channel ($n_e \sim 2.7 \times 10^{17}\text{cm}^{-3}$). The parameters from this experiment represent the state-of-the-art of modern accelerators, providing nC level charge at a duration of some tens of femtoseconds. The electron beam had a charge of about 2.9 nC ($N_e = 1.8 \times 10^{10}$ electrons), duration of 50 fs ($\sigma_z \simeq 15\mu$m) and was focused to a spot size of $\sigma_r \simeq 10\mu$m, which lead to a bunch density of $n_b \sim 3.5 \times 10^{18}\text{cm}^{-3}$.

In analogy to a ponderomotive driver, beam-driven blowout is reached if the driver strength $n_b/n_e \gg 1$. From the beam and plasma charge densities given above we deduce $n_b/n_e \sim 13$

and peak fields of up to ~ 50 GV/m were reported. Note that the beam is still rather long as the plasma wavelength is of the order of ~ 50μm, so $k_p\sigma_z \sim 1.9$.

In order to reach bunch densities that allow plasma wakefield acceleration, beams from conventional facilities have to be compressed and focused. In contrast, due to their short duration and micrometer source size, laser-accelerated electron beams intrinsically have a competitive charge density. For example, experiments using optical injection have reported beams of ~15 pC charge at ~2 fs duration [102], thus also reaching $n_b > 10^{19}\text{cm}^{-3}$. It is therefore desirable to use such beams for beam-driven wakefield acceleration experiments [103]. Indications for beam-driven wakefields laser-plasma accelerators were first reported in 2011 [104] and recently also other groups have attributed extended acceleration to beam-driven fields [105]. Both experiments relied on self-injection and it is desirable to replace this injector with a more controlled scheme.

Shock injected beams have properties very similar to the above mentioned example of optical injected beams. However, neither kind of injector is suited for beam-driven wakefield experiments. There are several reasons for this. As we have seen in sections 1.3.3 and 3.2 the wake excitation depends on the pulse envelope and is inefficient for small $k_p\sigma_z$. Also, as there is no wake structure at the immediate front of the bunch, there are no focusing forces that contain those electrons. This leads to head erosion, very similar to defocusing of the laser pulse front in ponderomotive self-focusing we have seen in Sec.1.3.4. As a result the plasma wave excitation moves towards the bunch tail, which is another argument against using very short drivers. And lastly, as sketched in Fig.3.7, there always needs to be a driver that excites the wake and a witness bunch that gets accelerated. So we either need a long bunch or a pulse train.

In **Chapter 2: Injection** we have seen that ionization injection in high-Z gases can produce electron beams of very high charge. Electrons in the bunch are arranged in a pulse train with ~ λ_p separation. This kind of beams are a promising candidate to observe beam-driven acceleration because their bunch density of $n_b \sim 10^{18-19}\text{cm}^{-3}$ is sufficient to create strong wakes in plasmas with $n_e \sim 10^{17-18}\text{cm}^{-3}$. In particular the bunch duration $\sigma_z \sim 50\mu$m is of the same order as the plasma wavelength at these densities, allowing resonant excitation. This specific kind of injector is also interesting because it is very stable and the final electron beam energies are quite low compared to acceleration in helium, which increases the sensitivity of the spectrum measurements.

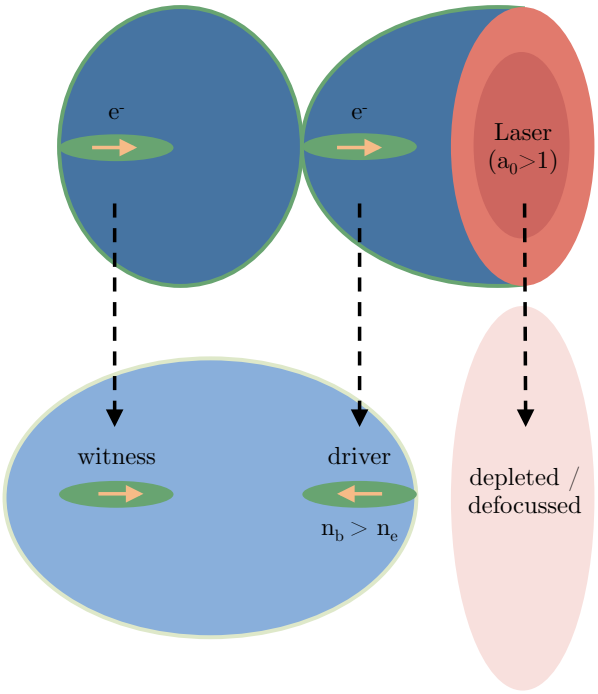

Figure 3.6 – Cartoon of the transition from laser-driven to beam-driven wakefield acceleration.

3.3.2 Experimental observation of reacceleration of ionization injected beams

In **Chapter 2: Injection** we have discussed how ionization injection in pure high-Z gases can lead to the production of high charge electron beams. We have seen that electron beam production in this regime is very stable and that the spectrum has a quasi-Maxwellian shape, which is almost independent of the laser energy.

These measurements were performed at rather high electron densities $n_e > 10^{19}\text{cm}^{-3}$. When reducing the plasma density to $n_e \sim 5 \times 10^{18}\text{cm}^{-3}$ we observe that the spectral shape changes significantly. As shown in Fig.3.7, the low-density spectrum rapidly decreases by about an order of magnitude from ~ 8 to 12 MeV, but remains almost constant in the range from ~ 15 to 40 MeV. In fact, the low-density spectrum contains less total charge, but greatly exceeds the high-density charge for energies > 20 MeV.

To understand this unusual behavior, we have performed Particle-In-Cell simulations with CALDER-CIRC.[1] When looking at the temporal evolution of the electron beam spectrum, we find that also the low-density spectrum initially has a thermal distribution, but then changes to the shape that resembles our experimental data (cf.Fig.3.8).

[1] The simulation parameters are the same as in Chapter 2: The mesh resolution is $\Delta z = 0.2k_0^{-1}$ and $\Delta r = 1.5k_0^{-1}$. Initially neutral nitrogen atoms are considered, represented by 100 macro-particles per cell. Their ionization is modeled using tunnel-ionization rates.

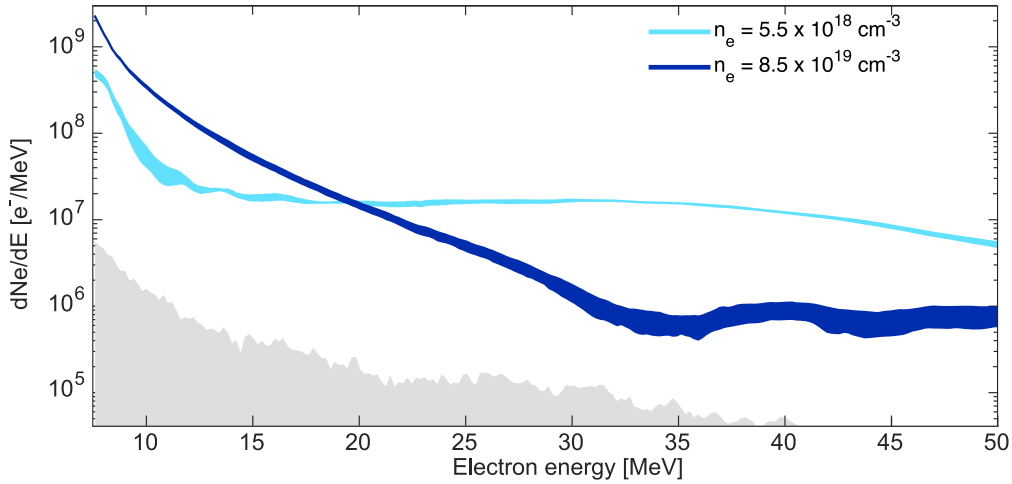

Figure 3.7 – Average electron spectra for five consecutive shots each, at $n_e = 5.5 \times 10^{18}\text{cm}^{-3}$ (lighter blue) and $n_e = 8.5 \times 10^{19}\text{cm}^{-3}$ (darker blue). The width of the lines corresponds to the standard deviation of the spectra.

To understand this effect we first have a look at the beam-wake structure at an earlier stage of the acceleration, where the spectrum is still quasi-maxwellian. This is shown in the upper frame of Fig.3.9. Electron injection commences at $z \approx 0.6$mm, the center of the gas jet is located at $z \approx 0.9$mm. As seen in Chapter 2, electrons have been injected in several wake buckets behind the laser, forming a multi-bunch structure. But this snapshot at $z = 1.2$mm is already located in the density downramp ($n_e \sim 3 \times 10^{18}\text{cm}^{-3}$) and we see that the separation starts to blur out due to the augmentation of λ_p. After another 0.5mm of propagation (close to the exit of the gas jet) the electrons form one macro-bunch of $\sigma_z \sim 60\,\mu$m length. The plasma density at this point has fallen to $n_e \sim 5 \times 10^{17}\text{cm}^{-3}$, meaning that the electron bunch length $\sigma_z \sim \lambda_p$ and can therefore excite the wakefield resonantly.

As typical for beam-driven acceleration, the driving part of the beam looses energy. This part consists of electrons from the first wakes the laser excited. Injected earlier than the rear electrons, these electrons contribute to the high energy part of the spectrum at $z = 1.2$ mm in Fig.3.8. On the other hand the electrons at the rear part of the beam experience an accelerating field, therefore gaining energy. The combination of deceleration of the front part and acceleration of the rear part leads to a rotation in the $z - p_z$ phase space, explaining the almost flat spectrum observed at the gas jet exit.

To enter this regime of beam-driven post-acceleration several conditions have to be fulfilled. Firstly the plasma wavelength has to be of the order of bunch length and secondly the beam charge density n_b needs to be significantly higher than the background density n_e. When operating the high-Z LPA at densities beyond $n_e > 10^{19}\text{cm}^{-3}$ these conditions are no longer fulfilled. As shown in Chapter 2 the length of the electron microbunches at maximum pulse energy 1.1 J is estimated to be $\gtrsim 50\,\mu$m. However, in this high density case the plasma wavelength at the end of the jet is much shorter, of the order of 10-20 μm. Also, we estimate

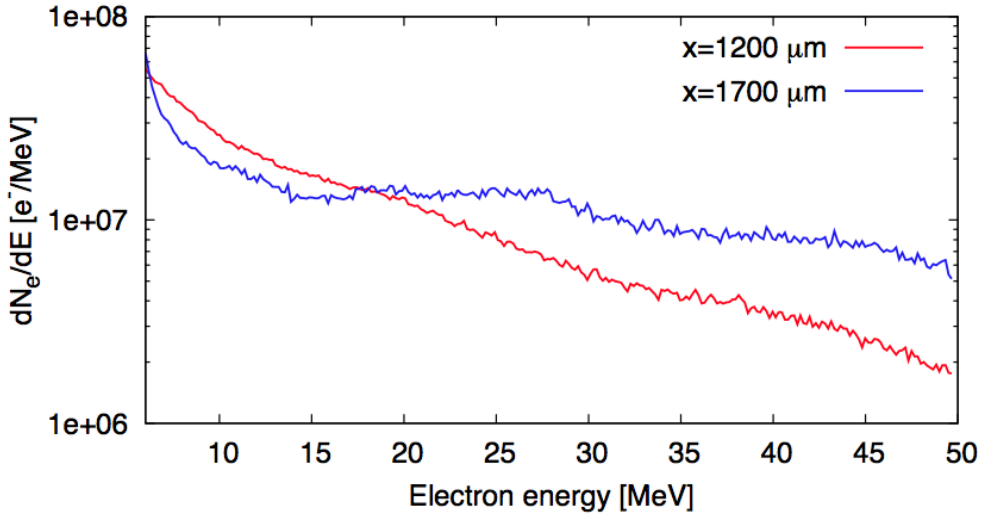

Figure 3.8 – Simulated electron spectra for different propagation lengths. In the beam-driven regime the sprectum flattens.

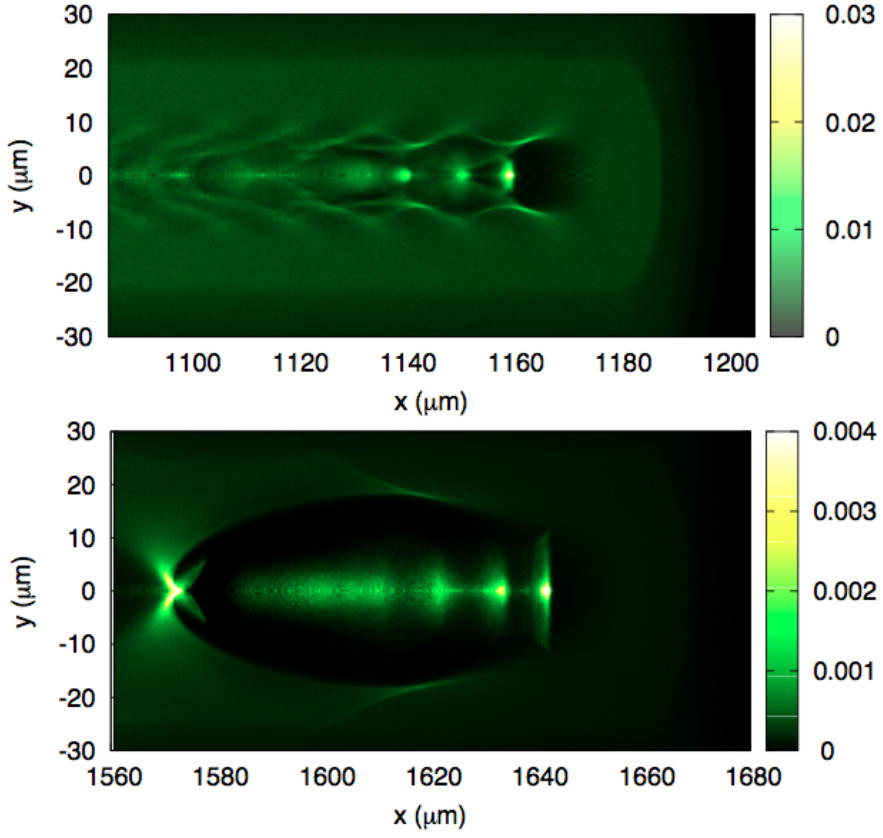

Figure 3.9 – Particle in Cell simulation of the plasma wake in the middle of the jet (laser-driven) and at the end of the jet, where the beam drives its own wake.

that the plasma wave excitation scales with n_b/n_e. So the increase of n_e by over an order of magnitude would need to be compensated by the bunch charge density. While the total bunch charge at high density is roughly an order of magnitude higher, the charge density decreases as the electron beam diverges. As the laser depletes earlier in the high density case (after $\sim$ 1mm of propagation) the divergence is higher. In consequence no transverse guiding is provided for the electron beam and the bunch density becomes insufficient to excite a wake.

3.4 Rephasing in laser-driven wakefields

In the preceding section we have discussed that the space-charge of a beam may under certain circumstances sustain wakefields beyond the laser depletion length. However, to date most LPAs are not operated in the laser depletion limited regime, but their maximum energy is restricted by the phase-slippage between the electron bunch and the laser driver, cf. Sec.3.2.2.

In this section we are going to discuss how the phase ϕ between an electron bunch and the laser-driver can be manipulated by means of density tailoring. Such phase manipulation can serve several purposes. Maintaining a phase close to the rear of the cavity ($\phi \to 0$) provides the highest acceleration gradient and therefore best conversion efficiency between laser and electron energy. Furthermore a phase locked accelerator would be limited by depletion instead of dephasing, potentially shifting the maximum attainable energy of the accelerator to higher energies. But beyond energy increase, phase manipulation can also be used to improve other beam parameters. By intentionally shifting electrons into the beginning of the decelerating phase a phase-space rotation can be induced, reducing the beam energy spread.

We start this section with a conceptual explanation upon which we will develop a phenomenological model of electron phase manipulation and discuss possible energy gain. Limits of this model are examined by means of idealized PIC simulations. We then present an experimental implementation, which matches with what we expect from simulations.

3.4.1 Rephasing of electrons via density modulation

The basic concept of electron rephasing in density gradients is inverse to downramp injection we discussed in **Chapter 2: Injection** . The basic picture, as sketched in Fig.3.10, is quite intuitive: After injection electrons are faster than the wake, so they advance inside the ion cavity. However, if the plasma density increases during propagation, the restoring force from the ion background augments, thus contracting the bubble. This contraction brings the rear of the bubble closer to the electron bunch and with that back into a (stronger) accelerating field.

The situation becomes less intuitive as one takes into account that the density change also effects the laser propagation. In order to maintain the electron phase stable, we need to solve the coupled equations of cavity size scaling and electron-driver dephasing. This is evaluated in the next section.

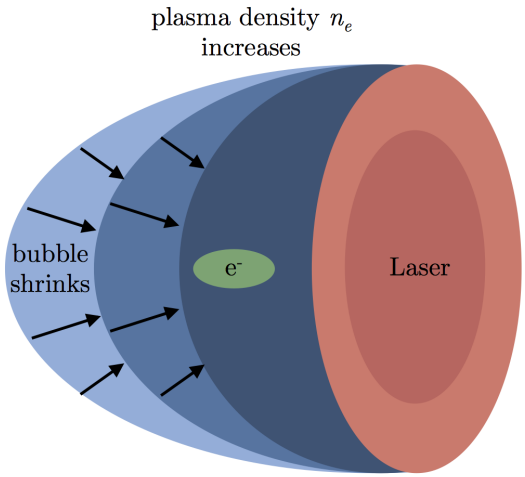

Figure 3.10 – Cartoon of the basic principle of rephasing via density tailoring. An electron bunch, shown in green, is initially at the center of the ion cavity where it would start to dephase. Changing the plasma density changes the ion density (shown in different blue tones) and therefore leads to shortening of the bubble. The electron bunch finds itself now located close to the rear part of the contracted cavity, i.e. again in an accelerating field.

3.4.2 Model of phase-adjustments in the blowout regime

Let first see under which circumstances the electron dephasing can be completely compensated by the wake evolution. This scenario is called phase-locking and has been studied in depth for guided linear wakefield accelerators [106, 107, 108].

Phase locking

We define the initial phase of a particle as $\phi_0 = \xi_0/\lambda_{\text{wake},0}$, where ξ_0 is the position of the electron with respect to the wake and $\lambda_{\text{wake},0}$ is the initial wakefield period. In order to maintain the phase constant, the phase slippage $\Delta\xi/\lambda_{\text{wake},0}$ has to be compensated by changing the wavelength. At each moment the infinitesimal change necessary is given by

$$\frac{d\lambda_{\text{wake}}}{dt} = \frac{v_e - v_\phi}{(1-\phi_0)} \tag{3.18}$$

Let us now assume that the electron is highly relativistic and therefore $v_e \approx c_0$. With this assumption there is also a constant dependence between time and propagation distance $z(t) = c_0 t + z_0$, and for the co-moving coordinates $\xi(t) = (c_0 - v_\phi)t + \xi_0$. Furthermore we assume that the driver propagates at the group velocity in underdense plasmas (at $n_e \ll n_c$),

i.e. $v_\phi \approx 1-(n_e/n_c)/2$. With these assumptions (3.18) reads

$$\frac{1}{c_0}\frac{d\lambda_{\text{wake}}}{dt} \approx \frac{n_e/n_c}{2(1-\phi_0)}. \tag{3.19}$$

Assuming a non-varying field amplitude[2] a_0, the cavity length is only dependent on the plasma density, i.e. $\lambda_{\text{wake}}(t) = \lambda_{\text{wake},0} \times \sqrt{n_0/n_e(t)}$. From this we get

$$\frac{d\lambda_{\text{wake}}}{dt} = \frac{\lambda_{\text{wake},0}}{2}\sqrt{n_0}\frac{\dot{n}(t)}{n(t)^{3/2}} \tag{3.20}$$

This dependence is actually true for the linear, 1d non-linear and 3d non-linear model, as all of them scale the same way with the plasma density. The cases differ however in the initial cavity size $\lambda_{\text{wake},0}$. Equations (3.19) and (3.20) can be rearranged to a first order non-linear ordinary differential equation of the type

$$\dot{n} - \alpha \times n^{5/2} = 0 \tag{3.21}$$

With the initial condition $n(t=0) = n_0$ the solution in the spatial domain reads

$$n(z) = \frac{n_0}{(1-z/L_0)^{2/3}}, \tag{3.22}$$

which is the result found by Pukhov and Kostyukov [107]. The density increases first close to linearly, but then the density ramp becomes increasingly steep until a singularity is reached at $L_0 = 3c_0/(2n_c(1-\phi_0)\lambda_{\text{wake},0}n_0^{1/2})$. Pukhov argues that in the linear wakefield regime the change of plasma density will also effect the resonance factor c_{env} and the wake gets damped when the density increases. They therefore included this effect in their calculations. The taper in Rittershofer's model has a similar shape [108], but the model is different as he considers a guided pulse and takes into account laser diffraction in the parabolic channel.

The above-mentioned models have only very limited validity, because they do not take into account the complete laser pulse evolution, as discussed in Sec.1.3.4. Especially pulse compression and self-focusing have to be included in a realistic model, since many experiments operate at densities around $\sim 10^{19}$ cm^{-3} and rely on self-guiding. The effects can compensate density induced changes of the wakefield period and phase-locking is not evident to achieve under these circumstances .

Phase reset

Instead, a simpler and more realistic scenario is a one-time phase reset. For this we keep the density constant and then adapt the phase once. In this case the wake velocity is $1-n_0/2n_c$, so the ODE becomes of the type $\dot{n} - \alpha \times n^{3/2} = 0$, with $\alpha = c_0\sqrt{n_0}/(1-\phi)n_c\lambda_{\text{wake},0}$. From there

[2] Note that especially in the self-guided blowout regime this assumption is not necessarily fulfilled. This point is discussed in more detail in the following section.

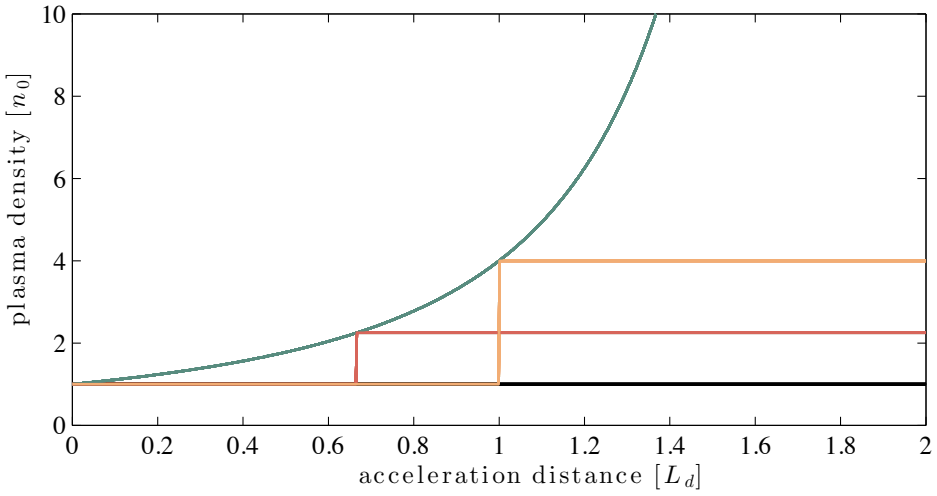

Figure 3.11 – Densities required for unique phase reset according to (3.24).

we find the reset density

$$n(z) = \frac{n_0}{\left(1 - \frac{1}{2(1-\phi)} \frac{n_0}{n_c} \frac{z-z_0}{\lambda_0}\right)^2} = \frac{n_0}{\left(1 - \frac{1}{(1-\phi)} \frac{z-z_0}{2L_d}\right)^2}, \tag{3.23}$$

where we have identified the dephasing length $L_d = (\lambda_{\text{wake},0}/2)/(1 - v_\phi/c_0)$ in the second step. For the more specific case of initial injection at the back ($\phi = 0$ and $z_0 = 0$), the equation simplifies to

$$n(z) = \frac{n_0}{\left(1 - \frac{z}{2L_d}\right)^2}, \tag{3.24}$$

which is equivalent to the intuitive result $n(\phi) = n_0/(1-\phi)^2$. The function is plotted in Fig.3.11. If we define the phase velocity including depletion, according to (1.25), we only have to change the constant α in the ODE (3.21). The solution is again (3.23), with the dephasing length from (3.11).

Energy gain for phase reset

We can now calculate the energy gain for such a phase reset in the blowout regime. For a first estimation we assume a boost when the electron is just dephased, i.e. $z = L_d$. In this case the required density transition (3.24) is $n_1 = 4n_0$. Once rephased, the electrons will essentially behave as if they were just injected into a new accelerator with density $n_1 = 4n_0$. So we can use (3.15) and sum the dephasing limited gain of those two 'stages', which gives

$$\Delta\gamma_{max} = \Delta\gamma_{max}(n_0) + \Delta\gamma_{max}(4n_0) = \frac{5}{4}\Delta\gamma_{max}(n_0). \tag{3.25}$$

The second stage contributes much less to the overall gain, as the dephasing length is shorter at higher density. Still, we expect a gain of around 25 percent.

Let us now evaluate the optimal case. To find the maximum achievable energy gain in a unique boost we take the position dependent gain in a sawtooth-shaped wakefield (3.16)

$$\Delta\gamma_1(z) = \left(\frac{2z}{L_d} - \frac{z^2}{L_d^2}\right) \times \Delta\gamma_{max}(n_0) \tag{3.26}$$

and add the density dependent gain (3.15) according to the rephasing density (3.24)

$$\Delta\gamma_2(z) = \left(1 - \frac{z}{2L_d}\right)^2 \times \Delta\gamma_{max}(n_0). \tag{3.27}$$

The complete energy gain is therefore

$$\begin{aligned}\Delta\gamma(z) &= \left(\left(1 - \frac{z}{2L_d}\right)^2 + \frac{2z}{L_d} - \frac{z^2}{L_d^2}\right) \times \Delta\gamma_{max}(n_0) \\ &= \left(1 + \frac{z}{L_d} - \frac{3}{4}\frac{z^2}{L_d^2}\right) \times \Delta\gamma_{max}(n_0).\end{aligned} \tag{3.28}$$

As shown in Fig.3.12, the global maximum is at $z = 2/3 \times L_d$ and leads to $\Delta\gamma_{max}\left(\frac{2}{3}L_d\right) = \frac{4}{3}\Delta\gamma_{max}(n_0)$. So we estimate that a phase reset can lead to gain in the order of one third of the dephasing limited energy gain. The results are in accordance with [109], where such a density step scenario was empirically studied using test particle simulations. It is worth noting that this relative energy augmentation is independent of the plasma density n_0. However, this situation will change if we take into account the laser pulse evolution. As we will discuss in the next section, the scheme is most likely to work best at high densities, where electrons gain significant energy over short distances.

3.4.3 Numerical modeling

The model we introduced in the preceding section has two main limitations: It assumes a constant laser intensity and a sawtooth-like wakefield. As we have discussed in Sec.1.3.4, self-focusing tends towards a matched spot-size w_0 which depends on the plasma density and the field strength a_0. So we have to expect that self-focusing will evolve as we change the density. But as the analytical framework of self-focusing has only been derived for the weakly perturbed regime ($a_0 \ll 1$), we need to perform Particle-in-cell simulations to study this phenomenon. This also help us to estimate the fields, as the Lu-model [110, 111] typically underestimated the longitudinal wakefields at the back of the ion cavity.

For these simulations we want to study purely the dynamics of the bubble and the laser, without any electrons. To do so we initiate the simulation with laser pulse parameters close to the matched spot size that we found in preceding simulations. The density transition is

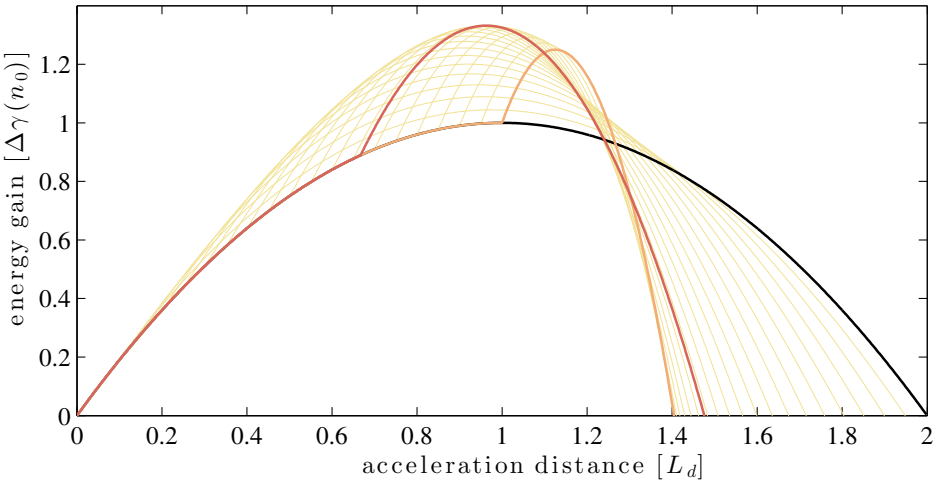

Figure 3.12 – Estimated energy gain curve for phase-rest to $\phi = 0$ at different positions along the acceleration. The density profiles from Fig.3.11 for rephasing at $z = \frac{2}{3}L_d$ and $z = L_d$ are plotted again in red and orange, respectively.

positioned very early in the simulation, as soon as a stable wake structure is established. This allows us to use high resolution and distortions by the electron beam are evaded. After these initial studies, we are going to model rephasing of shock injected electrons at full length.

Density transition width

First we want to study the bubble dynamics. As initial study we perform simulations for a laser pulse with 30 fs duration, initial waist of 9 microns and a relatively high peak field strength $a_0 = 8.0$. The relatively high laser power (~ 200 TW) was chosen because the ponderomotive force at lower laser intensity was not sufficient to ensure ponderomotive blowout during the whole propagation length. Also we start off with a strong focus in order to get closer to the self-focusing limit from the beginning.

The resolution for the simulations is $\Delta z = 0.15k_0^{-1}$, $\Delta r = 0.75k_0^{-1}$ and $\Delta t = 0.96\Delta z$, on a simulation mesh $n_z \times n_r = 3000 \times 500$. The initial plasma density is $n_0 = 1.0 \times 10^{19}\,\mathrm{cm}^{-3}$ and after ~ 100 µm a clear bubble structure has developed, but no electrons have been injected into the wake yet.

At this point ($z = 100\,\mu\mathrm{m}$) the density is increased linearly to $n_0 = 2.0 \times 10^{19}\,\mathrm{cm}^{-3}$. We chose two different transition widths, $z_{ramp,1} = 25\,\mu\mathrm{m}$ and $z_{ramp,2} = 125\,\mu\mathrm{m}$. The first corresponds to sharp transitions we encounter in shocks and in this case the transition length is of the same order of magnitude as the cavity size $z_{ramp,1} \sim 2r_B$. The second ramp is flatter $z_{ramp,2} \gg 2r_B$, but should be short enough too avoid self-focusing during the transition itself.

We find that the sharp transition leads to a broadening of the trajectory crossing region in the back of the cavity, as electrons recoil earlier at higher ion densities, cf. Fig.3.13. During

the transition the electron density falls down inwards the cavity, which reduces the peak longitudinal field, cf. Fig.3.13. Once the background density remains constant the peak profile reverses, with the peak pointing inwards, which increases the field strength. However, the broad crossing region disturbs the subsequent ion cavities, which then start to collapse.[3]

The softer density ramp in contrast shows a very clean density peak and the electric field rises significantly. Also, the wake structure is preserved in this case. The length of the cavities scales with $\sqrt{n_0/n_1} = 1/\sqrt{2}$, with a wake period of $\lambda_{\text{wake}} \sim 13\,\mu\text{m}$ compared to $\lambda_{\text{wake}} \sim 18\,\mu\text{m}$ without density transition.

So the fields at the back of the cavity generally exceed the field strengths assumed from Lu's model. The phase reset predicted by our calculation may therefore underestimate the gain in an actual experiment. Also, the width of the density transition crucially influences the wakefield evolution and should receive further attention in future studies.

Self-focusing

Following this we compared how the laser evolved for the three different cases. In Sec.1.3.4 we have reviewed how the laser undergoes self-focusing due to relativistic and ponderomotive effects. At a given plasma density the laser self-focuses approximately to the matched spot size. But changing the local plasma density will especially affect the ponderomotive component and change the laser pulse evolution. A density up-ramp typically leads to increased ponderomotive self-focusing of the laser, which then enhances relativistic effects and ultimately results in a cavity expansion by $a_0^{1/2}$. However, ponderomotive re-focusing needs some time to develop. Here we find that about $\sim 100\,\mu\text{m}$ of propagation are required for self-focusing to develop.

In consequence, step-like profiles as those shown in Fig.3.11 do not represent the ideal rephasing profile as self-focusing will eventually counteract the cavity contraction due to density augmentation. The same reasoning holds for phase-locking in the blowout regime, where the non-linearity of self-focusing makes it therefore difficult to deduce an actual phase-locking profile in the blow-out regime.

For any experiment on rephasing in the blowout regime this means that density plateaus should be avoided. Here the beam self-focuses, which re-expands the bubble and can lead to self-injection. Instead, another experimental configuration - phase-reset in shocks - might be more promising. With their characteristic width of just some hundred microns, shock structures will be less affected by self-focusing. Yet the strong field increase at the back of the bubble, can provide a boost that takes place in the first hundred microns after the shock.

[3] In the lower frame of Fig.3.13 we also observe a field fluctuation that resembles beam loading. However the cavity is not loaded with electrons at this point. The effect might be related to the strong self-focusing and disappears later in the simulation.

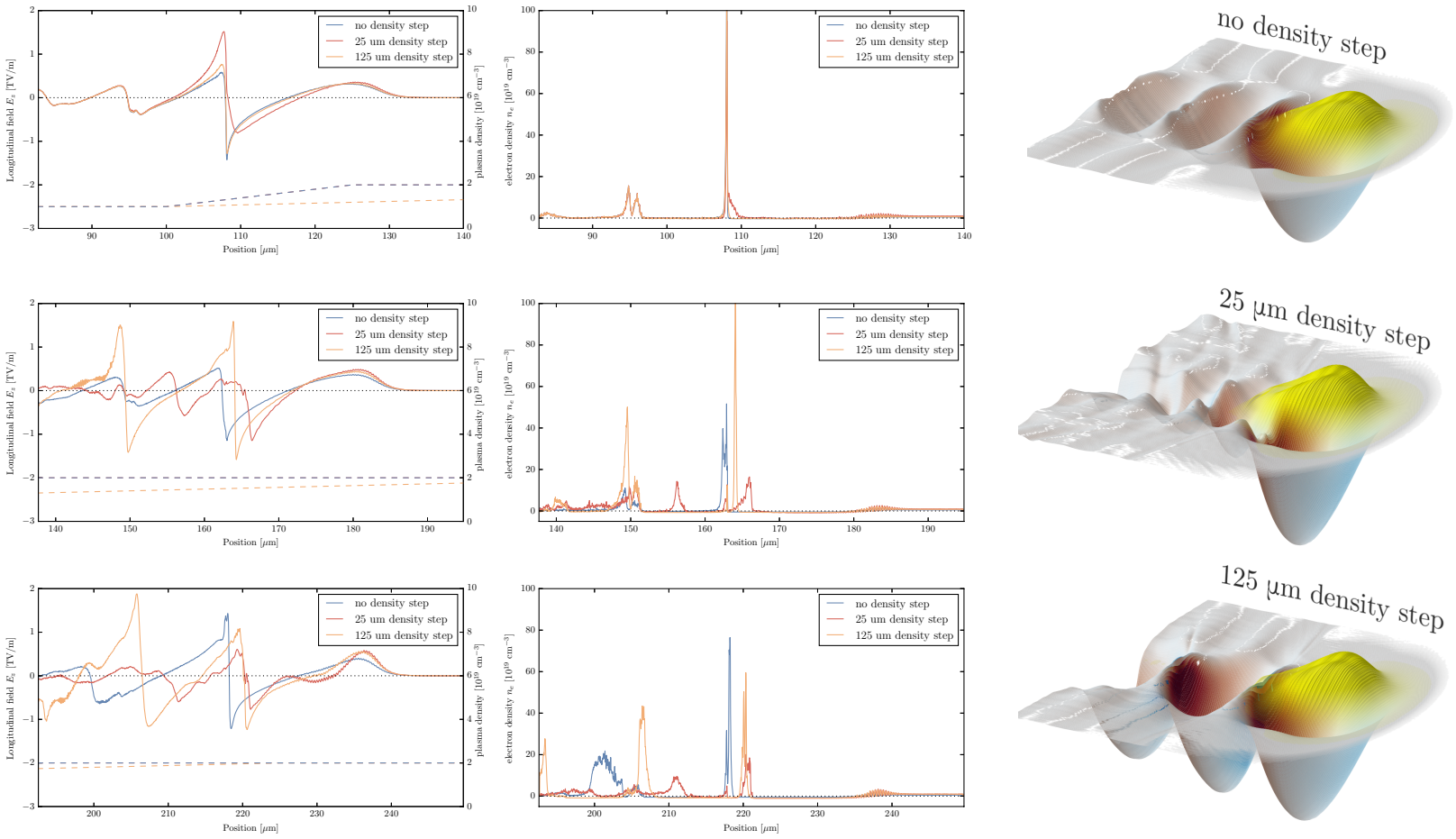

Figure 3.13 – On-axis evolution of the density profile (left) and longitudinal wakefield (middle) for a sharp density step (25 µm) and a moderate step (125 µm) to twice the initial density. The density profile is indicated with dashed lines. The images on the right visualize the two-dimensional wake potential (relief) and electric field (color map) at ~ 80 µm behind the density ramp begins, corresponding to the middle frame.

Rephasing of shock-injected electrons

The foregoing simulations focused on the laser-plasma dynamics with the purpose of estimating the limits of our analytical model. For this the simulations started close to the matched spot size and the total simulation length was some hundred microns. In the following we are going to include electrons into the model. In order to avoid beam-loading effects, which also alter the cavity size, we only inject a weakly charged electron beam via shock injection. For comparison we choose the initial same parameters as in **Chapter 2: Injection** , but let the simulation run longer in order to estimate the dephasing length.[4] The simulation resolution is $\Delta z = 0.3k_0^{-1}$, $\Delta r = 1.5k_0^{-1}$ and $\Delta t = 0.96\Delta z$, on a mesh $n_z \times n_r = 1500 \times 250$.

Here we have chosen to boost the beam after $z \sim 0.6L_d$, which according to (3.23) requires a density increase from n_0 to $2n_0$. The width of the step is put shock-like, with a transition length of $\sim 50\mu$m. As shown in Fig.3.14 the density step steepens the energy gain curve, resulting in an increase of the final beam energy of about 30 percent. Note the similarity to the prediction by our model, cf. Fig.3.28.

However, as we have discussed in the preceding sections, after some hundred microns of propagation self-focusing sets in, which then leads to self-injection. The large amounts of electrons injected through this mechanism provoke a cavity expansion which brings the shock injected beam faster into dephasing. We also observe that part of the beam is lost during rephasing. This is surprising, as we see in Fig.3.15b that the electron beam does not reach the rear of the bubble during dephasing. However, maintaining electron at the rear part of the bubble is delicate, because the focusing field are very weak in this region. We will discuss this effect in more detail in **Chapter 4: Beam Transport** .

The situation is worse when rephasing is overdone, for instance if we increase the density from n_0 to $3n_0$. This scenario is depicted in Fig.3.14c. In this case even more electrons are lost and the electrons run even faster into dephasing, due to the increased self-injection.

In general we observe that the self-focused laser field strength a_0 evolves delayed, but almost linear with the density profile. In consequence all cavity contractions in this regime are eventually compensated and if the density is high enough self-injection is triggered. We have therefore tested another profile, which reduces the density again after the step. As shown in Fig.3.14d, self-injection is suppressed, while electrons still gain additional energy.

[4] For this kind of simulation it is important to extract the dephasing length directly from the simulation. This is necessary because the simulated laser pulse is not only subject to physical, but also numerical dispersion. When solving Maxwell's equation using the common Yee algorithm (cf.Apx.B), the pulse is slower than the physical pulse, i.e. the dephasing length is shorter. Using Lehe's algorithm [112], which was designed to avoid numerical Cherenkov, it is faster. Numerical dispersion can be reduced using a finer mesh, but as we need maintain a CLF number close to unity, increasing the resolution by a factor X augments the computing time by X^{2-3}. More details on this are elaborated in the appendix on numerical methods.

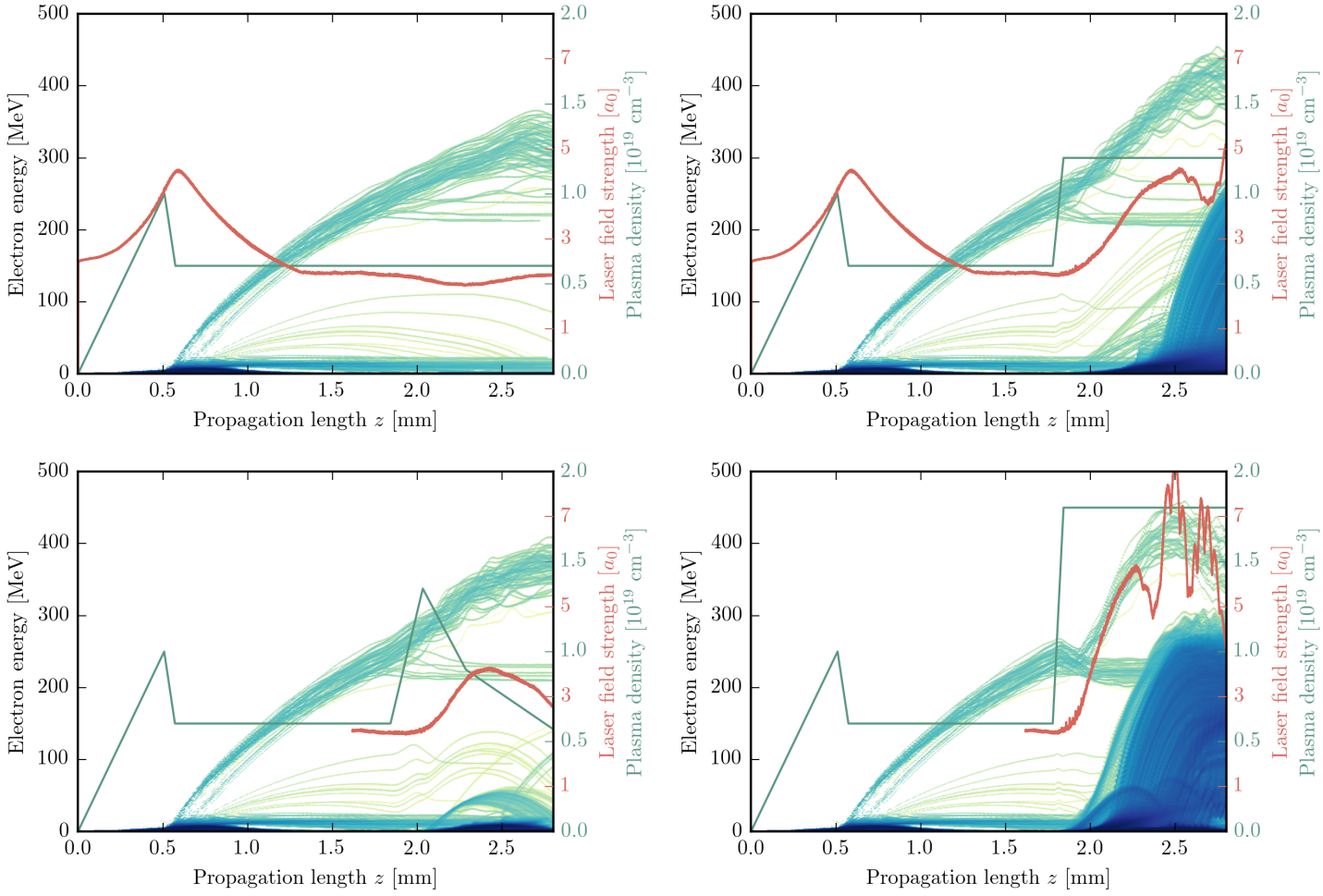

Figure 3.14 – Above: CALDER-CIRC simulation for shock injection as in Chapter 2. Electrons are injected at $z = 0.6$ mm and dephase after ~ 2 mm of propagation, reaching around 300 MeV. Below: Simulation with density step at $z \sim 0.6 L_D$,where the model (3.23) predicts $n_1 = 2n_0$. Electrons are clearly re-accelerated and reach around 400 MeV, which is in good accordance with the model prediction. Note that the laser self-focuses at higher density, which ultimately triggers self-injection at $z \sim 2.5$ mm.

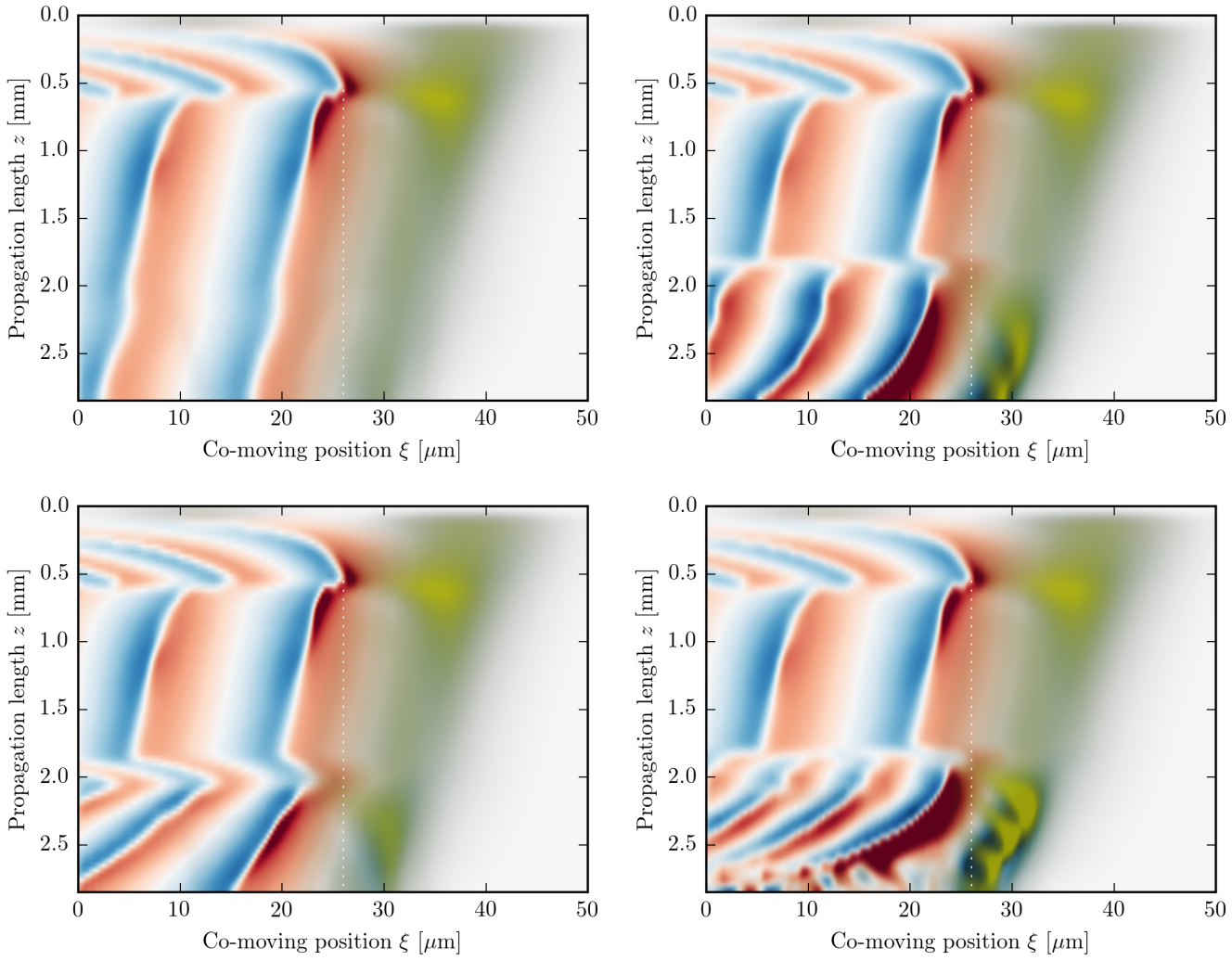

Figure 3.15 – On-axis longitudinal field and laser field for the same simulations as in Fig.3.14. The white dotted line indicates the position where electrons are injected.

3.4.4 Experimental observation of phase-reset in sharp density transitions

In the last section we have discussed several kinds of density profiles to perform a phase-reset. We found that shock-like profiles, as used for injection in **Chapter 2: Injection** , may be ideal for a proof-of-principle experiment. The reason for this is that the shock provides a rapid density increase, and therefore cavity contraction, but then the density decreases again, which prevents injection from self-focusing at high densities. The experimental setup (Fig.3.16) resembles the shock injection experiment from Sec.2.4, yet with the blade placed at the rear side of the gas jet.

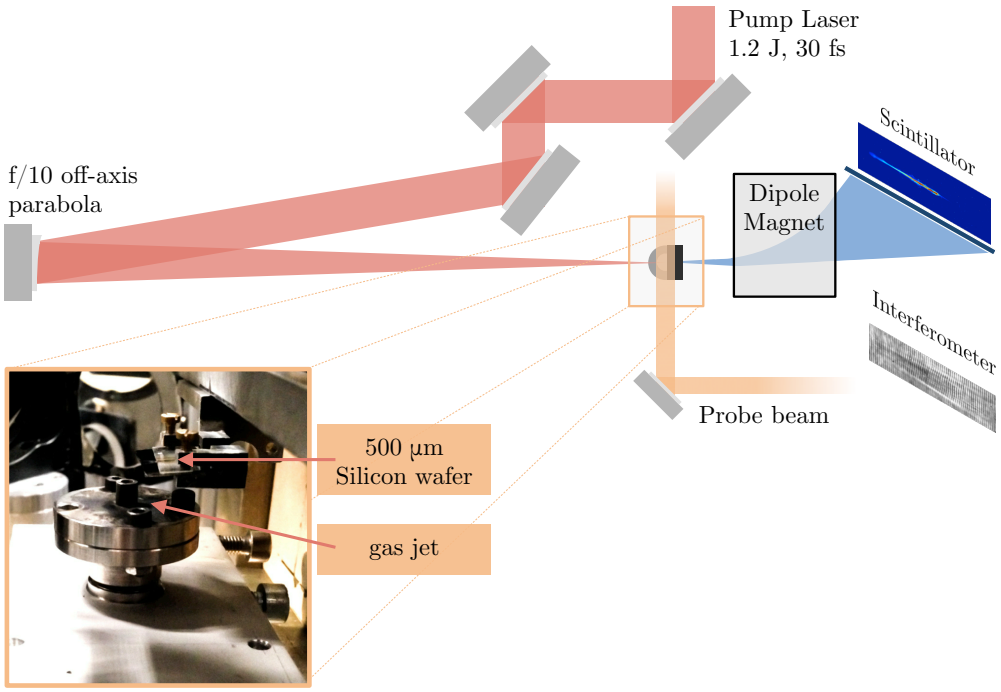

Figure 3.16 – Experimental setup used for electron rephasing. The laser is focused on a gas jet with a silicon wafer mounted at its rear side. When this blade is placed in the gas flow a shock front is formed, creating a sharp upward density step in the gas profile. The shock is almost perpendicular to the laser axis, which allows interferometric characterization of the plasma density via Abel transformation along the propagation axis. Electron spectra are measured using the deflection of electrons in a dipole magnet. A scintillating screen is placed behind the magnet, measuring electrons from ~ 50 – 600 MeV.

Experimental setup and observations

The experiment was performed at SALLE JAUNE, which delivered 1.2 Joule on target at 30 femtosecond duration during the experiment. The pulse was focused using an f/10 off-axis parabola, with a focal spot size of 15µm. This results in a peak intensity of $1.0 \times 10^{19}\,\mathrm{W/cm^2}$, which is equivalent to a normalized vector potential $a_0 \simeq 2.2$. As target we use a ^{2}He gas jet with a 1.5 mm supersonic de Laval nozzle. A 500 µm silicon wafer is mounted at the back of the nozzle, as shown in Fig.3.16. The shock front is formed when the gas flow encounters the blade. This leads to a sharp upward density step, which we characterize using interferometry, cf. Fig.3.17. Electron spectra are obtained from the deflection of the electron beam in a 10 cm, 1.1 T dipole magnet. The position and orientation of the scintillating screen (Kodak Lanex) allows detection of electrons in the range from $\sim 50 - 600$ MeV.

The bottom frame of Fig.3.17 shows the average electron spectra for different blade positions. In this experiment electrons are injected via transverse self-injection, which leads to a broad electron spectrum, with most charge below ~ 200 MeV and a cut-off around 280 MeV. The spectrum drastically changes when introducing a density step, i.e. by moving the blade inwards. We observe that part of the electron beam looses energy, while the cut-off energy increases beyond ~ 350 MeV.

The average spectra seem broadband, without any mono-energetic features. However, this is an effect of the averaging over many shots. When we look at representative single-shot spectra (Fig.3.18), we observe that the high energy component exhibits a quasi-monoenergetic feature.

Interpretation and validation via simulations

In our phenomenological model we had only considered monoenergetic electron beams at a distinct phase ϕ with respect to the laser. However, within a beam electrons cover a range of phases. So during the cavity contraction, some of the electrons will gain energy, but those which are still close to the rear of the cavity will end up in the second arc of the wake and where they are decelerated. This principle is illustrated in Fig.3.19b and it explains why we see part of the spectrum down-shifted, while another part is accelerated.

In order to verify this qualitative argumentation, we have performed partice-in-cell simulations with CALDER-CRIC. The resolution for these simulations was $\Delta z = 0.3 k_0^{-1}$, $\Delta r = 1.5 k_0^{-1}$ on a grid of 3672×400 cells. The density profiles are chosen according to the experimental data (Fig.3.17). In Fig.3.19a the computed electron spectra are presented, which resemble the experimentally obtained data. Due to the density upramp, electron injection starts rather late, close the center of the jet. Without a shock it continues from thereon up to $z \sim 1.3$ mm. This results in a long electron bunch with broad energy spread, as shown in the phase space map (Fig.3.19c). At the position shown, part of the bunch has already entered a decelerating phase.

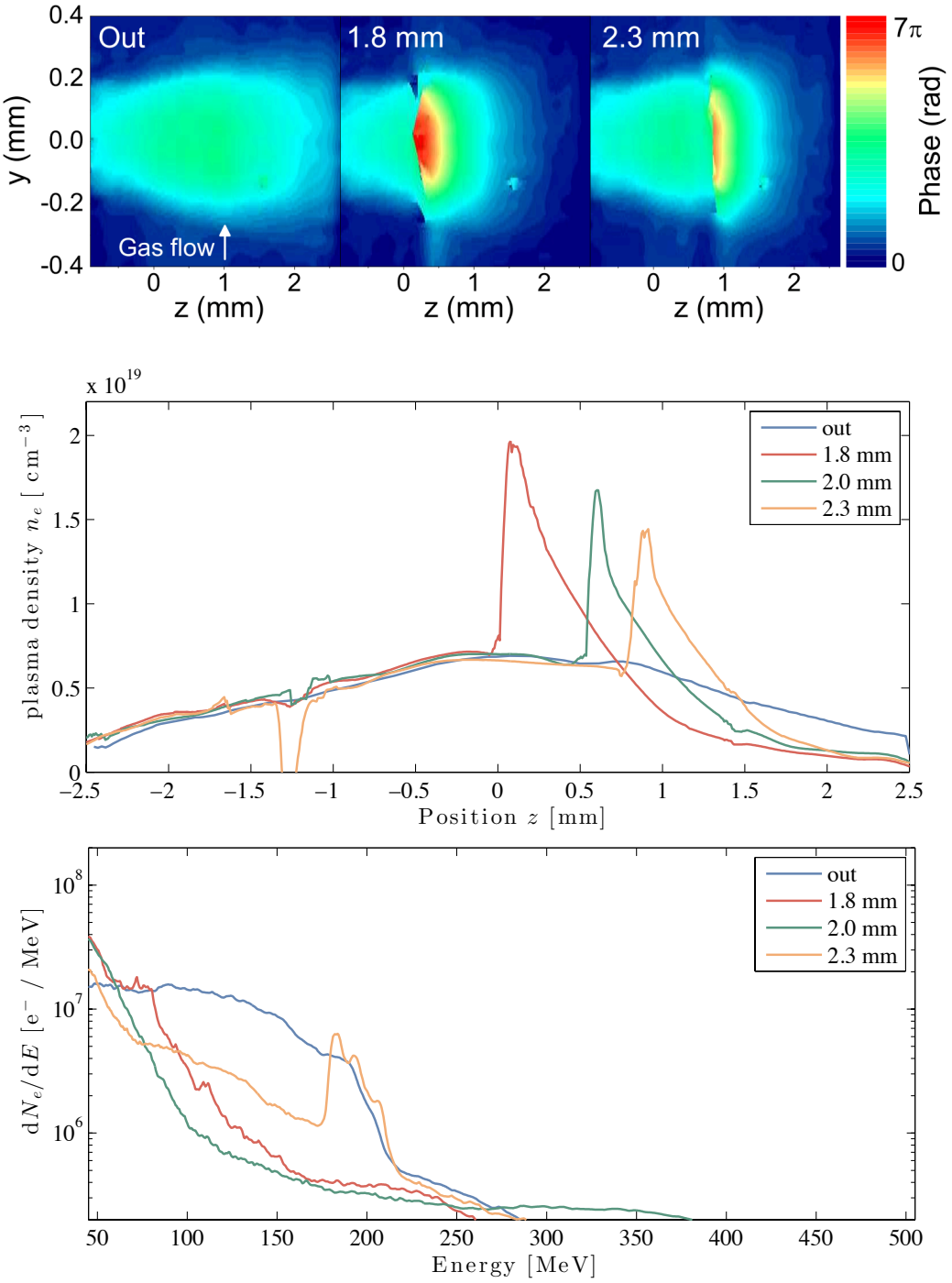

Figure 3.17 – Top: Phase maps retrieved from interferometry data for different blade positions. Middle: Density estimations using Abel inversion along the laser propagation axis. Bottom: Average spectra the different blade positions. Shots per position: 20, 5, 30, 5.

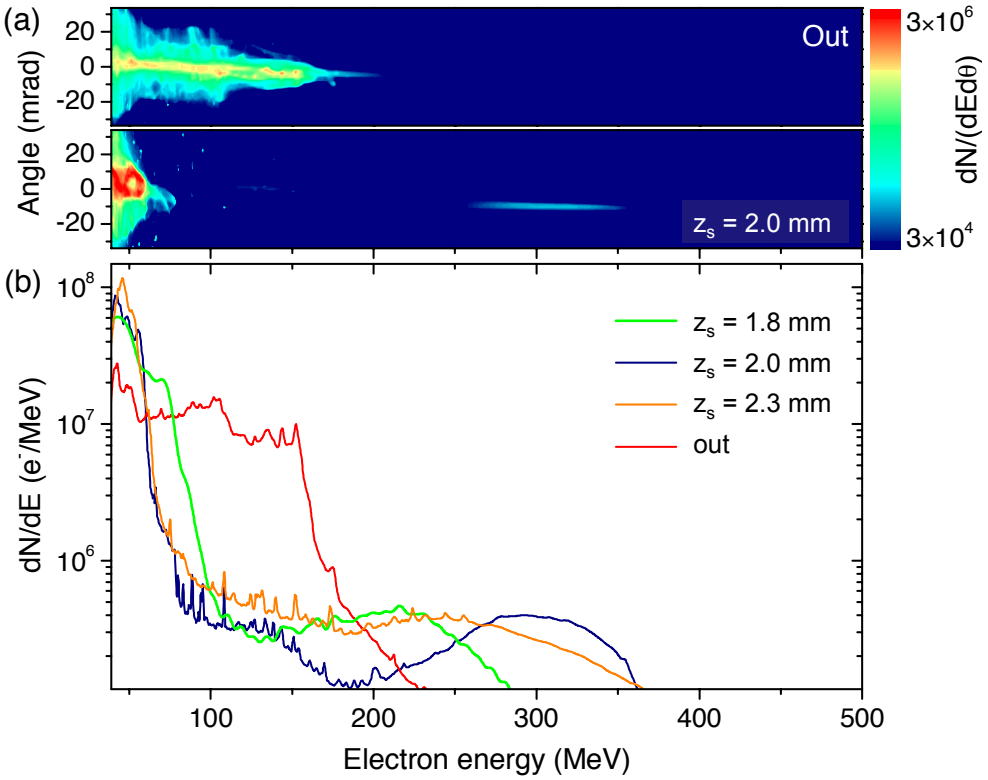

Figure 3.18 – Representative single-shot spectra without and with a density transition. In the single-shot we observe that the rephasing leads to the formation of a peak at high energies.

If we however introduce a density step just before this point, the situation changes drastically. First, the head of the bunch it again located completely within the accelerating phase. In fact, while the unperturbed density profile lead to sawtooth-like wakefields with a gradient of 0.05 (TV/m) / μm, the tailored profile results in an increased field gradient of ~ 0.19 (TV/m) / μm at the center and augments even stronger at the rear of the bubble. This corresponds to what we have seen in previous PIC studies (Sec.3.4.3). The beam that is now at the back of the bubble thus experiences very strong accelerating fields (exceeding TV/m) which results in a phase space rotation and reduces the energy spread of the bunch in the first cavity. The part of the bunch that was initially at the back of the bubble in contrast finds itself within the decelerating phase of the wake and looses energy, just as we have observed experimentally.

We have discussed before that density tailoring can also favor electron injection and the downramp after the shock could for instance lead to reinjection of electrons. In simulations we find that this indeed occurs, however, these electrons will quickly dephase and do not reach energies beyond > 150 MeV, as depicted in Figure 3.19e and 3.19f.

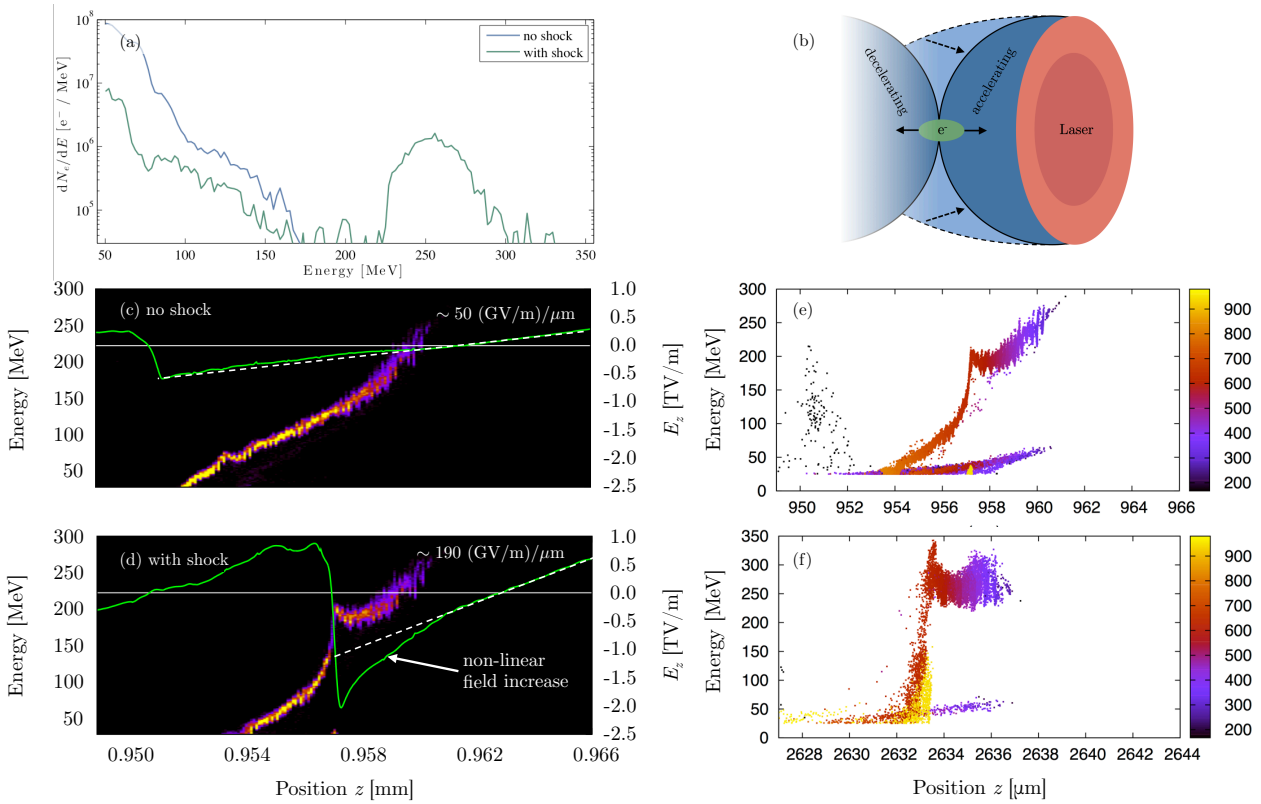

Figure 3.19 – Interpretation of the experimental results. (b) shows a cartoon of the basic principle of rephasing via density tailoring. An electron bunch, shown in green, is initially at the center of the ion cavity where it would start to dephase. Changing the plasma density changes the ion density (shown in different blue tones) and therefore leads to shortening of the bubble. The electron bunch finds itself now located close to the rear part of the contracted cavity, i.e. again in an accelerating field. (a) Results from PIC simulations in CALDER-CIRC with and without density tailoring. The spectra are in qualitative accordance with the behavior observed in experiments. (c-d) Dumps of the $z - p_z$ phase space from PIC simulations with and without density tailoring. The cavity contraction results in much higher accelerating field at the back of the shortened bubble, which results in a rapid acceleration of electrons at these position. This results in a phase space rotation and hence a reduced energy spread of this part of the beam. (e-f) Phase space $z - p_z$ as extracted from PIC simulations directly behind the shock and after another ~ 1.6 mm of propagation. The electrons are color-coded according to their injection position. Yellow corresponds to electrons injected in the downramp behind the shock, which as shown the second plot, do not contribute to the electron spectrum for > 150 MeV.

3.4.5 Energy spread reduction in propagation limited accelerators

The phase-space rotation that reduced the energy spread could also be reproduced in other experiments. During another campaign with similar setup, we observed that a beam distribution could be converted into a quasi-monoenergetic beam by means of a density gradient.

In this experiment the initial electron energies are substantially lower, reaching around 100 – 150 MeV, with maxwellian distribution. However, when introducing the shock, the energy spread reduced significantly and the broad spectrum turned into a quasi-monoenergetic beam, cf. Fig.3.21. But in contrast to the previous experiments, the cuf-off energy of the beam remains essentially unchanged.

In the preceding campaign electron energies of beyond 300 MeV were observed for similar laser parameters and also from simple scaling laws we estimate a dephasing length of ~ 2 mm with beam energies between 200 – 300 MeV. This suggests that the energy gain in this experiment was limited by the plasma length. Indeed, interferometric measurements show that the density profile (cf. Fig. 3.20) was steeper and the laser defocuses faster than in previous experiments, which could be enough to explain the reduced energy gain.

In this scenario the shock-induced phase change would act differently than in the aforementioned case. We have discussed before that the energy spread is always larger before dephasing - and this would be the case for a propagation limited accelerator. But if a density transition is introduced at the end of the accelerator, this would advance dephasing and thus result in a phase-space rotation, as sketched in Fig.3.20. It is however important that the acceleration terminates shortly after the density step, because otherwise the energy spread will increase again. Indeed we observed the quasi-monoenergetic behavior only for a short range of blade positions, which supports this interpretation.

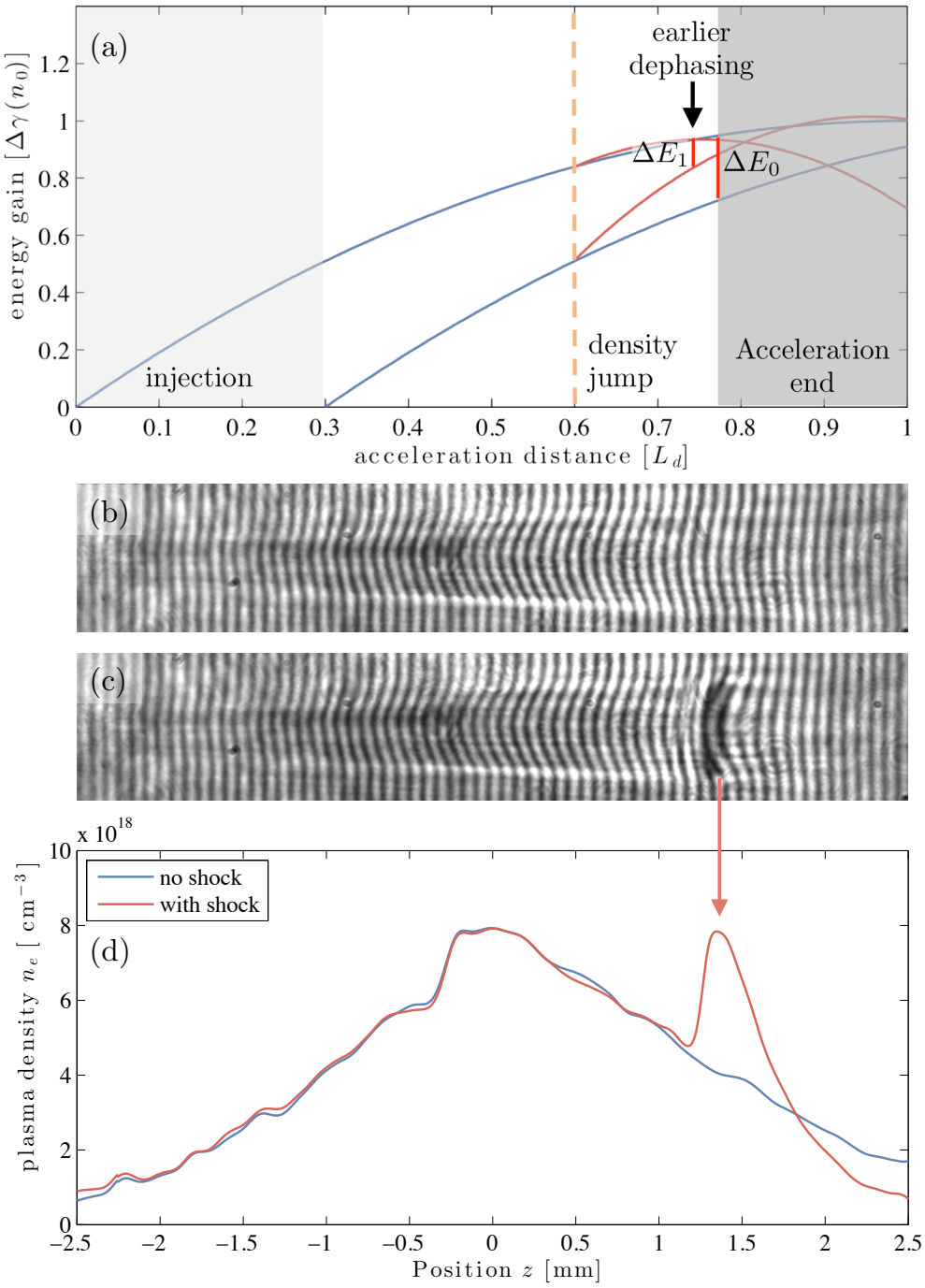

Figure 3.20 – (a) Schematic illustration how a density change before dephasing is reached can lead to a reduction of the beam energy spread. (b/c) Interferometry images with and without shock. (d) shows the density profile obtained from Abel inversion. Note that the resolution of the shock is limited by the fringe spacing of ~ 110 µm.

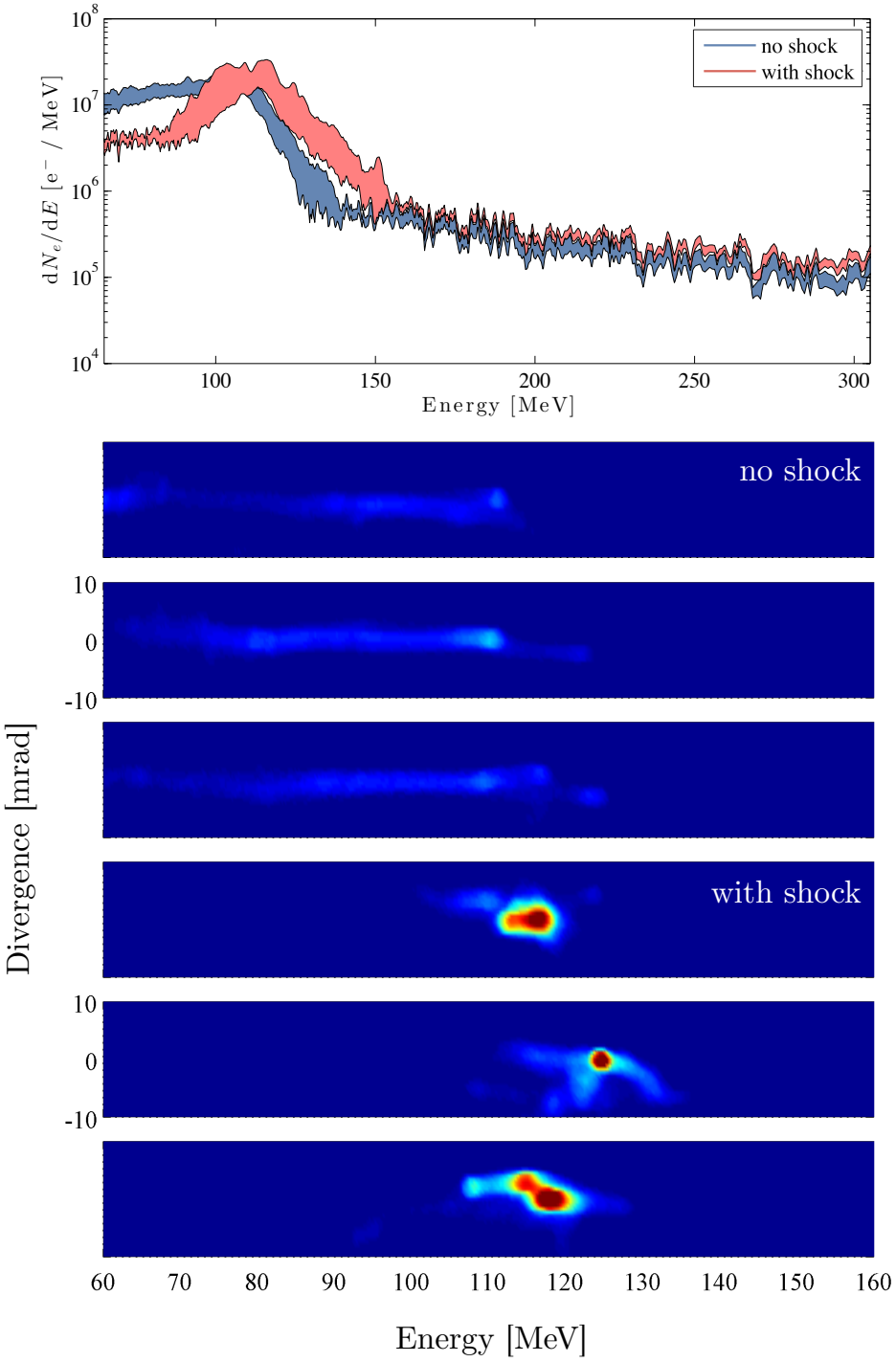

Figure 3.21 – Top frame: Electron spectra for 10 shots each with and without shock. The linewidth is the moving rms-error divided by $\sqrt{n}$. Below: Representative single shots. In the unperturbed density profile the energy spread is a hundred percent with a charge of 155 ± 13 pC, whereas the spread is < 10 percent with the shock in place and the charge remains similar (140 ± 13 pC).

3.4.6 Energy gain of shock-injected beams

The last study performed in this context is the demonstration of energy gain in tailored density profiles for mono-energetic electron beams. For this experiment we used shock injection in pure Helium, as described in **Chapter 2: Injection** . This time the density transition is formed with a small gas jet of ~ 500 μm diameter, subsequently referred to as 'needle'. The upward transition length of this setup is comparable to the setup with the razor blade, cf. Fig.3.22d.

The shock-injected electrons have a quasi-monoenergetic distribution, as shown in Fig. 3.22 (i), with a peak energy of 125 ± 2 MeV and a charge of 17 ± 2 pC (mean over ten shots). With the needle jet placed at the exit of the first jet we clearly observe an energy gain. As we increase the backing pressure of the second jet the electron energy increases up to 220 MeV. At even higher densities the electron beam is lost. This is in accordance with the behavior expected from rephasing, as there is a threshold at which ion cavity contracts too far and the beam is decelerated.

Though we observe a drastic energy gain, we have to examine whether this gain is completely due to rephasing or partly the result of an increased propagation distance: In contrast to previous experiments where the shocks created by the blade reduced the total propagation length, the plasma channel is clearly elongated as the needle jet is active. However, while there is a clear difference between the channel length with and without the jet, the propagation distance is very similar for different backing pressures of the second jet, Fig. 3.22 (ii-iv). So it is certain that the jet acts as second high density stage for the accelerator.

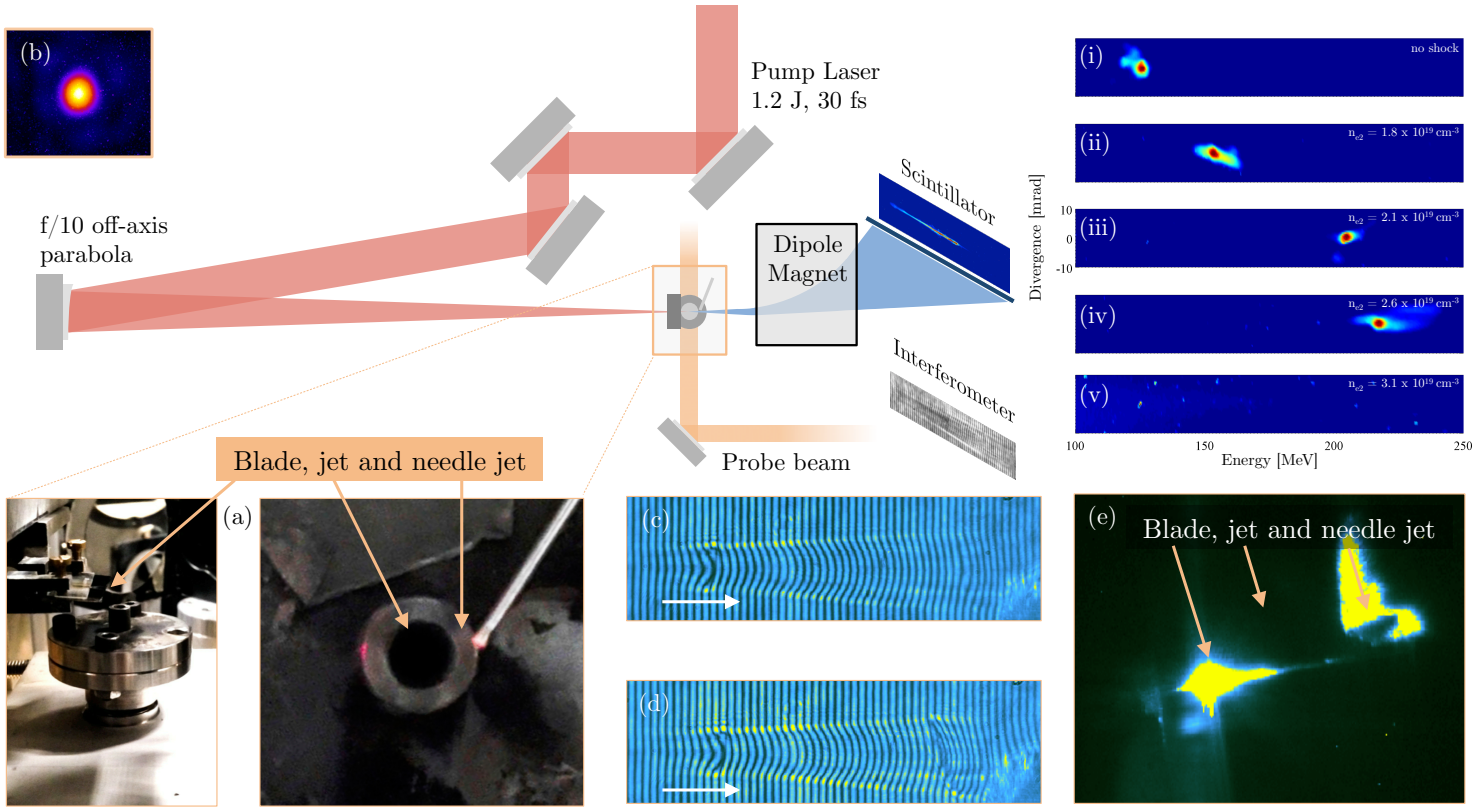

Figure 3.22 – Setup and results for the experiment on energy gain of shock injected beams. (a) shows photos of the target, (b) is the focal spot at the day of the experiment. Interferometric images of the plasma channel without (c) and with the needle jet (d) are accompanied by a top view image of the setup (e). As the shock created by the second jet is asymmetric with respect to the laser axis it is not possible to completely reconstruct the density profile for this geometry. We can however estimate the plasma density shortly behind the density transition. The measured beam spectra for different backing pressures of the needle jet are shown in (i)-(v).

3.5 Conclusions

In this chapter we have studied the laser wakefield acceleration process itself. In the introductory part we have discussed conventional resonant linacs and we have shown that laser wakefield accelerators can provide much higher accelerating gradients (up to TV/m). Yet the energy gain in both kinds of accelerators is limited by (i) the length over with the accelerating structure can be sustained and (ii) the phase matching between the field and the electron bunch. In a laser wakefield accelerator the former limitation (i) is mainly related to the depletion of the laser driver, while the latter dephasing (ii) is a result of the subluminal phase velocity of the laser-plasma wave. We have demonstrated two new regimes of operation for the accelerator that alleviate these effects: beam-driven self-acceleration and density induced rephasing.

For highly charged, long ($\sigma_z > \lambda_p$) electron beams the beam-driven wakefield can sustain a wakefield beyond depletion of the laser driver, which leads to continuous acceleration of the rear part of the bunch. We have experimentally observed this effect for electron beams from ionization injection in high-Z gases. However, the wake excitation depends critically on the ratio between bunch density and plasma density, as well as the bunch length and the plasma wavelength. Therefore the experimental parameters have to be carefully chosen and we observe such reacceleration only for a limited plasma density range.

Furthermore, we have studied how appropriate density tailoring permits to influence in the phase of electrons in a non-linear laser wakefield by means of analytical and numerical models. We find that electrons can gain significant energy from a single density transition. Here an increase of the local plasma density close to the dephasing length reduces the ion cavity size and resets electrons back into an accelerating phase. But as the higher plasma density further reduces the group velocity of the laser pulse, the acceleration length shorter than before rephasing. We estimate a maximum gain of the order of 30 percent. Furthermore we find that this kind of phase manipulation is restricted by self-focusing, which can either directly compensate the cavity expansion or induce self-injection. We also observe that the shape of the ramp influences the transformer ratio of the wakefield.

We have experimentally demonstrated the scheme in a setup very similar to electron injection with shocks, where we use the density upramp created by a razor blade placed at the exit of a supersonic gas jet. For broadband electron beams from self-injection we observe both acceleration of the beam head and deceleration of the tail, which is in accordance to Particle-in-Cell simulations. Furthermore we find that the method can be used to force electron beams in dephasing, which reduces their energy spread. In the final section we show that the density tailoring increases the final energy of monoenergetic electron beams by over 50 percent. Understanding the exact interplay of density increase, wakefield dynamics and self-focusing is an important area of future investigations.

4 Beam transport

Beam transport lines are used to connect different stages of accelerators without losing beam quality. In laser-plasma accelerators the injector and accelerator are directly coupled, which means that no additional beam transport is necessary between these sections. However, from the exit of the accelerator on the beam needs to be collimated. As we will discuss in this chapter, conventional beam optics are too weak to transport laser-accelerated beams without beam degradation. We show that in analogy with the longitudinal wakefield accelerators, the transverse wakefields are suited for beam collimation at unparalleled field strengths. In particular we present experimental results which show that a laser-driver can be used to focus ultrashort beams. We also show results on electron defocusing due to beam-bubble interactions, which is a promising mechanism to influence the amplitude of betatron oscillations.

Contents

In order to use a particle beam for applications, beam transport lines are necessary to guide the beam towards its destination. Throughout the beamline, the beam quality is characterized by the normalized emittance, which is the area the beam occupies in the phase space [113]. Due to the small ion cavity size, laser-accelerated electron beams have (sub-)micrometer source size. Even though the beam divergence is rather large (some milliradians), this leads to a good normalized emittance in the order of mm.mrad.[114, 115]

Together with their ultrashort pulse length - which results in a very competitive beam charge density n_b - this makes laser wakefield accelerated electrons a promising candidate for bright synchrotron sources and free-electron lasers (see **Chapter 5: Radiation**). However, whereas the normalized emittance is considered to be conserved in most conventional accelerator beam lines, laser-accelerated beams suffer from emittance growth during free propagation [116]. This is a consequence of their larger energy spread and divergence, which makes it imperative to collimate the beam shortly behind the accelerator.

Conventional beam optics are limited to field strengths of some Tesla, which even at smallest aperture would require several centimeters to collimate a laser-accelerated beam. Once again, the fields of the charge separation induced by a laser or particle beam can be orders of magnitude stronger. Just instead of the longitudinal fields we consider the transverse wakefields.

As for plasma wakefield acceleration, also plasma wakefield lensing was first studied in the context of conventional accelerators. The interest in strong lenses came mostly from the particle collider community, which has actively discussed the usage of plasma lensing at final focusing stage of future colliders [117, 118] and thereby increase the luminosity.

Plasma wakefield lensing, which is also called self-pinching in the accelerator community, was first demonstrated at Argonne National Laboratory in 1990 [119] and shortly later at Tokyo University[120]. Other key experiments include focalisaton of positron beam at SLAC [121] and streaking measurement of the electron beam focusing [122]. The latter showed that despite the observation of plasma lensing, the head of the electron bunch still diverged. This behavior - which we already discussed for beam-driven accelerators (Sec.3.3) - is related to the length required to excite the wakefield. Accordingly beam-driven plasma lensing is not possible for ultrashort electron bunches as we encounter in laser-wakefield accelerators. Here we demonstrate that for such beams, a laser pulse can be used to create focusing fields.

4.1 Conventional beam optics

In this section we will introduce the topic of linear beam optics to the reader, for further reading see [123] and [124]. In particular we will discuss the concept of emittance and twiss functions to describe beam evolution. For the latter we focus on the transfer matrix method. Then we solve explicitly the equations of motion for one of the most common beam optical elements, the quadrupole. This will serve as an example for the following analysis of electron motion in wakefields. We conclude this part with a discussion of emittance growth in laser-wakefield accelerators.

4.1.1 Fundamentals of beam optics

At a given time t an electron j is characterized by its phase space coordinates $(\vec{x}_j, \vec{v}_j)$. If the motion is predominantly in z-direction we can alternatively use its position $\vec{x}_j$, the deviation angle from the axis $\vec{x}_{j\perp}' = d\vec{x}_{j\perp}/dz$ and its energy γ_j as parameters.

An electron bunch is characterized in a similar way by the mean and the root-mean-square (rms) quantities of the ensemble of N_b electrons, cf. Fig.4.1

$$\begin{aligned}
\langle z\rangle &= \frac{1}{N_b}\sum_j z_j \qquad & \sigma_z^2 &= \langle z^2\rangle = \frac{1}{N_b}\sum_j z_j^2 \\
\langle x\rangle &= \frac{1}{N_b}\sum_j x_j \qquad & \sigma_x^2 &= \langle x^2\rangle = \frac{1}{N_b}\sum_j x_j^2 \\
\langle x'\rangle &= \frac{1}{N_b}\sum_j x_j' \qquad & \sigma_{x'}^2 &= \langle x'^2\rangle = \frac{1}{N_b}\sum_j x_j'^2 \\
\langle \gamma\rangle &= \frac{1}{N_b}\sum_j \gamma_j \qquad & \sigma_\gamma^2 &= \langle \gamma^2\rangle = \frac{1}{N_b}\sum_j \gamma_j^2
\end{aligned} \tag{4.1}$$

which are the beam center positions $\langle x\rangle$ and $\langle z\rangle$, the average energy $\langle\gamma\rangle$, bunch duration σ_z/c_0, bunch width σ_x, beam divergence $\sigma_{x'}$ and energy spread σ_γ. Note that the beam direction $\langle x'\rangle = 0$ in the paraxial approximation.

However, it is clear that these quantities evolve over time, e.g. the bunch width changes due to the beam divergence. When characterizing such a dynamical system it is therefore useful to refer to conserved quantities instead. For the motion of charged particles under linear transverse forces Liouville's Theorem is valid, meaning that the phase space volume is constant.

For reasons we will discuss later, it has become common to characterize this volume in each plane (k, k') as an ellipse (cf. Fig.4.2) parametrized by α (related to beam tilt), β (beam size), γ

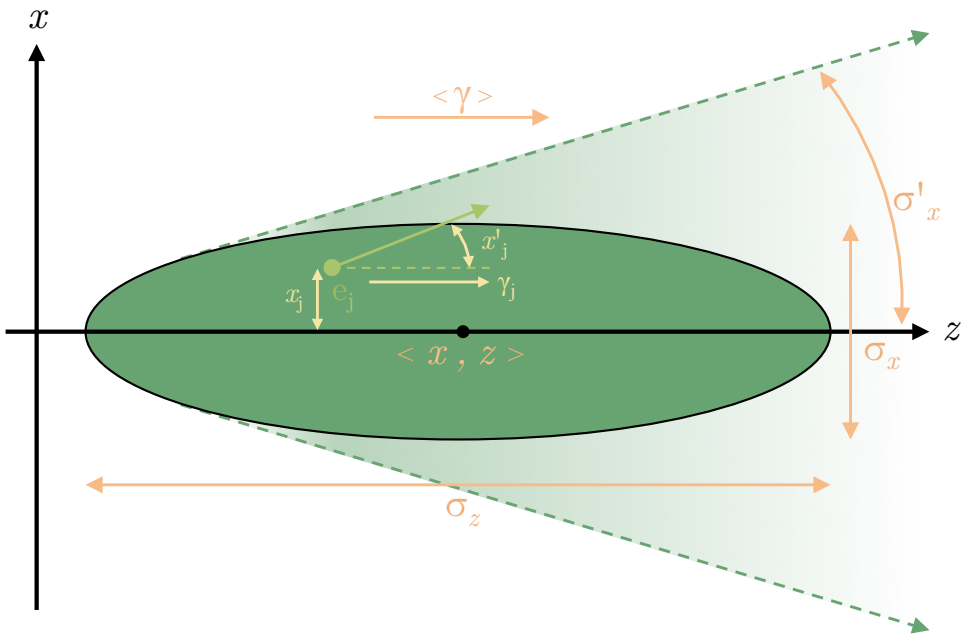

Figure 4.1 – Schematic illustration of the electron beam in the laboratory frame. While each individual electron e_j in the bunch has its proper position and momentum, the whole beam is characterized by the mean and root-mean-square quantities of the ensemble of particles.

(divergence) and ϵ (phase space area)[1]

$$\gamma^2 x^2 + 2\alpha x x' + \beta x'^2 = \epsilon. \tag{4.2}$$

The conserved phase space area ϵ, which is often interpreted as a kind of 'temperature' of the beam, is also called the **beam emittance**. A well-known equivalent for this is the beam parameter product in light optics ($\theta \times w_0 = \lambda/\pi$ for a diffraction limited Gaussian beam). When the beam is not at waist we have to take into account the beam tilt and therefore the emittance ϵ_x is calculated from the bunch width σ_x and the divergence $\sigma_{x'}$ and the correlation $\langle x\, x' \rangle = \frac{1}{N_b} \sum_j x_j x'_j$:

$$\epsilon_x = \sqrt{\langle x^2 \rangle \langle x'^2 \rangle - \langle x\, x' \rangle^2} \tag{4.3}$$

Geometrically it is clear that the phase space ellipse - or Twiss - parameters α, β and γ are not independent from each other for an ellipse of fixed area ϵ (cf. Fig.4.2), but it is found that they are related by

$$\alpha^2 - \beta\gamma = 1 \tag{4.4}$$

[1] The convention to parametrize with β and γ might cause some confusion with the velocity β and Lorentz factor γ. Also, note that two different signs of α are common in the literature. We have followed the convention from [124], which differs e.g. from the definition in [125].

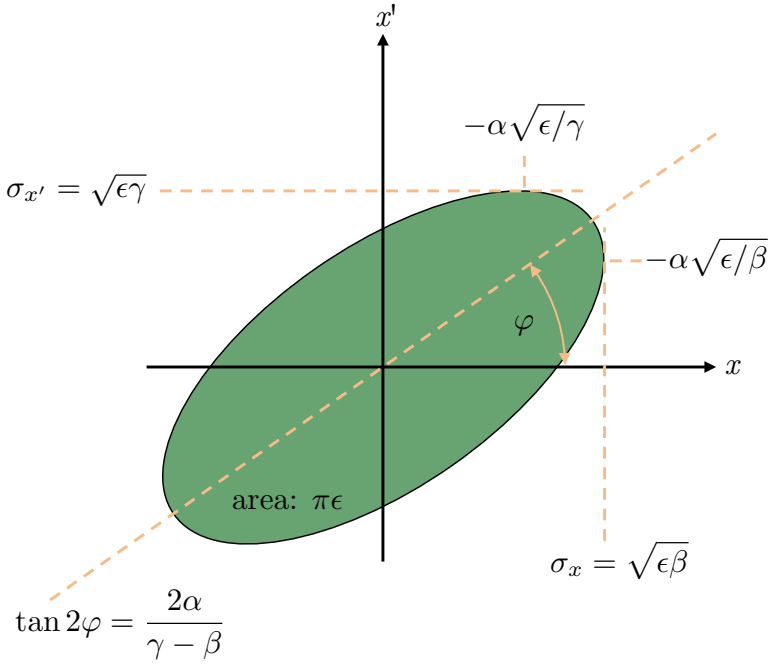

Figure 4.2 – Beam ellipse in the $x - x'$ (position-divergence) phase space.

The evolution of these parameters during beam propagation can be calculated in analogy to light optics via transfer/transport matrices. For a general transfer matrix $\mathcal{M} = (A, B; C, D)$ the beam evolves from its initial position (x_0, x_0') according to

$$\begin{pmatrix} x \\ x' \end{pmatrix} = \begin{pmatrix} A & B \\ C & D \end{pmatrix} \begin{pmatrix} x_0 \\ x_0' \end{pmatrix} \tag{4.5}$$

and with the intial ellipse equation $\gamma^2 x_0^2 + 2\alpha x_0 x_0' + \beta x_0'^2 = \epsilon$ we find that

$$\begin{aligned} \alpha &= -AC\beta_0 + (AC + AD)\alpha_0 - BD\gamma_0 \\ \beta &= A^2\beta_0 - 2AB\alpha_0 + B^2\gamma_0 \\ \gamma &= -C^2\beta_0 - 2CD\alpha_0 + D^2\gamma_0 \end{aligned} \tag{4.6}$$

Two frequently used examples are the transfer matrices of a free drift over a distance d and a thin lens of focal length f

$$\mathcal{M}_{\text{drift}} = \begin{pmatrix} 1 & d \\ 0 & 1 \end{pmatrix} \qquad \mathcal{M}_{\text{thin lens}} = \begin{pmatrix} 1 & 0 \\ -1/f & 1 \end{pmatrix}. \tag{4.7}$$

and with (4.5) and (4.6) we find immediately the impact in the beam ellipse. For example we find that in a free drift

$$\alpha_{\text{drift}} = \alpha_0 - d\gamma_0 \qquad \beta_{\text{drift}} = \beta_0 - 2d\alpha_0 + L^2\gamma_0 \qquad \gamma_{\text{drift}} = \gamma_0. \tag{4.8}$$

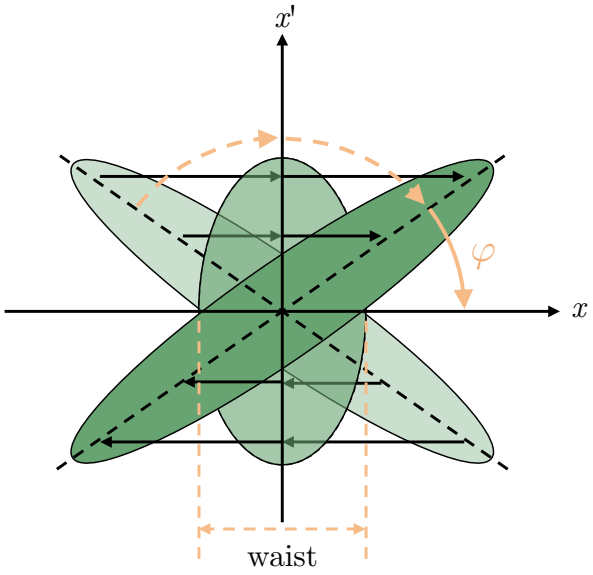

Figure 4.3 – Evolution of the beam ellipse during free drift.

The physical interpretation of this is straightforward: During free space propagation the divergence does not change ($\sigma_{x'} = \sqrt{\epsilon\gamma} = \text{const}$). But the beam size ($\sigma_x = \sqrt{\epsilon\beta}$) changes, which then obviously affects the tilt. The beam waist is reached at $d = \alpha_0/\gamma_0$, which corresponds to zero tilt α, cf. Fig.4.3.

With the transfer matrix formalism we have found a way to describe the beam evolution in terms of its rms quantities. However, in this approach we have no information about individual particle trajectories. Such can be found solving the equations of motion for particles in a given field. It turns out that the phase space ellipse is equivalent the phase space trajectory of a particle performing harmonic oscillations. The contour of the rms ellipse then corresponds to the trajectory of the particle with largest amplitude $\sqrt{\epsilon\beta}$. Historically these trajectories were derived to describe beam fluctuations in the betatron accelerator. This is why the trajectory parameters $\alpha(z)$, $\beta(z)$ and $\gamma(z)$ are also known as betatron functions, while the oscillations are referred to as **betatron oscillations**.

4.1.2 Quadrupole lenses

Quadrupole lenses are among the most common beam optical elements and essential to focus and collimate particle beams. We will now use the fields of electric and magnetic quadrupoles to solve the equations of motion of electrons within and derive the corresponding betatron phase-space coordinates $\big(x(z), x'(z)\big)$.

The field strength in a pure electric quadrupole is given by

$$E_x = -E_0\frac{x}{a} \qquad \text{and} \qquad E_y = E_0\frac{y}{a}, \tag{4.9}$$

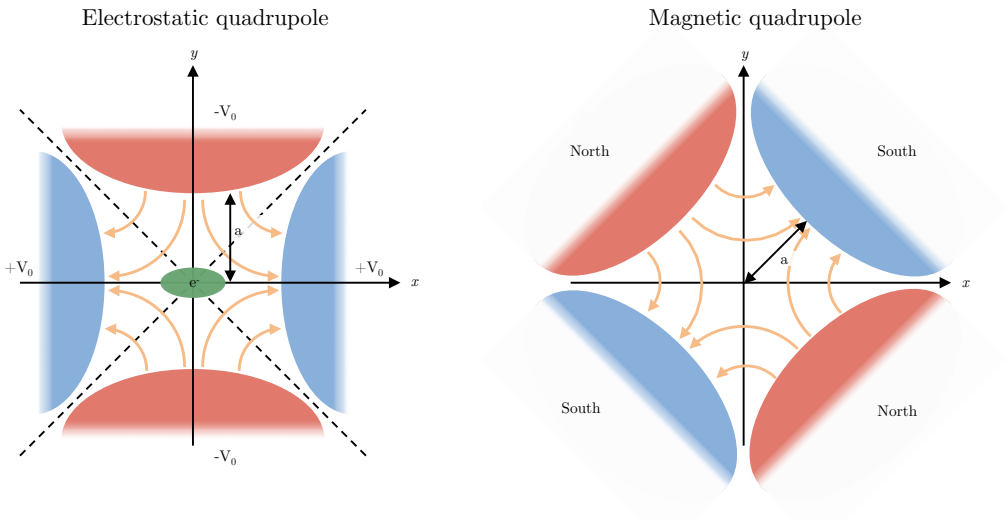

Figure 4.4 – Schematic layout of electrostatic and magnetic quadrupoles. The left side shows the force lines for an electron beam in an electrostatic quadrupole, where the components are focusing in the y direction and defocusing in x direction. The magnetic quadrupole on the right will act in the same focusing directions for an electron beam traveling in positive z^+ direction.

where a is the semiaperture as defined in Fig.4.4. In a similar way the magnetic quadrupole field is

$$B_x = B_0 \frac{x}{a} \qquad \text{and} \qquad B_y = B_0 \frac{y}{a}. \tag{4.10}$$

From Lorentz equation we can deduce the equations of motion of an electron in such fields

$$\frac{d^2x}{dt^2} = \frac{eE_0}{m\gamma a}x \qquad \text{and} \qquad \frac{d^2y}{dt^2} = -\frac{eE_0}{m\gamma a}y \tag{4.11}$$

and correspondingly in the magnetic quadrupole

$$\frac{d^2x}{dt^2} = \frac{ev_zB_0}{m\gamma a}x \qquad \text{and} \qquad \frac{d^2y}{dt^2} = -\frac{ev_zB_0}{m\gamma a}y, \tag{4.12}$$

which are all ordinary differential equations of the form $\ddot{\xi} \pm \omega_0^2\xi = 0$. The solutions are either the confined oscillatory motion $\xi = \xi_1 \sin\omega_0 t + \xi_2 \cos\omega_0 t$ or the diverging $\xi = \xi_1 \sinh\omega_0 t + \xi_2 \cosh\omega_0 t$. Thus, the quadrupole acts focusing in one plane and defocusing in the other. In order to characterize this lensing effect spatially, we convert to trace space coordinates using a constant dominantly longitudinal velocity ($dz/dt = v_z \simeq v = \text{const}$), i.e. $\xi'' \pm k_0^2\xi = 0$. The solutions to these equations are obtained analogously to the temporal domain. For initial ray

vectors (x_0, x_0') and (y_0, y_0') we find

$$\begin{pmatrix} x \\ x' \end{pmatrix} = \begin{pmatrix} \cos k_0 z & k_0^{-1} \sin k_0 z \\ -k_0 \sin k_0 z & \cos k_0 z \end{pmatrix} \begin{pmatrix} x_0 \\ x_0' \end{pmatrix} \tag{4.13}$$

and

$$\begin{pmatrix} y \\ y' \end{pmatrix} = \begin{pmatrix} \cosh k_0 z & -k_0^{-1} \sinh k_0 z \\ k_0 \sinh k_0 z & \cosh k_0 z \end{pmatrix} \begin{pmatrix} y_0 \\ y_0' \end{pmatrix} \tag{4.14}$$

For a short propagation length l through the quadrupole ($l \ll 1/k_0$) we can reduce the transfer matrix to its first order Taylor expansion.[2] This is the thin lens approximation and by comparison with $\mathscr{M}_{\text{thin lens}}$ from the previous section we can identify the focal length

$$\frac{1}{f} = \pm k_0^2 l \tag{4.15}$$

From (4.13) and (4.14) we then find the focal length for electric and magnetic quadrupoles

$$\frac{1}{f_E} = \pm \frac{eE_0 l}{m\gamma a v^2} \qquad \text{and} \qquad \frac{1}{f_M} = \pm \frac{eB_0 l}{m\gamma a v}. \tag{4.16}$$

When we compare the focal lengths of both kind of quadrupoles we see that

$$\frac{f_M}{f_E} = \frac{E_0}{\beta c_0 B_0}. \tag{4.17}$$

As discussed, high voltage breakdown limits electric fields to $E_0 \sim 10 - 100$ MV/m, while permanent magnets can reach field strength of $B_0 \sim 1 - 2$ T, which translates into $f_M/f_E \sim (0.01 - 0.3)\beta^{-1}$. In consequence, from the mildly relativistic regime upon, magnetic quadrupole lenses provide stronger focusing. In order to achieve focusing in both transverse directions, quadrupole doublets are used. In the simplest configuration, such doublets are constructed such that the focal lengths of both lenses are $f_1 = -f_2$ and the effective focusing with a drift d between both lenses is

$$\frac{1}{f_{\text{doublet}}} = \frac{d}{|f_1 f_2|}. \tag{4.18}$$

[2] The first order expansion around $z = 0$ is $\begin{pmatrix} \cos k_0 z & k_0^{-1} \sin k_0 z \\ -k_0 \sin k_0 z & \cos k_0 z \end{pmatrix} = \begin{pmatrix} 1 & z \\ -k_0^2 z & 1 \end{pmatrix} + \mathscr{O}(z^2)$.

4.1.3 Normalized emittance and emittance growth

In our derivation of the emittance we have used Liouville's theorem to argue that the emittance ϵ is constant. This definition is no longer true for an accelerated beam. Instead, the position-momentum $x - p_x$ space has to be considered, where the phase space area remains constant during acceleration. This quantity is called the normalized emittance ϵ^n:

$$\begin{aligned}\epsilon_x^n &= \frac{1}{mc}\sqrt{\langle x^2\rangle\langle p_x^2\rangle - \langle x\, p_x\rangle^2} \\ &\simeq \frac{1}{mc}\sqrt{\langle x^2\rangle\langle \gamma^2 x'^2\rangle - \langle x\,\gamma x'\rangle^2}\end{aligned} \tag{4.19}$$

Here γ is the relativistic factor and we assume again $\beta = v/c \simeq 1$.

Being conserved during acceleration the normalized emittance is an important characteristic of an accelerator system. It is, if no degradations are present, preserved from the injection on. However, emittance can augment due to various effects [123]. For laser accelerated electron beams the beam energy spread is a principal source of emittance degradation.

As shown in [116], we can rewrite (4.19) in terms of the rms quantities (4.1)

$$\epsilon_n = \frac{\langle\gamma\rangle}{mc}\sqrt{\sigma_{\gamma,\mathrm{rel}}^2\sigma_x^2\sigma_{x'}^2 + \epsilon^2} = \frac{\langle\gamma\rangle}{mc}\sqrt{\Delta\epsilon^2 + \epsilon^2}, \tag{4.20}$$

where $\sigma_{\gamma,\mathrm{rel}} = \sigma_\gamma/\langle\gamma\rangle$ is the relative energy spread. Without acceleration the conventional transverse emittance ϵ is still considered a conserved quantity, however, the term $\Delta\epsilon^2 = \sigma_{\gamma,\mathrm{rel}}^2\sigma_x^2\sigma_{x'}^2$ is not. From the beta functions of a free drift (4.8) we find that for long propagation $\sigma_x \simeq \sigma_{x'} \times d$, so the normalized emittance growth scales as

$$\Delta\epsilon \simeq \sigma_{\gamma,\mathrm{rel}}\sigma_{x'}^2 \times d. \tag{4.21}$$

In conventional accelerators this term is usually negligible as beams have a small energy spread ($\sigma_{\gamma,\mathrm{rel}} \ll 0.01$) and divergence ($\sigma_{x'} \ll 1$ mrad). As we have seen in **Chapter 2: Injection**, the divergence and energy spread in a laser wakefield accelerator is orders of magnitude higher. So even laser-accelerated electrons have a competitive emittance at the accelerator exit due to their small source size, this advantage is lost rapidly during free propagation. It is therefore paramount to collimate electrons and reduce their divergence as quickly as possible.

4.2 Transverse laser wakefields

Though we have already discussed the three-dimensional 'bubble' structure of laser-wakefields, up to now we have restricted our discussion to the longitudinal wakefields. In this section we are going to review transverse laser-wakefields in the linear and the blow-out regime.[3]

4.2.1 Linear wakefields

We have already discussed the one-dimensional linear plasma wave equation (1.16)

$$\left(\frac{\partial^2}{\partial\zeta^2} + k_p^2\right)\Phi = k_p^2\frac{\langle a^2\rangle}{2}. \tag{4.22}$$

which can be solved using Green functions. The more-dimensional solution is very similar and usually a cylindrical symmetric coordinate system is used.In this case we also have to define a radial pulse shape, which is often assumed gaussian $h(r) = \exp[-r^2/w^2]$. It can be shown that the corresponding potential is simply the one-dimensional solution with the imprint of the laser profile in transverse direction, i.e. $\Phi(r,\xi) = \Phi(\xi)\times h^2(r)$, where $\Phi(\xi)$ is the solution given by (1.17), i.e.

$$\Phi(\xi,r) = -c_{\mathrm{env}}\frac{a_0^2}{4}\sin[k_p(\xi-\xi_l)]\exp\left(-\frac{2r^2}{w^2}\right). \tag{4.23}$$

From this we find the wakefields via $E_z = -\partial_z\Phi$ and $E_r = -\partial_r\Phi$:

$$E_z = \frac{c_{\mathrm{env}}a_0^2}{4}\frac{mc\omega_p}{e}\cos[k_p(\xi-\xi_0)]\exp\left(-\frac{2r^2}{w^2}\right) \tag{4.24}$$

$$E_r = c_{\mathrm{env}}a_0^2\frac{mc^2 r}{ew^2}\sin[k_p(\xi-\xi_l)]\exp\left(-\frac{2r^2}{w^2}\right) \tag{4.25}$$

We notice that the transverse field is phase-shifted by $\pi/2$ with respect to the longitudinal field. One consequence of this is that linear wakefield acceleration is only accelerating and focusing over a quarter-wavelength $\lambda_p/4$, cf. Fig.4.5. Also, while the longitudinal field amplitude scales explicitly on the plasma density via ω_p, the radial field amplitude contains only the coupling factor c_{env}. Instead, it contains the component $r\times\exp[-2r^2/w_0^2]$. This means that the field vanishes on axis and then acts as a linearly focusing force. Note that the force becomes non-linear for positions approaching the beam waist w due to the $\exp[-2r^2/w_0^2]$ term. Physically speaking this is a consequence of the weaker plasma perturbation at outer radii, which weakens the restoring force.

[3] Note that even if we only provide explicit solutions for laser wakefields, the transverse fields in beam wakefields are very similar, cf. [126].

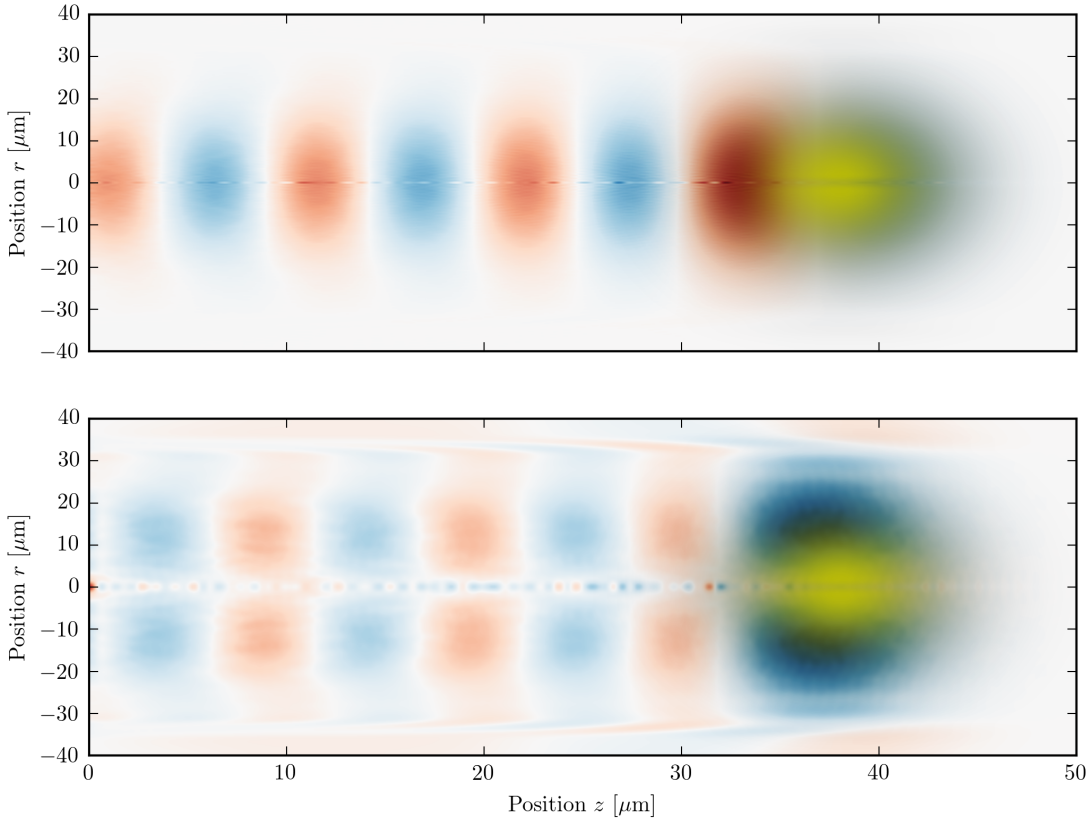

Figure 4.5 – Longitudinal (upper frame) and transverse (lower frame) electric fields in the linear wakefield regime. The laser pulse ($a_0 = 0.5$, $\tau = 30$ fs, $\sigma_r = 30\,\mu$m) is plotted in yellow, the plasma density is $n_e = 5 \times 10^{18}$ cm^{-3}. The colorscale is different for both cases, normalized to the maximal field of each. Note that these fields are the result of Particle-In-Cell simulations.

4.2.2 Blowout regime

On the contrary, the blowout is distinguished by the complete ion cavitation that is formed behind the laser. From Poisson's equation in cylindrical coordinates

$$\Delta\Phi = \frac{1}{r}\frac{\partial}{\partial r}\left(r\frac{\partial}{\partial r}\phi\right) = -k_p^2\frac{\delta n}{n_0} \tag{4.26}$$

we find that a constant charge density creates a parabolical transverse potential

$$\Phi(r) = \Phi_0\left(1 - \frac{r^2}{r_B^2}\right). \tag{4.27}$$

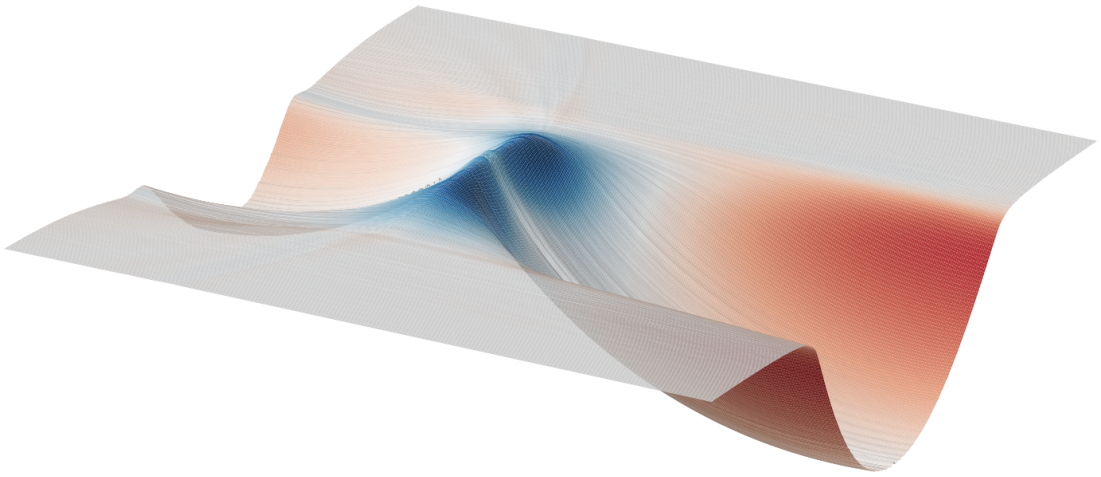

Figure 4.6 – Visualization of part of the wake potential Φ and transverse electric fields E_r in the bubble regime as simulated with CALDER-CIRC. Electrons in the focusing, parabolic potential (red) will perform harmonic betatron oscillations, while the repulsing area in the back (blue) leads to strong defocusing of the beam.

The case of complete electron blow-out ($\delta = -n_0$) leads to the strongest potential $\Phi_0 = k_p^2 r_B^2/4$. From this we compute the field again via $E_r = -\partial_r \Phi$, which yields to

$$E_r = \frac{m\omega_p^2 r}{2e}. \tag{4.28}$$

So the transverse fields in the bubble are purely linearly focusing. There are also very strong non-linear defocusing fields where electron trajectories cross. Though no analytical model has been proposed for these fields, they are however well resolved in particle-in-cell simulations cf. Fig.4.6.

4.2.3 Betatron motion in transverse wakefields

In the previous section we have seen that the 3D non-linear wakefield potential $\Phi \propto [1 - r^2/r_0^2]$ is parabolic and the 3D linear potential $\Phi \propto \exp[-2r^2/w_0^2]$ is quasi-parabolic[4] along the radius. The existence of such parabolic potentials suggests that particles in transverse wakefields perform harmonic betatron oscillations.

Indeed, when solving Lorentz equation ($m\gamma\ddot{r} = eE_r$) for the transverse blowout (4.28) we find the equation of an harmonic oscillator

$$\frac{d^2 r}{dt^2} = -\frac{\omega_p^2}{2\gamma} r \tag{4.29}$$

[4] Its Taylor expansion at $r = 0$ is $\exp[-2r^2/w_0^2] = 1 - 2r^2/w_0^2 + \mathcal{O}(r^3)$.

Its eigenfrequency

$$\omega_\beta = \frac{\omega_p}{\sqrt{2\gamma}}. \tag{4.30}$$

is called the **betatron frequency** of the eponymous oscillations. It is now clear that there is a strong analogy between the betatron oscillations in wakefields and in conventional focusing optics. However, there are two important differences. The first is that betatron fields act isotropically focusing in the transverse plane. And second, the electrons will always simultaneously experience the longitudinal wakefields (except at dephasing) and hence their energy is not constant $\gamma = \gamma(t)$. This basically means that the relativistic increase of particle inertia will damp the oscillations.

In case of adiabatic acceleration ($d_t\omega_\beta/\omega_\beta^2 \ll 1$) the WKB approximation can be used to solve (4.29), yielding [35]

$$r = r_0\left(\frac{\gamma_0}{\gamma(t)}\right)^{1/4}\cos\left(\int_{t_0}^{t}\omega_\beta(t')dt' + \phi_r\right). \tag{4.31}$$

From this equation we deduce that the initial betatron oscillation amplitude is damped during acceleration by $\gamma^{-1/4}$. Accordingly the transverse size of an electrons bunch decreases already due to mere acceleration. We can also estimate the corresponding electron divergence with $\theta \approx \dot{r}/c_0$,

$$\theta = -\frac{k_p r_0}{\sqrt{2\gamma_0}}\left(\frac{\gamma_0}{\gamma(t)}\right)^{3/4}\sin\left(\int_{t_0}^{t}\omega_\beta(t')dt' + \phi_r\right) \tag{4.32}$$

which in turn implies that the divergence scales with $\gamma^{-3/4}$.

4.3 Plasma wakefield lenses

In the preceding section we have seen that transverse wakefields are similar to quadrupole fields used in conventional beam optics. Using them for beam transport in form of a plasma lens is therefore a straightforward idea and was proposed early in the theoretical development of plasma wakefield acceleration back in the 1980s [127, 117, 118]. As in the previous **Chapter 3: Acceleration** we will start with a general discussion of plasma lenses, then move on to plasma lenses based on beam-driven wakefields, before finalizing the discussion with theoretical and experimental results on laser-driven plasma lenses.

Conventional versus plasma wakefield lenses

As for plasma wakefield acceleration, the main advantage of plasma wakefield lensing is that the fields exceed by far those achievable in conventional devices. From the introduction we know that electrostatic quadrupoles can provide up to $E_0 \sim 10-100$ MV/m, while magnetic

quadrupoles usually operate at $B_0 \sim 1-2$ T. For ultra-relativistic beams the latter translate into an equivalent of $cB_0 \sim 500$ MV/m. This value might be increased by a factor $2-3$ in superconducting [128] or pulsed [129] systems.

Yet the field strength is not only defined by the peak field, but also the aperture, cf.(4.9) and (4.10). This is why focusing optics are usually characterized in form of field gradients E_0/a and B_0/a, where a is the semi-aperture. The aperture is normally of the order of centimeters and typical field gradients are $B_0/a \sim 50$ T/m ($cB_0/a \sim 1.5$ GV/m^2). Higher fields gradients of $B_0/a \sim 500$ T/m have been reported for permanent magnets with millimeter-size aperture, but further amelioration is difficult to reach due to manufacturing issues, demagnetization effects and so forth.

Alternatively, strong focusing forces can be achieved using the magnetic fields in plasma discharges, see for example [130]. The magnetic gradient field in such a configuration is approximately given by the solution of a concentric current-carrying cylinder of radius r_0 [131], which reads $B' = (\mu_0 I)/(2\pi r_0^2)$. In laser-plasma accelerators discharges are often used as waveguides, so it is convenient to use such devices for focusing as well. Typical radii and currents, as for instance used in [132], are $r_0 \sim 200\,\mu$m and $I \sim 200$ A, which corresponds to field gradients of the order of $\sim$ kT/m.

Let us now compare these values to the transverse field gradients in linear (4.25) and non-linear (4.28) wakefields. To find the radial fields in the beam-driven regime, we can replace the ponderomotive driver ($a^2/4$) by the space-charge excitation (n_b/n_0). Recall that n_0 is the plasma density and $n_b = N_b/(2\pi)^{3/2}\sigma_z\sigma_r^2$ is the bunch density. Again, we get the potential by multiplying the one-dimensional potential with the beam envelope and from this we get the fields. The transverse field gradient in a linear beam-driven wakefield (also called overdense plasma lens as $n_b > n_e$) is then of the order of

$$\frac{dE_r}{dr} \sim \frac{4mc^2}{e}\frac{1}{\sigma_r^2}\frac{n_b}{n_0}, \tag{4.33}$$

where we assume $c_{\rm env}\sin\phi\exp[-(2r^2)/(\sigma_r^2)] \sim 1$, and scales with $E_r' \propto N_b/(n_0\sigma_z\sigma_r^4)$. In linear laser wakefields

$$\frac{dE_r}{dr} \sim \frac{mc^2}{e}\frac{a_0^2}{w^2} \sim 511\frac{a_0^2}{w^2\,[\mu\text{m}^2]}\ \text{PV/m}^2 \mathrel{\widehat{=}} 1.7\frac{a_0^2}{w^2\,[\mu\text{m}^2]}\ \text{MT/m} \tag{4.34}$$

e.g. for $a_0 = 0.1$ and $w = 30\,\mu$m we find $E_r' \sim 5$ TV/m^2, which is equivalent to ~ 20 kT/m. Since the intensity depends on the beam diameter and the power, we find an equivalent scaling as for beam beam-driven lenses and can rewrite the equation in terms of laser power, i.e. $E_r'/c \sim 124 \times \text{P [GW]}/w[\mu\text{m}]^4$ kT/m. So the gradient rapidly reduces when we increase the size of the lens, which corresponds to the aperture. From this scaling we see that it only makes sense to use plasma lenses for beams with micrometer-size diameter. Yet if one respects this condition, the plasma-lens provides field gradients many orders higher than in conventional lenses. An advantage of the linear regime is that depending on the phase $\sin\phi$, the lens can

work either radially focusing or defocusing. This also means, that the lens can be used to focus proton and positron beams.

For strong drivers we enter the blowout regime (also called underdense plasma lensing for in the beam-driven case), where the transverse field gradients are independent of the driver

$$\frac{dE_r}{dr} = \frac{m\omega_p^2}{2e} \sim 9 n_e[10^{18}\mathrm{cm}^{-3}]\ \mathrm{PV/m}^2 \mathrel{\widehat{=}} 30 n_e[10^{18}\mathrm{cm}^{-3}]\ \mathrm{MT/m} \tag{4.35}$$

In contrast the aperture is different for laser and beam-drivers, but still of the order of some microns. From the derivation of betatron motion in the previous subsection, we can also estimate the focal length of the plasma lens. As the equations of motion are very similar to those in a quadrupole, we can identify $k_0 = \omega_\beta / c$ and from (4.15) we immediately find the focal length of a short blowout/underdense plasma lens [126]

$$\frac{1}{f_P} = \frac{\omega_\beta^2}{c_0^2} l = (2\pi)^2 \frac{l}{\lambda_\beta^2} \tag{4.36}$$

where l is again the interaction length. It is important for plasma lenses to maintain l below $\lambda_\beta/4$ in order to avoid that the beam starts to oscillate.

Collimating laser-accelerated electron beams using plasma lenses

As discussed before, the expectations on a focusing system for laser-accelerated electron beams are rather conservative: To avoid beam emittance growth. However, this conservative goal requires quite unconventional solutions. As we will discuss later, to collimate a beam after one millimeter of free propagation requires that the focal length is of the order of a millimeter, too. Yet from (4.16) we can estimate the focal length of a 500 T/m quadrupole for a 200 MeV electron beam to

$$f_M(500\ \mathrm{T/m}, 200\ \mathrm{MeV}) \sim \frac{1.4\ \mathrm{m}}{l[\mathrm{mm}]}. \tag{4.37}$$

In contrast the betatron wavelength of a 200 MeV beam in an ion channel of $n_0 = 1 \times 10^{18}$ cm^{-3} is $\lambda_\beta \sim 0.9$ mm, so from (4.36) we find

$$f_P(10^{18}\ \mathrm{cm}^{-3}, 200\ \mathrm{MeV}) \sim \frac{20\ \mathrm{mm}}{l[\mu\mathrm{m}]}, \tag{4.38}$$

which means that employing a plasma lens could resolve the problem of emittance growth in laser-plasma accelerators. Yet the question remains whether such a plasma lens should be beam-driven or laser-driven.

For a beam-driven lens basically the same criteria apply as for beam-driven acceleration, meaning that the drive-beam should have a high charge density and be rather long. Again, of the injection schemes we discussed in **Chapter 2: Injection**, electron injection in high-Z gases

is the most appropriate candidate to meet these requirements. However, PIC simulations with CALDER-CIRC show that due to their large divergence, these beams suffer from the rapid reduction of n_b in free drift and it is therefore difficult to self-collimate them. Short, high quality beam as from shock or optical injection are, also in this beam-driven scheme, unsuitable. As for acceleration, this kind of beams requires a separate driver for the wakefield.

4.4 Laser-plasma lens

We have seen in the preceding section that beam-driven plasma focusing is - as well as beam-driven acceleration - limited to long electron bunches or bunch trains. In order to focus ultrashort electron beams as produced in laser wakefield accelerators, a separate driver for the focusing is needed. In order to avoid the synchronization and alignment problems a second laser pulse would impose, we opt for the simpler scheme of using the same driver as for acceleration.

4.4.1 Concept of the single pulse laser-plasma accelerator and lens

The basic scheme of the single pulse laser-plasma accelerator (LPA) and lens (LPL) is depicted in Fig. 4.7. During the first phase electrons are injected and accelerated via laser wakefield acceleration. The area the bunch occupies in phase space at this point is determined by the injection mechanism and the betatron phase mixing. As electrons and laser pulse exit the accelerator, both start to defract. As discussed, the drift acts as tilt towards the $x-$axis in phase space. But meanwhile both area ϵ and divergence γ are conserved, so the ellipse squeezes to compensate. So the longer the drift, the better electrons can be collimated. For LPA parameters, this free propagation length is typically millimeter scale. At the exit of the accelerator the laser pulse has already transfered significant energy to the plasma and such an additional unguided propagation will usually push the field strength below $a_0 < 1$. Once the laser reaches the second plasma region, it will excite a linear wakefield. The longitudinal field is usually too weak to significantly affect a highly relativistic electron beam. Yet the transverse fields suffice to bend and collimate the electron trajectories. As discussed before the jet has to be shorter than $l < \lambda_\beta/4$ to avoid oscillations. As the distance between laser and electron beam is determined during the acceleration, the phase $\phi = k_p(\xi - \xi_l)$ has to be adjusted by changing the density of the lens.

4.4.2 Theoretical background of the linear laser-plasma lens

As in Sec.4.2.3 we are now deriving the equations of motions in the transverse wakefield, this time for the linear regime given by (4.25):

$$\frac{d^2 r}{dt^2} = \frac{c_{\text{env}} c^2 \sin\phi}{\gamma} \times \frac{a_0^2}{w^2} \times r e^{-\frac{2r^2}{w^2}}. \tag{4.39}$$

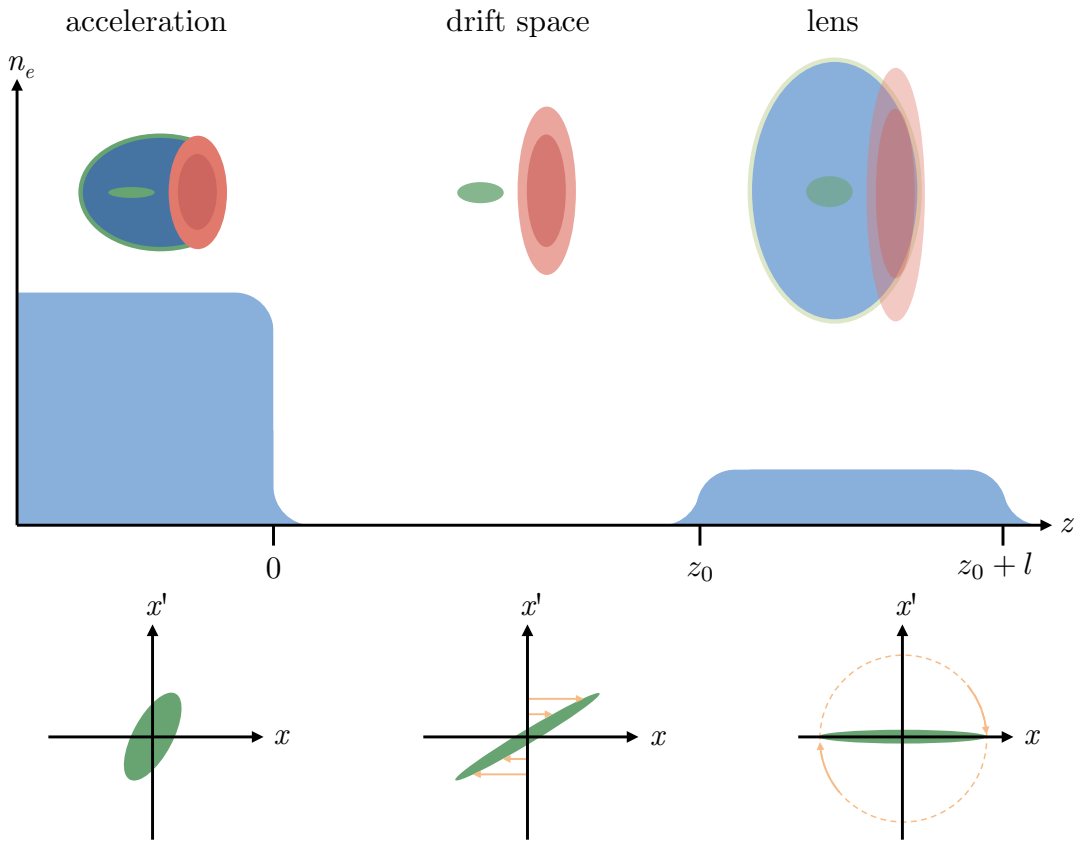

Figure 4.7 – Cartoon of the principle of the laser-plasma lens and corresponding evolution of the phase-space.

The equation is more complicated than a harmonic oscillator, but we can simplify it with a few approximations. As such we assume again that the electrons travel close to speed of light in z direction $z \sim ct$, the energy does not change significantly $\gamma = \text{const.}$ and dephasing can be ignored $\phi = \text{const.}$ The latter assumptions are valid for low density plasmas and weak longitudinal fields. Furthermore the electrons shall remain close to the axis, i.e. $\exp[-(2r^2)/(w^2)] \simeq 1$. With this we obtain

$$\frac{d^2 r}{dz^2} = \underbrace{\frac{c_{\text{env}} \sin\phi}{\gamma} \frac{a_0^2}{w^2}}_{=k_{\beta,\text{lin}}^2} r. \tag{4.40}$$

Now the equations of motion have the same form as for the blowout regime and quadrupoles. However, the excitation amplitude depends on the laser intensity a_0 and spot size w which evolve during propagation. Far from focus these change approximately as $a_0(z) \simeq a_0 \times z_R/z$ and $w(z) \simeq w_0 \times z/z_R$, where z_R is the Rayleigh length. The focal lens of a thin linear laser-plasma

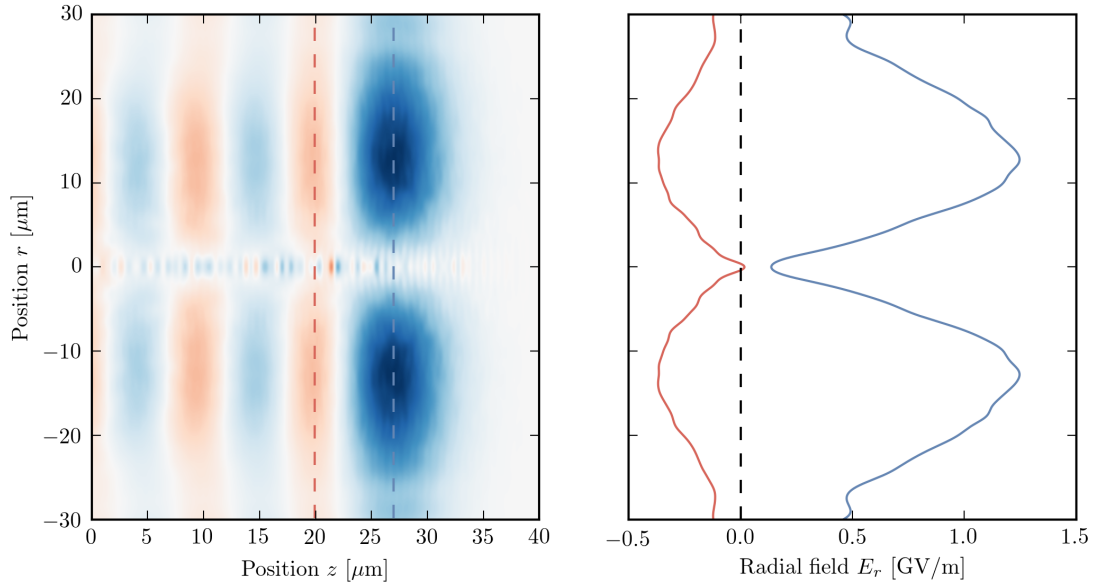

Figure 4.8 – Line-outs of the linear radial wakefields from the same simulation as Fig.4.5.

lens at position $z_0 \gg z_R$ is therefore

$$\frac{1}{f_{LP}} \simeq k_{\beta,\mathrm{lin}}^2 l \simeq \frac{c_{\mathrm{env}} \sin\phi}{\gamma} \frac{a_0^2}{w_0^2} \frac{z_R^4}{z_0^4} l. \tag{4.41}$$

The thin lens conditions in this case is $l \ll \lambda_\beta$ and we can assume a constant intensity and spot size if $l/z_R \ll z_0/z_R$. A curiosity of the linear regime, which we mentioned parenthetically in Sec.4.2.1, is that the radial fields are only weakly dependent on the plasma density via c_{env}. This property is inherited by the betatron period and the focal length. The dominant density dependence comes from the phase factor $\sin\phi$ between the electron bunch and the driver. For a given distance between electrons and laser (determined by the acceleration section), a density scan of the lens should therefore show oscillations between focusing and defocusing.

From the thin lens transfer matrix $\mathcal{M}_{\mathrm{thin\ lens}}$ (4.7) we can derive that the divergence reaches zero $x' = 0$ for

$$\frac{1}{f} = \frac{\sigma_{x_0'}}{\sigma_{x_0}} \sim \frac{1}{z_0}, \tag{4.42}$$

which is a relation well known from light optics. So we see that it becomes easier to focus beams the more they propagate. Using this we can estimate what focal strength is needed to collimate our beam. For example, let us consider a laser with a spot size of $w(0) = 6\mu$m and $a_0(0) = 5.0$ at the exit of the LPA. For a laser-plasma lens placed at $z_0 = 5z_R \simeq 750\mu$m behind and a matched electron beam ($c_{\mathrm{env}} \sin\phi = 1$) we estimate that $f \overset{!}{\sim} 750\mu$m. To reach this the lens would need a width $l \sim 500\mu$m. This result is of the same order as estimations from a

more rigorous model [133], differs however as $l \sim 2z_R$ which violates the model conditions that a_0/w remains about constant.

We can extend (4.41) to longer interaction length by calculating the average interaction length l'. This method is frequently used in accelerator physics to take into account fringe fields of quadrupoles [123]. In our case

$$l' = \frac{1}{k^2_{\beta,\mathrm{lin}}(z_0)} \int_{z_0}^{z_0+l} k^2_{\beta,\mathrm{lin}}(z)\,dz = \left[-\frac{z_0^4}{3z^3} \right]_{z_0}^{z_0+l} \tag{4.43}$$

As we still want to avoid the regime of betatron oscillations it is fair to assume that $z_0 > l$ and we carry on just terms of first order in l. The focal length then changes to

$$\frac{1}{f_{LP}} \simeq \frac{c_{\mathrm{env}} \sin\phi}{\gamma} \frac{a_0^2}{w_0^2} \frac{z_R^4}{z_0(z_0+l)^3} l \tag{4.44}$$

From this we see clearly that the focusing effect is reduced for thicker lenses. Physically this is an obvious consequence of the laser diffraction, which then diminishes the wakefield amplitude.

Alternatively there is also an analytical solution for differential equations of the above type $\frac{d^2x}{dz^2} = \frac{k_0^2}{z^4}x$, which is discussed in [133]. This solution is however more complex and therefore cumbersome to translate into a matrix formalism.

From (4.41) we also see that $f_{LP} \propto \gamma$, i.e. the laser-plasma lens is sensible to chromatic aberrations. This effect is shown in Fig.4.9. Also, at high charge densities we simultaneously drive a laser wake and a beam wake. As discussed before, this additional effect especially affects the tail of the electron bunch.[134]

4.4.3 Experimental demonstration of electron beam focusing using a laser-plasma lens

The theoretical framework established in the last sections helps us to understand how to design a working setup for a experimental demonstration of the laser-plasma lens. This is followed by the presentation of experimental results on electron beam focusing.

Considerations for choosing LPA parameters

The single-pulse laser pulse lens means to use the same laser pulse not only for acceleration, but also for focusing. It is therefore imperative to operate the accelerator below the depletion length. We also have to chose carefully the amount of dephasing we tolerate, as the $\sin\phi$ term will determine whether the lens is focusing or defocusing.

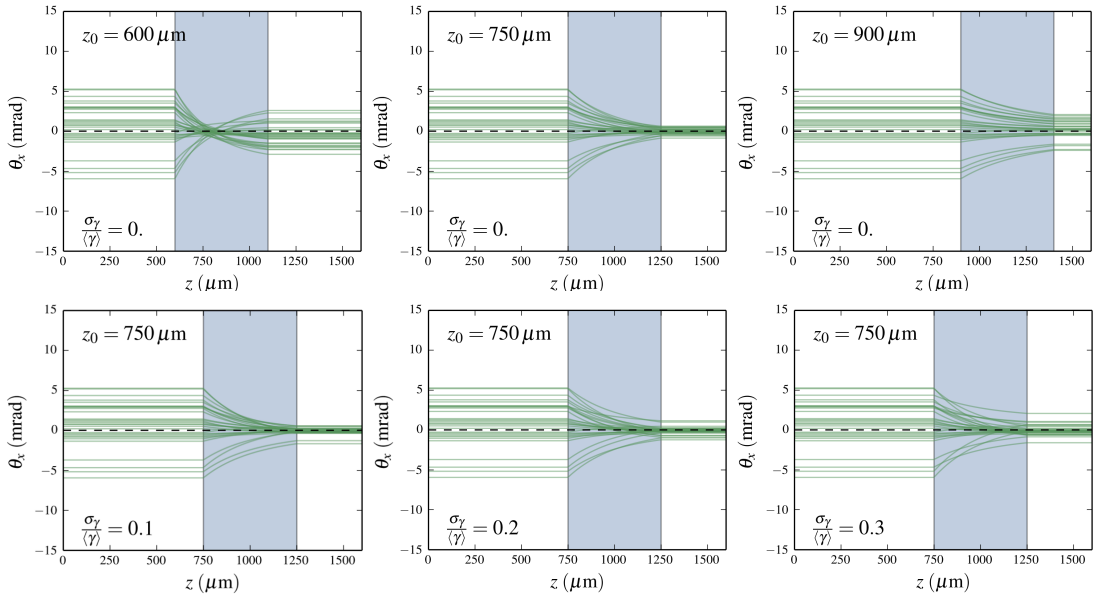

Figure 4.9 – Electron collimation using the model from [133]. Beam rms parameters are σ_θ = 3mrad, electron energy 300 MeV. The 1J, 30 fs, 800nm laser is focussed by an f/10 lens. The lens has a length of 500 microns at 1.0×10^{18} cm^{-3} and electrons are located at 15 microns laser pulse centre. Bottom row shows the effect of chromatic aberrations.

Another condition to maintain the laser-driver is that the Rayleigh length at the exit of the accelerator should be long, in order to reduce the intensity losses during the free propagation. Yet even we can increase the Rayleigh range by adequate choice of focusing optics, the curvature at the accelerator exit is likely to be higher as the laser undergoes self-focusing (cf. Sec.1.3.4). This is difficult to control, but as the relativistic self-focusing angle is proportional to the plasma density it might be favorable to operate at lower plasma densities.

Furthermore we require electron beams with an initial divergence in the range of some milliradiants. On one hand beam focusing will be easier to measure for beams with larger divergence. But on the other hand their divergence should be considerable lower than te laser beam divergence in order to avoid aberrations from the pulse shape term $\exp[-(2r^2)/(\sigma_r^2)]$.

In conclusion, we aim for electron beams of moderate energies and divergence. Also, if we want to characterize the chromaticity of the lens it is better to start of with a broad electron spectrum instead of monochromatic beams (no optical or shock injection). Furthermore we have mentioned that beam-loading can counteract the lensing effect, so the charge density must not be too high (no ionization injection, also unfavorable for transverse self-injection). And lastly, the electron source should be stable enough to be able to compare between shots with and without the lens with reasonable statistics. Taken all these criteria together we find that longitudinal self-injection is the best suited regime of operation.

Experimental setup

The experiment was conducted with the Salle Jaune Laser, which delivered on average ~ 1.7 Joule on target at 28 femtosecond duration during the experimental campaign. The laser was focused with an $f/10$ of axis parabola to a spot size of 12μm (FWHM), with $50-55\%$ of the energy in the central peak. From this we estimate a peak intensity of 1.0×10^{19} W/cm^2, equivalent to $a_0 \sim 2.2$. The Rayleigh length in vacuum is ~ 400 μm.

For acceleration the laser is focused 1.6 mm above at the entrance of a ^{2}He supersonic gas jet of 3 mm diameter and Mach number 3. At this height the gas forms a central pleateau region of 2.4 ± 0.1 mm, with gradients of 0.6 ± 0.1 mm around. The plasma density of $n_e = 9.2\pm0.5\times10^{18}$ cm^{-3} is caculated using Abel inversion of the phase shift measured with a Normanski interferometer.

The plasma for the lens is also created via ionization in a ^{2}He gas jet. This jet is shorter, with a diameter of 0.8 mm and an estimated Mach number of 1.6, which leads to a triangular density profile with gradients of 1.0 ± 0.1 mm, cf. Fig.4.10.[5]

A dipole magnet (1.1 T over 10 cm) is placed behind the lens, deflecting electrons depending on their energy. A Lanex phosphor screen is placed behind the magnet, covering energies from 110 MeV upon, and the scintillation light is imaged onto a 16-bit CCD. From this we obtain a spectrally resolved measurement of the beam divergence in vertical direction. To increase the angular resolution the screen is moved as far as possible away from the magnet (~ 50cm). The energy resolution of the diagnostic is affected by the horizontal divergence and lies between ~ 1% for 140 MeV electron with 1.5 mrad divergence and ~ 10% for 300 MeV at 4 mrad. The vertical angular resolution is 0.3 mrad.

Electron accelerator performance

The laser plasma accelerator was operated in the regime of longitudinal self-injection, producing electron beams of a few pC charge at a mean energy 241 ± 12 MeV and 4.1 ± 0.6 mrad divergence. Direct imaging of the undeflected electron beam showed that the divergence is very similar in the horizontal and vertical directions, which justifies to quantify divergence reduction with the spectrometer in place. The stability of the accelerator is shown in Fig.4.11.

[5] The reader might wonder about this choice of parameters for the second jet instead of shooting close to the exit of a small diameter supersonic nozzle. The reason for this is purely practical and the result of many iterations of the setup. The valves used in acceleration experiments have a diameter of 17 mm and therefore it is not possible to closely approach two parallel valves with the jet in their center. Neither can the nozzles be placed at 180 degrees, because in this case the gas flow is highly perturbed by the opposing jet. Tilting the nozzles is a compromise, but this usually disturbed the probe beam. We therefore started to investigate unconventional nozzles designs, where the jet nozzle is placed shifted with respect to the valve's exit. Yet such nozzles are more difficult to produce with conventional milling techniques, which is why we employed additive manufacturing instead. As described in the appendix we are limited to hole diameters in the order of ~ 1 mm and therefore no high Mach numbers can be reached.

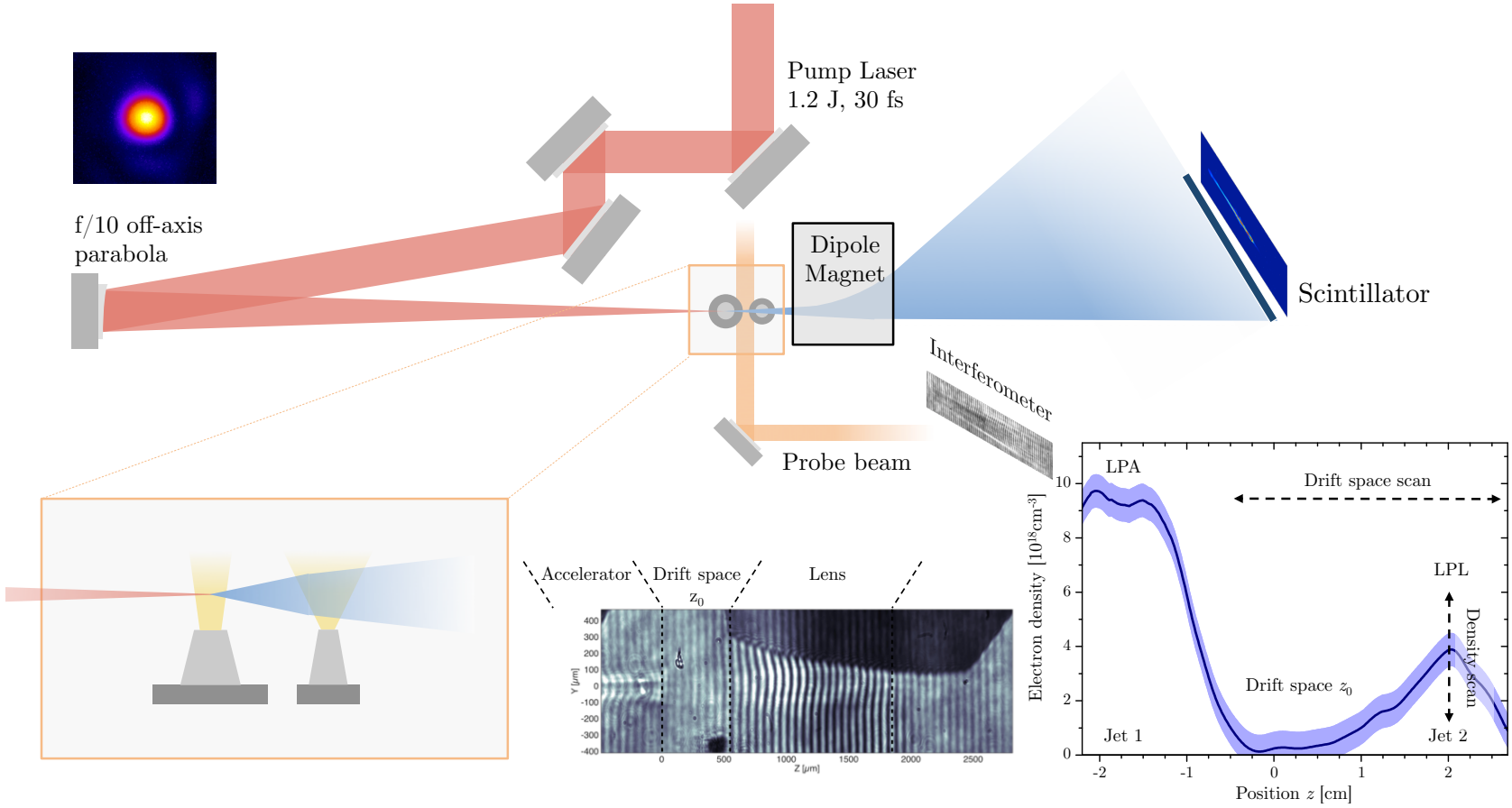

Figure 4.10 – Setup of the experiment for the laser-plasma lens. As shown in the cartoon on the lower left, we use one gas jet for acceleration and a second smaller jet for focusing. The lanex screen is placed as far as possible from the source in order to increase the angular resolution. The measured density profile is shown on the lower right for a drift space between the two gas jets of $z_0 \simeq 2.3$ mm (at half maximum). The density of the acceleration section is kept constant during the experiment, while the second jet can be tuned from 0 up to $\sim 6 \times 10^{18}$ cm^{-3}.

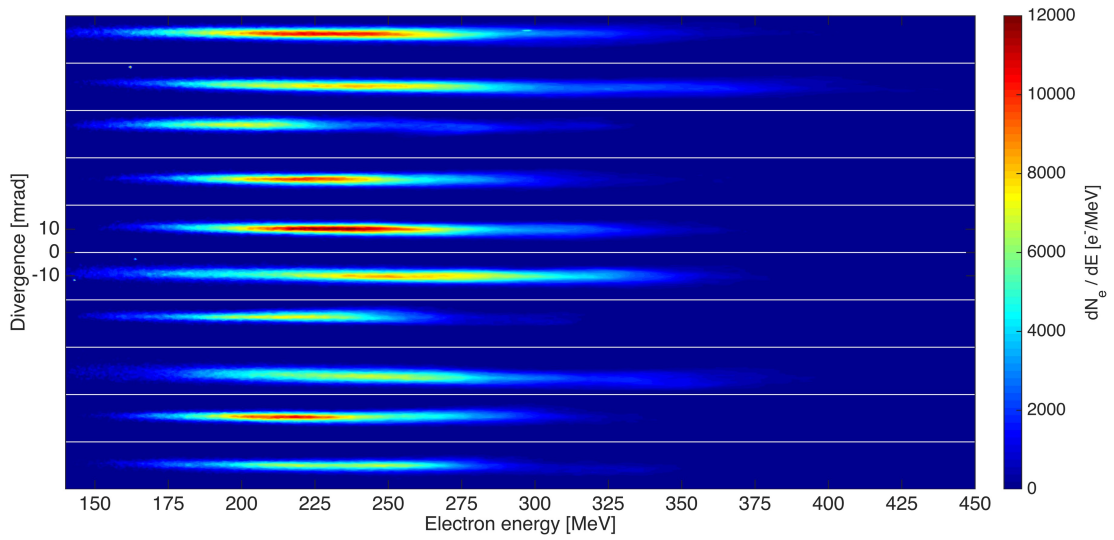

Figure 4.11 – Stability of the electron acceleration in longitudinal self-injection regime.

Focusing and influence of the drift length

Turning on the focusing jet significantly changed the electron beam divergence, while the spectral distribution remained essentially the same, cf. Fig.4.12. For a distance scan with $n_{LPL} \simeq 3.9 \times 10^{18}$ cm^{-3} we find that the divergence reaches a minimum at $z_0 \sim 1.8$ mm and then increases back up to the initial value, cf. Fig.4.13. At the best conditions, the divergence at 270 MeV reduced from initially 4.2 mrad to 1.6 mrad, corresponding to a reduction of 2.6 times.

To interpret these results let us first verify that we are indeed operating in the linear wakefield regime. As stated in the previous section, the Rayleigh length of the parabolic mirror is $z_R \sim 400\mu$m and we estimate a peak intensity at focus of $a_0 \sim 2.2$. As the laser self-focuses in the first jet we expect the Rayleigh length to reduce, while the vector potential increases. However, as both values are coupled and the laser overall looses energy to the wake, we can estimate $a_0(z_0 = 1.8\text{ mm}) \sim a_0(0)/(z_0/z_R) \lesssim 0.5$, which lies within the linear wakefield regime.

In this regime a scan of the drift distance primarily varies the focal length of the plasma lens. In this case the higher divergence at short drift lengths z_0 can be interpreted as overfocusing of the beam, which then reaches an optimum and re-augments afterwards as the focal length increases further. This interpretation is supported by trajectory estimations from Lehe's model, cf. Fig.4.13. These calculations are performed for a 270 MeV, 4.2 mrad electron beam, focused by a laser pulse of initially 1 J and 400µm Rayleigh length, within a 1 mm lens of constant density. Please note that the calculations only support our interpretation, but are not to be interpreted quantitatively as we are missing important information about the electron phase with respect to the laser. In this case we have chosen an average plasma density $n_{LPL} = 2 \times 10^{18}$ cm^{-3} and distance $d = 8$ microns, i.e. $\phi \sim \pi/2$.

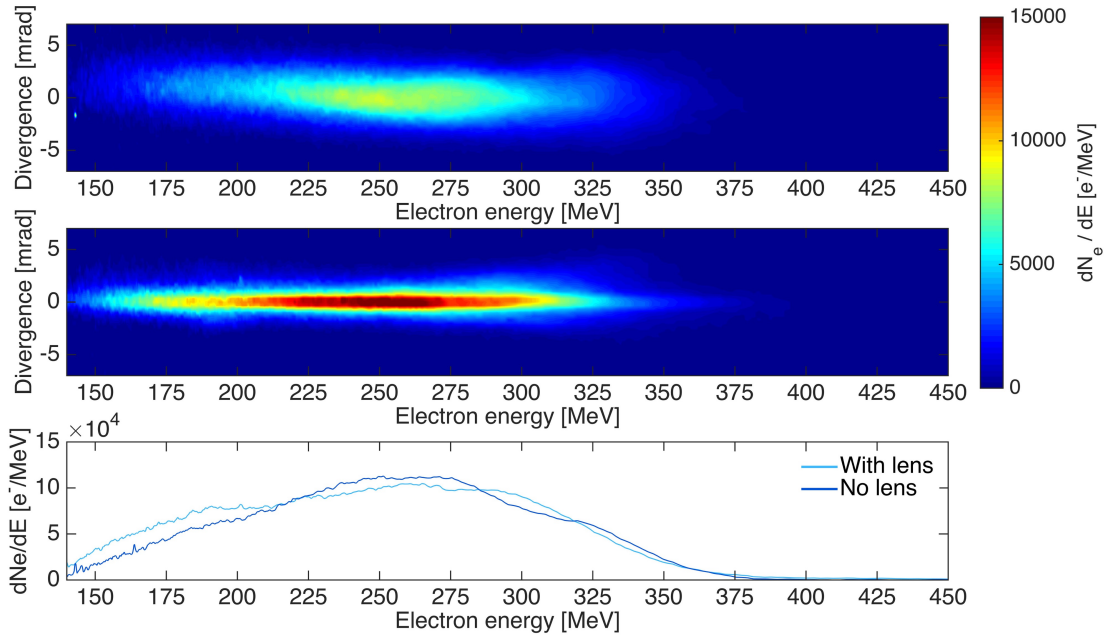

Figure 4.12 – Electron spectrum and divergence with and without the lens.

Electron phase and influence of the plasma density

In the single pulse scheme the distance d between the electron bunch and the laser is fixed behind the accelerator.[6] But we can vary the phase by changing the plasma density. Results on such density scan are shown in Fig.4.14. While the beam divergence is almost unaffected for peak densities below $n_{LPL} < 1.0 \times 10^{18}$ cm^{-3}, for higher densities the divergence changes only weakly, with a minimal divergence at $n_{LPL} \sim 4.3 \times 10^{18}$ cm^{-3}. Unfortunately the density in the second jet could not be increased beyond $n_{LPL} > 6 \times 10^{18}$ cm^{-3} and therefore we could not observe focus/defocus oscillations.

This effect is reproduced in theory, where calculations show that minimal divergence is reached at $n_{LPL} \sim 2.5 \times 10^{18}$ cm^{-3} and the density dependence is only weak in vicinity of this value. Note that the theoretical model assumes a constant density profile, while the experimental values are given in terms of the peak density.

[6] Actually the phase still changes due to dephasing, which is why it is important to operate the lens at low densities. For density of $n_{LPL} = 5 \times 10^{18}$ cm^{-3} the dephasing after 1 mm is almost $\Delta\phi \sim 1.3 \sim \pi/2$.

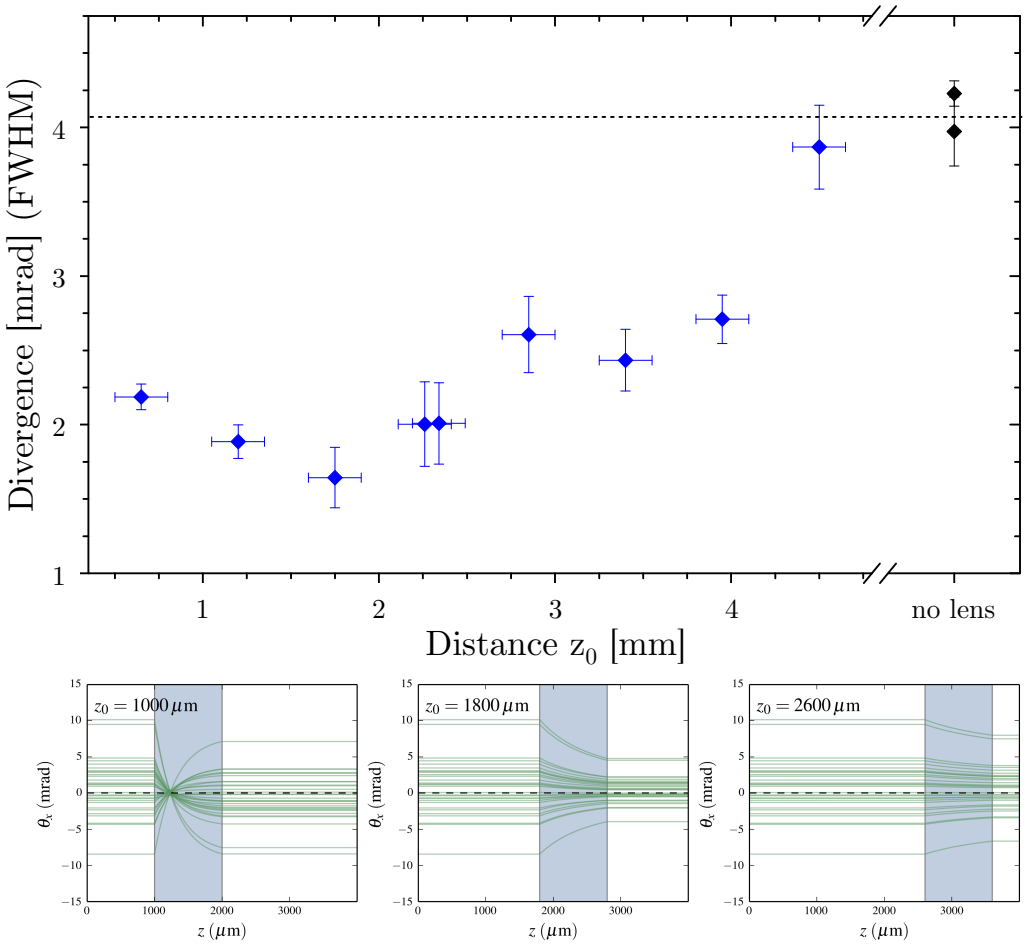

Figure 4.13 – Divergence at 270 MeV for different drift lengths z_0. Upper frame: Experimental data, showing the average over 10 shots at each position. Vertical error bars represent the standard error of the mean, while the horizontal bars correspond to the precision of the position measurement. Bottom frame: Estimations using the model from [133] for the same energy and divergence, which reproduce a similar tendency.

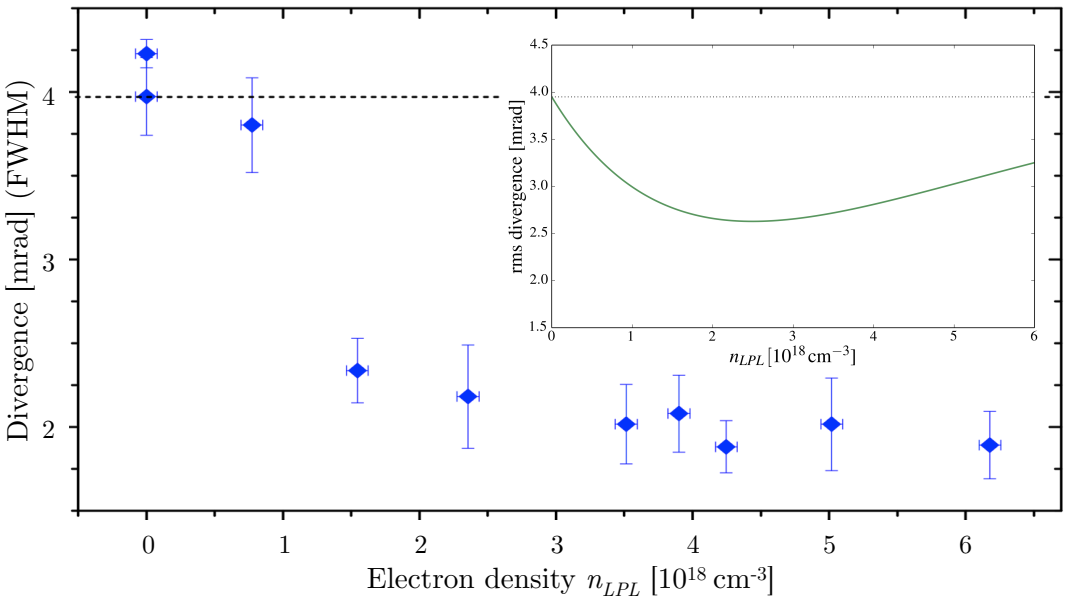

Figure 4.14 – Divergence at 270 MeV for different plasma densities n_{LPL} at z_0 = 2.3 mm drift length. Inlet: Estimations for Lehe's model [133] for the same laser, electron and lens parameters.

Chromatic effects

Up to now we have restricted our discussion to a single energy (270 MeV). But as discussed before, the focusing strength of plasma lenses depends on the beam energy γ and when looking at the whole spectrum we therefore expect an energy dependence of the focusing effect. However, as plasma lenses act radially, a single lens can be used to focus the beam, whose chromaticity is then determined by $\gamma/\sin\phi$, see (4.41). In contrast, conventional quadrupole systems need to use a doublet to achieve bi-directional focusing and the resulting focal length (4.18) has a γ^2 dependency.

Our measurements on chromatic effects are summarized in Fig.4.15, which represents a 2D map of the divergence reduction in dependence of the drift length and the electron energy. As expected the lens behaves shows a much weaker energy dependence than conventional systems as for instance shown in [135]. In fact, we find that the lens behaves almost achromatic when placed more than 2.5 mm from the accelerator. Closer to the jet we observe stronger focusing for high energy electrons, which is an unexpected tendency. It may however be caused by the phase term $\sin\phi$. To understand this better additional density scans, over a wider parameter range, are necessary.

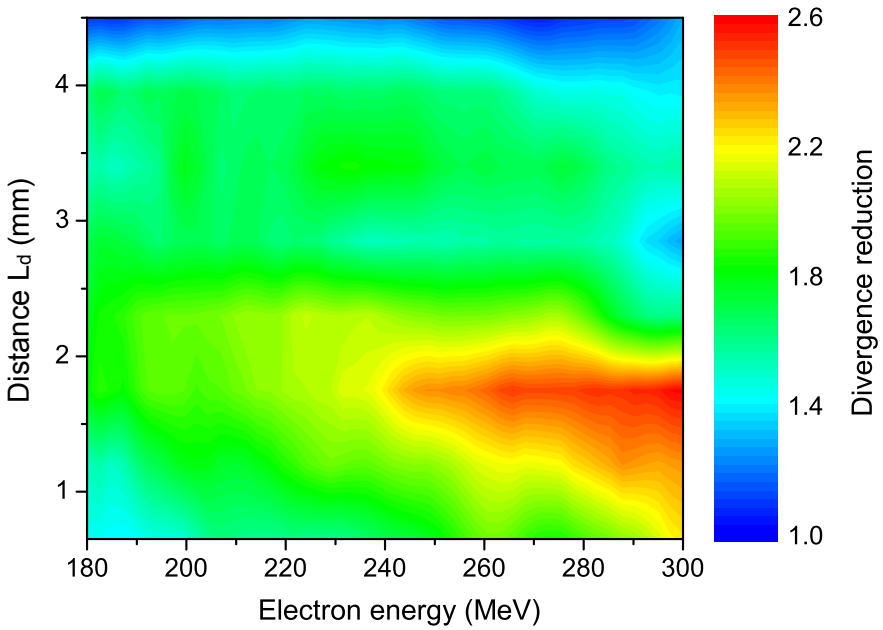

Figure 4.15 – Chromaticity of the laser-plasma lens. The plot shows the divergence reduction for different electron beam energies and drift distances. We observe that the lens is rather achromatic and the energy dependence becomes weaker the further the second jet is place away from the accelerator.

4.5 Bubble lens

In the previous section we have discussed plasma focusing in the linear wakefield regime. In this part we are going to briefly introduce a mechanism for rapid *de*focusing of an electron beam in the blowout regime.

As in the case of the linear laser-plasma lens, plasma lenses are usually operated at much lower densities and weaker fields than accelerators. One reason for this is that a lens has to fulfill the thin lens criterion $d \ll \lambda_\beta$. If not, the lens starts defocusing and eventually the beam would perform betatron oscillations. This can be avoided if the lens is short enough, but at high plasma density this would mean that the lens has to be of the order of some hundred micrometers, which is difficult to engineer. Also, operating a laser-plasma lens in the blowout regime is difficult as the aperture of the lens would be very small and therefore only very short drift space are tolerable.

As discussed in Sec.4.2, the non-linear blowout regime exhibits very strong defocusing fields at the rear of the bubble. As shown in Fig.4.16, the fields exceed the transverse strengths encountered inside the bubble by far and reach field gradients of 10^{18} V/m^2 or equivalently some GT/m. Even these fields are non-linear and will therefore not preserve the beam emittance, they may be useful for certain applications that mean to augment the transverse beam size.

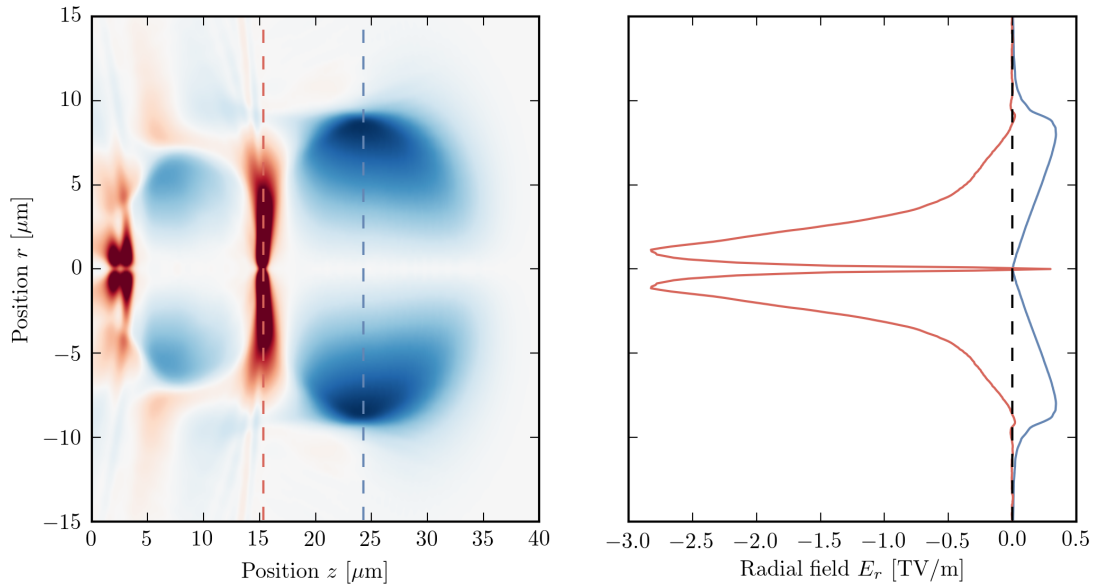

Figure 4.16 – Radial wakefields in the blowout regime. The defocusing fields at the rear part of the bubble are an order of magnitude stronger than the focusing fields inside the cavity.

One such application are plasma wigglers, which we are going to discuss in detail in the next chapter.

4.5.1 Conceptual idea and test particle simulations

Having identified the rear of the bubble as source for defocusing fields, we now need to find a way to take advantage of them. In most cases we aim for injection into the first ion cavity behind the laser, whose fields are the strongest. So electrons will only advance with respect to the rear of the bubble and thus never experience these fields. [7] In order to bring electrons into the defocusing region we need to change the cavity size. This is very similar to rephasing, except for the fact that we now want the bubble to shrink *beyond* the position of electrons in the wake. As we haven seen in **Chapter 3: Acceleration** , self-focusing eventually compensates the contraction, so ideally the electrons end up again in their original bubble.

For a computational test of the scheme we use test particle simulations. The wakefields are extracted from CALDER-CIRC and 1000 test particles are injected into the wake at 150 MeV with a normal distributed divergence of 5 mrad. The bubble is then contracted in shock-like conditions.

As shown in Fig.4.17 electrons are rapidly defocused as they pass through the back of the bubble, exceeding 100 mrad divergence. However, electrons which are too divergent cannot

[7] A difference are electrons injected into the rear wakes, however, as their transition occurs during the injection process, it is difficult for us to control.

be guided in the secondary arcs and are lost. In the plot those trajectories can be recognized by the fact that the divergence remains constant behind the density transition. Electrons with a divergence of less than ~ 70 mrad are however refocused and start betatron oscillations at increased amplitude.

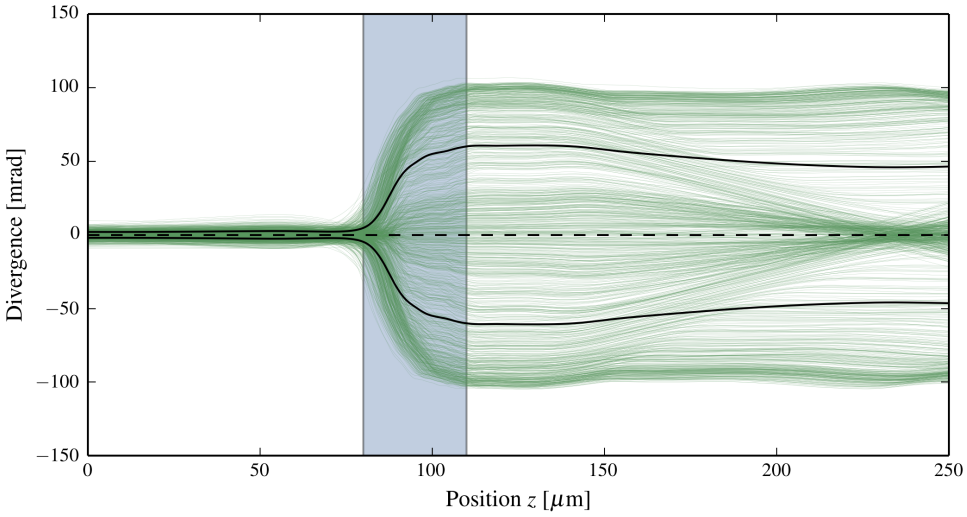

Figure 4.17 – Test particle simulation for electrons passing through a defocusing fields at the rear part of the bubble.

4.5.2 Experimental observation

In **Chapter 3: Acceleration** we have discussed that a long electron bunch going through rephasing may separate into an accelerated and a decelerated part. In fact, when we consider the angularly resolved profile of the beams, we observe that the beam is not only dephased but also defocused. The effect is for example visible in Fig.3.18a, which shows two spectra from the first rephasing experiment or in Fig.3.22 from the rephasing experiment that used shock injected beams. For the latter it is actually very clear that there is a threshold density at which the whole beam is defocused (Fig.3.22v).

We have therefore studied the defocusing effect in a separate experiment. To achieve pure defocusing we have to go beyond the ideal density of rephasing and thus need to create stronger density transitions than for rephasing. This is better to control with a second jet than with a shock, so we decided to use the needle gas jet for the experiment.

To get reliable broadband injection we used a gas mixture of 95:5 Helium/Nitrogen to facilitate injection. Without a density transition we measure a divergence of 4.6 ± 0.7 mrad and an average beam charge of 40 ± 10 pC.

With the second jet active we observe a very different behavior. Fig.4.18 shows the results for a positions scan with 10 shots at each location. As the fringes are asymmetric we cannot perform a complete Abel inversion on the image, so instead we manually compare the local fringe shift difference. For two positions (1.6 mm and 1.8 mm behind the jet entrance) we observe strong additional injection, with beam charges exceeding 100 pC for 3/10 and 5/10 shots, respectively. For the analysis we neglect these shots as they are obviously different from the general tendency, which is that the beam charge remains similar all along the jet. However, the total integrated divergence tends to increase from initially ~ 5 mrad to ~ 30 mrad at the position most inside the jet. We also observe that the average beam energy decreases from 140 ± 10 MeV to about 100 ± 10 MeV with the second jet active.

In order to assure that we are not missing charge at energies below the spectrometer cut-off (51 MeV), we imaged the electron beam directly with and without the second jet active. The electron beam profiles are mostly symmetric in horizontal and vertical direction. In this measurement the beam divergence increases by a factor of 3-4, while the charge remains similar.

A behavior similar to our observation is expected purely as a result of betatron oscillations, which according to (4.32) affect the divergence with $\theta \propto (\gamma_1/\gamma_0)^{-3/4} n_1/n_0$. Taking this into account the divergence would double in our conditions, so the observed divergence augmentation still exceeds the predictions for pure betatron oscillations. Also the fact that electron lose energy suggests that electrons enter a decelerating region, even this might also occur inside the primary bubble due to the reduced dephasing distance.

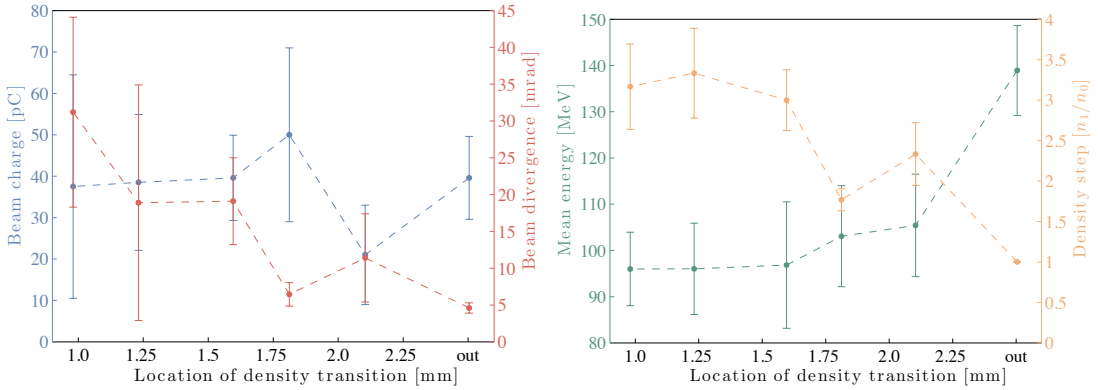

Figure 4.18 – Beam charge, energy and divergence in dependence of the position of the density transition, measured with respect to the gas jet entrance. While we observe a similar beam charge for all positions, the beam divergence increases significantly the more inwards the density transition is place. Furthermore, the average electron beam energy reduces when the second jet is active.

4.6 Conclusions

In this chapter we have discussed the physics of electron beam transport and the necessity of strong beam focusing to preserve the emittance of laser-accelerated beams. This is of great importance for the usage of the electron beam in subsequent stages, e.g. insertion devices for radiation generation. We have shown that the transverse wakefields are orders of magnitude stronger than the fields of conventional focusing devices, with the additional advantage of providing isotropic forces. It is therefore desirable to create wakefield lenses and we have derived expressions for the focal lens in the thin lens regime.

While first experimental results on beam-driven wakefield lenses were reported decades ago, such lenses are not suitable for ultrashort electron beams as encountered in laser-wakefield accelerators. We have demonstrated that such beams can be focused employing a linear laser wakefield lens instead. Here the lens uses the same laser as driver for both accelerator and lens. It is shown that the device can reduce the divergence of a femtosecond electron beam by almost three times over a distance of less than a millimeter.

The results are in accordance with theoretical predictions. However, for future use of the lens we need to establish better diagnostics of the laser beam. Furthermore, it is desirable to gain better control of the phase term $\sin\phi$, which would for example allow us to change between focusing and defocusing phase.

We have also discussed how the much stronger non-linear wakefields can be used to rapidly defocus an electron beam and present experimental evidence for this phenomenon. Such defocusing is of particular interest for radiation based on betatron oscillations, which we are going to discuss in the following **Chapter 5: Radiation** .

5 Radiation generation

In this chapter we are going to discuss different methods to create X and γ radiation from laser-accelerated electron beams. We start with a semi-conventional method, the production of γ from bremsstrahlung conversion using electrons from ionization injection. Then we are going to discuss synchrotron sources, in particular Compton backscattering using a plasma mirror and betatron radiation. For the latter we present two main results: Stable, polarized emission from ionization injected electrons and augmentation of emission in density tailored plasma channels.

Contents

5.1 Conventional X-ray sources

X-rays were first discovered by Wilhelm Conrad Röntgen in late 1895, while he was performing experiments with discharge tubes. As Röntgen did not patent the source, X-ray technology spread rapidly and first medical radiographies were performed only a few months after his discovery, in early 1896. As we have discussed in **Chapter 1: Introduction** , Röntgen's X-ray source was based on the emission of bremsstrahlung and characteristic line radiation of electrons hitting the anode.

To date, this method remains the most widely used to produce X-ray: In medical X-tubes a voltage of some tens to hundred kilovolt is applied to accelerate electrons and directly penetrate the target. Typical X-ray energies are 15-30 keV for mammography and dental radiographies, up to around 70 keV for computed tomography (CT) scanners. Some applications like mammography require narrow bandwidth radiation. Such X-ray can be produced by exciting K_α lines, e.g. $K_\alpha(_{42}\mathrm{Mo}) \sim$ 17.4 keV and $K_\alpha(_{45}\mathrm{Rh}) \sim$ 20.1 keV, and simultaneously reducing the bremsstrahlung contribution using X-ray filters. However, employing filters diminishes the photon flux significantly, while it increases the exposure time [136].

In non-distructive testing, e.g. for airport security scanners, even higher energies of up to some MeV are reached. Such devices usually operate pulsed, using small linear accelerators [137]. As K_α lines only extend to $\sim$ 100 keV, this regime purely relying on bremsstrahlung emission, cf. A.4.1. For the same reason X-ray filters are not adapted to shape the spectrum and thus the radiation is unavoidably broadband.

A major characteristic of X-ray generated when the energy of weakly relativistic electrons is converted into K_α and bremsstrahlung is that the radiation is emitted quasi isotropically. While this allows to design compact systems with a large field of view, it reduces the source's suitability for applications where only a small angular region is imaged. Examples are magnification views and phase contrast measurements. Such small aperture applications also require a reduced source size to avoid image blurring, which is usually achieved by stronger electron beam focussing. However, such micro X-ray tubes have to operate at much lower currents to avoid overheating the anode material, which reduces the available photon flux even more. Though solutions as liquid metal anodes [138, 139] have been proposed to increase the maximum power density (shown in Fig.5.1), continuously operating X-ray tubes are still limited to peak brightnesses below 10^8 photons/s/mm^2/mrad^2/0.1 % BW.

While the above-mentioned X-ray imaging techniques make use of the fact that X-rays can pass through matter, other applications take advantage of the high spatial resolution related to their (sub-)Ångstrom wavelength. Such a probe allows to study structures on the scale relevant for atomic physics and molecular chemistry, which lead to scientific breakthroughs such as the discovery of the DNA structure in 1953 [140, 141]. But while X-ray tubes have given access to spatial information about atoms and molecules, a continuous irradiation does not provide any temporal information.

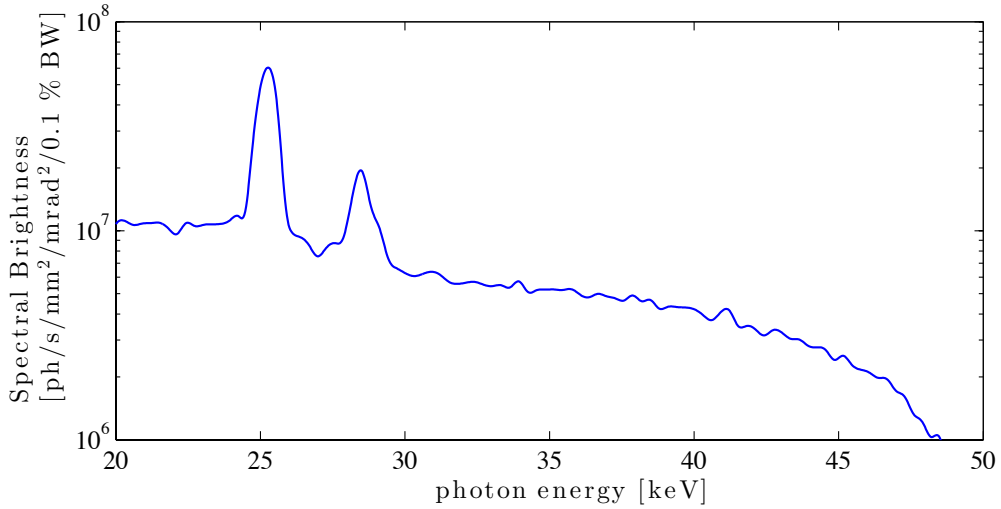

Figure 5.1 – Spectral brightness of a state-of-the-art liquid tin micro X-ray source. Highest brightness is measured around the $K_\alpha(_{50}Sn) \sim 25.3$ keV and $K_\beta(_{50}Sn) \sim 28.5$ keV lines. Data taken from [142].

5.1.1 Femtosecond laser-based X-ray tubes

In order to study processes governed by atomic motion, pulsed sources with durations of less than a picosecond are required [143]. The X-ray pulse duration is mainly dictated by the duration of the electron bunch that hits the anode. Re-calling our discussion on cathodes from Sec.2.1.1, one way to create short X-ray pulses is therefore to replace the commonly used thermionic cathode of the X-ray tube by a photocathode. Such a configuration has been demonstrated first using picosecond [144] and later with femtosecond [145] laser drivers. The latter estimates a X-ray pulse duration of below 5 ps, but reaching sub-picosecond durations is complicated by space-charge effects. A way to circumnavigate this limitation is to accelerate electrons from the anode material itself. Such an ultrashort X-ray source has been demonstrated in laser-solid interactions in the early 1990s [146, 147].

This regime is fundamentally different to laser-wakefield acceleration in underdense plasmas, as the laser pulse does no penetrate the target, but is reflected at the surface. The interaction with the pulse leads to electron heating via the $\vec{j} \times \vec{B}$ term and leads to thermal electron spectra. In this kind of experiment the drive laser is typically GW-class ($\sim$ 100 fs, $\sim$ 1 mJ), creating electrons with some tens of keV temperature. These electrons then stimulate K_α emission and bremsstrahlung, analogously to photocathodes. However, the pulse duration is sub-picosecond and strong focussing of the laser translates into a micrometer X-ray source size [148]. It has been shown that the source size is sufficiently small to be applied for propagation-based phase contrast imaging [149].

A main drawback of using solid targets is that the electrons used for radiation production originate from the surface and therefore the technique is unavoidably destroying the anode

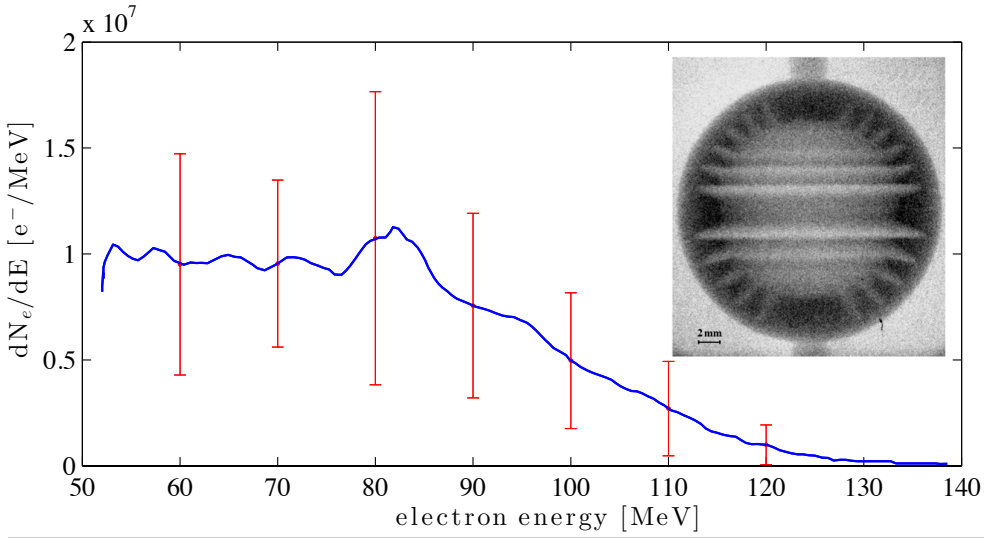

Figure 5.2 – Electron beam spectrum used for radiographies in [153]. The blue line indicates the average spectrum, while the rms error is shown in red. The instability of self-injection leads to strong fluctuations, resulting in an rms error of about 50 percent. Inlet: Radiography of a 20 mm tungsten object from the same experiment.

material. So even the sources provides a competitive brightness compared to conventional micro X-ray tubes, its usage is restricted to a research environment where ultra-short pulse durations are desired. This handicap can be overcome when the source is combined with liquid targets, for instance using a water jet [150].

Another way to provide ultrashort electrons bunches for penetration of the anode is to use a laser wakefield accelerator in place of the cathode. As discussed in the previous chapters, such beams intrinsically have a duration in the range of 1-100 fs. But they also reach much higher energies (MeV to GeV). Therefore the photon energies from this source are shifted into the MeV γ-ray regime, where the source is purely reliant on bremsstrahlung emission. The small electron source size and milliradiant beam divergence can result in a micrometer source size if the converter is placed close enough to the accelerator.

This kind of experiment was conducted for the first time in 2002 [151] and in 2005 first radiographies of complex dense objects were reported [152]. Since then several experiments have explored the setup [153, 154], yet all of them relied on self-injected electron beams and were therefore not operating very stably. In order to increase the technology readiness level of the source it is indispensable to increase the electron beam stability, which we are going to discuss in the following.

5.1.2 Stable bremsstrahlung γ-ray source using ionization injection

In order to improve the reliability of laser-driven bremsstrahlung sources we need to replace the transverse self-injection used in previous studies by a more reliable injection mechanism. Conceivable candidates are therefore (cf. **Chapter 2: Injection**) longitudinal self-injection, optical injection, shock injection, downramp injection and ionization injection.

The bremsstrahlung spectrum does not benefit significantly from a low energy spread, but in contrast the highest beam charge as possible is desired. This eliminates the first three mechanisms, which typically lead to high beam quality at the disadvantage of lower beam charge. In **Chapter 2: Injection** we found that ionization injection and acceleration in pure high Z gases leads to very stable electron acceleration, with nC-level charges per shot. The maximum beam energy is lower than for acceleration in helium, but this is in fact desirable for practical reasons: Highest energy γ-ray ($\gtrsim$ 100 MeV) do not contribute significantly to absorption contrast, yet will require additional radioprotection measures, cf. A.4.1. Unlike typical single-shot LPA experiments [152, 153], this experiment was limited by the laser repetition rate and radioprotection regulations and the LPA was operated continuously at 1 Hz over several hundred shots.

Just as in a conventional X-ray tube we create radiation via penetration of a solid target with electrons. As converter material we use foils of $_{73}$Ta and we use different thicknesses (0.5 mm, 1.0 mm and 1.5 mm) in order to study their influence on the source size. Using the continuous-slowing-down approximation [155] we estimate a stopping range of ~ 0.5 mm for 1 MeV electrons, which means that they will slow down to rest within the converter. Though most of the stopping power goes into coulomb collisions, about $\sim 10\,\%$ of electron energy is converted into radiation. At 10 MeV the stopping range increases to ~ 3.7 mm, meaning that these electrons are not stopped within the converter. However, the ratio of radiative stopping power to collision stopping power increases significantly between 1 and 10 MeV, and accordingly we estimate a radiation yield of $\sim (6-20)\,\%$ of their energy for $(0.5-1.5)$ mm target thickness. As a first rough estimation, we expect the production of $\sim 10^{-4}$ Joule of X and γ-ray per shot.

The converter foils were placed behind the gas jet at distances between 5 and 20 millimeters, cf. Fig.5.3. The X-ray signal was measured using photostimulable phosphor plates (Fuiji BAS TR). The response of these image plates (IPs) depends essentially on the energy deposited in the phosphor layer and will therefore drop significantly for photon energies above 100 keV [156]. We estimate the photon spectrum using GEANT4 [157] simulations, cf. Fig.5.4.

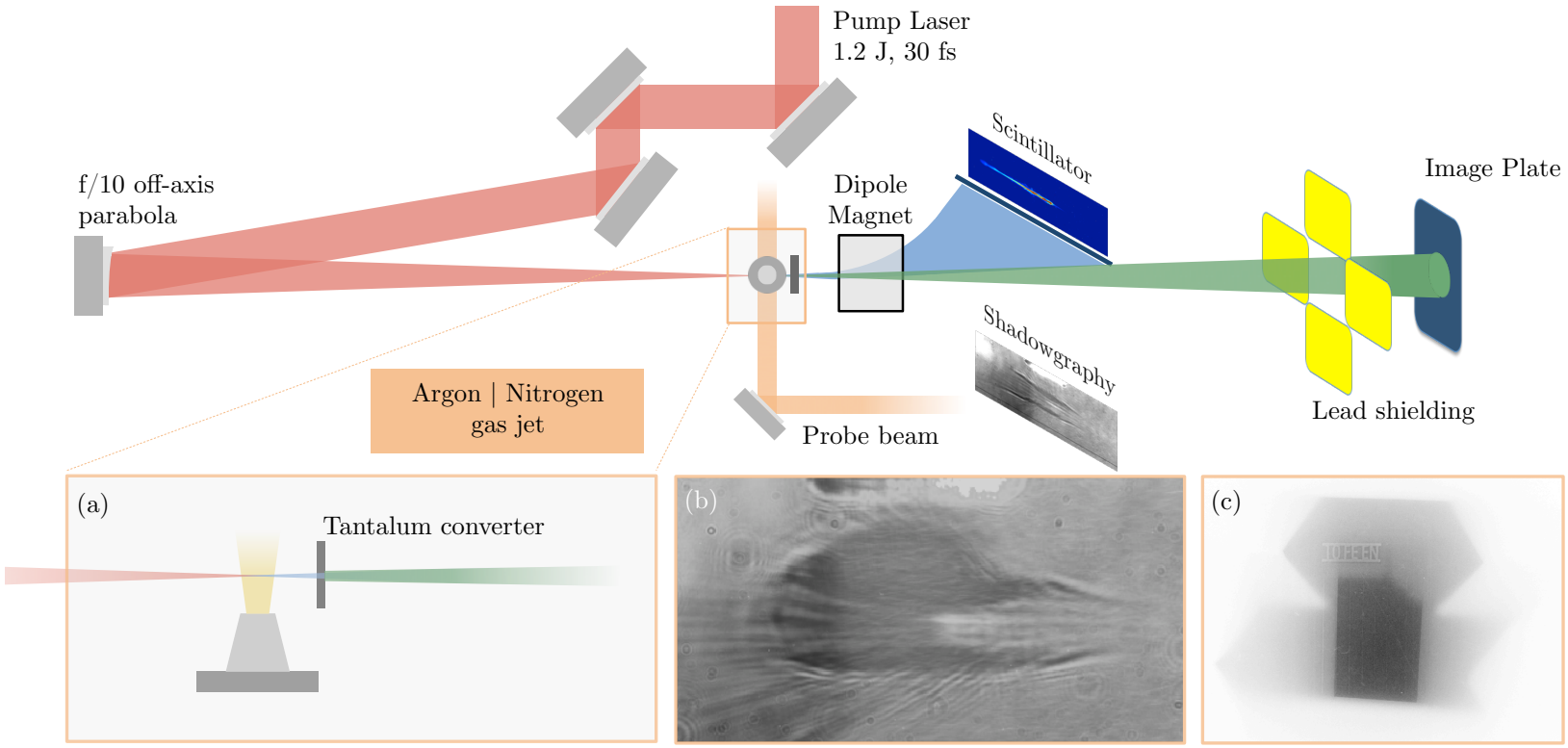

Figure 5.3 – Schematic setup of the experiment. The multi-TW laser pulse is focussed into a gas jet of nitrogen or argon. Electrons are ionization injected into the wake of the pulse and accelerated. Once they exit the gas jet, they penetrate a tantalum foil, leading to the emission of bremsstrahlung, cf. inlet (a). This bremsstrahlung is then detected on an image plate, while the electrons are deviated in a magnet spectrometer. (c) shows a cropped image plate scan, where regions of highest radiation exposure have turned dark. The triangular shape around the object is the shadow cast by the lead shielding. (b) shows a typical shadowgraphy image.

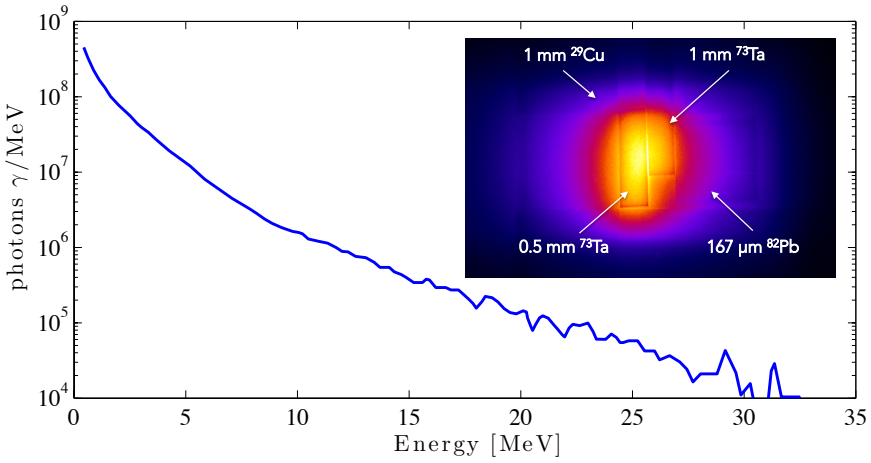

Figure 5.4 – γ-ray spectrum retrieved from GEANT4 simulations. Inlet: Absorption contrast of different filters.

Using a knife-edge we measured the X-ray source size for different distances d between the gas jet exit and the converter. At $d = 0.5$ mm from the exit the source size is estimated to be ~ 65 μm and no significance influence of the converter thickness (0.5 mm,1 mm and 1.5 mm) was observed. As shown in Fig.5.5 the source size remained below < 100 microns at 1.5 mm distance. Due to the electron beam divergence it augmented to ~ 350 μm at 3.5 mm from the gas jet. While the results are fairly in accordance with monte carlo simulations of the source size for a 0.5 mm tantalum converter placed at $d = 2$ mm from the exit, it should however be noted that the source size depends strongly on the properties of the scattered electrons. As discussed above, we expect low energy electrons to undergo strong scattering, up to complete stopping inside the converter. Furthermore the initial beam divergence is about an order of magnitude larger for low energy electrons than it is for electrons with energies $\gtrsim 10$ MeV. This tendency is reproduced in simulations (cf.Fig.5.5), where we see that the γ source size increases significantly at lower energies.

In the experiment we initially noticed a very low image contrast, due to the high background noise level. It was found that this noise was due to Bremsstrahlung emitted from the electrons hitting the chamber wall and the signal to background noise ratio could be improved significantly by applying additional lead shielding. While the strong local noise prevents to image weakly absorbing objects, we were still able to perform some radiographies in order to assess the suitability of the source for imaging applications. As an example, Figure 5.6 shows radiographies of industry standard (DIN EN 462) image quality indicators. The smallest features resolved have a size of ~ 200 micrometer.

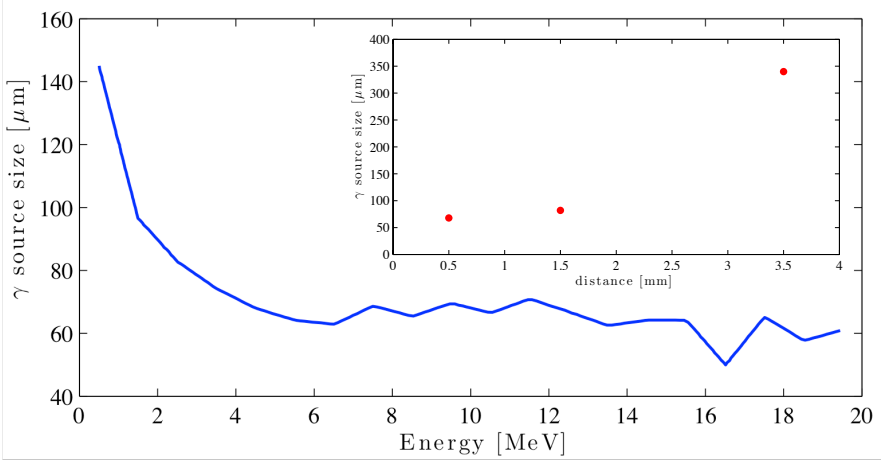

Figure 5.5 – GEANT4 simulation of the source size at 2mm from the jet. Inlet: Knife edge measurements for different distances.

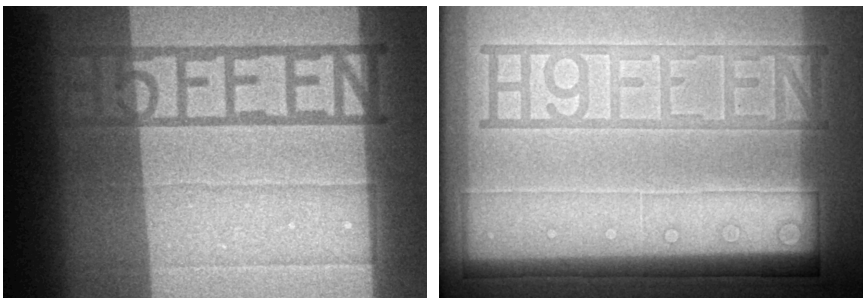

Figure 5.6 – Images of step-hole image quality indicators. Dark areas are where part of the lead shielding is in front of the image plate.

5.2 Synchrotron sources

The particle trajectories of electrons penetrating a target are random, determined by the scattering cross sections. This leads to very broad spectra as the one shown in Fig.5.4. In contrast, particle orbits in synchrotron sources are controlled, relying on transverse deflection of the electron beam using magnetic, electrostatic or electromagnetic fields. This results in the emission of much brighter radiation, called synchrotron radiation. In this section we are introducing the theoretical foundations of these sources, inspired by [131, 158, 124].

5.2.1 Radiation from relativistic particle beams

The emission of radiation from accelerated particles is a direct consequence of the Maxwell equation

$$\nabla \times \vec{B} = \frac{4\pi \vec{j}}{c} + \frac{1}{c}\frac{\partial \vec{E}}{\partial t} \tag{5.1}$$

We can describe the particle beam as a sum of point sources at positions $\delta(\vec{x} - \vec{r}_i(t))$ and the movement of these charges at a velocity $\vec{v}(t)$ forms a current. Treating the particles as point-like sources allows us to use Green's functions to find solutions to the associated potential, known as Liénhard-Wiechert [159] potentials:

$$\Phi(\vec{x}, t) = \left(\frac{e}{(1 - \vec{\beta}\cdot\vec{n})R}\right)_{ret} \tag{5.2}$$

$$\vec{A}(\vec{x}, t) = \left(\frac{e\vec{\beta}}{(1 - \vec{\beta}\cdot\vec{n})R}\right)_{ret}. \tag{5.3}$$

where *ret* means that the expression has to be evaluated at the retarded time $t_{ret} = t - R/c$ and $\vec{n}$ is the observation direction. The corresponding electric field is given by

$$\vec{E}(\vec{x}, t) = e\left(\frac{\vec{n} - \vec{\beta}}{\gamma^2(1 - \vec{\beta}\cdot\vec{n})^3 R^2}\right)_{ret} + \frac{e}{c}\left(\frac{\vec{n} \times ((\vec{n} - \vec{\beta}) \times \dot{\vec{\beta}})}{(1 - \vec{\beta}\cdot\vec{n})^3 R}\right)_{ret} \tag{5.4}$$

In this solution we see that the field consists of two distinct parts, which differ in their temporal and spatial structure. In the particle rest frame ($\beta' = 0$) the first term reduces to the electrostatic Coulomb field of a point charge $\vec{E}(\vec{x}') = \vec{n}e/R^2$. When $\beta \neq 0$ the field tilts with $(\vec{n} - \vec{\beta})$ into the direction of propagation and the Coulomb field is reduced by the $1/\gamma^2$ term for highly relativistic particles.

In contrast, the second term of (5.4) is also dependent on the acceleration $\dot{\vec{\beta}}$ and therefore cannot be reduced to an electrostatic form. This regime is called radiation regime and it reaches much further than the Coulomb regime, decreasing with $1/R$. In the following discussion we will restrict us to this second far field term and ignore the Coulomb term. For this case the magnetic field is related to the electric field by $\vec{B} = \frac{1}{c}(\vec{E} \times \vec{n})_{ret}$. Then the radiation flux towards the observer given by the Pointing vector is

$$\vec{S} = \left(\frac{c}{4\pi}|\vec{E}^2|\vec{n}\right)_{ret} \tag{5.5}$$

and the radiated power per unit angle is

$$\frac{dP(t)}{d\Omega} = R^2(\vec{S}\cdot\vec{n})_{ret} = \left(\frac{c}{4\pi}R^2|\vec{E}^2|\right)_{ret}. \tag{5.6}$$

One has to consider again the retarded fields to get the power at a certain moment t, as the signal has to arrive first. Sir Joseph Larmor evaluated this radiated power for the case of a

non-relativistic particle ($\beta \ll 1$), for which the radiation field reduces to

$$\vec{E} = \frac{e}{c}\left[\frac{\vec{n}\times(\vec{n}\times\dot{\vec{\beta}})}{R}\right]_{ret}. \tag{5.7}$$

With (5.6) we get $dP(t)/d\Omega = e^2/4\pi c^3|\vec{n}\times(\vec{n}\times\dot{\vec{v}})|^2$. Let θ be the angle between particle acceleration $\dot{\vec{v}}$ and the observer $\vec{n}$ this gives

$$\frac{dP(t)}{d\Omega} = \frac{e^2}{4\pi c^3}|\dot{\vec{v}}|^2\sin^2\theta. \tag{5.8}$$

A common example for this donut-shaped radiation distribution is the special case of dipole radiation, cf. Fig.5.7. Note that the radiation field vanishes along the axis of acceleration. Integrating over the solid angles Ω, we obtain Larmor's well-known formula for the total radiated power

$$P = \frac{2}{3}\frac{e^2}{c^3}|\dot{\vec{v}}|^2. \tag{5.9}$$

An important feature of this equation is that the radiated power is proportional to the square of the acceleration $\dot{v}$. Similarly, a more careful analysis leads to its relativistic generalization

$$P = \frac{2}{3}r_e mc\gamma^6\left[\dot{\vec{\beta}}^2 - \left(\vec{\beta}\times\dot{\vec{\beta}}\right)\right] \tag{5.10}$$

where we used the classical electron radius $r_e = \frac{1}{4\pi\epsilon_0}\frac{e^2}{mc^2}$. In this form the term $\left(\vec{\beta}\times\dot{\vec{\beta}}\right)$ introduces a dependence on the direction of acceleration with respect to the particle propagation vector $\vec{\beta}/|\vec{\beta}|$. Reminding that $1-\beta^2 = \gamma^{-2}$ we find the scalings

$$P_\parallel \propto \gamma^6\dot{\vec{\beta}}_\parallel \qquad \text{and} \qquad P_\perp \propto \gamma^4\dot{\vec{\beta}}_\perp \tag{5.11}$$

for acceleration parallel $\dot{\vec{\beta}}_\parallel$ and perpendicular $\dot{\vec{\beta}}_\perp$ to the direction of propagation. At a first glance it might seem that the γ^6 term for longitudinal acceleration overweights the γ^4 component, however the perpendicular acceleration is actually much more efficient: At highly relativistic velocities the particle velocity is very close to $\vec{\beta}\approx 1$, so the velocity derivative is small ($\vec{v} = \gamma^{-3}\dot{\vec{p}}$).The emitted power is then independent of γ and scales linearly with the accelerating field

$$P_\parallel \propto \left(\frac{d\vec{p}_\parallel}{dt}\right)^2. \tag{5.12}$$

In contrast the transverse velocity change is simply given by the Lorentz force $d\vec{p}_\perp/dt = \gamma m\dot{\vec{v}}$ and therefore scales as

$$P_\perp \propto \gamma^2\left(\frac{d\vec{p}_\perp}{dt}\right)^2. \tag{5.13}$$

So we see that transverse deflection produces by γ^2 more radiation than longitudinal acceleration and therefore radiation sources rely on this transverse component.

Next we consider the relativistic generalization of (5.8)

$$\frac{dP}{d\Omega} = \frac{r_e mc}{4\pi c^2}|\dot{\vec{v}}|^2 \frac{(1-\beta\cos^2\theta)-(1-\beta^2)\sin^2\theta\cos^2\phi}{(1-\beta\cos\theta)^5}. \tag{5.14}$$

where we assume that the velocity is dominated by the longitudinal component, while acceleration occurs in transverse direction. The angles ϕ and θ are defined as shown in Fig.5.7. As this is basically a lorentz-boosted version of (5.8) we expect that the radiation cone is contracted by $1/\gamma$. Indeed, for $\gamma \gg 1$ and $\phi = 0$, we find that this expression scales with $(\gamma^{-2}+\theta^2)^{-3}$. This means that $P(\phi = 0, \theta = 1/\gamma) = P(0,0)/8$ and thus most radiation is contained within

$$-\frac{1}{\gamma} < \theta < \frac{1}{\gamma}. \tag{5.15}$$

This is shown for an electron at rest and an electron with $\beta = 0.9$ in Fig.5.7. To conclude this general discussion of radiation properties we come back to the radiation field given by (5.4). We obtain the spectrum of radiation by Fourier transformation,

$$\left[R\vec{E}\right]_{ret}(\omega) = \frac{1}{\sqrt{2\pi}}\frac{e}{c}\int_{-\infty}^{+\infty} \frac{\vec{n}\times[(\vec{n}-\vec{\beta})\times\dot{\vec{\beta}}]}{(1-\vec{\beta}\cdot\vec{n})^2}\cdot e^{i\omega(t-\vec{n}\cdot\vec{r}(t)/c)}\,dt \tag{5.16}$$

From this we obtain a general expression for the radiation from a charged particle in motion

$$\frac{d^2I}{d\omega d\Omega} = \frac{e^2}{4\pi^2 c}\left|\int_{-\infty}^{+\infty} \frac{\vec{n}\times[(\vec{n}-\vec{\beta})\times\dot{\vec{\beta}}]}{(1-\vec{\beta}\cdot\vec{n})^2}\cdot e^{i\omega(t-\vec{n}\cdot\vec{r}(t)/c)}\,dt\right|^2 \tag{5.17a}$$

$$= \frac{e^2}{4\pi^2 c}\left|\int_{-\infty}^{+\infty} [\vec{n}\times(\vec{n}-\vec{\beta})]\cdot e^{i\omega(t-\vec{n}\cdot\vec{r}(t)/c)}\,dt\right|^2. \tag{5.17b}$$

The first term $(1-\vec{\beta}\cdot\vec{n})^2$ contains information about the collimation of the emitted radiation, as we have discussed above. From $\vec{n}\times[(\vec{n}-\vec{\beta})\times\dot{\vec{\beta}}]$ we refind the power laws derived previously. New information comes from the phase term $e^{i\omega(t-\vec{n}\cdot\vec{r}(t)/c)}$, which we can locally approximate as $e^{i\omega(1-\beta)t}$. For highly relativistic particles ($\gamma \gg 1$) we can replace $(1-\beta) \simeq 1/2\gamma^2$, so the frequency is upshifted by $2\gamma^2$. This is generally interpreted as Doppler upshift and we will discuss this effect in detail in the next section.

In conclusion we have shown that a transverse acceleration of relativistic particles leads to emission of radiation within a cone of opening angle $\theta \sim 1/\gamma$, while the emitted power is proportional to $(\gamma\dot{\vec{p}}_\perp)^2$.

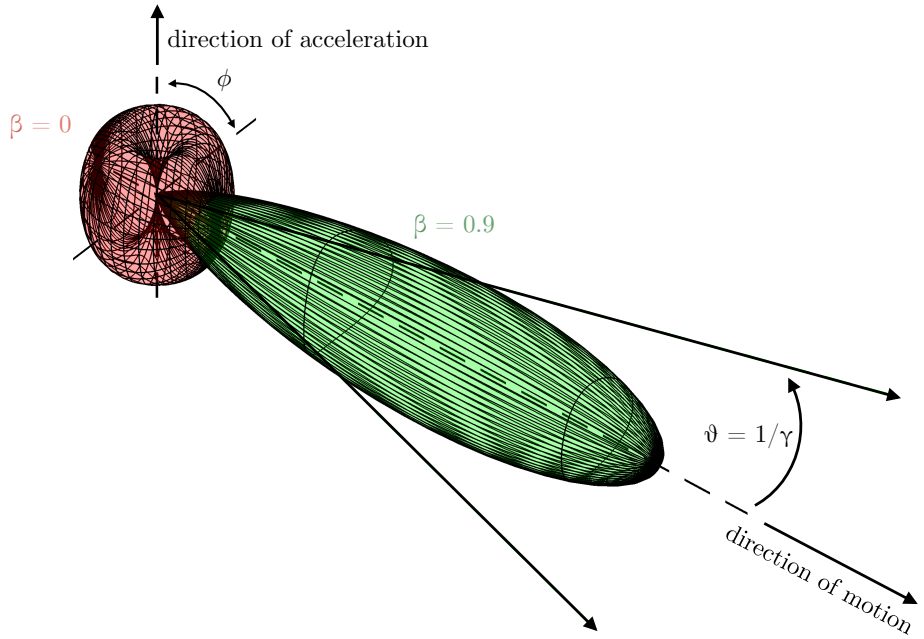

Figure 5.7 – Visualization of the angular distribution of the radiation emission given by (5.14). In red for an electron in its rest frame, where the isosurface shows the typical donut form known for dipole radiation. In green the emission for a relativistic electron with longitudinal velocity $\beta = 0.9$, i.e. $\gamma \approx 3.2$, is shown. We observe that the radiation is concentrated along the direction of motion, within an angle of $\theta \sim 1/\gamma$. While the radiated power scales with γ^2, for visualization purposes, the green isosurface has been normalized to have the same transverse extension as the $\beta = 0$ case.

5.2.2 Undulator and Wiggler radiation

Starting from (5.17b) we will now discuss the radiation emitted for certain trajectories $\vec{x}(t)$. Historically circular particle motion has been the first to be examined, by J. Schwinger [7], and this the first two generations of synchrotrons relied on this kind of trajectory. Nevertheless, since the introduction of insertion devices in third generation lightsources, radiation emission uses electrons that follow a periodic quasi-sinosoidal trajectory, leading to significant enhancement of brightness.

In conventional sources, such kind of trajectory is driven by alternating magnet arrays. As we will discuss later, this method has severe technological limitations and a main objective of this work is devoted to the development of alternative methods using electrostatic and electromagnetic fields.

However, being realizations of the same force, we can discuss all methods using the same formalism. For this we first consider the motion of a free particle initially at rest in an elec-

tromagnetic field. Consider a plane wave of frequency $\tilde{\omega}$ propagating along $\vec{k} = (0,0,k_z)$ with the normalized vector potential $\vec{a} = (a_x, a_y, 0)$. We have briefly mentioned in **Chapter 1: Introduction** that the equations of motion in this case are

$$\frac{d\vec{x}}{d\tau} = \left(a_x, a_y, \frac{\vec{a}^2}{2}\right). \tag{5.18}$$

From this we see that in first order the particle momentum equals the vector potential $|\vec{p}| \sim |\vec{a}|$. Furthermore, the transverse field does not only induce motion in the perpendicular plane, but also in direction of motion. However, this term is second order $\vec{a}^2$, so for a sinusoidal excitation we find $\vec{a}^2 \propto |\sin\tilde{\omega}\tau|^2 = \frac{1}{2}(1-\cos(2\tilde{\omega}\tau))$. This means that the field induces a drift along the direction of wave propagation, combined with an oscillation at twice the initial frequency $2\tilde{\omega}$.

Relativistic doppler-upshift of radiation

At the moment we will restrict us to the dominant fundamental component $\tilde{\omega}$. The above description is equivalently valid for the rest frame of a particle with velocity $\vec{\beta} = (0,0,\beta_z)$. As long as the scattering wave's potential is non-relativistic ($a_0 \ll 1$), we can treat the motion in the rest frame as classical dipole. As such, the emitted frequency equals the frequency of excitation $\tilde{\omega}$. Yet boosting back to the laboratory frame, the observer perceives a doppler-shifted frequency $\tilde{\omega}'$. As we consider an electron at relativistic velocity β we get

$$\tilde{\omega}' = \frac{\tilde{\omega}}{\gamma(1-\beta\cos\theta)}. \tag{5.19}$$

For $\gamma \gg 1$ and observation close to the propagation axis ($\theta \ll 1$) we can approximate with $\cos\theta \simeq 1-\theta^2/2$ and $\beta \simeq 1-1/2\gamma^2$. Keeping only terms up to second order this yields to

$$\tilde{\omega}' \simeq \frac{2\gamma\tilde{\omega}}{1+\gamma^2\theta^2}. \tag{5.20}$$

As consequence of the boost, the radiation is upshifted to a frequency of up to $2\gamma\tilde{\omega}$ on-axis. However, we also see that there is an angular dependence of the frequency. This means that even for a monochromatic emission in the electron rest frame, the spectrum is broadened in the laboratory frame and the signal has to be observed through a pinhole to reduce the bandwidth.

Up to now we have looked at the electron motion in its rest frame at frequency $\tilde{\omega}$. In order to apply this result to practical applications we need to establish an expression related to the period of the wiggling field λ_0. We will consider three different cases. (a) An electromagnetic wave at incident angle ϕ and wavelength λ_0. (b) A magnetic insertion device of period $\lambda_0 = \lambda_u$. (c) Betatron oscillations in an co-moving plasma wave with $\lambda_0 = \lambda_\beta$.

Again, we are interested in the motion of the electron in its rest frame. For this we proceed analogously to the previous section, but now we consider a moving source instead of a moving receiver. The general expression for this is then

$$\tilde{\omega} = \gamma\left(1 - \beta\cos\phi\right)\omega_0. \tag{5.21}$$

So the wave frequency from case (a) depends on the incident angle and the upshift reaches up to 2γ for a counter-propagating wave. The case (b) of an insertion device which is static in the laboratory frame is equivalent to $\phi = 90°$, so the upshift in this case scales with γ. The betatron case (c) is particular as the oscillation length depends not only on the field strength (determined by the blowout density), but also on the particle energy. We have seen in Sec.4.2.3 that corresponding the betatron wavelength is $\lambda_\beta = \sqrt{2\gamma}\lambda_p$.

Hence the combination of both receiver and emitter upshift leads to emission of radiation at a fundamental wavelength of

$$\lambda_{\theta=0} = \frac{\lambda_0}{2\gamma^2(1-\beta\cos\phi)} \qquad \text{(EM-WAVE)} \tag{5.22a}$$

$$\lambda_{\theta=0} = \frac{\lambda_u}{2\gamma^2} \qquad \text{(Undulator)} \tag{5.22b}$$

$$\lambda_{\theta=0} = \frac{\lambda_\beta}{2\gamma^2} = \frac{\lambda_p}{(2\gamma)^{3/2}} \qquad \text{(Betatron)} \tag{5.22c}$$

As mentioned above these values have to be multiplied by $(1+\gamma^2\theta^2)$ for a non-zero observation angle.

Undulator radiation and harmonics

So far we have assumed that the dipole motion of the electron in its rest frame leads to the emission of radiation at frequency $\tilde{\omega}$, i.e. $E(t) \propto \exp(i\tilde{\omega}\tau)$. For an infinite periodic motion the Fourier transformation of this kind of function is obviously the monochromatic solution $\tilde{\omega}$. Yet any real undulator will have a limited spatial extension, so the integration length $[-\infty,\infty]$ has to be replaced by a finite value $[-\tau_0,\tau_0]$. In this case the Fourier transformation

$$E(\omega) \propto \int_{-\tau_0}^{\tau_0} e^{i(\tilde{\omega}-\omega)\tau} \propto \frac{1}{\tau_0}\frac{\sin(\tilde{\omega}-\omega)}{\tilde{\omega}-\omega}. \tag{5.23}$$

So the spectral intensity

$$I(\omega) \propto |E(\omega)|^2 \propto \mathrm{sinc}^2\xi, \tag{5.24}$$

where $\xi = \pi N_{osc}\frac{\tilde{\omega}-\omega}{\tilde{\omega}}$. The width of this distribution scales inversely with the number of oscillations

$$\Delta\omega \approx \frac{\tilde{\omega}}{N_{osc}} \tag{5.25}$$

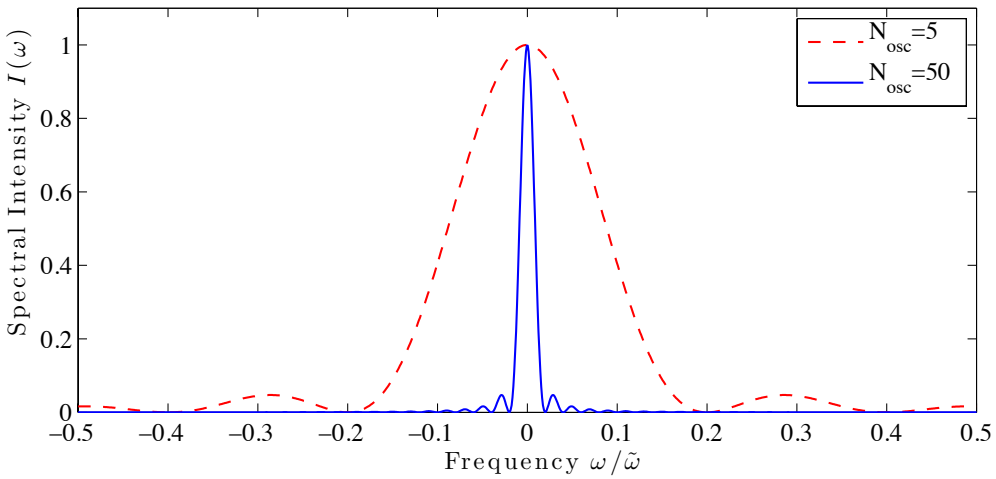

Figure 5.8 – Bandwidth of undulator radiation is reduced by constructive interference.

Up to now we have supposed that the electron motion in the transverse plane is non-relativistic ($a_0 \ll 1$). If the wiggling field get stronger, a number of additional effects influence the radiation spectrum.

One effect that we already mentioned briefly is that in the case of a highly relativistic electron ($\beta \to 1$) oscillations in the transverse plane will impose oscillations in the longitudinal direction as well, cf.(5.18). For small $|\beta_\perp| \ll 1$ the change of velocity is given by

$$\beta_\parallel = \sqrt{\beta^2 - \beta_\perp^2} \simeq \beta\left(1 - \frac{\beta_\perp^2}{2\beta^2}\right) \simeq \beta\left(1 - \frac{\beta_\perp^2}{2}\right). \tag{5.26}$$

For a sinusoidal transverse motion $\beta_\perp(t) = \beta_{\perp_0}\sin(\omega t)$ this results in the aforementioned drift part and oscillation at twice the frequency in the parallel direction:

$$\beta_\parallel = \beta_0\left(1 - \frac{\beta_{\perp_0}^2}{4} - \frac{\beta_{\perp_0}^2}{8}\sin(2\omega t)\right) \tag{5.27}$$

The peak angular deflection $\beta_{\perp_0}$ is commonly expressed in terms of the so-called (Wiggler) strength parameter K, defined as $\beta_{\perp_0} = K/\gamma$. Integrating this equation over one wiggler period we find that the average velocity is reduced due to the drift term $\langle\beta_\parallel\rangle = \beta_0\left(1 - K^2/4\gamma^2\right)$. When discussing the doppler shifts in the preceding section, we assumed that the motion is predominantly longitudinal, so $\beta_\parallel \approx \beta$. For large oscillation amplitudes this is no longer the case and for the boost in longitudinal direction we need to use $\langle\beta_\parallel\rangle$ instead. This correction gives us the effective Lorentz factor

$$\gamma_{\text{eff}}(K) = \frac{\gamma}{\sqrt{1 + K^2/2}}. \tag{5.28}$$

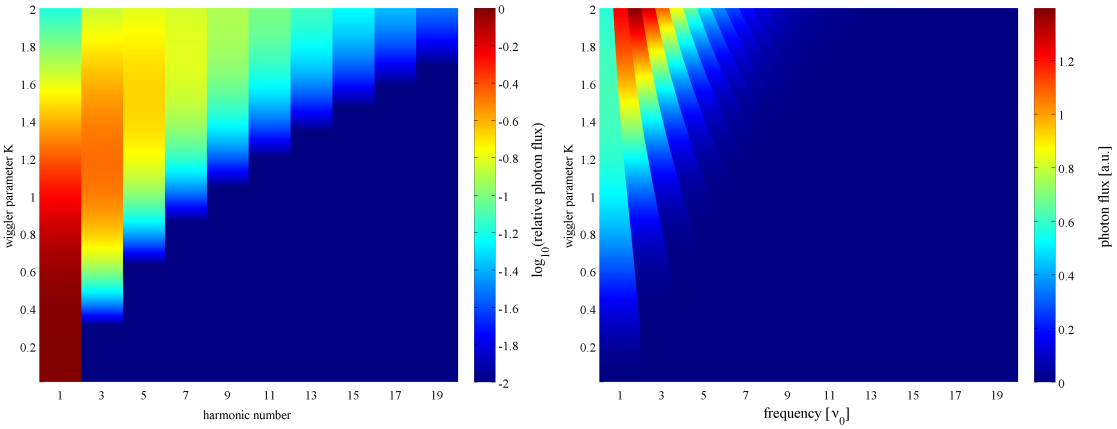

Figure 5.9 – Left: Emission of harmonics as function of the wiggler parameter K. For $K \ll 1$ all emitted radiation is confined within the fundamental, yet for $K > 1$ the spectrum shifts to higher harmonics and gets much broader. Right: Photon flux as function of the wiggler parameter K. Although more and more harmonics are excited as K increases, we observe that the absolute flux at the fundamental reaches its maximum around $K \simeq 1.3$. Note that the frequency shifts down due to the decreasing effective Lorentz factor.

Once the transverse momentum of a particle becomes relativistic, its reaction to the Lorentz force is modified by γ. In consequence the oscillations of the particle are no longer purely sinusoidal. This leads to the emission of harmonics, where the amplitude of the nth harmonic is given by [124]

$$A_n(K) = \frac{n^2 K^2}{(1+\frac{1}{2}K^2)} \left[J_{\frac{1}{2}(n-1)}\left(\frac{nK^2}{4+2K^2}\right) + J_{\frac{1}{2}(n+1)}\left(\frac{nK^2}{4+2K^2}\right)\right]^2 \tag{5.29}$$

and J_α are Bessel functions of the first kind: $J_\alpha(x) = \sum_{m=0}^{\infty} \frac{(-1)^m}{m!\,\Gamma(m+\alpha+1)} \left(\frac{x}{2}\right)^{2m+\alpha}$. The relative contribution of harmonics to the spectrum from (5.29) is visualized in Fig.5.9 for strength parameters up to $K = 2$. Up to $K \simeq 0.3$ radiation is only emitted at the fundamental. At $K \simeq 1.3$ the second harmonic contribution surpasses the fundamental and for $K \simeq 2$ we observe a broad spectrum with > 20 harmonics. The same figure includes also a visualization of the absolute amplitude of the emitted frequencies, where we see how the frequencies are downshifted by the aforementioned effective gamma factor $\gamma'(K)$. As already discussed the emitted power increases the stronger the oscillation is. The maximal photon flux at the fundamental is reached for $K \simeq 1.3$.

Wiggler radiation

Increasing the angular deflection $K \gg 1$ ultimately has the consequence that the radiation is emitted into a field of view larger than the proper radiation cone ($\sim 1/\gamma$). This means that we can no longer assume that radiation is constructively interfering over the whole particle

path, as shown in Fig.5.8. Instead an observer will see separate flashes of radiation, each of duration Δt. The typical energy related to this pulse length is about $\hbar\omega_c \sim (\Delta t/2)^{-1}$, which can be shown to lead to

$$\omega_c = \frac{3c\gamma^3}{2\rho} = \frac{3}{2}\gamma^3\omega_0'. \tag{5.30}$$

Here we have denoted the local radius of curvature as ρ. For a particle on a sinusoidal trajectory most radiation is emitted at the turning points and we define the fundamental frequency $\omega_o' = c_0/\rho$, which is the local circular frequency at the turning point:

$$\rho_{(z=0)} = \left.\frac{(1+r'(z))^{3/2}}{r''(z)}\right|_{z=0} = \frac{\gamma}{K}\frac{\lambda_\beta}{2\pi} \tag{5.31}$$

From this we find that the critical radiation frequency

$$\omega_c = \frac{3}{2}K\gamma^2\omega_0 \tag{5.32}$$

scales linearly with the peak deflection K and by the square of the particle energy γ^2.

The spectrum can be derived more rigorously from (5.17b). We have already shown that the phase term scales with $1/2\gamma^2$, so now we also need to simplify the triple vector product $\vec{n}\times(\vec{n}\times\vec{\beta})$. For a sinusoidal motion we find that along the polarization vectors $\vec{u}_\parallel$ and $\vec{u}_\perp$

$$\vec{n}\times(\vec{n}\times\vec{\beta}) \simeq \left[-(vt/\rho)\vec{u}_\parallel + \theta\vec{u}_\perp\right]\beta. \tag{5.33}$$

With these approximations (5.17b) can be solved analytically to find the electric fields in frequency space. In the Wiggler limit ($K \gg 1$) we assume incoherent addition of these fields and the resulting intensity distribution is

$$\frac{d^2I}{d\omega d\Omega} = \frac{e^2}{6\pi^2 c}\left(\frac{\omega\rho}{c}\right)^2\left(\frac{1}{\gamma^2}+\theta^2\right)\left(\mathcal{K}_{2/3}^2(\xi)\vec{u}_\sigma + \frac{\theta^2}{\gamma^{-2}+\theta^2}\mathcal{K}_{1/3}^2(\xi)\vec{u}_\pi\right) \tag{5.34}$$

with $\xi = \frac{\omega}{\omega_c}\left(1+\gamma^2\theta^2\right)^{3/2}$. We also introduced modified Bessel functions of second kind $\mathcal{K}_\nu$. Such functions decay exponentially as the argument x becomes large compared to the order ν, i.e. $\mathcal{K}_\nu(x\gg\nu) \approx \sqrt{\frac{\pi}{2x}}e^{-x}$. In the on-axis case such behavior occurs for $\omega > \omega_c$. We also find that the radiation spectrum has two orthogonal polarization components, which show a very different behavior. The dominant mode is the σ mode (along the particle deflection $u_\parallel$), which is maximum on axis. The weaker π mode is emitted into two lobes with peak intensity around $1/\gamma$, while it vanishes on axis, cf. Fig.5.10. So on-axis radiation ($\theta = 0$) will be completely polarized in the plane of motion and (5.34) reduces to

$$\left.\frac{d^2P}{d\omega d\Omega}\right|_{(\theta=0)} = \frac{e^2}{6\pi^2 c}\left(\frac{\omega\rho}{c}\right)^2\frac{1}{\gamma^2}\mathcal{K}_{2/3}^2(\xi) \tag{5.35}$$

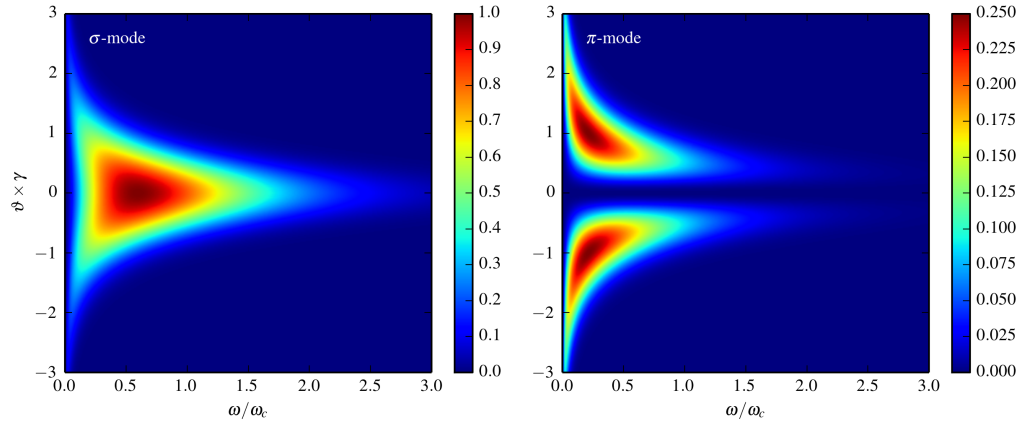

Figure 5.10 – Wiggler intensity according to (5.34). Radiation is emitted into two polarization modes, the σ mode along the deflection and π orthogonal to it.

The angularly integrated spectrum becomes

$$\frac{dI}{d\omega} = \frac{P_\gamma}{\omega_c}\frac{9\sqrt{3}}{9\pi}\frac{\omega}{\omega_c}\int_{\omega/\omega_c}^{\infty}\mathcal{K}_{5/3}(x)dx \tag{5.36}$$

Free-Electron-Laser

In the previous sections we have based our discussion on the radiation emission from a single particle, where we found two regimes: The undulator regime - in which radiation fields sum up coherently $P \propto N_{osc}^2 \times K^2$- and the wiggler regime - with incoherent broadband emission $P \propto N_{osc} \times K$.
Similarly we can separate the combined emission from electrons in a bunch into regimes of coherent or incoherent emission. In analogy to the laser process this is also called stimulated and spontaneous emission. As the stimulated emission scales with the electron number squared N_e^2, such a Free-Electron-Laser (FEL) has potentially much higher brightness than undulators relying on spontaneous emission.
Coherent emission can only occur if the electron phases are similar, meaning that the electrons have to be periodically bunched at the radiation wavelength. One way such microbunching can occur is via the interaction of the electrons and their proper radiation field, which over long distances leads to a redistribution of the electrons. This process is called self-amplified spontaneous emission (SASE). Yet a drawback of amplifying spontaneous emission is the lack of temporal coherence in such sources. Alternatively a 'seed' can be used. In this case a laser pulse is superposed with the electron bunch, inducing the microbunching.
Unfortunately we cannot cover FEL physics in detail, so the interested reader may consult the following references for more information about FELs in general [160, 161, 20] and in the context of laser-wakefield accelerators [158, 35].

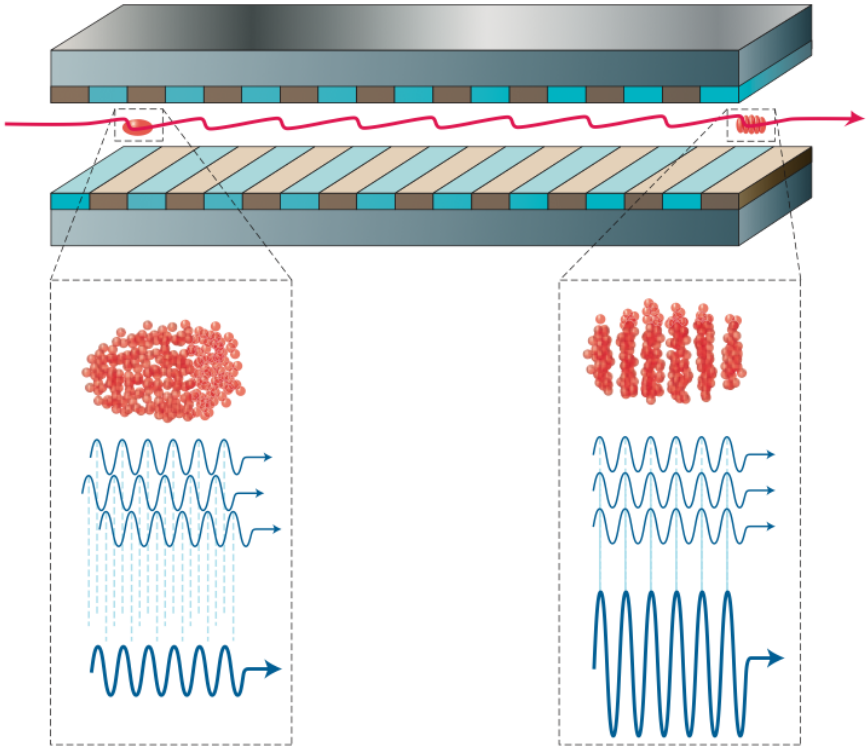

Figure 5.11 – Principle of a SASE Free Electron Laser: An incoherent electron bunch enters an undulator (left) and, after interaction with the synchrotron emission along propagation, forms microbunches that emit coherently (right). Illustration from [23].

5.3 Conventional insertion devices

Since their third generation, synchrotron sources use sections of alternating magnetic field, so-called insertion devices, to provoke transverse oscillations of highly relativistic electrons beams. Depending on the oscillation amplitude we distinguish between wigglers and undulators.

5.3.1 Magnet undulators and wigglers

In **Chapter 4: Beam Transport** we have derived the equations of motion (4.13-4.14) for an electron within a quadrupole. There we saw that electrons will perform oscillations in the focusing plane. However, such configuration cannot be used for wiggling the electrons as they will diverge in the perpendicular plane.

Instead, as proposed by Motz in 1951 [13], sets of dipole magnets are used, whose polarity switches each $\lambda_u/2$, just as illustrated in Fig.5.11. If the magnets are placed close enough to each other, the magnetic field will not have hard edges, but instead the fringe fields superimpose and form fields of a form similar to $B_y = B_0 \sin(k_u z) + \mathcal{O}(nk_u)$, which then impose electron oscillations in the x-plane. Close to the beam axis the amplitude can be assumed

constant, thus leading to the approximate equations of motion

$$\ddot{x} = -\frac{eB_0}{m_e\gamma}\cos k_u z \qquad \text{and} \qquad \ddot{y} = 0. \tag{5.37}$$

Again we assume that $z = c_0 t$ and in consequence

$$x = \frac{eB_0}{k_u^2 m_e\gamma}\cos k_u z \qquad \text{and} \qquad x' = \frac{eB_0}{k_u m_e\gamma}\sin k_u z \tag{5.38}$$

The strength of the Wiggler fields is characterized by the peak angular deflection

$$K = \gamma\theta \simeq 0.934 B_0[\mathrm{T}]\lambda_u[\mathrm{cm}]. \tag{5.39}$$

As discussed before, according to their different radiation features the regime $K \ll 1$ corresponds to the undulator limit, while $K \gg 1$ is the Wiggler limit. Yet in practice the threshold between what is called an undulator and a wiggler lies rather around $K \sim 2.5$, which is where the spectrum changes from a harmonic form to a broadband, cf. Fig.5.9.

The above equations of motion are only taking into account lowest order terms. Any actual magnet will however have additional higher order components nk_u. Also, the Motz configuration is not free of fields in the B_x plane. The latter issue has been significantly reduced since the introduction of magnets multipole arrays in the Halbach configuration [162]. Synchrotron radiation originating from such sources is intrinsically linearly polarized. A common extension of the Halbach-type configuration is for example the APPLE (Advanced Planar Polarized Light Emitter) type helical undulator [163], where four Halbach arrays are arranged in blocks that can be shifted with respect to each other. This way the field strength along B_x and B_y can be adapted, allowing to produce either horizontally, vertically or cylindrically polarized radiation.

5.3.2 Coupling with laser-accelerated electron beams

Since laser-plasma accelerators nowadays reach electron beam energies comparable to medium energy synchrotron radiation facilities, but at drastically reduced size, it is straightforward to try coupling them to conventional insertion devices.

The first proof-of-concept of such a combination was presented in 2007 [165], when electron bunches between 55 and 75 MeV were sent directly from the accelerator into a 1-m-long undulator ($\lambda_u = 20$mm, $K = 0.6$). The emitted synchrotron radiation was in the visible and near-infrared range (700-1000 nm) and a peak spectral brightness of 6.5×10^{16} ph/(s mrad^2 mm^2 0.1% BW) was estimated.

Shortly later, a more refined experiment demonstrated synchrotron emission in the XUV range, with photon energies of up to ~ 130 eV [166, 167]. In this experiment electrons between 150-220 MeV where accelerated and sent through two quadrupole lenses into a 30 cm long undulator ($\lambda_u = 5$mm, $K = 0.55$). An advantage of this configuration is especially that the

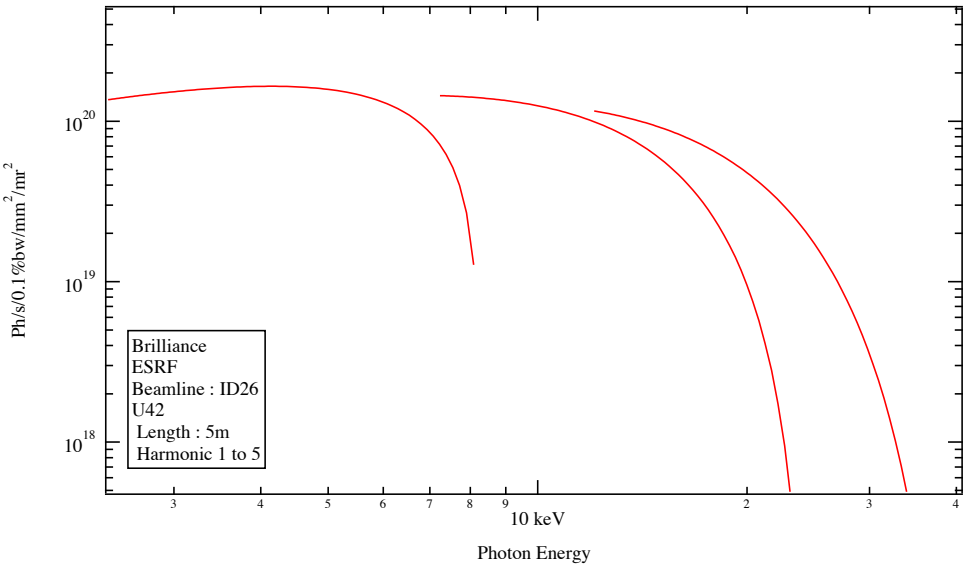

Figure 5.12 – Example for a synchrotron spectrum of the first three harmonics from the 6.04 GeV ESRF beam sent into an undulator with 5m length, $\lambda_u = 42$ mm period and $K = 2.2$. Calculated with RADIA [164].

quadrupole pair allowed energy selection. The brightness of this source is estimated to be of the order of 1.3×10^{17} ph/(s mrad^2 mm^2 0.1% BW). Also there are studies [168] that propose to use a laser-plasma accelerator as injector for a conventional storage ring synchrotron, thus replacing entirely the electron gun and booster section.

Even more, high current beam from laser-plasma accelerators would be a promising electron source to realize a table-top FEL [169]. However, the FEL gain is only possible for a beams with small energy spread and emittance. The latter is already of the order of 1.mm.mrad, which would be sufficient for many applications, if properly transported e.g. using a laser plasma lens. Yet the electron energy spread remains of the order of some percent. Recently it was shown that a transverse gradient undulator could be used to shift the dependence from the total energy spread towards the sliced energy spread. Simulations have shown that in this case FEL-gain would be possible in a state-of-the-art LPA, which has motivated several projects on LPA-based FEL sources, e.g. LUNEX5 in France [170].

5.4 Inverse Compton back-scattering

As mentioned earlier, not only magnetic structures can be used to force electrons to oscillate, but also electromagnetic waves as from lasers. An advantage of such an optical undulator is that the fundamental wavelength λ_0 can be orders of magnitude shorter than in conventional insertion devices.

Synchrotron sources based on Compton backscattering have been proposed in 1963 by Milburn [171] and Arutyunian and Tumanian [172]. First experimental results were obtained only shortly later at the Cambridge Electron accelerator, when a ruby laser [18] was employed to obtain γ-ray from scattering with a 6.0 GeV electron beam [173]. Since then, compton scattering beamlines have been established at many conventional accelerator facilities [174]. Not only does this scheme allow to create high energy radiation, it is also a convenient method to produce ultrashort X-ray pulses at such facilities: By scattering at an angle of 90° femtosecond laser pulses can be used to create scattered radiation of similar duration, without need to compress the electron beam [175].

However, just recently this technology has been combined with laser wakefield acceleration, resulting in a ultra-compact source of X/γ-ray. The difficulty of the scheme lies in the fact that one needs to overlap both temporally and spatially two terawatt class laser pulses. The first proof-of-principle experiment has been presented in 2006 [176], however in this experiment electrons were only accelerated to a few MeV and scattered radiation was in the soft X-ray range (up to ~ 2 keV). A mayor breakthrough was the production of X-ray in the range of hundreds of keV via Compton backscattering using a plasma mirror (see below) [177]. Since then several groups have used either this scheme [178] or the conventional two-pulse scheme [179] to produce X/γ-ray from laser-accelerated electron beams.

Notable results are precise measurements using shock-injected electron beams [180] and the production of quasi-monoenergetic radiation up to 1 MeV [181]. Higher beam energies, yet broadband, have been reached at PW-class laser systems [182] or using laser harmonics for scattering [183].

5.4.1 Numerical study of different scattering geometries

As discussed previously, most medical imaging techniques operate at energies below 100 keV. Beyond 100 keV both detection and filtering of the radiation becomes much more difficult, which is why especially the 50-100 keV region is of interest. A radiation source in this range, with reasonable energy spread and small source size, would be for instance interesting for phase contrast imaging.

Laser-wakefield accelerators with an optical or density-transition driven injector have shown great potential to produce stable electron beams with small energy spread, see **Chapter 2: Injection** . Though both higher and lower beam energies have been reported, the sweet spot of operation for a typical 30 fs, 1-2 Joule Ti:Sa laser (e.g. SALLE-JAUNE, Lund TW Laser, etc.) lies within the 100-200 MeV range. In a counterpropagating beam configuration the fundamental backscattered energy would be therefore $4\gamma^2\hbar\omega_0 \approx 250 - 1000$ keV.

But optical undulators offer an additional degree of freedom that is not exploited in conventional devices: The angle between the electron beam and the undulating structure. From

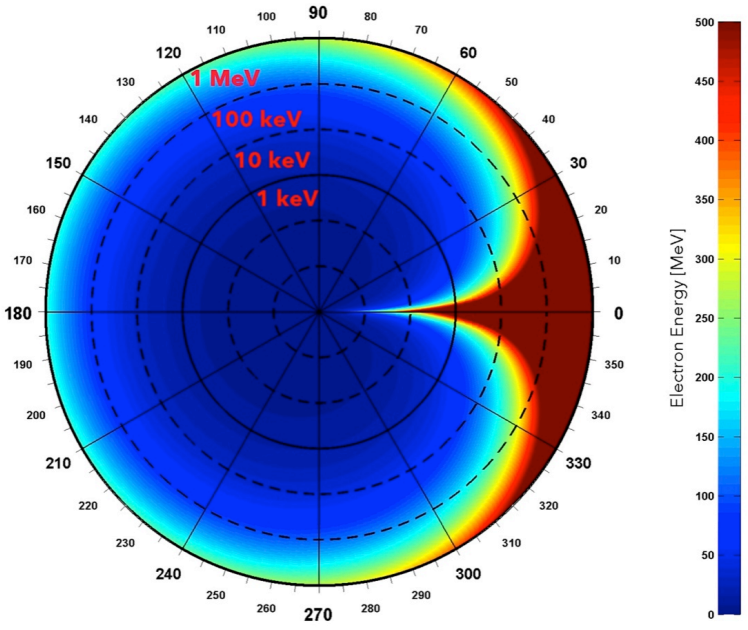

Figure 5.13 – Emitted fundamental wavelength (5.22a) as function of the initial electron energy and the scattering angle for a Ti:Sapphire scattering pulse at 800 nm.

(5.22) we see that an incident laser angle changes the backscattered energy according to

$$\frac{\hbar\omega(\phi)}{\hbar\omega(180°)} = \sin^2\frac{\phi}{2},$$

which is illustrated in Fig.5.14. One setup of interest would be to use a scattering beam at $\phi = 30°$ incident angle. In this configuration the fundamental energy is down-shifted by a factor of ~ 15, meaning that scattering with electron beams of 100 to 250 MeV results in the emission of X-ray in the range of ~ 15 to 100 keV. We simulated this scenario with PLARES [184] for electron beams of 1 percent energy spread and 1 milliradiant divergence. For accurate modelling of the distribution 2000 test particles were used. The scattering beam is weakly non-linear ($a_0 = 1.0$), with 30 fs duration and 20 μm FWHM spot size at the interaction point. The results shown in Fig.5.15 demonstrate that it would be possible to create narrow bandwidth radiation using electron beams of ~ 100 MeV energy. However, as the radiation is emitted within a cone that scales with $1/\gamma$, the electron divergence smears up the energy spread. We observe that at 250 MeV the X-ray energy spread is then limited by the electron beam divergence.

In fact, to reach the same photon energy at smaller scattering angles ϕ the electron beams have to be more energetic, which increases the energy blur. For example, in order to obtain a

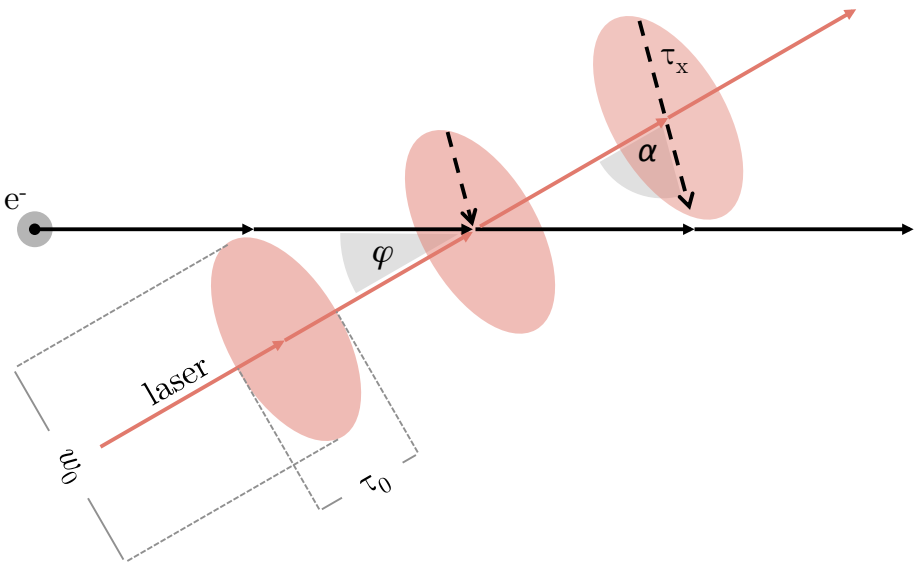

Figure 5.14 – Scattering geometry.

backscattered energy of 100 keV for angles from 30 to 180°, the γ factor varies by a factor of ~ 4. The resulting difference in backscattered beams is shown in Figure 5.16. In Fig.5.17 the on-axis ($\theta < 3$mrad) spectrum is shown for 30°, 45°, 90° and 180°. Even though the simulations are performed for the best achievable LPA beam parameters ($\Delta E/E = 0.01$. Divergence 1.0 mrad), the X-ray energy spread is significant (~ 5 – 20%). When the beam divergence is increased to 5 mrad the spectrum broadens even more, up to some 20 – 40%.

When using different collision angles ϕ, it is important to estimate the consequences for the interaction time. For this we consider a simple geometric model, shown in Fig.5.14. We approximate the electron beam as point-like, while the laser beam is described as an ellipse with the diameters $a = \tau_0$ and $b = w_0/c_0$. The electron beam propagates at a velocity close to the speed of light c_0, so the laser beam ellipse is cut at an angle $\alpha = (180° - \phi)/2$. From the polar form of the ellipse equation we get then

$$\tau_x(\phi) = ab\left[(b\cos\alpha)^2 + (a\sin\alpha)^2\right]^{-1/2}.$$

For $\phi = 180°$ we get as expected $\tau_x = \tau_0$, meaning that the interaction time is given by the laser pulse length. In co-propagating geometries ($\phi \to 0°$) the laser waist is the defining parameter. Also, for a given waist w_0 and $\tau \to \infty$, the interaction time is $\tan\alpha \times w_0/c_0$. At $\phi = 30°$ for example this value is about $3.7\,w_0/c_0$, so at a typical waist of 20 microns the interaction time cannot exceed ~ 250 fs. This is an important issue because the amount of photons emitted depends on the number of laser cycles n at the wavelength $\lambda_0/\sin^2\phi/2$ the electrons perceive (e.g. $n_{max} \sim 10$ for the before-mentioned case).

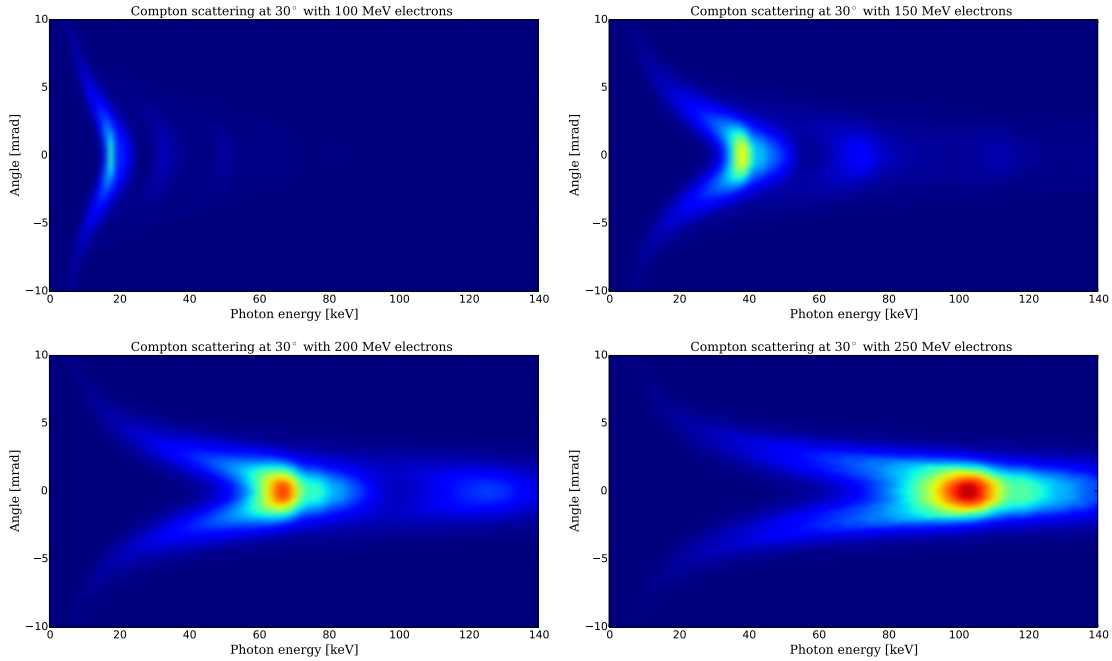

Figure 5.15 – Backscattered photon spectra in the plane of laser polarization for an incident laser angle of $\phi = 30°$ and different electron beam energies. Simulations performed using 2000 test particles. $\Delta E/E = 0.01$. Divergence 1.0 mrad. Scattering beam $a_0 = 1$, 60 fs duration, 20 μm FWHM.

The problem can be resolved by spatially tilting the laser wavefront, as proposed in the travelling-wave undulator [185]. Depending on the tilt direction, the laser will then cross the electron beam at $\alpha = 0°$ or $\alpha = 90°$ and the interaction length is therefore τ_0 or w_0/c_0, respectively.

In conclusion, optical undulators offer the possibility to tune the backscattered energy not only by means of the undulator period and the electron energy, but also by using different collision angles ϕ. When operating at small ϕ, the beam collimation is increased with respect to equivalent counter-propagating Compton-sources. However, this makes the source's spectrum also more sensitive to the electron beam divergence. Another drawback is the limited interaction time. The latter problem can be in principle solved using a tilted wavefront, while plasma lenses as introduced in **Chapter 4: Beam Transport** could help to collimate the electron beam before collision, although this would be a trade-off with the source size.

Yet all those schemes require further R&D before they can be applied to experiments. In the following we will discuss a simpler scheme, based on retro-reflection with a plasma mirror, which provides the best energy conversion efficiency.

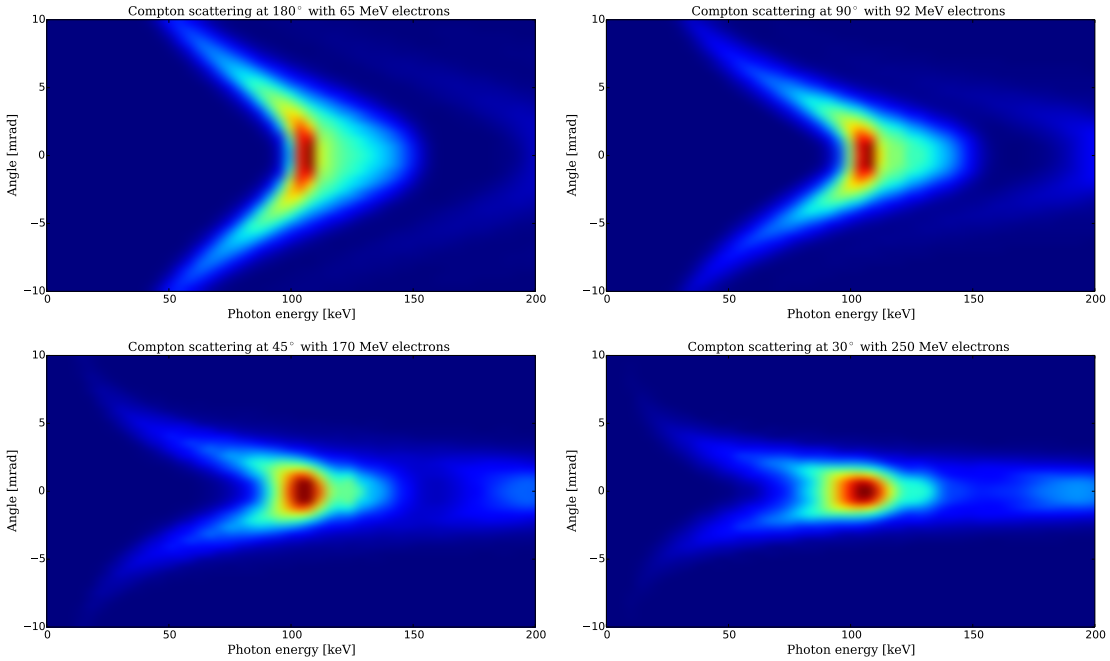

Figure 5.16 – Simulations for Compton backscattering of 100 keV photons in different scattering configurations. Performed using 2000 test particles. $\Delta E/E = 0.01$. Divergence 1.0 mrad. Scattering beam $a_0 = 1$, 30 fs duration, 20 μm FWHM.

5.4.2 Compton backscattering using a plasma mirror

In 2011 Ta Phuoc and co-workers demonstrated that hard X and γ ray can be created from backscattering using a single high power laser pulse, i.e. the laser acts both as driver of the accelerator as well as scattering pulse [177]. The idea is that a plasma mirror is placed at the accelerator exit, thus retro-reflecting the pulse which then immediately collides with the electron bunch traveling in its wake. The scheme has several advantages to the conventional two-pulse method. Most importantly it provides inherent spatial and temporal synchronization with the electron beam, which greatly simplifies the experimental setup. Also it is very efficient as unused laser energy is 'recycled' to create radiation - and as the scattering angle is 180° the conversion efficiency is the highest possible. The disadvantage, similar to all combined solutions e.g. single-pulse plasma lenses, is that using a single pulse limits the parameter space. In particular, in this scheme we have less control over the scattering intensity and cannot adjust the pulse duration.

Experimental setup

The experiment was performed at the SALLE JAUNE Ti:Sa Laser System at Laboratoire d'Optique Appliquée, which delivers linearly polarized laser pulses at 28 femtosecond duration at full width at half maximum (FWHM). Using a spherical mirror of 700 mm focal length the ~ 1.6 J pulse delivered from the laser were focussed at the entrance of a supersonic $_2$He gas jet of 2

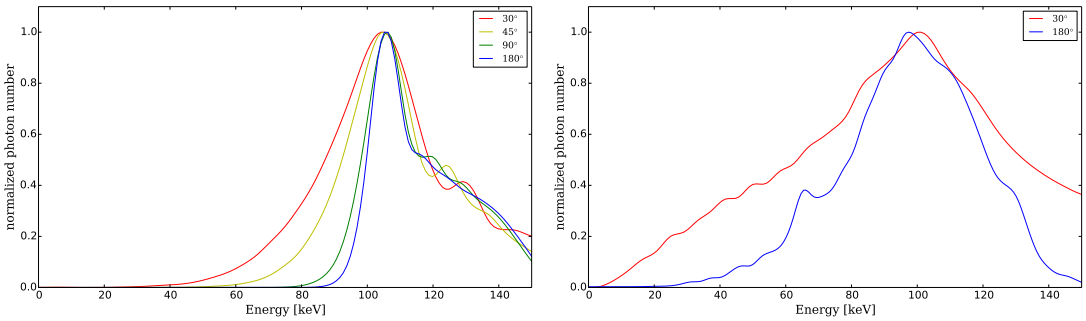

Figure 5.17 – Left: On-axis lineout of the spectra shown in Fig.5.16. Right: The same geometry for an electron beam of 5mrad divergence. It becomes clear that the photon energy spread increases significantly, to ~ 20 and 30 percent.

mm diameter. The focal spot contained 50-55% of the beam energy, leaving a pulse of ~ 0.9 J for acceleration.

The laser-plasma accelerator was operated in the transverse self-injection regime, producing beams of 100 - 200 pC charge at beam energies mostly in the range of 100 - 150 MeV. Electron charge and spectra were measured using a dipole magnet spectrometer combined with an absolutely calibrated phosphor screen. In contrast to previous experiments [177] the electron beams in this study showed important quasi-monoenergetic features.

For the plasma mirror a 100 μm cellophane foil was used. This choice of the plasma mirror material aims to reduce the production of bremsstrahlung as electrons pass through the plasma mirror (more details below). The foil is a mounted on a three-axis translation stage and slightly inclined with respect to the laser axis in order to avoid back-reflection to the laser chain. It also permitted to observe the plasma channel the reflected beam formed in the gas jet, cf. Fig.5.18(d-e). Furthermore the reflected laser beam was imaged on a screen Fig.5.18(c). After each shot the foil was moved to provide a flat, undamaged mirror surface.

X-rays were detected using a GdOS based scintillator, fiber-coupled to a low-noise 16-bit CCD (Princeton Instruments Quad-RO 4320). The total detector area was 5×5 cm^2, divided into 2084×2084 pixels of 24 μm edge length each. Placed on the laser axis at 90 centimeters from the interaction, this leads to a field of view of $\sim 55 \times 55$ mrad^2.

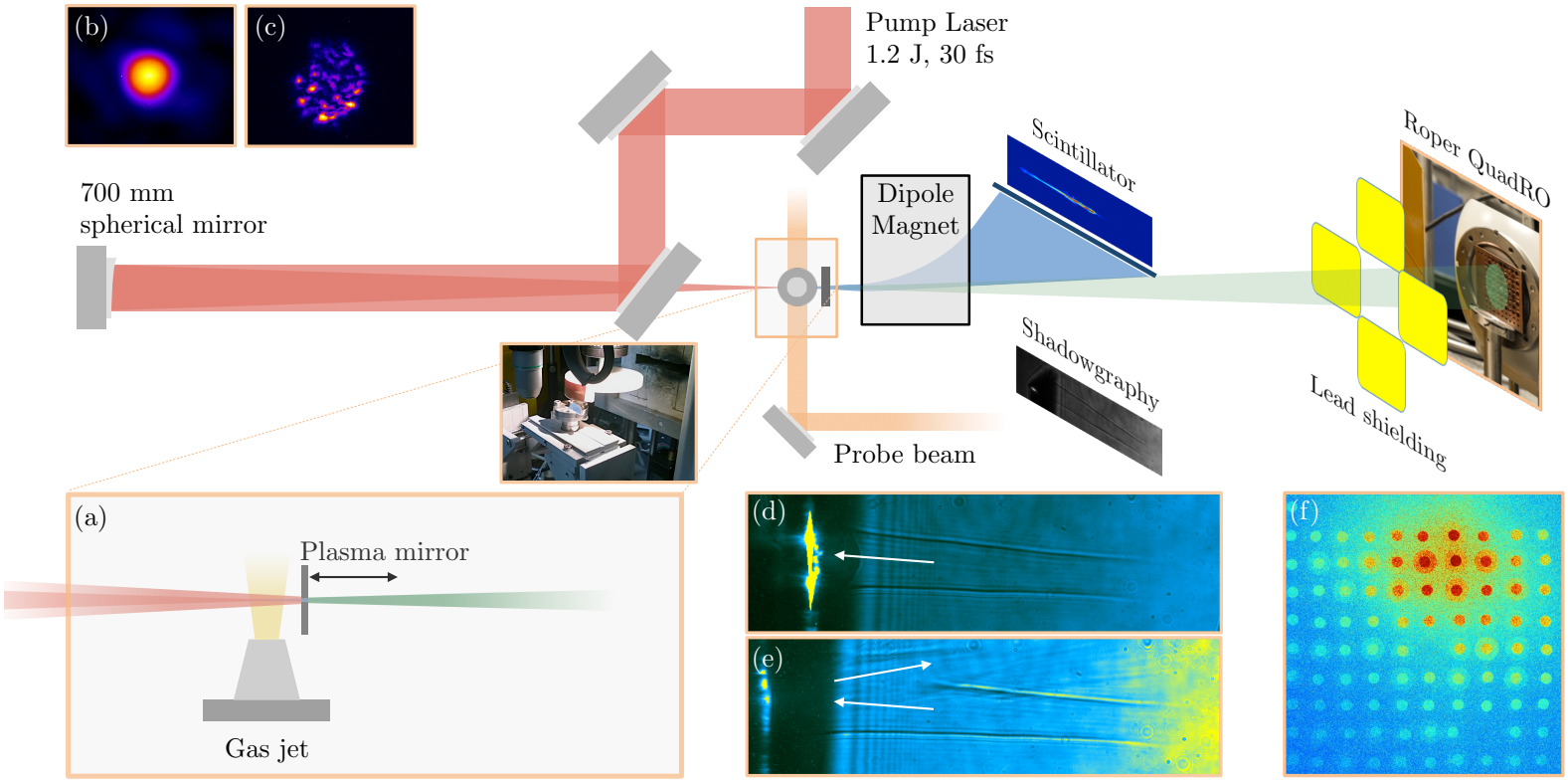

Figure 5.18 – Setup of the Compton backscattering experiment. The spherical mirror was replaced in a follow-up experiment by an off-axis parabola. The foil which acts as plasma mirror is placed at the exit of the gas jet, as shown in (a). The foil can be moved along the axis to distinguish between bremsstrahlung and backscattering. (b) shows the focal spot at the gas jet entrance. There are two diagnostics for the back-reflection: (c) shows an image of the backscattered light on the foil, which is recollected using a lens system. Though not absolutely calibrated, this measures the relative intensity of the backscattered light. Also, when there is no reflection we observe a clear plasma channel on the shadowgraphy (d). Once the foil is in place we can also see the channel created from the reflected beam. The emitted X-rays are detected downstream on a Gadox scintillator, fiber-coupled to a low noise Roper QuadRO CCD. The temperature of the radiation is estimated using a filter array, as shown in (f).

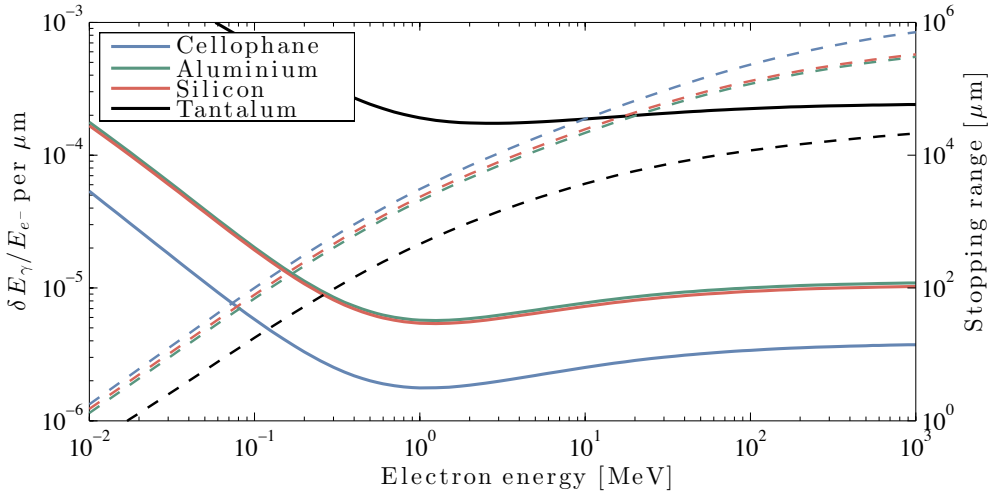

Figure 5.19 – Conversion efficiency of electron energy into radiation for different target materials (solid lines). Multiplication with the stopping range (dashed lines) gives the maximal photon conversion efficiency. Data from NIST-ESTAR database [155].

Conversion efficiency into backscattering and bremsstrahlung

In Section 5.1.2 we have used electron stopping within a converter material as radiation source. As the plasma mirror setup is very similar (cf. Fig.5.18), we need to assure that the emission is dominated by Compton scattering.

Earlier in this chapter we derived the emitted power for a relativistic particle accelerated in transverse direction (5.10). For a particle on a sinusoidal trajectory with peak angular deflection K/γ we can use (5.10) and (5.31) to write this expression explicitly as average power

$$\langle P_\gamma \rangle = \frac{\pi e^2 c}{3\epsilon_0}\left(\frac{\gamma K}{\lambda_0}\right)^2 = 5.68\times 10^{-3}\left(\frac{\gamma K}{\lambda_0\,[\mu\mathrm{m}]}\right)^2 \;[\mathrm{eV/fs}] \tag{5.40}$$

For a realistic scattering pulse with $a_0 = 2$ and 30 fs duration this means that in terms of the electron energy a fraction

$$\frac{E_\gamma}{E_{e^-}} \sim 2.1\gamma\times 10^{-6} \tag{5.41}$$

of the energy is converted into radiation. For $\gamma = 300$ and the above scattering pulse the formula evaluates to about $\sim 0.063\,\%$ .We also see that for high K and γ values the radiated power can reach a significant fraction of the electron energy. Strictly speaking this would be the Compton regime, while at lower energies scattering (in the laboratory frame) occurs in the Thomson limit. On the other hand 150 MeV electrons passing through a 100 μm cellophane foil ($\rho \simeq 1.5\mathrm{g.cm}^{-3}$) emit radiative stopping power of ~ 3.5 MeV cm^2/g. This means that about $\chi \sim 0.015\,\%$ of electron energy are converted into bremsstrahlung, which is roughly a

fourth of the backscattered energy. As shown in Fig.5.19 this is orders of magnitude less than bremsstrahlung emission in heavy targets as Tantalum.

Even though less energetic electrons undergo stronger scattering, slightly less of the particle's total energy is converted into radiation than lost in collisions. The normalized radiative stopping power ranges from 1.2×10^{-2}cm^2/g at 1 MeV to over 2.3×10^{-2}cm^2/g at 100 MeV, to 2.5×10^{-2}cm^2/g at 1 GeV. This means that in experiments using backscattering with a plasma mirror, the ratio between backscattered and bremsstrahlung photons increases about linearly the higher the electron energies.

In conclusion we expect for our experimental conditions a measurable, but inferior, contribution of bremsstrahlung to the high energy photon signal. The ratio increases in favor of the backscattered signal the higher the electron beam energy.

Experimental results

As the Rayleigh length of the laser is about 0.8 millimeters, any signal observed at one centimeter behind the gas jet is not due to Compton backscattering but a result of bremsstrahlung produced by electrons passing through the foil. This background signal is rather stable, with a relative rms error of $\sigma_{brems} \approx 0.1$. When moving the foil inwards we observe a signal increase, up to about 3.2 ± 0.6 times the bremsstrahlung background at the optimal foil position at the gas jet exit. The results are in agreement with previous studies [177] and the estimations from the preceding section. Also, in a second campaign we added a backscattering diagnostic in order to measure the intensity of backscattered light on a single-shot basis. The correlation with the X-ray emission shows the expected tendency, cf. Fig.5.20.

Additionally, we could distinguish the signals due to their very different spectral content. For this, we placed a 5.1 mm copper filter in front of the detector, which cuts off the spectrum below ~ 70 keV. Holes inside the plate (see Fig.5.18f) permit reconstruction of the unperturbed signal level, which is shown in Fig.5.20. For this reconstruction the existing data are interpolated onto a grid using a bi-linear spline. Complete beam profiles are then reconstructed by upscaling the data again with a bi-cubic spline. This reconstruction is done by applying a 2D spline fit to the data. The original hole positions are indicated in Fig.5.20 as crosses. The reconstructed profiles are very similar to the profiles observed without any filters.

The ratio between both the filtered signal I_1 and the signal that passes through the holes I_0 allows to roughly estimate the spectral content. We observe an important difference between the beams we attribute to bremsstrahlung and the beams from backscattering: Shots with the foil close to the jet show a high contrast ratio of 0.6, the contrast being defined as $1 - I_1/I_0$. When moving the foil outwards of the jet, the contrast reduces to 0.1. This implies that the Compton X-ray are stronger attenuated and therefore contain less signal content beyond 100 keV than the bremsstrahlung signal (which extends far into the MeV range).

In a later experiment we replaced the copper filter with a mesh of lead stripes, each 1 mm thick. One millimeter of lead absorbs essentially all radiation below 100 keV, while at the superposition the cut-off is around 150 keV. The transmission difference of these two continuum filters peaks around 250 keV. Figure 5.22 shows an example of the backscattering signal from to two consecutive shots. The first shot has an electron energy around hundred MeV, while the second exceeds 200 MeV. From the transmission we can estimate that the first shot has an energy off less than ~ 200 keV, while the second shot clearly has significant signal content above the cut-off energies. Also, as expected this shot is much more collimated.

The large field of view permits us to measure the beam divergence, which for the Compton backscattering is close to isotropic, with an FWHM beam divergence of $\Theta_x = (12.7 \pm 3.6)$ mrad and $\Theta_y = (13.0 \pm 4.0)$ mrad, where x is plane of laser polarization. The pointing stability is 8.3 mrad and 6.4 mrad, respectively.

The duration of the pulse is approximately given by the electron bunch duration [158], which is a few femtoseconds for electrons beams in our regime of operation. To get a better estimate of the X-ray spectrum, we used a reduced version of PLARES [184] and simulated the backscattering for a laser pulse of $a_0 = 1.0$ and 30 fs duration for an electron beam of 140 MeV peak energy, 5 percent energy spread and 5 mrad divergence, similar to the electron beam distributions shown in Fig.2. The angularly resolved X-ray spectrum, shown in Fig.5.21, is in fair agreement with the experimental data. The large energy spread is a consequence of the initial electron energy spread, as well as the electron beam divergence. Simulations for various beam parameters show that the latter is usually the dominating effect for laser-accelerated electron beams.

To demonstrate that the X-ray flux from Compton backscattering is sufficient to be considered for imaging, we performed radiographies of macroscopic objects, placed in front of the detector. As an example Fig.5.23 shows the radiography of a clock. Its structural parts consist of different metal alloys, while the gears are made of plastic. The different materials are clearly distinguishable in the radiography due to their distinct absorption coefficients. As discussed previously the bremsstrahlung component is very energetic (> 100 keV) and therefore adds to the image mostly in form of a subtractable background noise. Due to the small source size [177] a subject placed closer to the source will show significant edge enhancement (propagation-based phase contrast imaging).

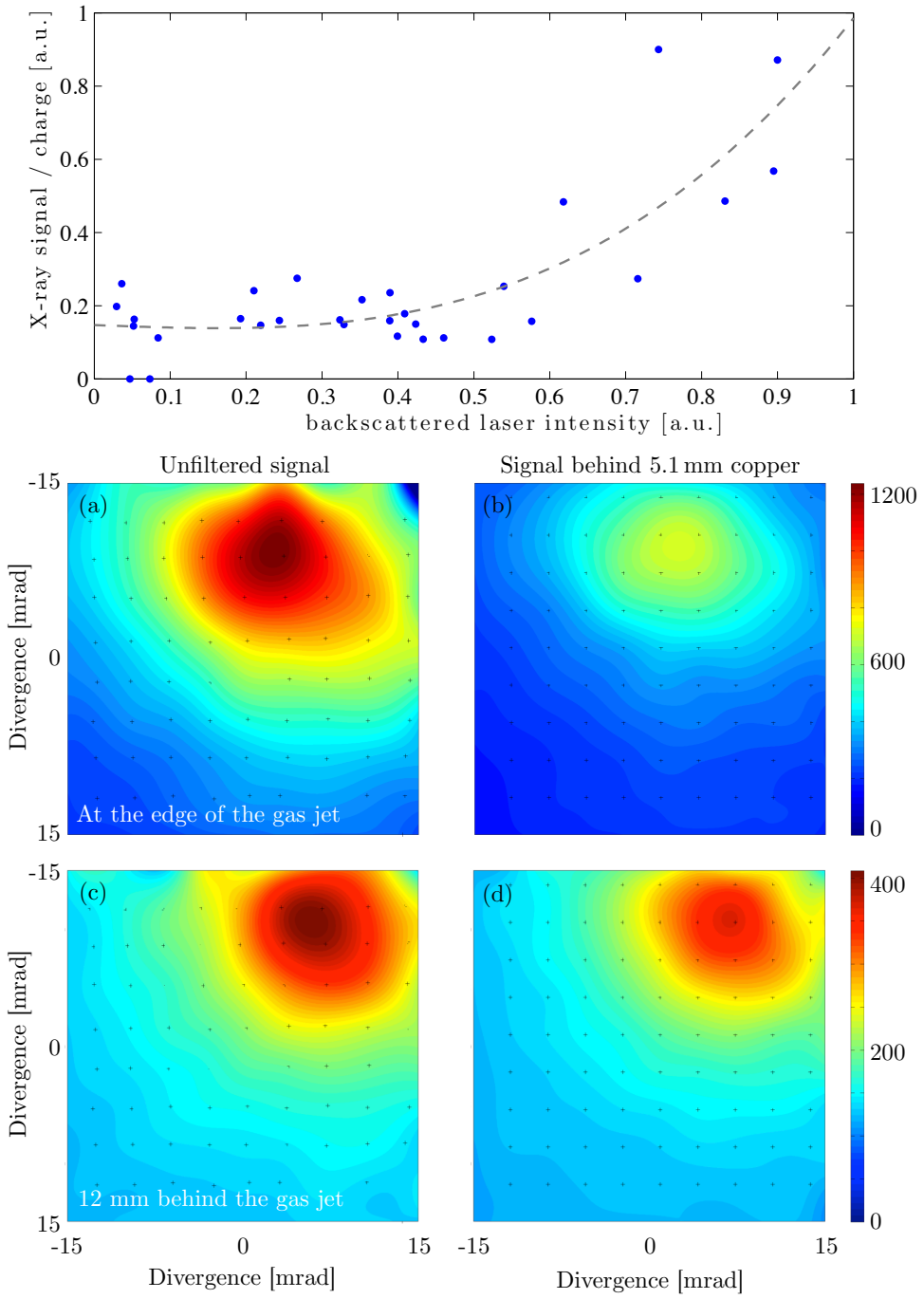

Figure 5.20 – Top: Normalized X-ray signal as function of the backscattered beam intensity for a series of 30 consecutive shots while scanning the foil position. The dashed trendline is a third order polynomial fit. Bottom: Reconstructed beam profile for the unfiltered signal (a/c) and the signal behind 5.1 mm of copper (b/d). The signal close to the jet is not only much more intense, but is also significantly absorbed by the copper filter. In contrast, the signal much behind the jet is barely disturbed, indicating that the photon energy is much higher. The electron beams for both shots had comparable charge and energy.

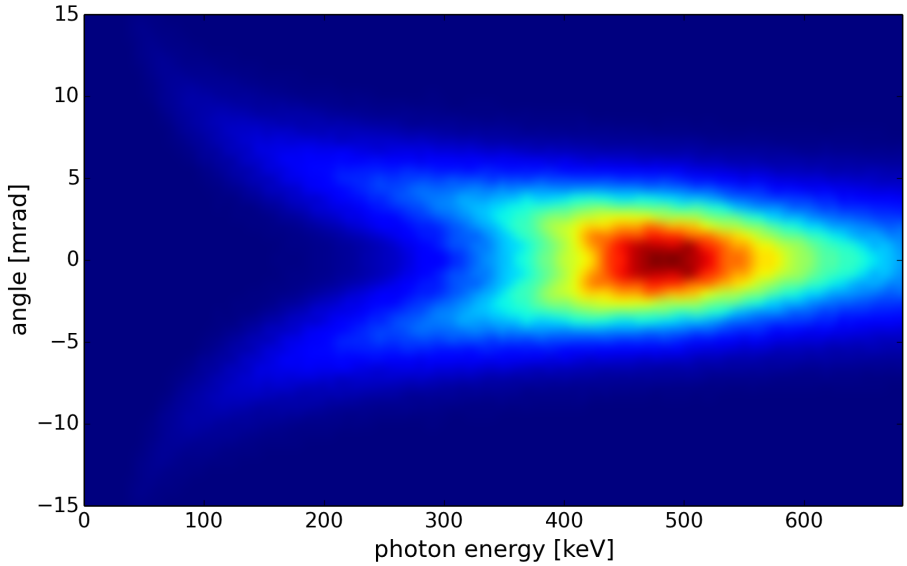

Figure 5.21 – Simulated backscattered photon spectrum for an electron beam with 140 MeV peak energy.

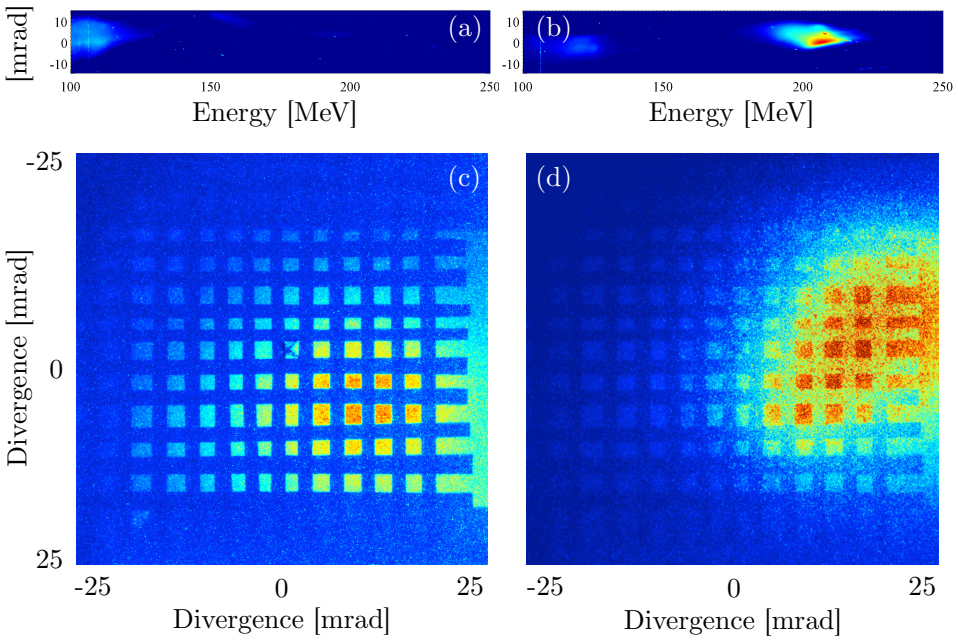

Figure 5.22 – Comparison of Compton signal for different beam energies. (a) and (b) electron spectra from the same series of self-injected beams. (c) and (d) corresponding X-ray signal. The filter-grid consists of stripes of 0.5 mm lead. As expected the more energetic electrons emit much higher energy.

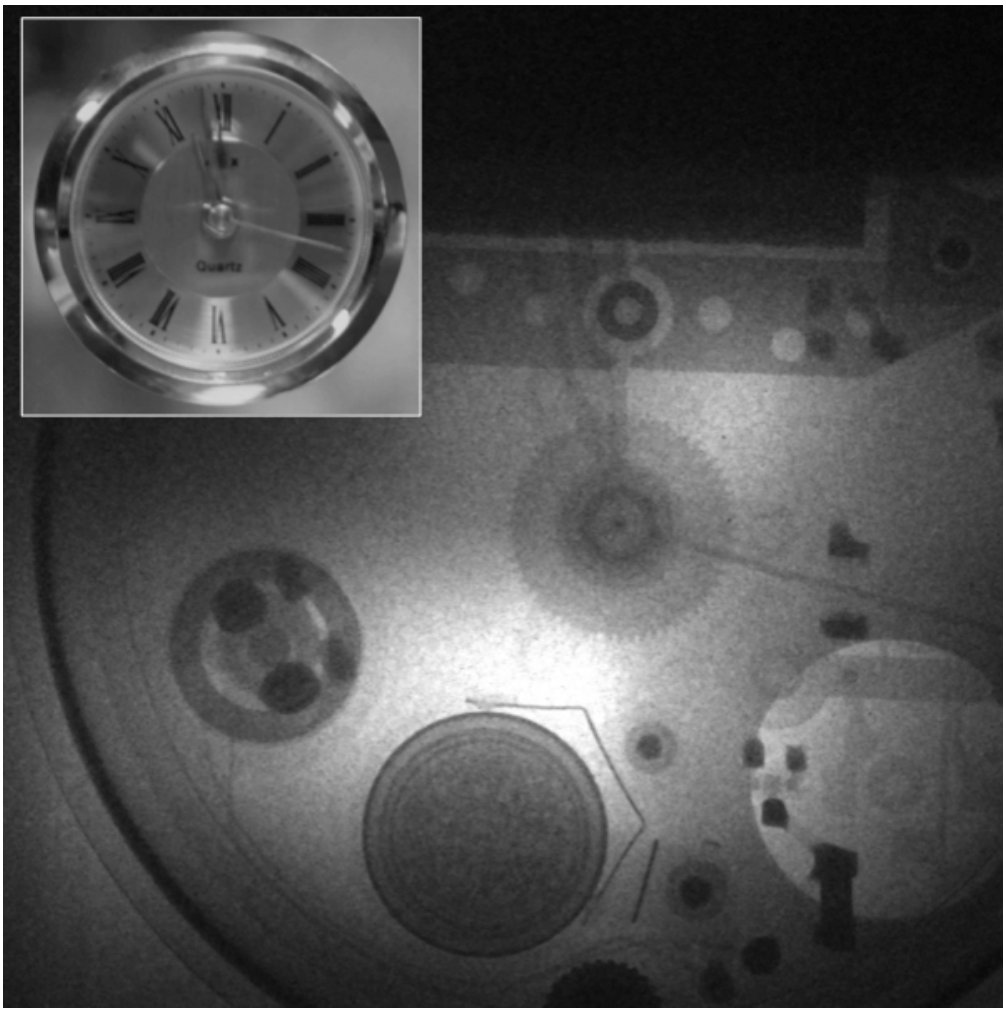

Figure 5.23 – Single-shot radiography of a clock. The different absorption contrast of metal and plastic parts is clearly visible. Inlet: Photography.

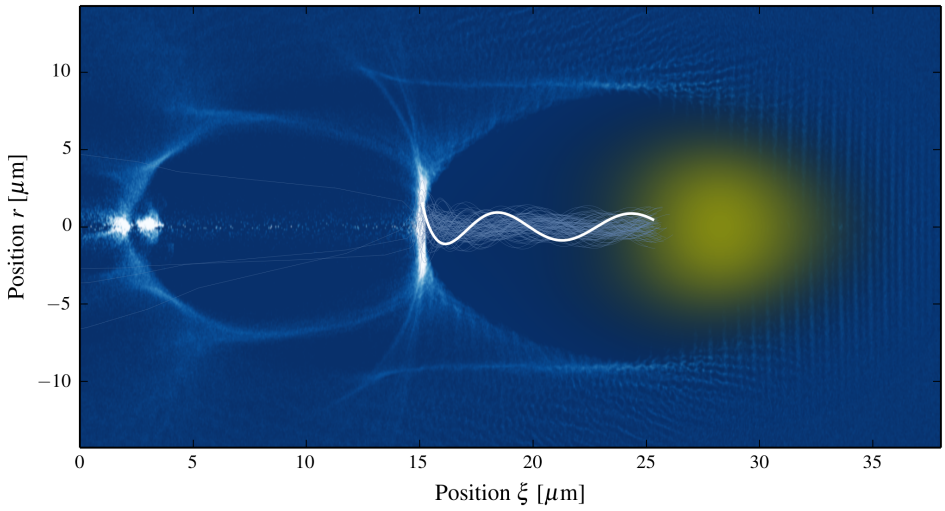

Figure 5.24 – Illustration of betatron oscillations, from a test particle simulation with 100 particles. The betatron wavelength visibly increases as electrons gain energy while they advance inside the ion cavity. Also visible, but less pronounced, is the damping of the oscillation amplitude, which scales as $r_\beta \propto \gamma^{-1/4}$.

5.5 Betatron radiation

In **Chapter 4: Beam Transport** we have discussed how a short plasma lens can be used to collimate the beam. We observed that if the density length product of the plasma is sufficiently large, the electron beam reached focus within the plasma itself. Increasing the transverse field strength further reduces the focal length and ultimately the electron beam starts to undergo betatron oscillations. Therefore the regime of betatron oscillations can be seen as an extension of the plasma lens theory we have already developed in the preceding chapter.

So it is no surprise that shortly after the plasma lens had been conceived, proposals were made to use the transverse oscillations in order to create a radiation source. However the ion-channel laser, ion-ripple laser, etc. which were proposed at the time aimed for an FEL-like operation, with unrealistic requirements on the beam emittance in order to achieve lasing.

The wiggler regime has much more relaxed requirements and broadband synchrotron radiation was measured for the first time in 2002 in a beam-driven wakefield [186]. The setup was very similar to the original plasma lens setup, with the main differences that SLAC managed in the meantime to compress their beam further and to increase the plasma length. Shortly after this *betatron radiation* was also observed in laser-driven wakefield accelerators [187, 188]. This spawned new interest in the source and the synchrotron formalism, as presented before, was adapted for the new betatron source [189, 190].

In the first decade after the discovery of betatron radiation in laser-plasma accelerators many efforts were dedicated to the full characterization of the source and its brightness [158, 191]. While such properties can be directly retrieved from Particle-In-Cell simulations with radiation post-processing, the experimental verification is much more elaborated. The source size (some microns) has been measured using knife-edge techniques [192]. An experimental upper limit on the betatron pulse duration was set using the solid-liquid phase transition in indium antimonide as Bragg switch. This experiment showed that the betatron radiation has certainly a sub-picosecond duration, with a best fit found at ~ 100 fs [193]. The temperature of betatron radiation is often estimated using X-ray filters, supposing that the spectrum is synchrotron-like. This assumption was later verified with photon counting techniques [194]. Combining all those measurements it was shown that the betatron source has a competitive brightness, with peak values as high as 10^{22} photons / (second mrad^2 mm^2 0.1% bandwidth) being reported [195].

It is important to underline that the properties of betatron radiation depend entirely on the electron beam and the transverse wakefields. So on one hand betatron radiation can be used as non-interfering diagnostic of the laser-plasma accelerator, see e.g. [196, 197, 115].

But on the other hand this means that the betatron source is directly related to the performance of the laser-plasma accelerator. For betatron radiation this is even more important than for other radiation sources (Compton, Bremsstrahlung, etc), as up to now, the betatron oscillations could not be influenced without affecting the accelerator itself.

5.5.1 Basic properties and scalings

Let us now discuss some basic properties of betatron radiation in laser wakefield accelerators. The deflection parameter for betatron oscillations in a 100-200 MeV laser wakefield accelerator is typically of the order of $K = \gamma k_\beta r_\beta \sim 10$. This is clearly the Wiggler limit, hence the emitted radiation is incoherent and broadband. We have introduced all necessary physics in sections 4.2 and 5.2, which we can now readily apply to describe the source.

Photon energy

We have already derived an expression for the critical frequency emitted in a Wiggler (5.32), which we can now combine with our definition of the fundamental betatron wavelength (5.22c) into

$$\omega_c = \frac{3}{2} K \gamma^2 \omega_\beta = \frac{3}{2^{3/2}} K \gamma^{3/2} \omega_p \propto \frac{r_0}{\lambda_p^2} \gamma^{7/4} \propto r_0 n_0 \gamma^{7/4}. \tag{5.42}$$

So we see that due to the wavelength lengthening and amplitude reduction, betatron emission scales much weaker with beam energy than other synchrotron sources. Furthermore, we have seen that the maximum electron energy in a LPA is limited by the dephasing between the

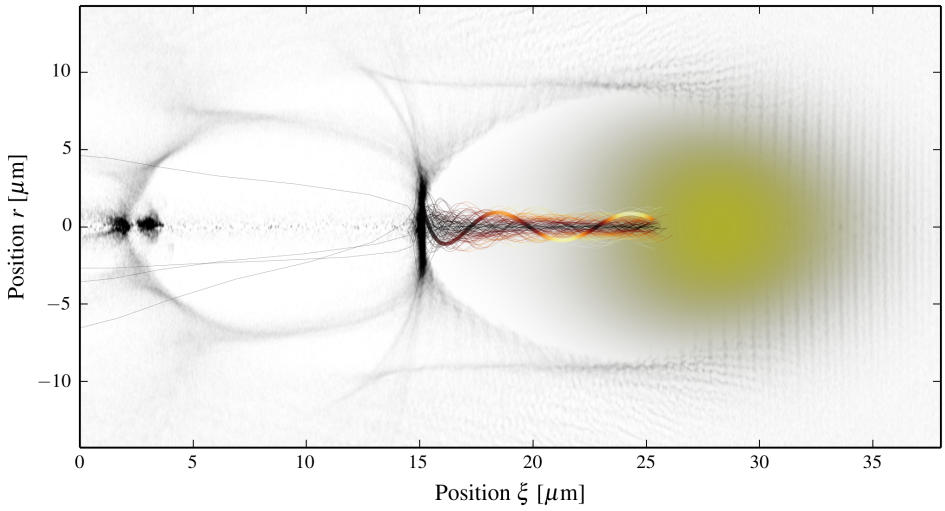

Figure 5.25 – The same electrons as in Fig.5.24, but now their trajectory is color-coded with the momentarily emitted power $P_\perp \propto \gamma^2 \left(\frac{d\vec{p}_\perp}{dt}\right)^2$. It is clearly visible that the electrons emit the most in the turning point and at highest energies.

electron bunch and the laser pulse, which scales with n_e^{-1}. If we take this into account, the betatron oscillation length scales with $\lambda_\beta \propto \gamma^{-1}$, counteracting the γ^2 upshift. For example, in a recent experiment acceleration up to 2 GeV in a $4.8 \times 10^{17}\mathrm{cm}^{-3}$ has been reported [198], which corresponds to a betatron oscillation length of about 4 mm. In this experiment betatron emission peaked at 25 keV, which is roughly 10 times the energy typically observed in a 200 MeV LPA.

Again, most applications of incoherent X-ray sources requires photon energies between $\sim 10-100$ keV, so it is important to find other ways to increase the betatron energy. For instance, the spectrum can also be shifted to higher energies by increasing the amplitude or the density, cf. Sec.5.5.3.

Photon number, divergence and polarization

We can estimate the emitted photon number per period and electron from the emitted power (5.40), by using an average photon energy of the synchrotron spectrum $\langle\hbar\omega\rangle \simeq 0.3\hbar\omega_c$, which yields

$$N_\gamma \simeq 3.31 \times 10^{-2} K. \tag{5.43}$$

For typical parameters we find that N_γ per electron is of the order of unity. So for a beam charge of ~ 100 pC (which corresponds to 6.2×10^9 electrons), we expect a photon number in the order 10^{8-9}.

Being a Wiggler-type source, the beam is emitted within an angle $\sim K/\gamma$. However, there is a fundamental difference between a magnet wiggler and a plasma wiggler: In conventional insertion devices oscillations occur only in the dipole plane. But the transverse wakefields act radially and isotropically, so the betatron oscillations have no preferred plane of oscillation. Instead, betatron radiation from self-injected beams is usually a superposition of randomly polarized emissions and the exact shape depends on the electron trajectory [199]. Additionally, in three dimensions electrons can also carry angular momentum [200], which can lead to donut-like emission.

5.5.2 Stable, polarized betatron radiation from ionization injected beams

A principal drawback of betatron radiation from self-injected beams is that the X-ray signal fluctuates as much, if not more, as the electron beam. In order to reach better stability it is therefore desirable to use a controlled injection mechanism. Of those that we have discussed in **Chapter 2: Injection** , ionization injection in gas mixtures is the most favorable, as it provides stable highly charged beams in the range of some hundred MeV. For this application it is no problem that the electron spectrum from this injector is maxwellian, as the betatron emission itself is broadband, too.

A peculiarity of ionization injection - beyond its stability - is that is can lead to the production of polarized radiation, which we are going to discuss in the following.

Electron orbits during ionization injection

As discussed in detail in **Chapter 2: Injection** , the key principle of ionization injection is the create an asymmetry between accelerating and decelerating longitudinal wakefields, giving the electron the possibility to gain net energy from the wake, which results in injection successively. The source of the asymmetry is late ionization of higher ionization states, which occurs close to the laser pulse's peak. However, the electrons liberated from this process do not only experience unbalanced longitudinal wakefields, but are also able to gain net transverse energy from the laser itself. As a result ionization injected beams can have a preferential plane of motion along with the laser polarization [74]. However, this behavior is not always observed, so we need to discuss the mechanism behind this unbalance in the momentum distribution.

We recall from earlier that tunneling ionization increases exponentially with the field strength

$$W \propto \exp\left(-\frac{4\zeta_i}{3\gamma}\right) = \exp\left(-\frac{2\omega(2\zeta_i)^{3/2}}{E}\right) \tag{5.44}$$

where ω is the laser frequency, γ is the Keldysh parameter and ζ is the ionization potential. Please note that though we have the convention to measure the electric field in units of the normalized vector potential a_0, we have to bare in mind that the electric field and the vector potential are phase shifted, $E(t) = -c^{-1}\partial_t a(t)$. An immediate implication is that ionization

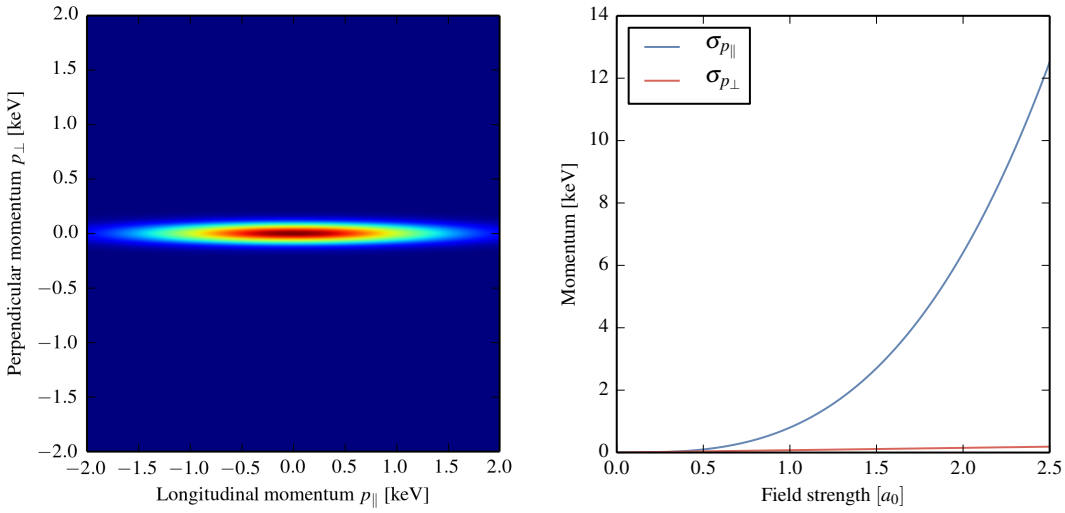

Figure 5.26 – Left: Initial momentum distribution after ionization according to (5.45). Calculated for N^{6+} with an ionization energy $\xi = 552$ keV with a pulse of peak field strength $a_0 = 1.2$. Right: Width of the momentum distributions for different laser field strengths.

peaks at the minimal vector potential, so the majority of electrons is ionized at rest. According to [201] the tunneling ionization rate by a linearly polarized pulse for a fixed momentum value is given by

$$W = W(0)\exp\left(-\frac{2\zeta_i\gamma^3}{3\omega}p_\parallel^2 - \frac{\gamma}{\omega}p_\perp^2\right) \tag{5.45}$$

This relation is visualized in Fig.5.26. We see that the electron distribution is essentially polarized in direction of polarization $p_\parallel$, yet the momenta are only some keV. However, there are more mechanisms through which electrons gain potential energy. Let us first consider the ionization region.

For a laser with a gaussian intensity profile, we can estimate that electrons are isotropically ionized within a radius of

$$r_{\text{ion}} \sim w\sqrt{\log\frac{a_0}{a_T}}, \tag{5.46}$$

where we define a_T as the threshold field strength and w the rms width of the pulse. The value of a_T is chosen in a way that describes onset of significant ionization, e.g. $W(a_T) = 0.01\text{fs}^{-1}$. As seen in Sec.4.2.2, the potential energy in an ion cavity is $\Phi = k_p^2 r^2/4$, so the transverse fields inside the ion cavity convert this spatial distribution into a momentum distribution with a width of about $p_\perp \sim (k_p r_{\text{ion}}/2)^2$. So the momentum gain depends on the ionization radius and the plasma density. For instance, an electron born at $r_{\text{ion}} = 1\mu\text{m}$ in a plasma of density $n_e = 1.5\times10^{19}\text{cm}^{-3}$ gains potential energy of ~ 100 keV. This value rapidly increases with the ionization radius.

The third mechanism is the ponderomotive motion of electrons. As its interplay with the above phenomena is not straightforward, we performed 3D test particle simulations. We include transverse and longitudinal laser field components [202] and a recoil term for the ion cavity. As expected we find that the final momentum distribution depends on ionization region. Electrons born close to the axis have a polarization degree similar to Fig.5.26, but with increasing ionization radius the momentum ratio $\sigma_{p_\parallel}/\sigma_{p_\perp}$ approaches one, resulting in an isotropic distribution.

In a laser-plasma accelerator it is not only important where electrons are ionized, but also whether they are trapped. To get a better insight in this we performed Particle-in-Cell simulations with CALDER-CIRC. The plasma is formed of a mixture of 99% Helium and 1% Nitrogen. The driver is a 30 femtosecond pulse focused 12μm waist with a peak potential $a_0 = 1.2$. It is found that electrons trapped are born close the laser axis and their orbits depend essentially on their initial position and the laser phase at ionization, cf.Fig.5.27. As found in the test particle simulations, the injected electron beam oscillates preferentially in the plane of polarization.

In conclusion, electrons that are ionization injected and trapped close to the laser axis can gain significant momentum in the direction of polarization due to the ponderomotive force. However, for electrons born far from the axis the isotropic wakefield potential dominates and the polarization ratio approaches $\sigma_{p_\parallel}/\sigma_{p_\perp} \sim 1$.

Experimental setup

The experiment was performed with the Salle Jaune laser, whose 28 femtosecond pulses were focused using an off-axis parabola to a waist of 18 μm. Containing 55% of the total laser energy, an energy of 1.2 Joule was delivered on target, resulting in an intensity of $3.5 \times 10^{18}\mathrm{W/cm^2}$ or $a_0 = 1.2$. The laser polarization is adjusted using a $\lambda/2$ plate.

A supersonic nozzle of 3 mm diameter is mounted on a parker series 9 gas valve, connected to a reservoir of 99% Helium and 1% Nitrogen. The electron spectrum is measured by deflection in a permanent magnet (1.1 T over 10 cm). X-ray are detected either on a scintillator coupled to a low-noise 16-bit CCD (Roper QuadRO) or directly on an X-ray CCD (Princeton Pixis).

Betatron polarization

Electrons were injected via ionization injection, leading to about 40 pC per shot with a broadband spectrum which extends up to ~ 250 MeV. We find that the FWHM beam divergence is anisotropic, with $\theta_\parallel = 16$ mrad in direction of polarization and $\theta_\perp = 4$ mrad in perpendicular direction.

A similar behavior is found for the X-ray signal, whose FWHM divergence is $\Theta_\parallel = 24 \pm 1$ mrad and $\Theta_\perp = 10 \pm 1$ mrad. In order to verify that the electron and X-ray polarizations are a result

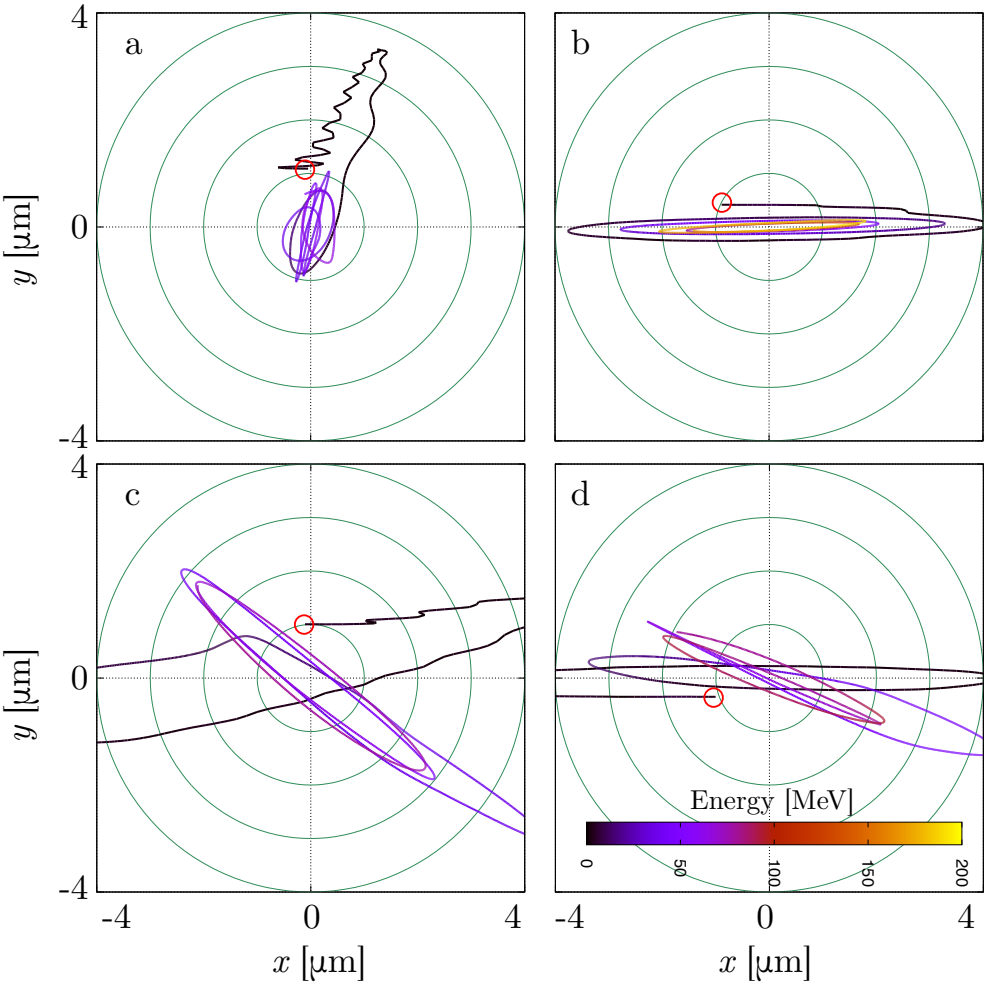

Figure 5.27 – CALDER-CIRC simulation of electron orbits from ionization injection (laser polarized along x). (a) the electron experiences a ponderomotive drift away from the beam center and performs weak oscillations in x direction. However, it then drifts back to the center due to the longitudinal ponderomotive force, resulting an elliptical orbit at weak amplitude. (b)-(d) electron is in phase with the ponderomotive force, resulting in an amplification of the oscillation. Electrons perform strong oscillations in the plane of polarization.

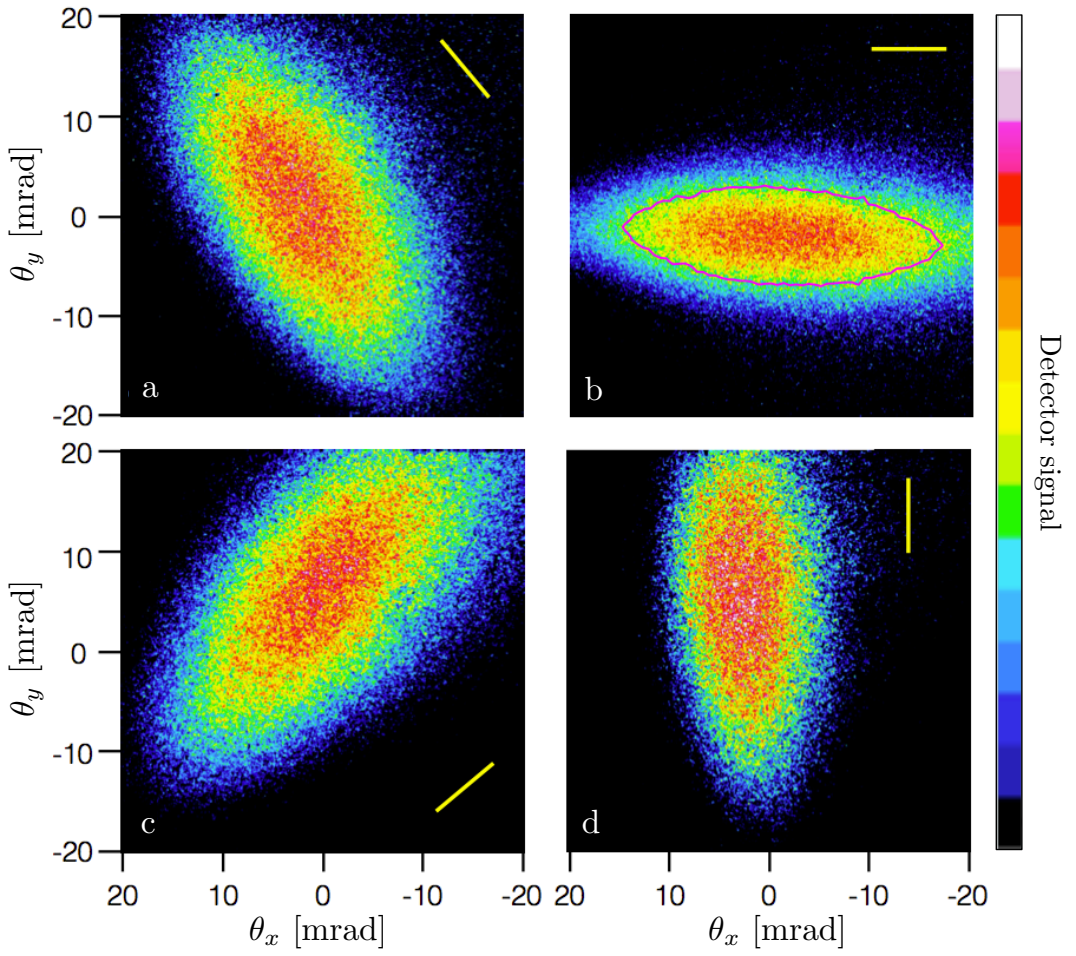

Figure 5.28 – Betatron x-ray beam profiles measured for four orientation of the laser polarization. The laser polarization axis is indicated by the yellow line. The line in figure (b) represents the FWHM contour of the beam profile obtained from the test particle simulation.

of the laser polarization, we have turned the laser polarization. The X-ray signal followed accordingly, as shown in Fig.5.28.

Apart from the apparent ellipticity of the beam in Fig.5.28 we also measured the source size ratio to be 3:1, with a source size of 5 ± 1 micron in polarization direction. These values could be reproduced in test particle simulations, where the radiation emission is calculated according to (5.17b). In simulations we find a polarization degree $D_p = 80 \pm 5$ percent.

Stability of the source

As we have mentioned before, ionization injection provides significantly better beam stability than self-injection. Consequently, also the betatron emission sets new standard in terms of pointing stability, divergence, signal level and beam energy.

We have measured the beam energy with two methods. In a first experiment we used a filter-based method. To deduce the spectrum from the x-ray signal through the filters we introduce an adaptive least squares algorithm. For this we start with an initial guess distribution (a flat spectrum) and locally modify the spectrum. If the change decreases the total least squares residual of the correlated filter transmissions it is taken into account, otherwise discarded. The algorithm continues until convergence is reached. The error $\sigma/\sqrt{n}$ is estimated by adding gaussian noise to the measurements and applying the algorithm to the noisy data. For the figure 30000 iterations on the spectrum were performed, while the error is estimated using 100 noisy data sets. The estimated spectrum agrees significantly better with the data than a usual least-squares fit with only the critical energy as free parameter. Note that we can only reconstruct the spectrum of X-ray that passes the X-ray window. The spectrum obtained using this method is presented on Figure 5.29c.

In a second experiment we measured the beam energy using photon counting, with the camera placed 8.5 meters away from the source. The measured spectrum over 60 consecutive shots has a similar temperature of $E_c = 6.7 \pm 0.5$ keV, which is comparable to pure Helium ($E_c = 6.5$ keV). For a series of 50 consecutive shots we measured that the center is stable within a standard deviation of 1 mrad and the signal maximum varies by 15 percent.

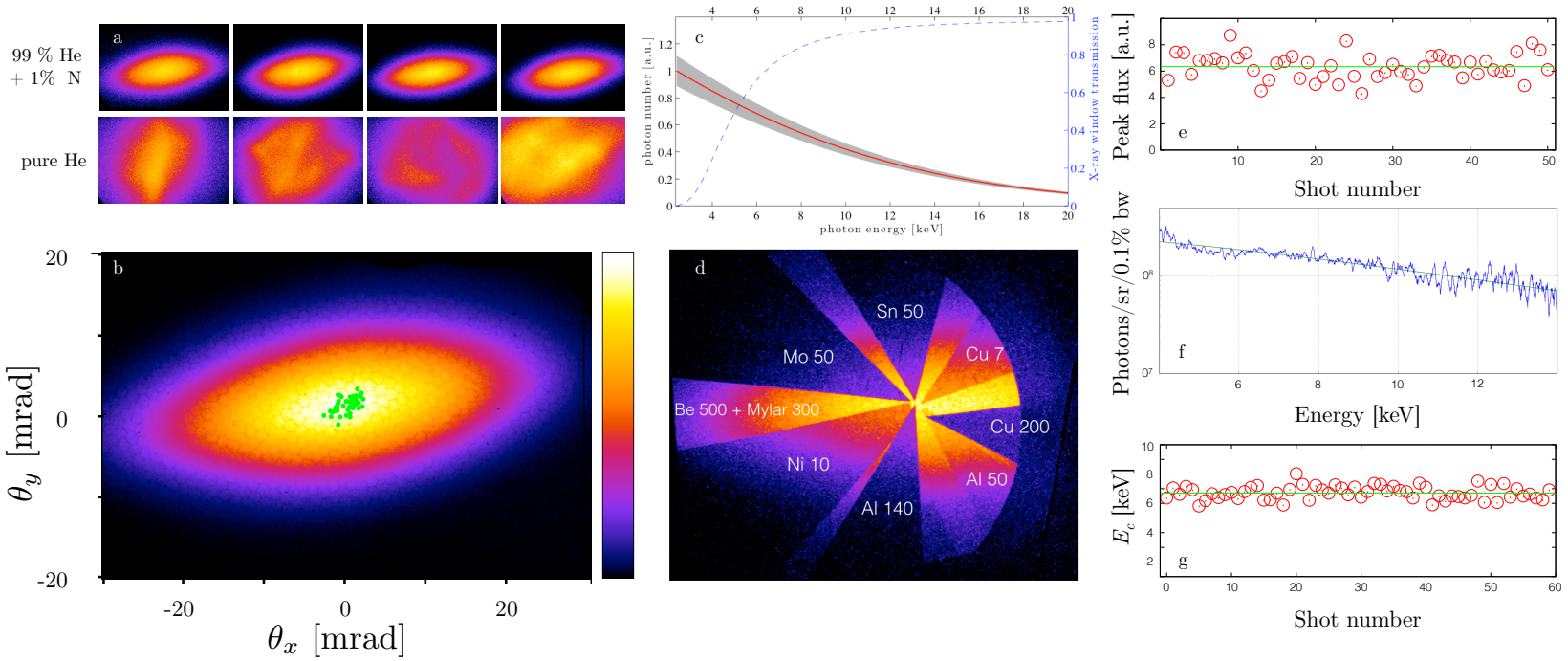

Figure 5.29 – Collage of the experimenal results on betatron radiation with ionization injection. (a) shows consecutive shots either in the gas mixture or in pure helium. (b) is the sum of 50 consecutive shots, with the center of mass of each shot marked as green dot. (c) shows the estimated spectrum from the filter transmission ratios in (d). (e) shows the flux fluctuations for 50 shots. (f) shows a typical photon spectrum as measured form photon counting, with a synchrotron spectrum fitted in green. The spectral stability is shown in (g) where the synchrotron fits for 60 consecutive shots are plotted.

5.5.3 Augmentation of betatron radiation in tailored plasma density profiles

We have seen before that the betatron emission depends on the electron beam energy, the transverse oscillation amplitude, the oscillation length and the number of oscillations performed by the radiating electron. It has been proposed to manipulate these parameters by appropriate tailoring of the plasma density profile [109]. In particular, it is desirable to circumnavigate the weaker energy scaling of betatron radiation by adapting r_β and λ_β.

In **Chapter 3: Acceleration** we have already discussed extensively how density tailoring can be used to augment the beam energy. Furthermore, the bubble lens concept we have introduced in **Chapter 4: Beam Transport** may be used to increase the betatron amplitude, cf. Fig.5.30.

The betatron oscillation length depends on the beam energy and the plasma density, where it is clear that decreasing the beam energy to increase the radius of curvature is counterproductive. However, augmenting the plasma density is a valid option to increase not only the betatron frequency, but also the oscillation number. Yet we have seen in **Chapter 3: Acceleration** that density steps usually trigger self-injection. While additional charge is beneficial to increase the total photon number, this does not provide a path towards higher beam energies.

Over the course of this thesis we have tested a variety of configurations: As injectors we have assessed self-injection, ionization injection in gas mixtures and shock injection; for the density tailoring we used different jets or shocks; we measured X-ray using various scintillators and CCD cameras. All of these experiments have shown to some extent augmented betatron signals compared to a single jet. But as explained above, density tailoring can affect electron beams in many ways and it is crucial to distinguish which process is responsible for the signal increase.

In the following we are going to present in detail the results of two campaigns from 2014 and 2015. The first experiment relied on self-injection, two equally sized gas jets and a scintillator with filters as X-ray detector. In a refined setup we used ionization assisted injection, a smaller 'needle' jet and both scintillators and X-ray CCD cameras.

Experiment I (June 2014)

The experiment was conducted at Laboratoire d'Optique Appliqueé with the 'Salle Jaune' Ti:sapphire laser system, which delivers 1 J/28 fs (FWHM) pulses at a central wavelength of 810 nm and with a linear polarization. The laser was focused with a 100-cm-focal-length off-axis parabola, to a focal spot size of 12 μm (FWHM).

As target we use a system of two helium gas jets. It is found that mounting the jets at an angle of about 135 degrees is optimal to avoid the formation of shock fronts. Furthermore 3D printing technology is used to design nozzles that can be placed as close as possible to each other. Both jets are motorized in order to scan the focus and superposition.

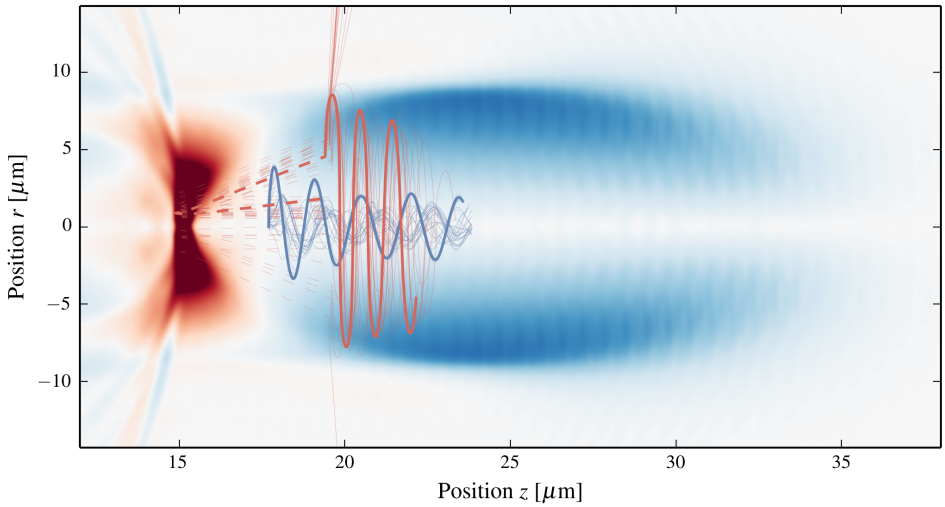

Figure 5.30 – Test particle simulation demonstrating betatron augmentation in density steps via interaction with the rear part of the bubble.

A 800 nm probe beam propagates through the plasma channel in orthogonal direction. The plasma density is characterized using a Nomarski interferometer. The field of view is about 7 mm x 1.6 mm at 8.125 µm resolution. The region of optimal fringe visibility is approximately 3.5 mm. As the plasma channel is close to symmetric around the pump laser propagation axis, we can deduce the local plasma density using an Abel transformation.

In order to measure the energy of the electrons the beam is dispersed by a 10cm 1.1 Tesla permanent bending magnet placed 6 cm behind the gas jet. The electrons are deflected according to their relativistic mass and measured on a phosphor screen (Kodak Lanex) which converts a part of their energy into 546 nm scintillation light. The screen is imaged using a Nikon f1.8/50mm lens mounted on an Andor DV420 16-bit CCD camera. The field of view covers energies from 70 to 600 MeV.

The X-ray signal is measured using another Lanex phsosphor screen, which is imaged onto a 16-bit CCD camera at a resolution of $(0.4\text{mm})^2$. This leads to a radial resolution of $\approx (0.7\text{mrad})^2$, while the field of view is about $105 \times 88\ (\text{mrad})^2$. The screen is protected from laser light by 26 microns Aluminum, absorbing almost all radiation below 3 keV. The absorption rate of the phosphor is quasi-constant below 20 keV, which makes the signal proportional to the emitted power in the X-ray range that passes the filter. As the beam is only weakly asymmetrical all pixels are grouped according to their distance to the center of gravity of the beam. The resulting radial distribution can be well described by a normal distribution. This is used to estimate the total X-ray signal of beams exceeding the field of view due to their divergence.

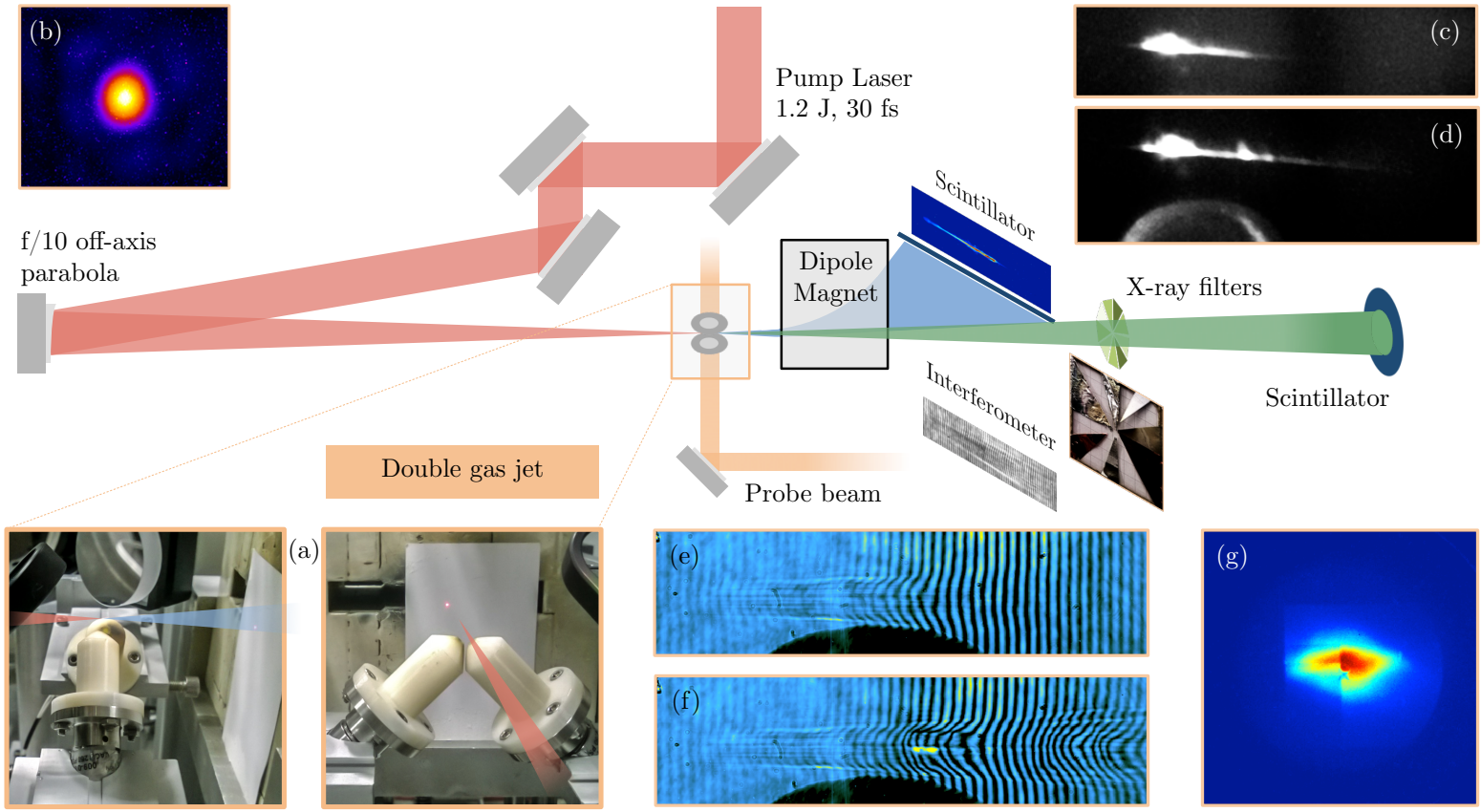

Figure 5.31 – Experimental setup for betatron radiation in tailored density profiles. The double gas jet used in the experiment is shown in (a). This setup at 90° was later replaced in the second experiment for a configuration at 135°. Fig.(c/e) shows top view and side view images without the second jet, (d/f) are with the second jet actived. X-ray filters are placed in front of a scintillating screen. Different filter sets were used in the experiments, a sample image is shown in (g).

The X-ray energy is estimated using Aluminium filters. For each filter pixel an algorithm compares the signal level to the local mean of unperturbed X-ray, leading to a local filter transmission ratio. In the case of betatron radiation it has been shown by photon-counting techniques that the spectrum is synchrotron-like [194]. Assuming that the spectral shape resembles the on-axis intensity distribution $d^2I/d\omega d\Omega \propto (E/E_{crit})^2 K_{2/3}(E/E_c)^2$ (where $K_{2/3}$ is a modified Bessel function of second kind), we can define a unique temperature E_c for each pixel.

Results

In this proof-of-principle experiment we create a density step using two independent gas jets. The first jet serves as usual LPA, operated in the transverse self-injection regime [62, 64, 63]. This permits to produce electron beams of rather high charge while containing some quasi-monoenergetic features. At the end of the LPA stage electron beams have a total charge of $\sim 108 \pm 26$ pC and $\sim 140 \pm 40$ MeV mean energy. The second jet is placed in the rear part of the first jet. In the region where the two gas flows meet the density rapidly increases. If the second jet is placed far inwards a shock front forms that disturbs the electron propagation. Far outwards a plateau at initial density n_0 is formed. Between these two cases a region of high density n_1 is created. As shown in Fig.5.32 the electron beam spectrum does not change significantly as we turn on the second stage, while the charge between 100 and 200 MeV increases slightly. Note that even individual shots may show quasi-monoenergetic features, the unstable nature of transverse self-injection leads to a maxwellian-like mean spectrum. Importantly, the charge augments only weakly. This means that even if there seems to be some reinjection of electrons in the second jet, the contribution to the total charge is only about one tenth. We also tested for reinjection in the second jet separately by reducing the backing pressure of the first gas jet below the self-injection threshold.

While the spectrum and charge remain similar for both cases, the electron beam divergence increases significantly. Also there is with no doubt a strong influence on the X-ray emission. As shown in Fig.5.33, activating the second jet leads an increase of the peak X-ray signal by a factor of 3-5, while the X-ray divergence augments from 28 ± 2 mrad to around 38 ± 5 mrad. From this we estimate that the total X-ray signal increases by up to an order of magnitude.

To understand which process is responsible for the gain we use X-ray filters to estimate the X-ray temperature, under the assumption that the spectrum is synchrotron-like. The results are represented in two histograms of 20 and 24 shots, respectively (Fig.5.34). First, it is clear that with the second jet much higher signal levels are obtained. But also, the energies we estimate for these pixels tend to increase, the spectrum gets hotter. Note that the algorithm sometimes estimates very high beam energies. At low signal level this is usually due to noise issues. This can be especially an issue if we try to assign a single X-ray temperature to the spectrum. The histogram representation at hand is less sensitive to such noise and beam energies around $2-7$ and $3-12$ keV are measured. We estimate that the critical energy on axis

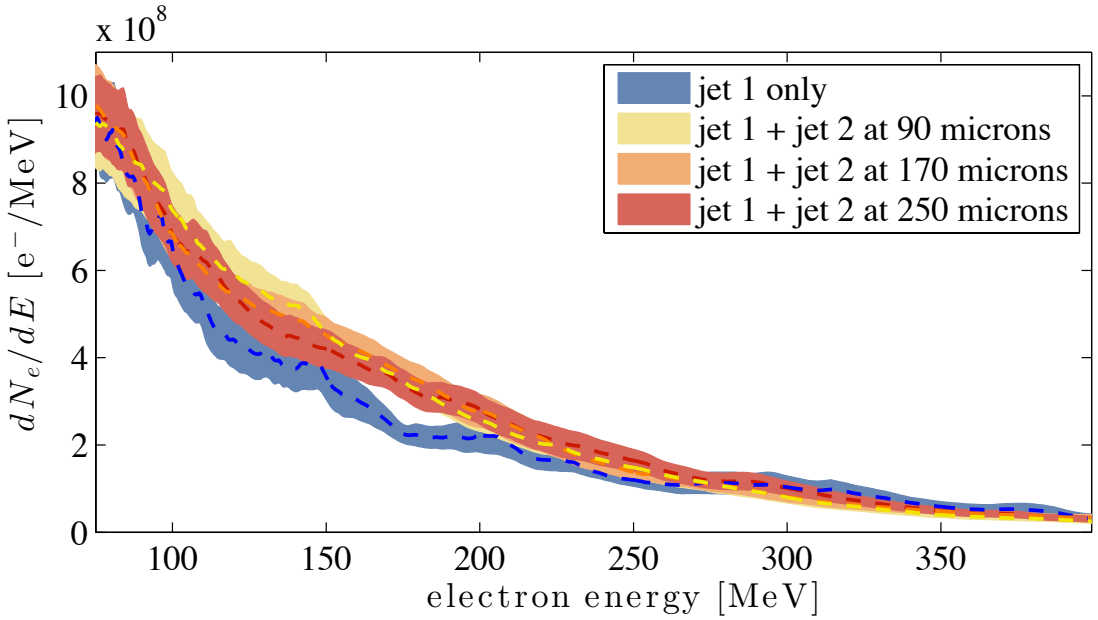

Figure 5.32 – (a)Average electron spectrum with only accelerating stage (blue, 17 shots) and with wiggler stage (90 shots binned into three positions with 30 shots each). Shaded curves correspond to the standard error $\sigma/\sqrt{n}$. With the second jet the total charge increases by 11-13 percent, depending on the position. The distance is measured moving inwards of the first jet.

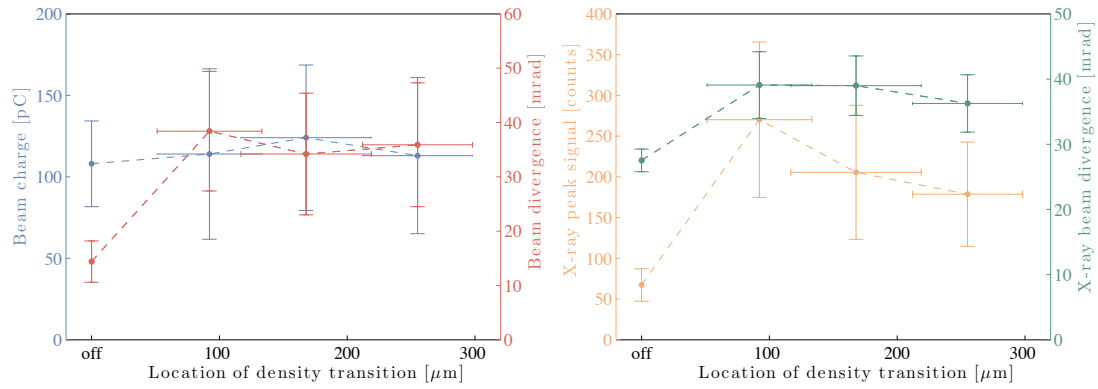

Figure 5.33 – Electron beam charge and divergence vs. X-ray beam peak signal and divergence for only jet 1 and for jet 1 and 2 at the three different positions from Fig.5.32. While the electron beam charge does not change beyond the errors, the beam divergence increases significantly. This behavior is inherited, though weaker, by the X-ray beam. Remarkably the peak signal level augments by more than four times when the second jet is turned on. Thus the total X-ray signal, which is estimated as the peak signal times the divergence squared, increases by about an order of magnitude.

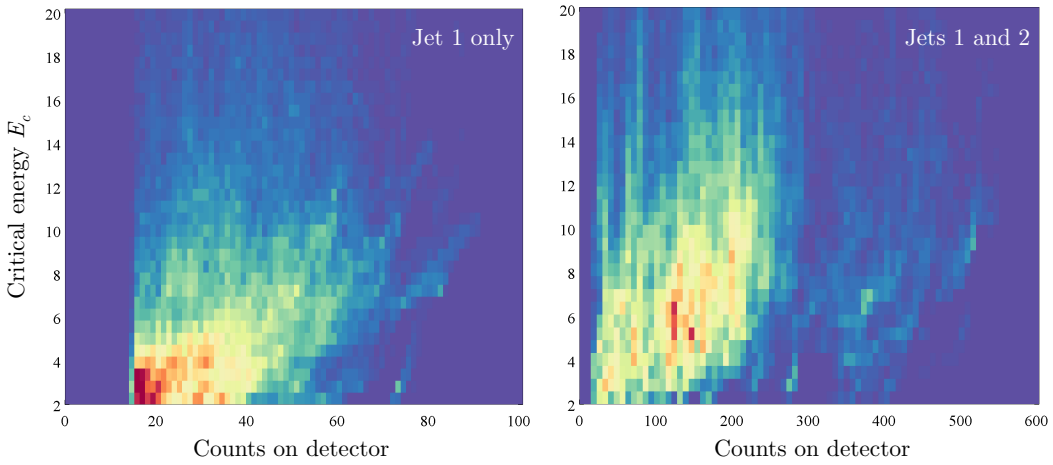

Figure 5.34 – Filter-based energy estimation. All filter pixel are used as separate detector for which the critical energy is estimated using filter transmission ratios for synchrotron-type spectra. The local signal level is estimated from the surrounding filter-free regions. Pixel with less than 15 counts are ignored due to noise issues. The plot shows the histogram of signal versus energy for 24 shots with only jet 1 and 20 shots with both jets, giving a total dataset of ~ 30000 events each. We see a clear tendency that the spectrum is hotter the stronger the signal level.

increases from ~ 9 to 12 keV. In a radial representation of the data it is also observed that the spectrum cools down angularly.

To conclude, we have observed augmented X-ray production in a two-stage gas jet configuration. While we observe little influence on the electrons' spectral distribution, the higher plasma density in the superposition region ($n_1 \approx 1.8 \times 10^{19}\mathrm{cm}^{-3}$ vs $n_0 \approx 1.0 \times 10^{19}\mathrm{cm}^{-3}$) leads to a measurable increase of electron beam divergence as well as X-ray energy and divergence. We estimate that the emitted power increases by over an order of magnitude.

Experiment II (June 2015)

While the experiment from the preceding section showed clear indications of increased betatron yield in a two-jet configuration, there remained several uncertainties: In post-processing we found that very divergent electron beams were partly clipped by the magnet spectrometer, whereby we might not have collected the entire beam charge; furthermore the X-ray filter set was not optimal chosen and did not allow quantitative beam energy measurement; and last, with both jets having a size of ~ 3 mm, there always remains uncertainty for the electron dynamics throughout the second jet.

However, the strong increase of beam divergence indicates that the signal yield might be related to the bubble lens effect we introduced in Sec.4.5. We therefore sought after a unambiguous demonstration of the concept. Such became possible when we started to use the small diameter 'needle' jet for rephasing experiments, cf. Sec.3.4.6.

In **Chapter 4: Beam Transport** we have discussed how the beam divergence increased when a density step was introduced. In this section we are going to discuss the same experiment from the point of view of X-ray emission.

To recall, in this experiment electron injection relied on ionization injection in a 95:5 Helium-Nitrogen mixture. A density ramp was created using a small needle jet, placed close to the exit and the laser axis.

We found that the second jet had weak influence on the beam charge and the average electron energy was reduced. However, we also observed that the beam divergence was greatly increased, by up to 6 times the initial value. The results of a series of 60 shots (10 each for only one jet and 5 positions of the second jet) are summarized in Fig.4.18.

We measured the X-ray signal for the same shots by indirect detection on a Princeton Instruments Quad-Ro camera. Placed at 80 cm from the source we obtain a field of view of about 60×60 mrad^2, which is however reduced by a circular flange around the 100 microns mylar window at the chamber exit. The average beam profiles for each scan position are shown in Fig.5.36. As for the self-injection experiment from the preceding section, we find again that a second jet has a strong impact on the X-ray yield. Note that while the first experiment covered only a scan range of less than 200 microns, the position scan in this experiment goes over more than a millimeter and we see the signal both rising and falling again.

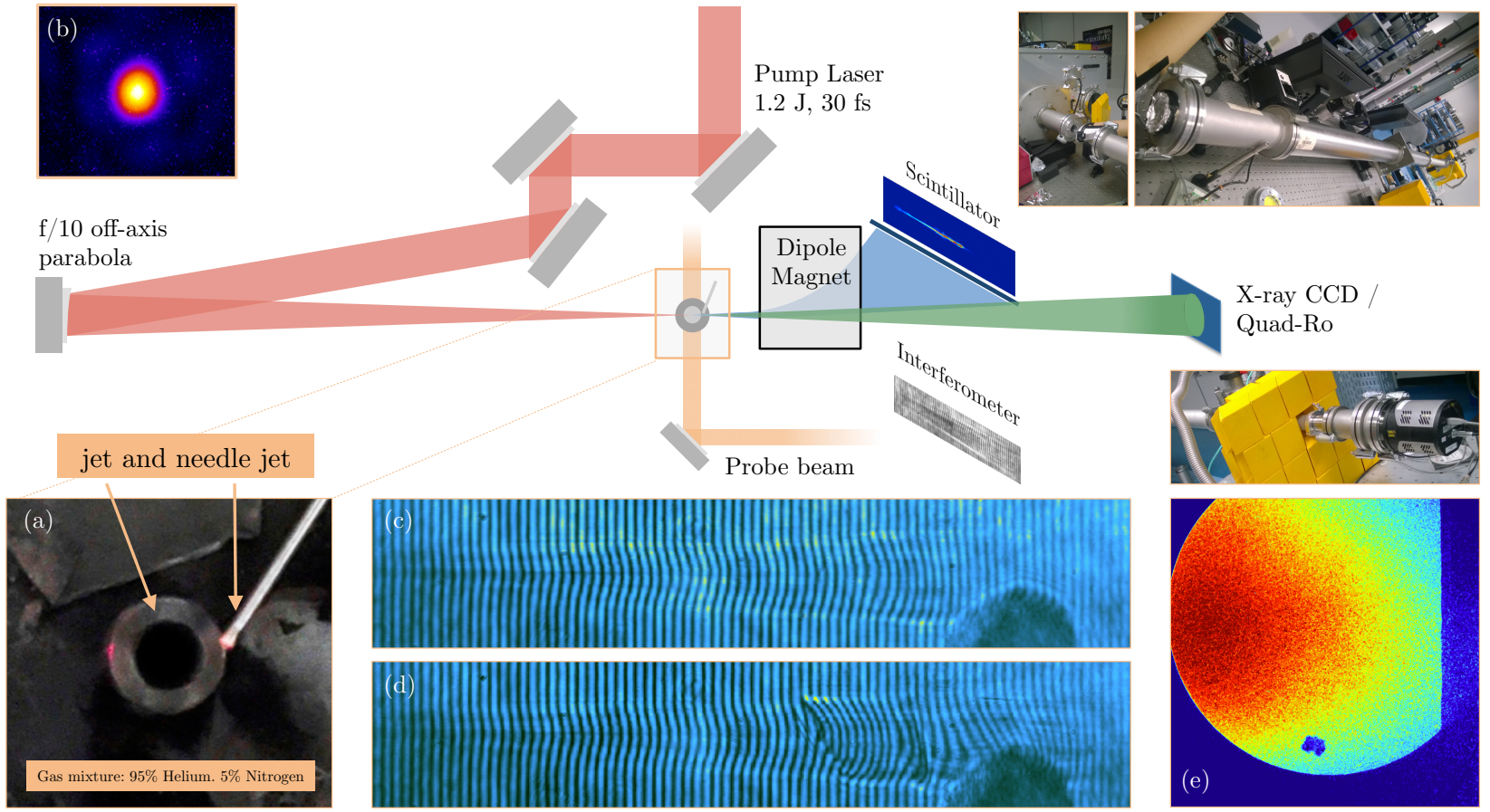

Figure 5.35 – Setup pf experiment II on betatron radiation in tailored density profiles. This time we use a normal gas jet together with a small 'needle' jet, both connected to a reservoir of 95% Helium and 5% Nitrogen. Sample interferometry images without (c) and with the second jet (d) are shown. X-ray are both measured with a Princeton Instruments Quad-Ro fiber coupled to a scintillator - sample picture shown in (e) - and an X-ray CCD camera, placed at variable distance from target in photon counting mode.

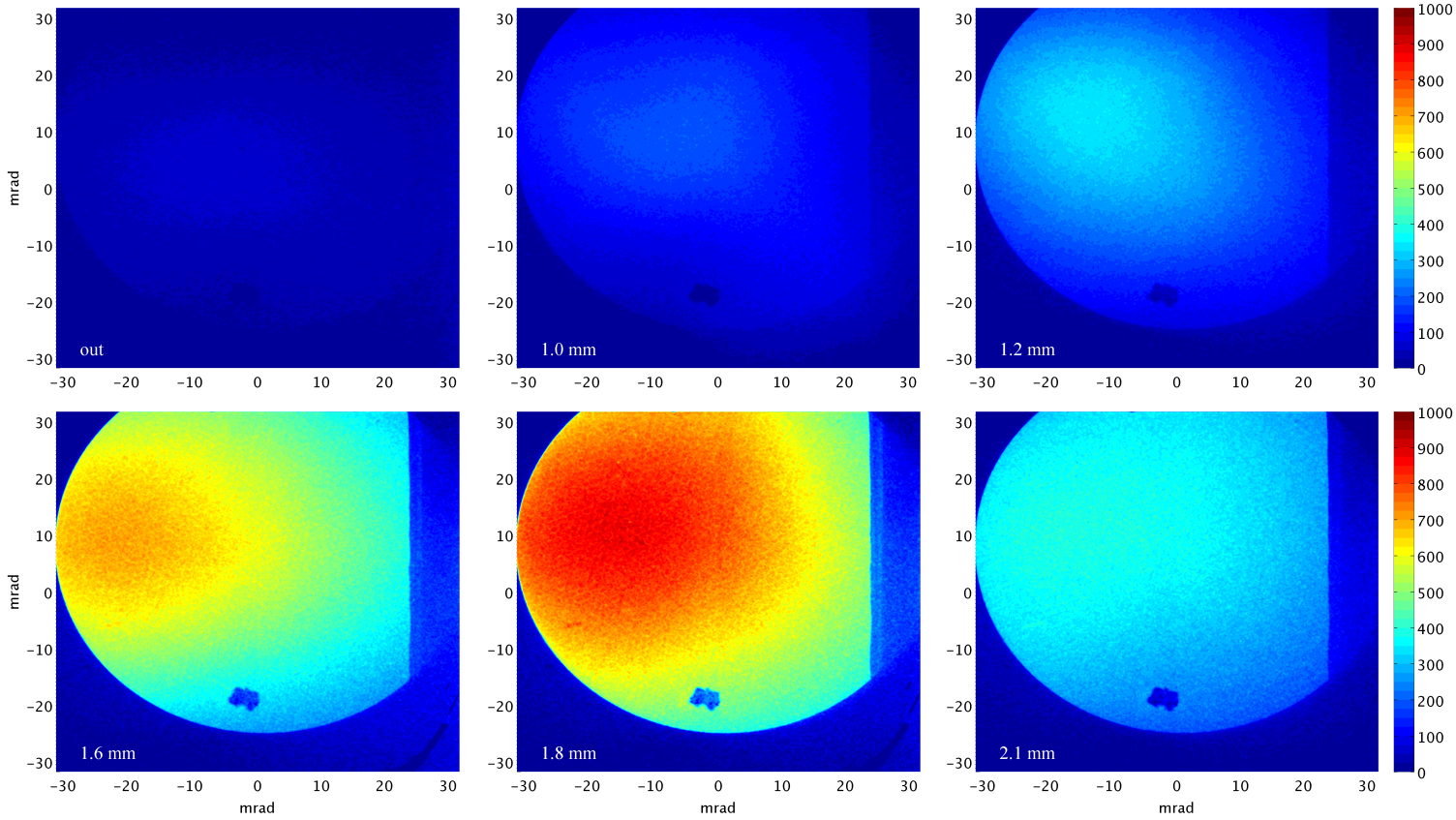

Figure 5.36 – Average X-ray beam profiles (10 shots each) for the position scan from Sec.4.5.2. The peak signal increases by more than an order of magnitude from 60 ± 5 counts to 870 ± 20 with the density transition at 1.8 mm. The average beam profile with only one jet ('out') is asymmetric, with an FWHM divergence of ~ 60 mrad along polarization vs. 30 mrad perpendicular to it. With the second jet the profiles become more symmetric and with increasing distance we measure 40, 60, 70, 80, 90 and 80 mrad along the mayor axis.

We find that the noise-subtracted signal augments from a peak value of 60 ± 5 counts up to a maximum of 870 ± 20 when the density transition is located 1.8 mm after the jet entrance. At the same time the beam divergence augments to 90 mrad. As we are again using a Gadox screen as detector, the total signal should be approximately proportional to the emitted power. Unfortunately we were not able to collect the whole beam, but we can estimate that the emitted power increases by 20 (field of view) to 60 (extrapolated) times. This is well above anything that could be explained by charge fluctuations and suchlike, indicating that we have indeed managed to influence the electron trajectories.

This is supported when we look at single shots from the series. Figure 5.37 shows two shots, one without a second jet and one at the optimal position 1.8 mm. Here we see clearly how both electron and X-ray properties change: While the beam on the left is well collimated and weakly radiating, the beam on the right is much more divergent and the radiated power is significantly higher.

We also measured the radiation spectrum in this configuration using an X-ray CCD camera in photon counting mode. The measurement reproduces our estimations on the increase of emitted photons. However, contrary to our expectations the temperature of the spectrum increases only weakly, by 10-30 percent. An example, for one jet solely and with the second jet at 1.6 mm, is shown in the lower frame of Fig.5.37.

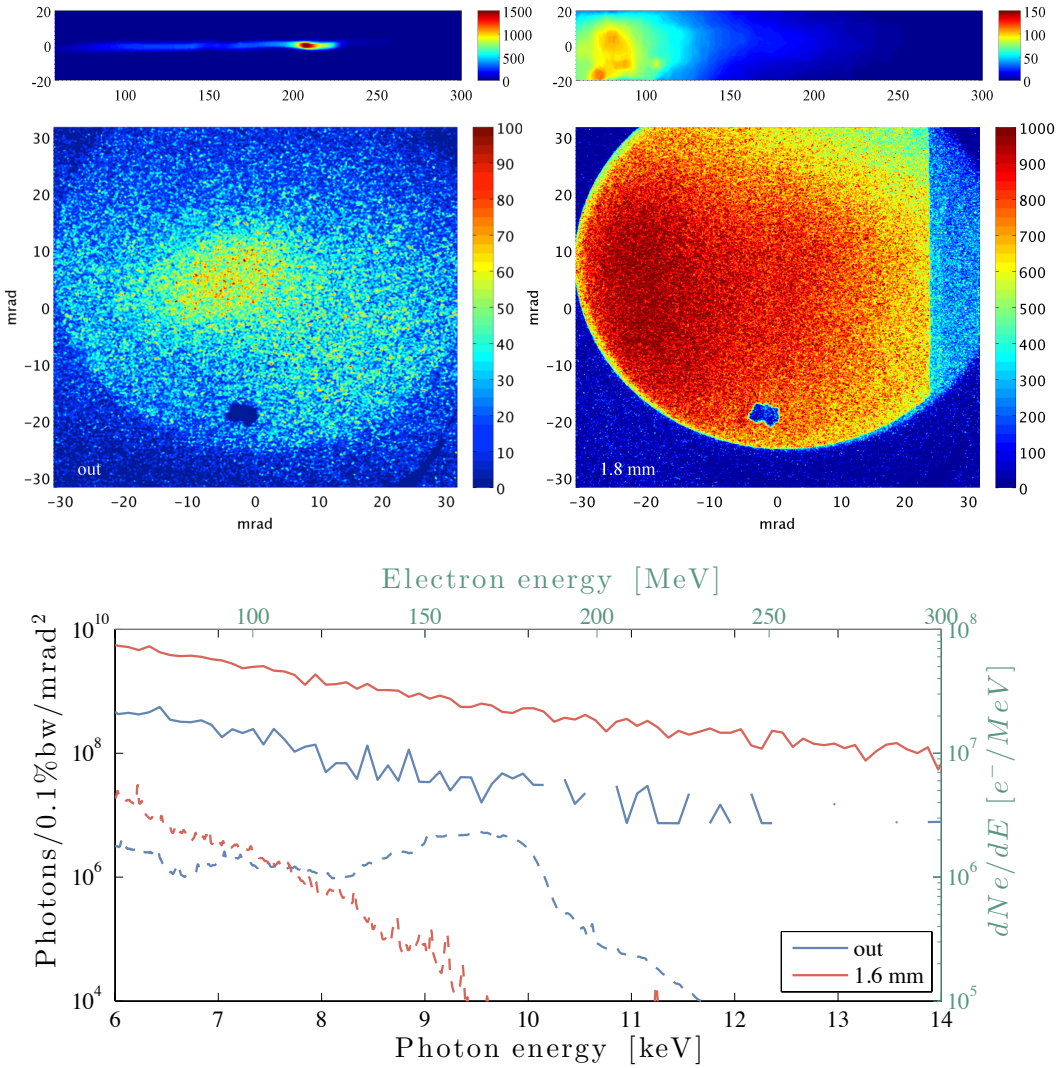

Figure 5.37 – Upper part: Representative single shot images for the scan shown in Figures 4.18 and 5.36. The beams on the left were measured with only one jet active. The electron beam has a charge of 33.5 pC, with a quasi-monoenergetic feature at 207 MeV, containing ~ 7 pC charge. The beam divergence is about 4 mrad. The beam on the right was obtained with the second jet active. The beam contains an integrated charge of 46.7 pC at a divergence of ~ 41 mrad. Though both beams have comparable charge, the X-ray signal from the second beam is much stronger, note the different colorscales for each frame.
Lower part: Photon spectra (solid lines) and angularly integrated electron spectra (dashed). Both beams have comparable charge (36.5 vs 26.5 pC), while the divergence is very different (3.4 vs 26.8 mrad). The total photon number is significantly higher for the second case, however the temperature of both spectra rests similar.

5.6 Conclusions and outlook

In this chapter we have applied the different techniques we developed for injection, acceleration and transport in order to optimize X-ray production. As this part concludes the work, we will also review the principal findings of the first chapters and discuss research perspectives that arise from the results of this thesis.

5.6.1 Summary of the results

The aim of the first three stages has been to extend our control over the laser-plasma accelerator. In **Chapter 2: Injection** we have discussed how ionization injection and injection in sharp density transitions can be used to produce electron beams whose stability outperforms common self-injection by far. Using the SALLE JAUNE laser system we measured that ionization injection in high-Z gases provides beams with a stable maxwellian spectrum at tunable charge of up to 1 nC. Shock-injected beams contain less charge, but are monoenergetic and tunable in energy.

Chapter 3: Acceleration was dedicated to extensions of acceleration beyond the limitations set by laser depletion and dephasing. In particular we have discussed how density tailoring can be used to influence the electron phase in a wakefield in a way that allows them to maintain for a longer time in an accelerating phase. While this rephasing allowed us to affect the longitudinal beam dynamics, we also demonstrated schemes for the control of the transverse evolution. In **Chapter 4: Beam Transport** we have demonstrated that a laser-plasma lens can serve as tool for rapid collimation of ultrashort electron beams. Furthermore we have shown that interaction of the electron bunch with the rear part of the ion cavity can defocus the beam, thus increasing its betatron oscillation amplitude.

Such an increase of the oscillation amplitude can significantly increase the X-ray signal, as we have seen in the present **Chapter 5: Radiation** . Another important result has been that beams injected via ionization injection radiate much more stably than found in any preceding experiment. Furthermore, the physics of injection permits to create polarized X-ray beams, which relies on the fact the electrons can directly gain transverse momentum from the laser. This effect is most evident for electrons born close to the laser axis.

We have also made first steps towards applications of X/γ-ray sources, using either bremsstrahlung conversion or Compton backscattering to perform radiographies.

5.6.2 Future prospects

The results described in the preceding section have both immediate and long-term implications. As near-term we consider tasks that directly arise from the project results, but could not be performed yet. Mid-term prospects include future experiments that can be performed based on existing infra-structure or reasonable developments. We conclude with a discussion of long-term perspectives of the field for the next years.

Near-term setup improvements

Many experiments performed in the context of the thesis relied control of the longitudinal density profile. In order to create such tailored density profiles we have used either two gas jets or a supersonic gas jet combined with a blade to create a shock front. Unfortunately neither of these techniques allows us to vary the transition position and the density completely independently. Instead there is always an interplay between the two gas flows or the gas flow and the shock front, respectively. Yet for better control and understanding of all schemes relying on density tailoring it is indispensable to have complete control of those parameters. A first step will therefore be to perform a complete characterization of the ensemble. In our case this would require tomographic density measurements of the source over a wide range of backing pressures and positions.

Most experiments also shared the same diagnostics, consisting of a topview, sideview, electron spectrometer and X-ray detector. Useful additions to this standard setup would be for example to include integrating current transformers (ICTs) to measure the beams charge. Furthermore additional diagnostics for the laser beam would be helpful for many types of experiments, e.g. to get better insight in the laser evolution. We also intend to improve the X/γ detectors. In particular it remains difficult to measure radiation beyond 100 keV, which is why we performed initial tests that measured the response of different scintillating crystals. These could be included into a sensor array to measure high energy γ-ray.

Near and mid-term research prospects

Beyond such immediate improvements to the experimental setup, the results from this thesis can be extended in various ways. In the following we will therefore discuss some examples of experiments that could built up on our results.

One of the principal findings of the thesis is the stable production of betatron radiation using ionization injection. The discovery of this regime is an important step towards more sophisticated applications of femtosecond X-rays, e.g. time-resolved crystallography.

Another important result has been that we can influence the betatron oscillation amplitude via defocusing in at the rear part of the bubble. In fact, changing the amplitude does not only increase the radiation emission, but is also changes the effective velocity at which the electrons

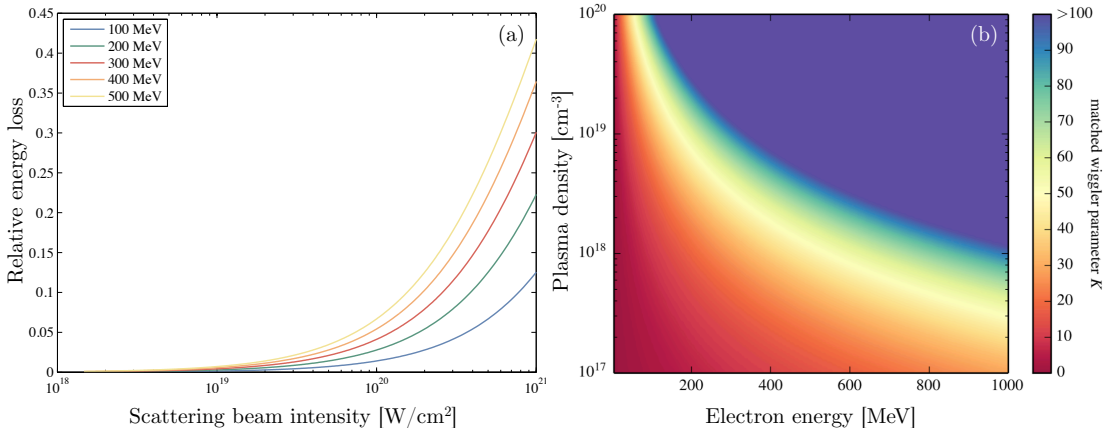

Figure 5.38 – a) Calculated energy loss due to classical radiation reaction for a 30 fs scattering pulse at 180° incident angle. b) Wiggler parameter for which the effective Lorentz factor γ_{eff} equals the phase velocity γ_ϕ as function of the electron energy and the plasma density.

propagate in direction of the laser. Therefore a regime of interest for future investigations might be to increase the betatron amplitude of to a peak deflection at which the effective Lorentz factor $\gamma_{\text{eff}} = \gamma/\sqrt{1+K^2/2}$ matches the phase velocity of the wake γ_ϕ. Such a configuration would be phase-locked and could provide an alternative to density matching discussed earlier. An estimation for the required Wiggler parameters is shown in Fig.5.38b.

Plasma focusing devices, like the laser-plasma lens or the proper wakefields of highly charged particle beams from ionization injection, will also enable many new developments. Such devices could be employed to reduce the source size in bremsstrahlung conversion, or to improve the radiation bandwidth in Compton-backscattering.

Our results on Compton backscattering also motivate to pursue the usage of the source for imaging applications. One example would be to take advantage of the small source size to perform phase contrast imaging. Or, varying the electron beam energy one could perform dual-energy imaging. An interesting fundamental physics experiment would be to measure radiation reaction [203]. Given the stability we have achieved using shock injected beams, it might be possible to directly observe classical radiation reaction with the two main beams of the SALLE JAUNE laser. Estimations for this are shown in Fig.5.38a. However, this effect will be much easier to observe at petawatt-class laser facilities.

Mid and long-term goals

While we have presented a number of individual improvements on each stage of laser-plasma lightsources, we have not yet explored a combination of all those schemes. In the near future, many hybrid solutions will explored, e.g. using a wakefield accelerator as electron gun, coupling a conventional undulator directly to a laser-wakefield accelerator [170] or to explore

combinations of conventional accelerators and Compton scattering [204]. It is also likely that plasma lenses will be an important element to maintain the beam emittance in such setups.

Still, the long term perspective remains to create compact, reliable, tunable, bright, all optical lightsources. A major step into this direction has been the combination of backscattering with controlled injection using shocks, as published recently [180]. Future sources should also provide higher repetition rate, which unavoidably requires further developments in laser technology. But at the same time the plasma accelerator should operate as efficiently and stably as possible. In this context we expect a high impact of our results on ionization injection and density tailoring.

A Experimental methods

In this chapter we review the basic experimental techniques that were used to obtain the results from the main text. The discussion of the laser system, plasma and electron diagnostics is intentionally brief. Instead we focus more on target development, with emphasis on new additive manufacturing techniques, and discuss X-ray diagnostics for ultrashort laser-plasma lightsources.

Contents

A.1 Laser System

The experiments in this work were performed at the SALLE JAUNE Laser system situated at Laboratoire d'Optique Appliquée in Palaiseau, France. The system delivers two laser pulses of up to 3 Joule energy each with a duration of ~ 30 femtoseconds at a repetition rate of 1 Hertz.

The system is based on chirped-pulse amplification [205], where laser pulses with a large spectral content are first stretched, then amplified and finally compressed. The Salle Jaune system starts off with 4 nJ, 9 fs pulses at 800 ± 150 nm (FWHM). These are then stretched to picosecond duration, amplified and compressed to 400 µJ at 20 fs duration. Then the pulse is cleaned in an XPW (Cross Polarized Wave) module, which enhances the contrast via non-linear wave mixing.

After the XPW the pulse goes through a second stretcher and enters an acousto-optic tunable filter [206], which allows to control the spectral phase. The pulses are then amplified by a series of five Ti:Sapphire multi-pass amplifier stages, which are pumped with frequency-doubled (532 nm) Nd:YAG lasers. After the last amplifier the beam is split into three parts: Two 3 Joule beams that will serve as driver and a weaker beam (50 mJ), which is usually used as a probe.

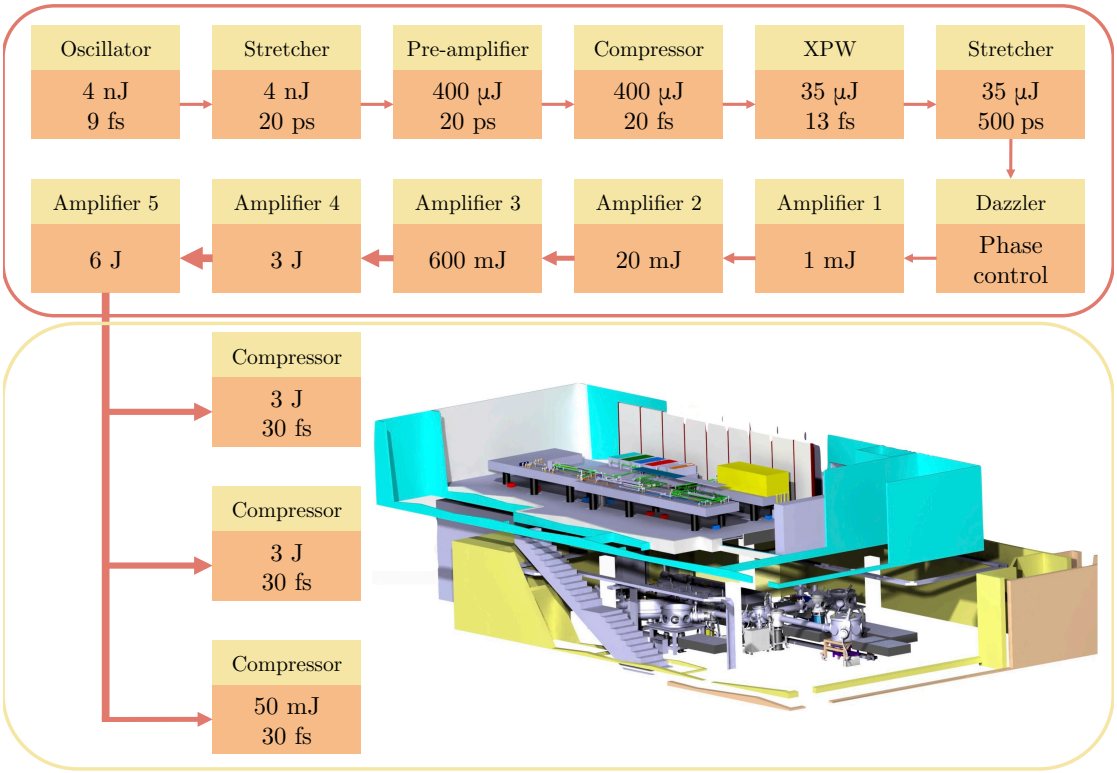

Figure A.1 – Schematic layout of the SALLE JAUNE laser system.

Laser influence on electron and X-ray production

Being the driver of the wakefield accelerator, the laser quality has important influence on the electron and X-ray yield. This is in particular the case for self-injection, which relies heavily on self-focusing. There are for example data which show the influence of coma aberrations on the beam divergence [207]. At Salle Jaune we have studied the influence of the third order spectral phase on laser pulse propagation [208]. There are also empirical data which show that high contrast leads to better beam stability and divergence [209]. Furthermore, it has been shown that the pulse front orientation [210] and the wavefront in general [211] have important influence on the wakefield acceleration.

A.2 Gas target

There are a number of different types of targets used for laser wakefield acceleration, among whose gas jets, gas cells, dielectric capillary tubes and discharge capillary tubes are the most popular.

An advantage of gas cells is that some designs allow to vary the cell length, which permits optimization of the accelerator for dephasing and so forth. Dielectric capillaries intend to provide guiding for the laser, especially the outer Airy modes. It has been reported that these designs can lead to higher betatron yield and increased stability. Discharge capillary tubes aim to provide a parabolic radial density profile, which should allow laser guiding beyond the self-guiding regime.

While all of these solutions have certainly advantages compared to a simple gas jet, this comes in hand with increased experimental complexity. Notably dielectric capillaries have to be carefully aligned, as a misalignment will lead to immediate destruction of the waveguide. The main challenge of discharge capillaries is the reliability of the plasma generation. Also, for both types of capillary targets it is difficult to add plasma diagnostics.

In this work we exclusively used gas jet targets, which among all targets provide the highest flexibility and due to their open design, side and top view diagnostics can be used to characterize the plasma and laser propagation. In particular, we have explored the usage of multiple gas jets and creation of tailored density profiles along the propagation axis.

Gas jets

The most common gas jet system used in laser-plasma accelerators is the Series 9 pulse valve by Parker Hannifin Corp., which operates at up to 50-80 bar and a sub-millisecond reaction time. On this valve different nozzles can be mounted, which are typically using a conical De Laval layout. These nozzles have usually exit diameters of a few millimeters, up to more than a centimeter for GeV electron acceleration. Note that recently also gas jets for laser-driven

proton acceleration have been developed. However, in order to achieve near-critical plasma densities, these jets operate at very high pressure (>100 bar) and small exit diameters (<1mm).

To date, such gas jet nozzles are usually made of aluminum, produced using CNC milling machines.

3D printing of gas jet nozzles

There are three principal motivations for the usage of 3D printers. Firstly, pieces can be produced directly from a CAD drawing, which make it ideal for rapid prototyping. The time from finishing a 3D model to using it ranges from a few hours (if an in-house printer is available) to a few days (for outsourced production). Furthermore the field is rapidly evolving and recently a number of enterprises offer manufacturing at very competitive prices (usually more than twenty times cheaper than milling). Lastly, additive manufacturing can offer more freedom in the design than conventional milling does. For this last argument to hold, we need however to respect some guidelines, which we will briefly discuss in the following.

What is commonly called 3D printing is a number of different technologies for additive manufacturing. These technologies have been essentially developed since the 1980s and have recently drawn a lot of public attention. The most common types are fused deposition modeling (FDM), selective laser sintering (SLS) and stereolithography (SLA). For our studies we have used commercial SLS and SLA systems. For the former nozzles have been printed using an EOS Formiga P110 printer, which employs a 30 W CO_2 laser coupled to an F-theta scanning lens. The printer material is a PA 12 based fine polyamide (PA 2200) with an average grain size of 60 μm. The layer thickness is 60 - 150 μm. As example of SLA we used a Stratasys Objet30 Pro printer, with layer thickness of 28 μm and an xy resolution of 42 micrometers. The Stratasys Objet offers currently the highest accuracy on the market (for non-specialized applications).

It has to be clarified that the nominal resolution of a 3D printer is not the smallest feature size, and especially, not the smallest hole size. After some unsuccessful tests to print nozzles with small inner diameter, we performed several systematic tests. An example is shown in Fig.A.2. We find that it is not recommendable to print gas channels with diameters below one millimeter and larger diameters are preferred.

In this work we have used 3D printed jets twice: Once in **Chapter 4: Beam Transport** for the focusing jet and also in Sec.5.5.3 in order to place two jets very close to each other. The larger the jet, the more similar its performance to conventional nozzles, as can be seen for instance in Fig.A.3.

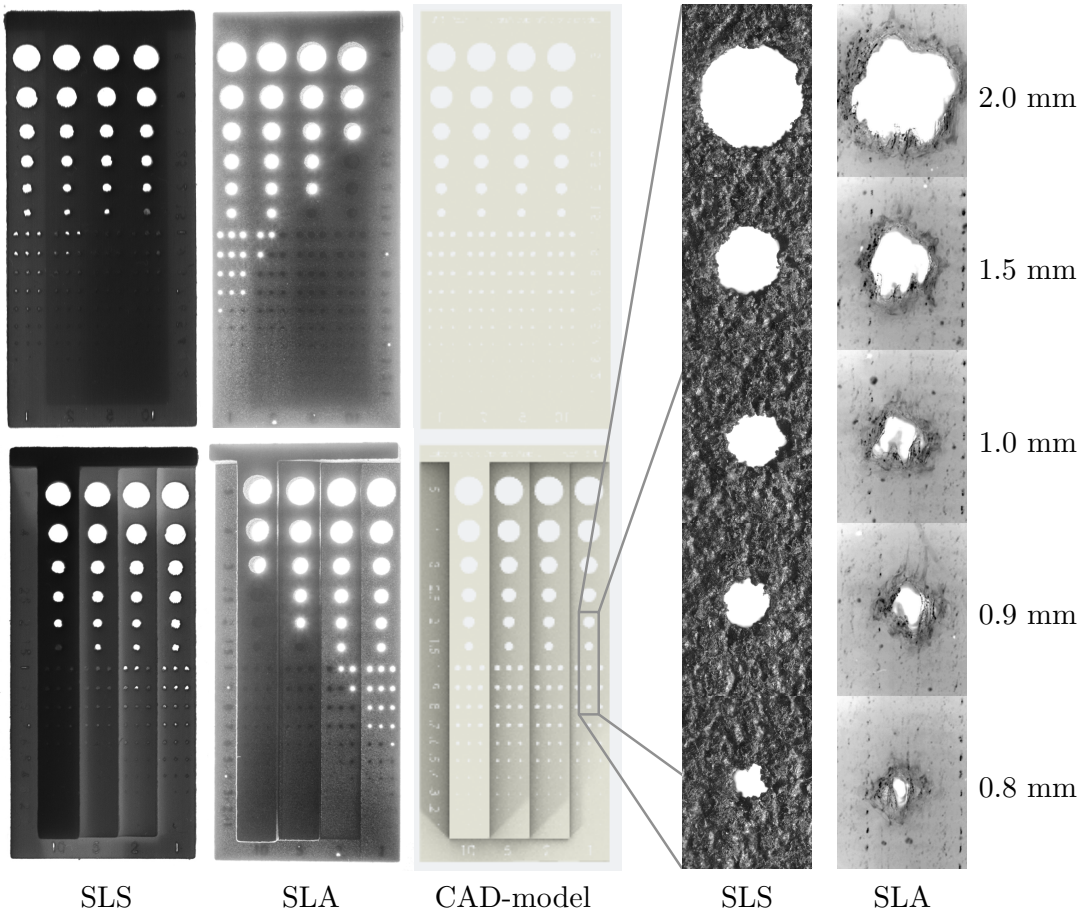

Figure A.2 – Back-lighted test prints for circular holes in plates of different thickness using SLS (plastic) and SLA (resin). The rendered CAD model is shown in white. We find that the smaller the hole diameter and especially the deeper the hole, the less well the tubes are resolved.

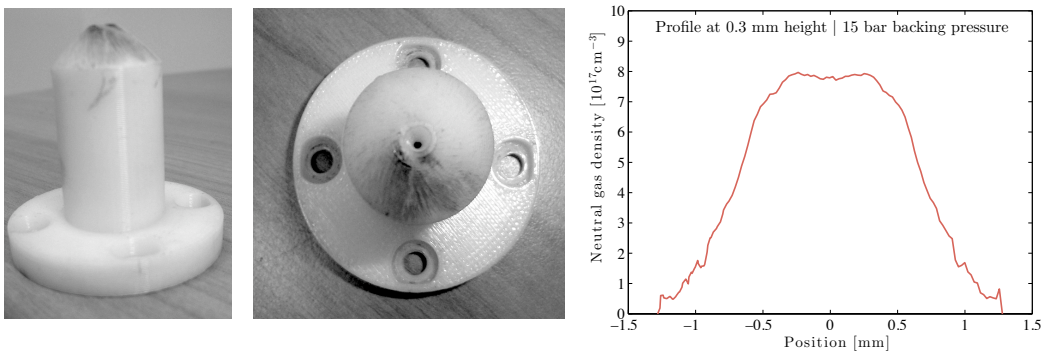

Figure A.3 – Photos and neutral gas characterization of the gas jets used in Sec.5.5.3. Density profile at 300 microns above the jet with 9 bar backing pressure.

A.3 Plasma and electron beam diagnostics

In the experiment we have two plasma diagnostics in place, called top- and sideview, and we measure the electron beam properties using a combination of magnet spectrometer and phosphor screens. In the following we briefly discuss these diagnostics.

Topview

The topview is a passive imaging system that looks at the target from above. It views as straight as possible above the gas jet, though under some circumstances this is geometrically not possible and we image at an angle. The diagnostic mainly collects light emitted from the plasma channel. It is therefore an important diagnostic during the alignment phase, as it allows us to verify the horizontal position of the nozzle with respect to the laser. Also, as it is sensible to wavebreaking radiation the injection position can be estimated and tuned.

Sideview

The sideview is an active imaging system employing an 800 nm probe beam, which is sent through the target perpendicular to the gas target. The sideview diagnostic can be operated either shadowgraphy or interferometry mode. For the former we directly image the beam outside of the chamber. Plasma formation will disturb the propagation and modify its intensity.

Alternatively we can use an interferometer to retrieve the phase shift the beam experiences while passing through the plasma. Common configurations are Michelson and Mach-Zehner interferometers, see for instance [33]. However. for our experiments we have been using Nomarski interferometers. This type of interferometer consists of a Wollaston prism and polarizers before and after the beam splitter. Its main advantage to other schemes is the simplicity and robustness of the alignment.

Electron beam charge and divergence

Most conventional accelerator facilities measure the beam charge in a non-invasive way with current transformers. For high current beams at produced in laser-wakefield accelerators it can be passively measured by employing integrating current transformers (ICTs). Unfortunately the laser-plasma interaction creates strong EMP signal which can disturb the ICT measurement. In a comparative study with scintillating screens, it was found that ICTs overestimated the beam charge significantly under LPA conditions. However, ICTs are regaining popularity. Some experiments mount them further downstream, while others successfully managed to shield their ICTs.

In this work we solely use absolutely calibrated scintillating screens, more precisely terbium activated Gadolinium oxysulfide (Gd_2O_2S:Tb) powder screens, brand name Kodak Lanex Fine.

For highly relativistic electrons the energy deposited in the scintillator is almost constant and therefore the signal level uniquely depends on the beam charge. Usually we measure the charge by integrating the whole signal on the electro spectrometer (see below), however for some measurements we need to verify the amount of charge below the cut-off and electrons are measured directly onto a screen.

The electron beam divergence is measured from the spatial charge distribution from the imaging screen. With the spectrometer in place this measurement is reduced to one dimension and it is therefore important to verify by direct transmission that the electron beam is sufficiently symmetric.

The spectrometer itself consists of a dipole magnet, which deflects electrons according to their energy onto the 35 mm × 177 mm large scintillating screen. In this work we used two different magnets: a 10cm, 1.1 Tesla permanent magnet for electrons in the range of around 50-500 MeV; and a 2cm 0.76 Tesla magnet for lower energies. The phosphor screen is imaged with commercial lenses (Nikon 50mm f/1.8 or Tamron 70-200mm f/2.8) onto a 16 bit CCD. To avoid noise an interference filter is added, which selects the emission wavelength of the screen.

The deflection geometry is shown in Figure A.4. Depending on the placement of magnet and screen with respect to the beam axis, the energy range and resolution can be varied. An example for this is shown in right frame of the figure.

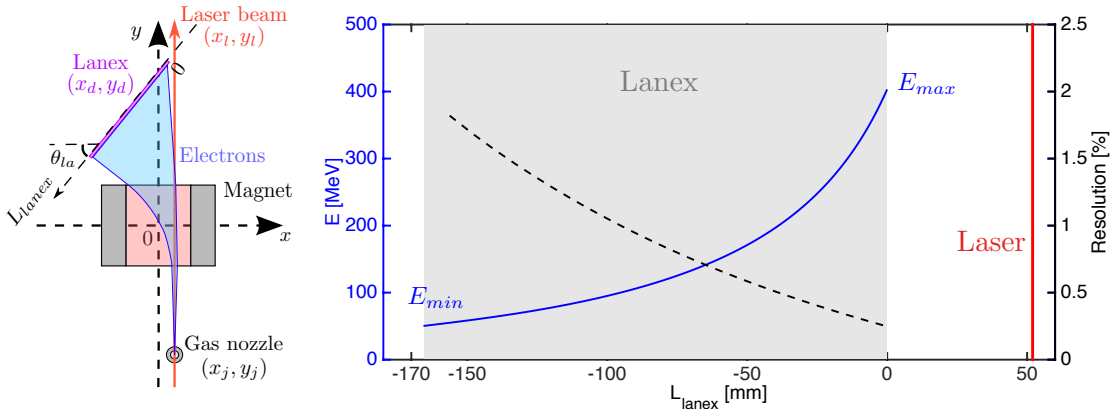

Figure A.4 – Electron spectrometer setup for experiments at Salle Jaune [89]. Left: Spectrometer geometry. Right: Corresponding energy range and resolution.

A.4 X-ray diagnostics

The main objective of this work is the production of X and γ radiation. In this section we are going to discuss their detection and how we can measure properties such as the photon number, energy and so forth. For this we will first recall some basic physics of photon-matter interaction. Thereafter we discuss the two main types of X-ray detectors used throughout this work, scintillators and CCDs.

A.4.1 Photon interaction with matter

The main effects in photon interaction with matter are the photoelectric effect, Compton-scattering and pair-production. Less important corrections arise from other effects as coherent Rayleigh scattering and photonuclear reactions. Therefore the total cross section for matter-photon interaction is approximately given by the sum

$$\sigma_{\text{tot}} \simeq \sigma_{\text{photo}} + \sigma_{\text{scattering}} + \sigma_{\text{pair}}. \tag{A.1}$$

Typically the photoelectric effect is dominating up to around 100 keV and then Compton-scattering becomes important. Pair-production can only occur above 1 MeV and starts to dominate in the γ-ray regime. The contribution of the three effects to the total scattering cross sections is illustrated in Figure A.5. A quantitative evaluation of the cross sections is shown in Figure A.7 for the cases of a low Z material (aluminum) and a high Z material (lead).

The absorption in a material can be calculated from the cross section accoring to

$$\frac{I}{I_0} = \exp\left[-\frac{\sigma_{\text{tot}}}{uA}x\right] \tag{A.2}$$

where A is the relative atomic mass and u is the unified atomic mass unit ($uc^2 \simeq 931.5$ MeV). From this we can immediately relate to the more intuitive mass attenuation coefficient

$$\mu/\rho = \sigma_{\text{tot}}/uA \tag{A.3}$$

which describes the attenuation over a distance x in a medium of density ρ. However, it is important to notice that this quantity is not equal to the dose deposed in the medium nor the energy absorption.

$$\mu_{tr}/\rho = \left(f_{\text{photo}}\sigma_{\text{photo}} + f_{\text{scattering}}\sigma_{\text{scattering}} + f_{\text{pair}}\sigma_{\text{pair}}\right)/uA \tag{A.4}$$

and the mass energy-absorption coefficient takes into account the emission of radiation by interaction of the secondary electrons with the medium[1]

$$\mu_{en}/\rho = (1-g)\mu_{tr}/\rho. \tag{A.5}$$

[1] This kind of secondary emission is used in so-called intensifying screens.

This correction becomes important at energies above ~ 10-30 keV, and it significantly reduces the amount of energy deposed inside the target. Importantly the emission of scintillating screens depends on the mass energy-absorption coefficient and not the mass absorption coefficient.

A.4.2 Scintillation

In the preceding section we have discussed how photons interact with matter. In particular any absorption process means that energy is deposited in the object. Such energy deposition can result in heating and so forth, but for radiation diagnostics the most important is photoluminescence, which means that the absorbed photon energy is re-emitted in form of photons.

Among photoluminescence processes we distinguish two categories according to their typical lifetime, which is the long living phosphorescence (typically milliseconds to hours) and the prompt fluorescence (usually nanoseconds).

Materials that show photoluminescence are called scintillators or also phosphors.[2] While the absorption is determined by the scintillator material, the emitted light is defined by its dopants. Common phosphors are caesium iodide (CsI), gadolinium oxysulfide (Gd_2O_2S) and bismuth germanium oxide (BGO).

Such scintillators are mainly characterized by four different properties. Their *light yield (LY)* describes the conversion efficiency of ionizing radiation into light. The *scintillation decay time* (τ) is the time until the emission decreases to $\exp(-1)$. For laser-plasma sources this parameter is usually negligible, because the X-ray pulse has a sub-picosecond duration, while the camera integrates the signal over several milliseconds. The *emitted wavelength* (λ) is an important parameter important for the detection, e.g. for coupling a CCD to the scintillator. It should be be chosen to be in the range of best quantum efficiency of the detector. As said before, the emitted wavelength is determined by the dopant, while the *absorption efficiency* is mainly determined by the scintillator density ρ and its effective nuclear charge Z_{eff}.

The following table lists those parameters for four typical scintillators.

material	name	LY [ph/keV]	τ [ns]	λ [nm]	ρ [g/cm^3]	Z_{eff}	type
NaI(Tl)		38	250	415	3.67	50	crystal
CsI(Tl)		54	1000	550	4.51	54	crystal
$\mathbf{Bi_4Ge_3O_{12}}$	BGO	8-10	300	480	7.13	75	crystal
$\mathbf{Gd_2O_2S{:}Tb}$	GOS/Gadox	60	$\sim 10^6$	545	7.32	59.5	powder

Such phosphors usually come in two types, crystal and powder converter screens.

[2] In the literature there is no consensus whether both are considered synonyms or not

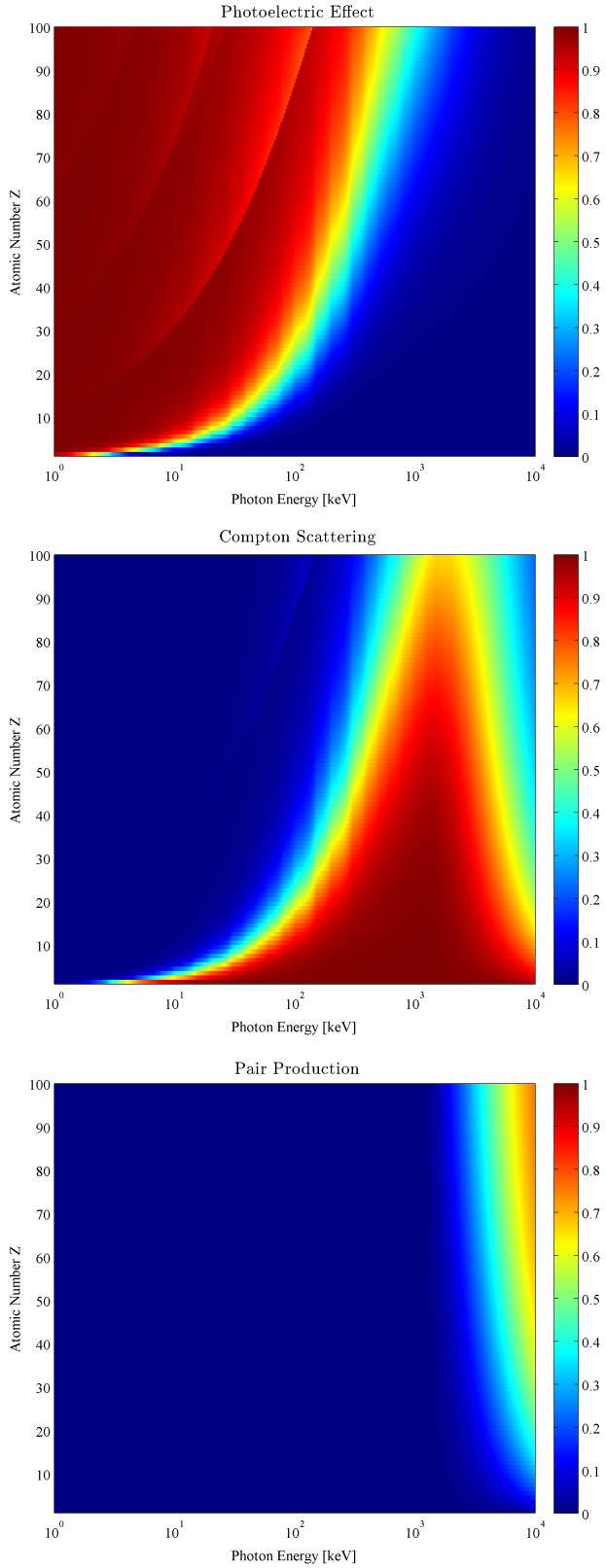

Figure A.5 – Relative contribution of the photoelectric effect, Compton scattering and pair production to the total cross section as function of the atomic number Z.

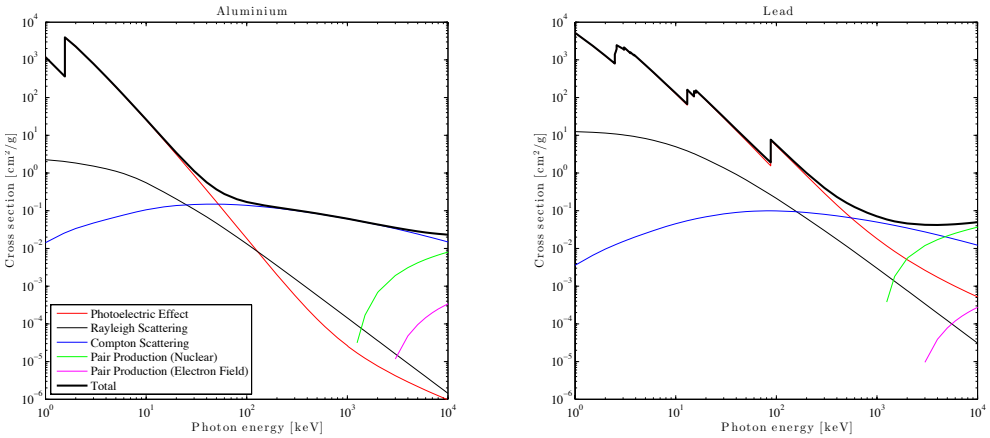

Figure A.6 – Cross sections of Aluminum ($Z = 13$) and Lead ($Z = 82$). The absorption in Lead is dominated by the photoelectric effect for energies up to 500 keV, while the absorption of aluminum is reduced to the compton cross section for >100 keV.

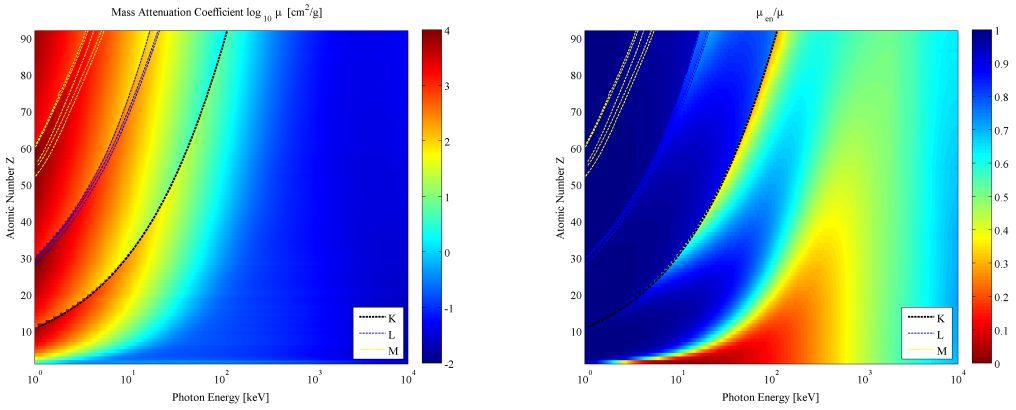

Figure A.7 – Left: Mass attenuation coefficients from Hydrogen ($Z = 1$) to Uranium ($Z = 92$). Also marked are the absorption edges at which the attenuation increases rapidly. Right: Ratio between the mass energy-absorption coefficient μ_{en} and the mass attenuation coefficient μ. While both agree well below 10 keV, there is an increasing discrepancy towards higher energies, especially at the k edges.

Powder converter screens

In powder screens small grains of phosphor are deposited on a substrate. The most common material for this kind of scintillators is Gd_2O_2S:Tb, also called GOS or Gadox. It is well-known by the Eastman Kodak trade name Lanex, while competitors sell it as Rarex, P43, etc. An example of the layer structure of a Lanex screen is shown in Fig.A.8.

In contrast to crystal screens, powder screens are only produced with thin layers of phosphor coating, e.g. 50 to 305 microns for Kodak Lanex screens. Furthermore the density of a powder is usually in the order of half the solid density (7.32 g/cm^3 for Gadox). According to Eastman Kodak the Lanex Fast back screens of 290 microns thickness have an average phosphor coverage of 124 g/ft^2, which leads to a slightly higher value of 4.6 g/cm^3.[3]

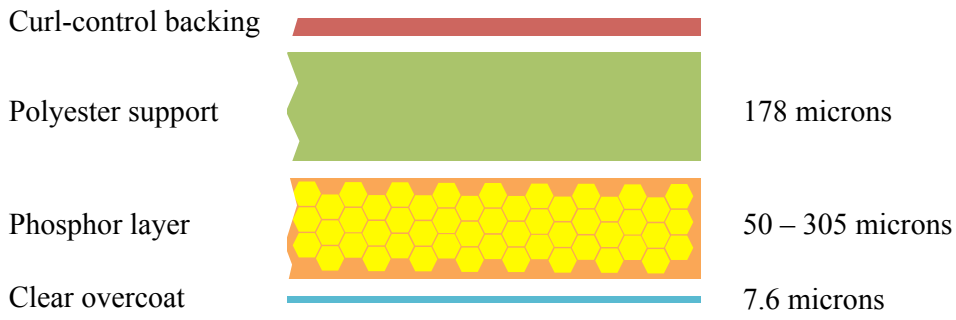

Figure A.8 – Layers of a Lanex Screen.

Being thinner and less dense, powder screens are therefore only efficient for X-ray detection up to ~ 100 keV. In this range the absorption is dominated by the photoelectric effect, and the K-edge at 50 keV. In the energy range up the 20 keV Lanex Fine / Regular absorb about ~ 95 / 99 percent of the incident photons. This means that for an X-ray source emitting at less than 20 keV, the scintillator signal is approximately proportional to the X-ray power. Another particularity of Gadox screens is their long decay time of up to a millisecond.

Crystal converter screens

Crystal converter screens use the scintillator crystals as they are grown. Two of the most common scintillator materials are caesium iodide (CsI) and Gadolinium oxysulfide (Gd_2O_2S). Furthermore BGO is often used.

The absorption for these three filter types is shown in Fig.A.10. The plot reads in two directions: While the horizontal lineout give information about the response curve for a scintillator of a given thickness, the vertical direction allows to estimate the absorption distance in a stack

[3] There is an ambiguity in the literature concerning the thickness of Phosphor screens, because sometimes the equivalent thickness of a solid is considered, while sometimes the actual thickness of the coating is meant.

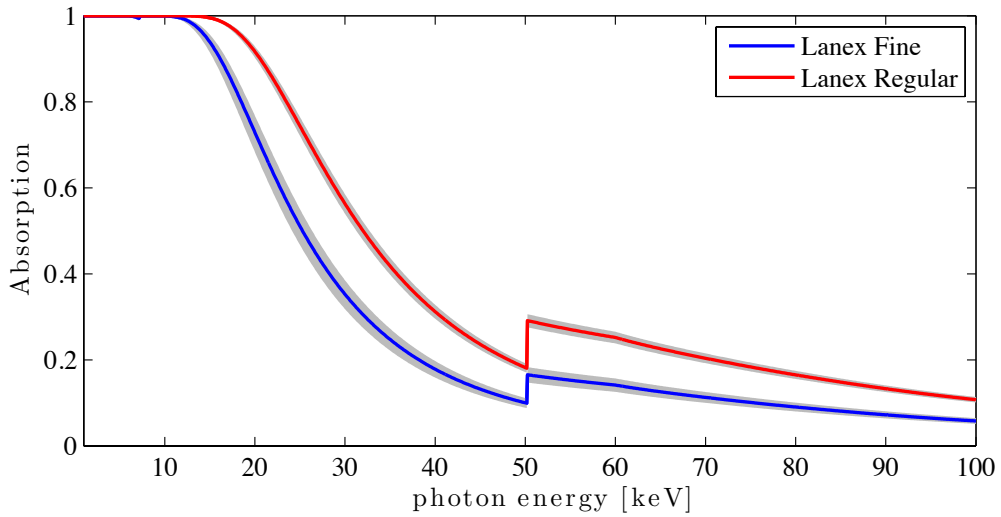

Figure A.9 – Estimated energy absorption using the NIST database for Lanex Fine (84±10 microns) and Lanex Regular (160±10 microns).

of scintillators. From the absorption we can also get the locally deposed energy, which is $dA(E)/dx \times E_\gamma$.

From the plots we see that in order to detect efficiently photons of more than a hundred keV, millimeter thick scintillators are needed. This is why we have for example tested 3mm thick CsI crystals to detect radiation from Compton scattering. A drawback of these thick crystals is that the spatial resolution is reduced. This can be partly solved by means of special crystal growth techniques, but such structures are not yet available for millimeter thickness.

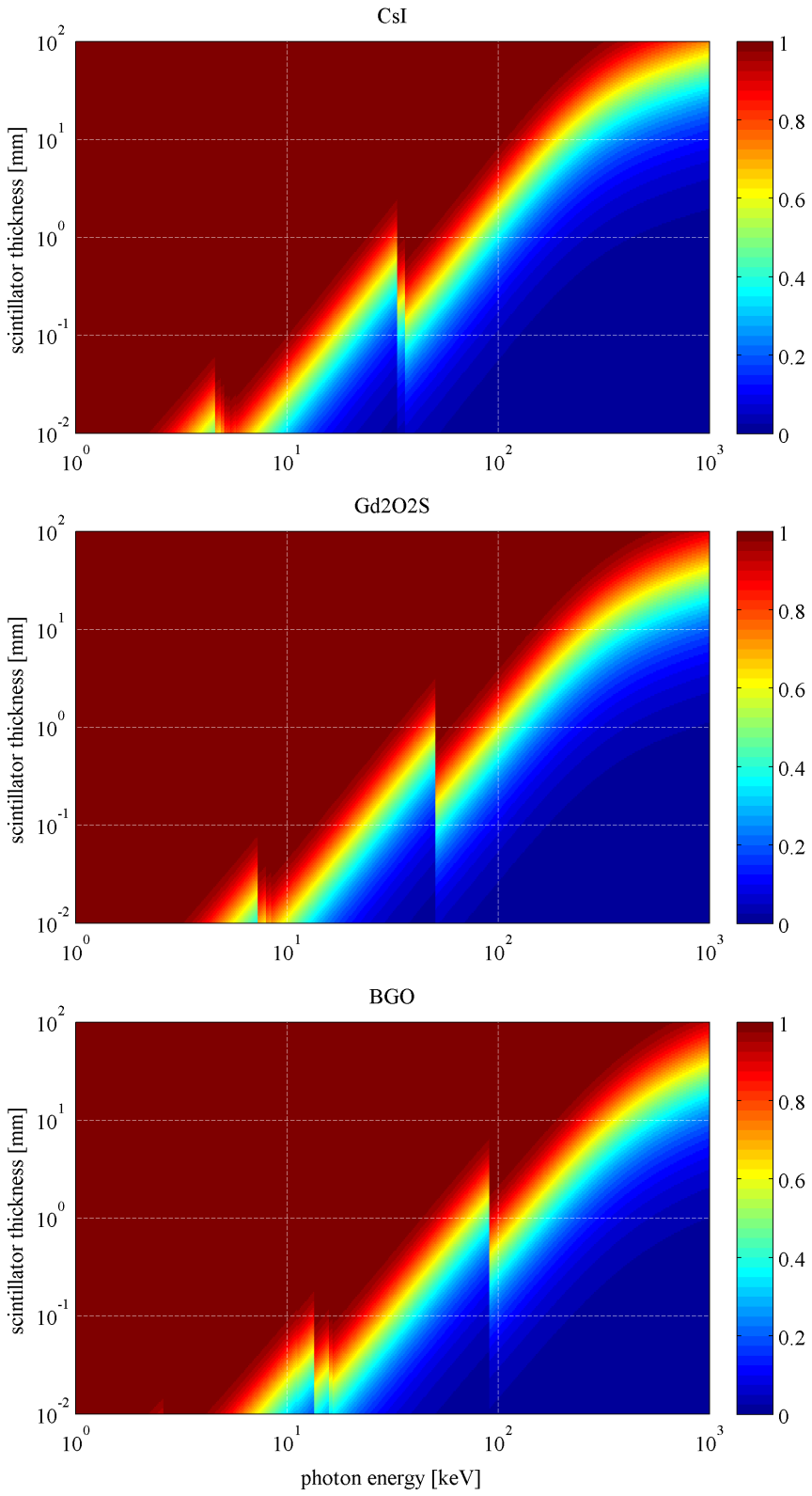

Figure A.10 – Absorption of CsI, Gadox and BGO scintillators as function of scintillator thickness and photon energy.

A.4.3 X-Ray filters

Also non-scintillating materials are of interest for X-ray detection. The attenuation of a X-ray beam when passing through a material con be used to estimate the X-ray energy. As we have already discussed above, the intensity of an X-ray beam behind a filter is given by (A.2):

$$\frac{I}{I_0} = \exp\left[-\frac{\sigma_{tot}}{uA}x\right] \tag{A.6}$$

The reversely means that a material thickness x is needed to attenuate a beam to I/I_0

$$x = -\frac{\log[I/I_0]}{\rho\mu} \tag{A.7}$$

A useful approximation to quickly estimate the order of magnitude to achieve significant attenuation of a beam is to assume $\rho \sim 5\text{g/cm}^3$ and $I/I_0 = 0.1$, which then leads to $x_0 \sim 5\,\text{mm}/\mu[\text{g/cm}^2]$, where the attenuation coefficient μ can be extracted from Fig.A.7. The amount of attenuation when radiation passes through filters can be used to extract information on the spectral content. This method is frequently used for ultrashort laser-based sources, as those exhibit significant shot-to-shot fluctuations and require single-shot diagnostics.

There exist a number of different implementations of such filer-based spectrometers. When the filters are balanced information about the difference can be extracted. If informations about the shape of the spectrum is known, a least squares fit can be used to fond the best agreement. Or more generally, we present an adaptive algorithm, which optimizes an initial guess spectrum to closely match the observed transmission ratios. However, it is difficult to retrieve exact radiation spectra from filters and for energies below ~ 30 keV, photon counting in charge-coupled devices can be used instead.

A.4.4 X-ray CCD

Charge-coupled devices (CCDs) are designed to generate electron hole pairs in the epitaxial layer when absorbing (visible) photons. But as we have established in the preceding sections, also X-ray can deposit energy when travelling through the layers of a CCD. Below 150 keV this energy deposition is dominated by the photoelectric effect. In this case its whole energy is absorbed by the silicon and electron-hole pairs are created corresponding to the primary photon energy. As the energy required to produce such pair is known (3.65 eV), the amount of electrons measured can be used to deduce the initial photon energy.

In such photon counting mode, single pixel events are isolated and their signal level is related by the camera gain to the original photon energy. However, high energy photons can excite several neighboring pixels at once, which is why the photon counting algorithm also needs to isolate multi-pixel events. Once all events are identified, the results are combined to a histogram, as shown for example in Fig.5.37 of the main body.

B Numerical methods

As complete analytical solutions can only be derived for simplified models like the one-dimensional linear wakefield model, a more realistic treatment requires numerical solutions. In laser plasma interactions, most computational methods rely on a finite difference time domain approach.

Comprehensive solution of the laser-plasma interaction is done by solving the Vlasov-Maxwell equations for a number of macro-particles. The particle-in-cell code CALDER-CIRC is discussed, as are stability and accuracy.

Contents

B.1 Finite Difference Methods

Finite Difference methods are widespread in computational physics due to their simplicity and numerical robustness. They are based on the idea of replacing differential equations by difference equations. To do so we approximate the function $f(x)$ by its Taylor expansion at the point $x_0 + \Delta x$

$$f(x_0 + \Delta x) = f(x_0) + \Delta x \frac{\partial f(x)}{\partial x} + \frac{\Delta x^2}{2} \frac{\partial^2 f(x)}{\partial x^2} + \mathcal{O}(\Delta x^3). \tag{B.1}$$

From this we can estimate the first derivative as

$$\frac{\partial f(x_0)}{\partial x} = \frac{f(x_0 + \Delta x) - f(x_0)}{\Delta x} + \mathcal{O}(\Delta x). \tag{B.2}$$

However this approximation has a weak scaling of $\mathcal{O}(\Delta x)$, because it is basically "forward-looking". We can compensate for this by using a second "backward-looking" series

$$f(x_0 - \Delta x) = f(x_0) - \Delta x \frac{\partial f(x)}{\partial x} + \frac{\Delta x^2}{2} \frac{\partial^2 f(x)}{\partial x^2} + \mathcal{O}(\Delta x^3). \tag{B.3}$$

and by subtracting respectively adding (B.3) and (B.1), we end up with the central difference, which is second order $\mathcal{O}(\Delta x^2)$

$$\frac{\partial f(x_0)}{\partial x} = \frac{f(x_0 + \Delta x) - f(x_0 - \Delta x)}{2\Delta x} + \mathcal{O}(\Delta x^2) \tag{B.4a}$$

$$\frac{\partial^2 f(x_0)}{\partial x^2} = \frac{f(x_0 + \Delta x) - 2f(x_0) + f(x_0 - \Delta x)}{\Delta x^2} + \mathcal{O}(\Delta x^2). \tag{B.4b}$$

Solving the non-linear plasma wave equation

A simple example for the use of finite difference methods is the solution of the non-linear plasma wave equation (1.15) that we have used extensively during the first chapters

$$\frac{\partial^2}{\partial \zeta^2} \phi = \frac{1}{2} \left(\frac{1 + a^2}{(1 + \phi)^2} - 1 \right) k_p^2. \tag{B.5}$$

The solution of this equation is straightforward given the methods mentioned above: We can use (B.4) to solve the potential with second order accuracy:

$$\phi_{k+1} = 2\phi_k - \phi_{k-1} + [(1 + (a_{k+1})^2)/(1 + \phi_k)^2 - 1] k_p^2 \Delta x^2 / 2 \tag{B.6}$$

Here we have used the common abbreviated notation $f(k\Delta x, i\Delta t) := f_k^i$. The solution is static and we are not concerned about accumulation of numerical errors, so for convenience the electric field and density were evaluated at first order B.2.

Solving Maxwell's equations

A more complex problem is the solution of Maxwell's equations, e.g. in order to calculate the propagation of an electromagnetic wave. Such propagation would be described by the dynamic part of Maxwell's equations (Ampère's and Faraday's laws) as

$$\partial_t \mathbf{E} = c \cdot \nabla \times \mathbf{B} \qquad \text{and} \qquad \partial_t \mathbf{B} = -c \cdot \nabla \times \mathbf{E} \tag{B.7}$$

which in one dimension reduces to

$$\partial_t E_x = -c \cdot \partial_z B_y \qquad \text{and} \qquad \partial_t B_y = -c \cdot \partial_z E_x. \tag{B.8}$$

We can convert these two PDEs to difference equation using the central difference formula from above (as we are in one dimension we drop the indexes, i.e. $E = E_x$ and $B = B_y$):

$$\frac{E_k^{i+1/2} - E_k^{i-1/2}}{\Delta t} = -c \cdot \frac{B_{k+1/2}^i - B_{k-1/2}^i}{\Delta x} \tag{B.9a}$$

$$\frac{B_{k+1/2}^{i+1} - B_{k+1/2}^i}{\Delta t} = -c \cdot \frac{E_{k+1}^{i+1/2} - E_k^{i+1/2}}{\Delta x} \tag{B.9b}$$

So the field at the next time step $(i+1/2)$ is

$$E_k^{i+1/2} = E_k^{i-1/2} - \rho \cdot (B_{k+1/2}^i - B_{k-1/2}^i) \tag{B.10a}$$

$$B_{k+1/2}^{i+1/2} = B_{k+1/2}^i - \rho \cdot (E_{k+1}^{i+1/2} - E_k^{i+1/2}) \tag{B.10b}$$

where $\rho = c\Delta t/\Delta x \leq 1$ is the Courant-Friedrich-Lewy (CLF) number. The above discretization method has been introduced by Yee. It solves the electric field on a so-called primary lattice, while the magnetic field is solved on a dual lattice, shifted by half a step, cf. Fig.B.1. The extension to three dimensions follows the same idea and is for example written out in [212].

Boris push

Once the fields for a certain charge and current distribution are known, one can calculate the motion of a particle in these fields. This is often done using the Boris push, which for this explicit problem reads

$$\vec{p}' = \vec{p}^{\,n-1/2} + q\vec{E} \cdot \Delta t/2 \tag{B.11a}$$

$$\vec{p}'' = \vec{p}' + q(\vec{p}' \times \vec{B}) \cdot \frac{1}{\sqrt{1+\vec{p}'^2}} \Delta t/2 \tag{B.11b}$$

$$\vec{p}''' = \vec{p}' + q(\vec{p}'' \times \vec{B}) \cdot \frac{1}{\sqrt{1+\vec{p}'^2}} \cdot \frac{1}{1+\vec{B}^2} \Delta t/2 \tag{B.11c}$$

$$\vec{p}^{\,n+1/2} = \vec{p}''' + q\vec{E} \cdot \Delta t/2 \tag{B.11d}$$

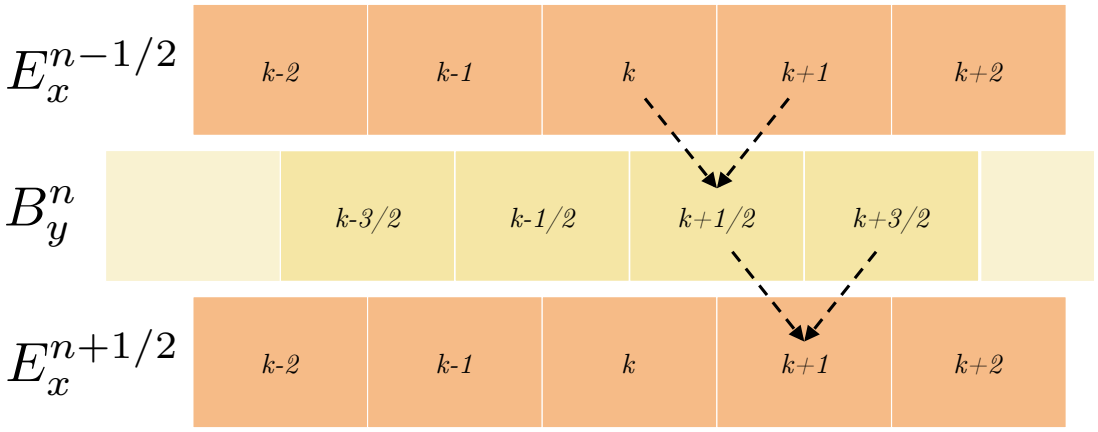

Figure B.1 – Schematic principle of the one-dimensional Yee algorithm.

B.2 Test particle simulations

The idea of test particle is to analyze the behavior of a particle in an environment, while ignoring the particle's feedback on the environment. For laser-plasma interactions this means that we do not solve the complete Maxwell-Vlasov system, but instead just model the response of the particle to a given field.

Such a reduced system is by orders of magnitude faster to solve than Maxwell-Vlasov, and as we have complete control of the fields we apply to the simulation, the results are also much cleaner and easier to interpret.

On the other hand the reduced physics included in test particle simulations may lead to results significantly different from reality. In the following we are going to discuss test particle models used in this work, with focus on their range of application.

Electron motion in a given potential

In **Chapter 4: Beam Transport** and **Chapter 5: Radiation** we have used test particle models to get an idea of the electron motion in certain wakefield patterns. These models used actual electric fields from CALDER-CIRC, which were assumed static. However as the test particles move continuously we use a bicubic interpolation to estimate the fields at the particles position. The equations of motion are then integrated using a leap frog scheme. The accuracy was tested using solutions of the wave equation and placing particles within the wake potential. Trapped particles would perform many revolutions inside the potential without noticeable deviation from their initial path.

The main advantage of this code is that orbits for few test particles can be solved instantaneously. This allows interactive adaption of particle and field parameters, which is often missing in more sophisticated numerical systems as PIC. It is adequate for order of magnitude estimations as done in **Chapter 4: Beam Transport** , or for short term trajectory calculations which can assume quasi-static fields. Also it is appropriate to estimate static properties, for instance the trapping threshold for ionization injection.

Thomson scattering

For the simulations on Thomson scattering we used a reduced version of the PLARES code. Here the laser propagation is implemented analytically, while the particle interaction is calculated using a standard Boris push.

Particles can be initiated in different spatial and momentum distributions, where we usually define a certain initial energy spread and divergence. Once their trajectories are calculated the Liénard-Wiechert potentials are solved in post-processing in order to find the resulting radiation emission.

B.3 Particle-In-Cell Simulations

Since their introduction in 1962 by Dawson [213] Particle-In-Cell codes have become an indispensable tool in plasma physics. Especially underdense laser-plasma interactions can be excellently modeled in moving simulation window systems. Nowadays there exists a large variety of commercial, open-source and close-source codes. Examples for popular codes to date are OSIRIS, WARP, VORPAL, CALDER, EPOCH, PIConGPU and so forth.

B.3.1 The Particle-In-Cell method

The idea of Particle-In-Cell is to solve the Vlasov-Maxwell system in a way that the particle distribution is sampled using so-called macroparticles.[1] The particles are initiated according to the particle distribution we wish to sample. The PIC algorithm then calculates the fields associated with this distribution by projecting to particles onto a discrete grid. As the macroparticles 'live' in a continuous space, they will usually lie between several grid points. They are therefore weighted according to a shape function, e.g. in the one-dimensional case the density is

$$\rho_i^{n+1} = \sum_i q_i S(x_i - x_j), \tag{B.12}$$

[1] When working with particle-in-cell it is actually more descriptive to express electron densities in particles per μm^{-3} or $pC\mu m^{-3}$, than to use the conventional cm^{-3}. In fact, a density of $6.3 \times 10^{18} cm^{-3}$ is equivalent to 1 $pC\mu m^{-3}$. For laser wakefield simulations a macroparticle therefore represents typically a charge in the order of ~ fC.

with the first order shape function $S = 1 - \frac{|x_i - x_j|}{\Delta x}$. Once the fields are calculated, the response of the macroparticles to them is calculated. Note that during the field initialization also external fields as laser pulses can be introduced. The response is usually calculated with a pusher, like the Boris push we discussed above. Once the particles are moved we again gather the new densities and integrate to find the fields.

It is evident that the complexity and runtime of the code is increasing with each dimension taken in account. For our case it is not sufficient to do a one-dimensional simulation, since the ponderomotive force is acting in the transverse direction, moving particles away from the center of the beam.

Good qualitative results can be obtained using two dimensions. In 2D every macroparticle can be thought to be an infinitely long cylinder, moving in the plane perpendicular to is extension.The main problems why a 2D PIC simulation cannot yield to quantitive results are

- It is well known that the external field of a charged cylinder falls with $1/r$ - by contrast a point charge's field falls with $1/r^2$. This means that a 2D PIC overestimates forces between macroparticles with rising distance.
- In two dimensions self-focussing does not lead to correct field intensities as the intensity does not increase with the square of the spot size but just linearly. Therefore 2D PIC codes have to be initialized with field intensities higher then the actual experimental parameters.

B.3.2 CALDER-CIRC

Throughout this work we have performed Particle-In-Cell simulations using CALDER-CIRC. The advantage of this code is that it uses a quasi-cylindrical geometry (r, θ, z) and decomposes the fields, e.g. the electric field

$$\vec{E}(r,\theta,z) = E_r(r,\theta,z)\vec{e}_r + E_\theta(r,\theta,z)\vec{e}_\theta + E_z(r,\theta,z)\vec{e}_z,$$

in their Fourier components to θ. So each field F can be written in form of a series

$$F(r,\theta,z) = \sum_{m=-\infty}^{+\infty} \tilde{F}^m(r,x)e^{-im\theta},$$

with

$$\tilde{F}^m(r,x) = \frac{1}{2\pi}\int_0^{2\pi} F(r,\theta,z)e^{im\theta}d\theta.$$

The great advantage of this method is that, as we write down consequently Maxwell's equations, there is no coupling between different modes. Thus each mode can be calculated separately and as a result one does not need to perform a full $3D$ simulation, but a $2D \times n_m$, where n_m is the number of included Fourier modes. For laser propagation in vacuum it is sufficient to use

$m = 1$. However Vlasov's equation is non-linear and introduces coupling between the modes. But as a wakefield is nearly axisymmetric there is almost no dependence on θ and it suffices to include the order $m = 0$.

Thus, as discussed and verified in [214], CALDER-CIRC allows the user to perform simulations at a speed that is of the same order as a 2D code, while still allowing a quantitative simulation of physical phenomena that is comparable to real 3D codes. To do so it is sufficient to include the first two modes, $m = 0$ for the wakefield and $m = 1$ for the laser beam.

B.3.3 Resolution and numerical dispersion

After this general discussion let us now consider some explicit rules we need to follow when simulating laser wakefield acceleration with PIC codes, in particular CALDER-CIRC.

Resolution

If we want to study the plasma dynamics it is sufficient to resolve the plasma wavelength. For underdense laser-plasma interactions the critical time scale is however the laser period, which is why we need to have a longitudinal resolution that satisfies the Nyquist criterion. In transverse direction we still only need to resolve the plasma dynamics, so in this direction the resolution can be reduced.

An important issue to study dephasing is properly describe the driver dynamics. Firstly the resolution has to satisfy the Nyquist criterion. Beyond this we also have to take into account numerical dispersion.

Numerical dispersion

Let us consider the propagation of an electromagnetic wave in vacuum.

$$c^2 \partial_z^2 E - \partial_t^2 E = 0 \tag{B.13}$$

If we use a first order discretization scheme as the Yee Algorithm, a time derivative is represented as

$$\partial_z E(z,t) = \frac{E^i_{j+1/2} - E^i_{j-1/2}}{\Delta z} \tag{B.14}$$

$$\partial_t E(z,t) = \frac{E^{i+1/2}_j - E^{i-1/2}_j}{\Delta t} \tag{B.15}$$

$$\frac{1}{\Delta t^2}\left(E_i^{j+1} - 2E_i^j + E_i^{j-1}\right) = \frac{c^2}{\Delta z^2}\left(E^j_{i+1} - 2E^j_i + E^j_{i-1}\right) \tag{B.16}$$

An electrical field of the form $e^{i(kz-\omega t)}$ leads to the dispersion relations

$$\omega^2 = c^2 k^2 \tag{B.17}$$

and therefore the phase velocity

$$v_\phi \equiv \frac{\omega}{k} = c \tag{B.18}$$

which is in this case equal to the group velocity

$$v_g \equiv \frac{\partial \omega}{\partial k} = c \tag{B.19}$$

$$\frac{1}{\Delta t^2}\sin^2\frac{\omega\Delta t}{2} = \frac{c^2}{\Delta z^2}\sin^2\frac{k\Delta z}{2} \tag{B.20}$$

so for $k\Delta z \ll 1$

$$v_\phi = \frac{2}{k\Delta t}\arcsin\left(\frac{c\Delta t}{\Delta z}\left(\sin\frac{k\Delta z}{2}\right)\right) \simeq 1 - \frac{k\Delta t}{48}\left(1-\frac{\Delta t^2}{\Delta x^2}\right)(k\Delta x)^2 \tag{B.21}$$

$$v_g = \left[1+\left(1-\frac{\Delta t^2}{\Delta x^2}\right)\tan^2(k\Delta x/2)\right]^{-1/2} \simeq 1 - \frac{1}{8}\left(1-\frac{\Delta t^2}{\Delta x^2}\right)(k\Delta x)^2 \tag{B.22}$$

In a cold, collisionless plasma the dielectric function is given by $\epsilon(\omega) = 1-\omega_p^2/\omega^2$ and the wave equation is

$$c^2\partial_z^2 E - \partial_t^2 E - \omega_p^2 E = 0 \tag{B.23}$$

which leads to the modified physical dispersion relation

$$\omega^2 = k^2 + k_p^2 \tag{B.24}$$

and numerical dispersion relation

$$\frac{1}{\Delta t^2}\sin^2\frac{\omega\Delta t}{2} = \frac{c^2}{\Delta z^2}\sin^2\frac{k\Delta z}{2} + \frac{k_p^2}{4} \tag{B.25}$$

with the group velocity

$$v_g = \left[\left(1+\frac{k_p^2\Delta x^2}{4\sin^2(k\Delta x/2)}\right)\left(1+\left(1-\frac{\Delta t^2}{\Delta x^2}\right)\tan^2\left(\frac{k\Delta x}{2}\right) - \frac{k_p^2\Delta t^2}{4\cos^2(k\Delta x/2)}\right)\right]^{-1/2}. \tag{B.26}$$

The important question is, how does the plasma density effects the numerical laser propagation. For low plasma densities and $k\Delta x \ll 1$ we find

$$v_g = 1 - \frac{1}{2}\frac{k_p^2}{k^2} - \frac{1}{8}\left(1+3\frac{k_p^2}{k^2}\right)\left(1-\frac{\Delta t^2}{\Delta x^2}\right)(k\Delta x)^2 \tag{B.27}$$

which means that there is also an additional numerical error, but it is only a fraction of the numerical error in vacuum.

C Formulary

This chapter sums up some of the most useful relations.

Relativistic optics

Normalized vector potential a_0 and fields in units of a_0

$$a_0^2 \simeq 7.3 \times 10^{-19} [\lambda(\mu\text{m})]^2 I_0 [\text{W/cm}^2] \tag{C.1}$$

$$E\ [\text{TV/m}] \simeq 3.21 a_0 / \lambda [\mu\text{m}] \tag{C.2}$$

Normalized velocity and Lorentz factor

$$\beta = v/c_0 = \sqrt{1 - 1/\gamma^2} \simeq 1 - 1/2\gamma^2 \tag{C.3}$$

$$\gamma = \sqrt{\frac{1}{1-\beta^2}} = \frac{1}{\sqrt{(1+\beta)(1-\beta)}} \tag{C.4}$$

Plasma physics

Plasma frequency, wavelength and wave number

$$\omega_p \simeq 178\ \text{THz} \times \sqrt{n_e\,[10^{19}\ \text{cm}^{-3}]} \tag{C.5}$$

$$\lambda_p \simeq 10\,\mu\text{m} \times \sqrt{n_e\,[10^{19}\ \text{cm}^{-3}]} \tag{C.6}$$

$$k_p = 2\pi/\lambda_p \tag{C.7}$$

Laser-wakefield acceleration

Non-linear laminar plasma wave equation

$$\frac{\partial^2}{\partial\zeta^2}\Phi = \frac{1}{2}\left(\frac{1+a^2}{(1+\Phi)^2}-1\right)k_p^2. \tag{C.8}$$

Exact solutions for weak excitation (linear plasma wave)

$$\Phi = -c_{\text{env}}\frac{a_0^2}{4}\sin[k_p(\xi-\xi_l)]\exp\left(-\frac{2r^2}{w^2}\right) \tag{C.9}$$

$$E_z = \frac{c_{\text{env}}a_0^2}{4}\frac{mc\omega_p}{e}\cos[k_p(\xi-\xi_0)]\exp\left(-\frac{2r^2}{w^2}\right) \tag{C.10}$$

$$E_r = c_{\text{env}}a_0^2\frac{mc^2 r}{ew^2}\sin[k_p(\xi-\xi_l)]\exp\left(-\frac{2r^2}{w^2}\right) \tag{C.11}$$

$$c_{\text{env}} = [1-(k_p\sigma_z/\pi)^2]^{-1}\sin(k_p\sigma_z) \qquad (\sin^2 \text{ pulse}) \tag{C.12}$$

$$c_{\text{env}} = \sqrt{\pi/4\log(2)}(\omega_p\tau)\exp[-(\omega_p\tau)^2/16\log(2)] \qquad \text{(gaussian pulse)} \tag{C.13}$$

Velocity and corresponding Lorentz factor of a laser excited plasma wave

$$\beta_\phi = \sqrt{1-\omega_p^2/\omega_0^2} \qquad \text{and} \qquad \gamma_\phi = \omega_0/\omega_p \tag{C.14}$$

Potential and fields in the bubble regime, (3.8) and (4.28)

$$\Phi = \frac{k_p^2}{4}\left(r_B^2 - r^2\right) \tag{C.15}$$

$$E_z = -\frac{m_e\omega_p^2}{2e}(1-\phi)r_B \tag{C.16}$$

$$E_r = \frac{m\omega_p^2 r}{2e} \tag{C.17}$$

Matched cavity size in bubble regime [41]

$$r_B \approx 2\sqrt{a_0}\lambda_p \tag{C.18}$$

Dephasing length (3.11)

$$L_d = \frac{r_B}{1-\beta_\phi} \tag{C.19}$$

Maximum dephasing limited energy gain (3.15)

$$\Delta\gamma_{\max} \approx \frac{2}{3}\frac{n_c}{n_e}a_0 \tag{C.20}$$

Synchrotron radiation

Intensity of radiation emitted by a relativistic particle (5.17b)

$$\frac{d^2I}{d\omega d\Omega} = \frac{e^2}{4\pi^2 c}\left|\int_{-\infty}^{+\infty}[\vec{n}\times(\vec{n}-\vec{\beta})]\cdot e^{i\omega(t-\vec{n}\cdot\vec{r}(t)/c)}dt\right|^2 \tag{C.21}$$

Doppler upshift for different insertion devices (5.22)

$$\lambda_{\text{Compton}} = \frac{\lambda_0(1+\gamma^2\theta^2)}{2\gamma^2(1-\beta\cos\phi)} \tag{C.22}$$

$$\lambda_{\text{Undulator}} = \frac{\lambda_u(1+\gamma^2\theta^2)}{2\gamma^2} \tag{C.23}$$

$$\lambda_{\text{Betatron}} = \frac{\lambda_\beta(1+\gamma^2\theta^2)}{2\gamma^2} \tag{C.24}$$

Betatron oscillation wavelength (4.30)

$$\lambda_\beta = \sqrt{2\gamma}\lambda_p \tag{C.25}$$

Emission in the Wiggler regime (5.34)

$$\frac{d^2I}{d\omega d\Omega} = \frac{e^2}{6\pi^2 c}\left(\frac{\omega\rho}{c}\right)^2\left(\frac{1}{\gamma^2}+\theta^2\right)\left(\mathcal{K}_{2/3}^2(\xi)\,\vec{u}_\sigma + \frac{\theta^2}{\gamma^{-2}+\theta^2}\mathcal{K}_{1/3}^2(\xi)\,\vec{u}_\pi\right) \tag{C.26}$$

Critical frequency of betatron radiation

$$\omega_c = \frac{3}{2}K\gamma^2\omega_\beta \propto r_0 n_0 \gamma^{7/4}. \tag{C.27}$$

Bibliography

[1] WILHELM CONRAD ROENTGEN. **Ueber eine neue Art von Strahlen**. *Sitzungsberichte der Wuerzburger Physik.-Medic.-Gesellschaft*, 1895.

[2] JULIUS EDGAR LILLIENFELD. **Anordnung zur Erzeugung von Röntgenstrahlen beliebiger, momentan einstellbarer Härte im Dauerbetrieb**. pages 1–5, March 1914.

[3] GÜNTER DÖRFEL. **Julius Edgar Lilienfeld und William David Coolidge – ihre Röntgenröhren und ihre Konflikt**. *Max Planck Institute for the History of Science*, pages 1–68, September 2007.

[4] WILLIAM D COOLIDGE. **A powerful Röntgen ray tube with a pure electron discharge**. *Physical Review*, **2**:1–22, December 1913.

[5] J H FREMLIN AND J S GOODEN. **Cyclic accelerators**. *Reports on Progress in Physics*, **13**(1):295, 1950.

[6] D. IWANENKO AND I. POMERANCHUK. **On the Maximal Energy Attainable in a Betatron**. *Phys. Rev.*, **65**:343–343, June 1944.

[7] J. SCHWINGER. **On the Classical Radiation of Accelerated Electrons**. *Physical Review*, **75**:1912–1925, 1949.

[8] EDWIN MCMILLAN. **The Synchrotron—A Proposed High Energy Particle Accelerator**. *Physical Review*, **68**(5-6):143–144, September 1945.

[9] F. K. GOWARD AND D. E. BARNES. **Experimental 8 Mev. Synchrotron for Electron Acceleration**. *Nature*, **158**:413, 1946.

[10] F. R. ELDER, A. M. GUREWITSCH, R. V. LANGMUIR, AND H. C. POLLOCK. **A 70 MeV Synchrotron**. *Journal of Applied Physics*, **18**(9):810–818, September 1947.

[11] F ELDER, R LANGMUIR, AND H POLLOCK. **Radiation from Electrons Accelerated in a Synchrotron**. *Physical Review*, **74**(1):52–56, July 1948.

[12] D M P HOLLAND. **The Daresbury Synchrotron Radiation Source**. *Physica Scripta*, **36**(1):22, 1987.

[13] H MOTZ. **Applications of the Radiation from Fast Electron Beams**. *Journal of Applied Physics*, **22**(5):527–535, May 1951.

[14] H MOTZ, W THON, AND R N WHITEHURST. **Experiments on Radiation by Fast Electron Beams**. *Journal of Applied Physics*, **24**(7):826–833, 1953.

[15] ALBERTO BRAVIN, PAOLA COAN, AND PEKKA SUORTTI. **X-ray phase-contrast imaging: from pre-clinical applications towards clinics**. *Physics in Medicine and Biology*, **58**(1):R1–R35, December 2012.

[16] JOHN M J MADEY. **Stimulated Emission of Bremsstrahlung in a Periodic Magnetic Field**. *Journal of Applied Physics*, **42**(5):1906–1913, April 1971.

[17] D DEACON, L ELIAS, J MADEY, G RAMIAN, H SCHWETTMAN, AND T. SMITH. **First Operation of a Free-Electron Laser**. *Physical Review Letters*, **38**(16):892–894, April 1977.

[18] T. H. MAIMAN. **Stimulated Optical Radiation in Ruby**. *Nature*, **187**:493–494, 1960.

[19] A M KONDRATENKO AND E L SALDIN. **Generation of coherent radiaition by a relativistic electron beam in an ondulator**. *Particle Accelerators*, **10**:207–216, August 1980.

[20] ZHIRONG HUANG AND KWANG-JE KIM. **Review of x-ray free-electron laser theory**. *Physical Review Special Topics-Accelerators and Beams*, **10**(3):034801, March 2007.

[21] S V MILTON, E GLUSKIN, N D ARNOLD, C BENSON, W BERG, S G BIEDRON, M BORLAND, Y C CHAE, R J DEJUS, P K DEN HARTOG, B DERIY, M ERDMANN, Y I EIDELMAN, M W HAHNE, Z. HUANG, K. J. KIM, J W LEWELLEN, Y LI, A H LUMPKIN, O MAKAROV, E R MOOG, A NASSIRI, V SAJAEV, R SOLIDAY, B J TIEMAN, E M TRAKHTENBERG, G TRAVISH, I B VASSERMAN, N A VINOKUROV, X J WANG, G WIEMERSLAGE, AND B X YANG. **Exponential Gain and Saturation of a Self-Amplified Spontaneous Emission Free-Electron Laser**. *Science*, **292**(5524):2037–2041, January 2001.

[22] P. EMMA, R. AKRE, J. ARTHUR, R. BIONTA, C. BOSTEDT, J. BOZEK, A. BRACHMANN, P. BUCKSBAUM, R. COFFEE, F. J. DECKER, Y. DING, D. DOWELL, S. EDSTROM, A. FISHER, J. FRISCH, S. GILEVICH, J. HASTINGS, G. HAYS, HERINGPH, Z. HUANG, R. IVERSON, H. LOOS, M. MESSERSCHMIDT, A. MIAHNAHRI, S. MOELLER, H. D. NUHN, G. PILE, D. RATNER, J. RZEPIELA, D. SCHULTZ, T. SMITH, P. STEFAN, H. TOMPKINS, J. TURNER, J. WELCH, W. WHITE, J. WU, G. YOCKY, AND J. GALAYDA. **First lasing and operation of an angstrom-wavelength free-electron laser**. *Nature Photonics*, **4**(9):641–647, 2010.

[23] BRIAN W. J. MCNEIL AND NEIL R. THOMPSON. **X-ray free-electron lasers**. *Nature Photonics*, **4**(12):814–821, November 2010.

[24] ALEXANDER ZHOLENTS. **Next-Generation X-Ray Free-Electron Lasers**. *Ieee Journal of Selected Topics in Quantum Electronics*, **18**(1):248–257, February 2012.

[25] J AMANN, W BERG, V BLANK, F. J. DECKER, Y. DING, P. EMMA, Y FENG, J. FRISCH, D FRITZ, J. HASTINGS, Z. HUANG, J. KRZYWINSKI, R LINDBERG, H. LOOS, A LUTMAN, H. D. NUHN, D. RATNER, J. RZEPIELA, D SHU, YU SHVYD'KO, S SPAMPINATI, S STOUPIN, S TERENTYEV, E TRAKHTENBERG, D. WALZ, J. WELCH, J. WU, A. ZHOLENTS, AND D ZHU. **Demonstration of self-seeding in a hard-X-ray free-electron laser**. *Nature Photonics*, pages 1–6, September 2012.

[26] G. LAMBERT, T HARA, D. GARZELLA, T TANIKAWA, M LABAT, B. CARRE, H KITAMURA, T SHINTAKE, M. BOUGEARD, S INOUE, Y TANAKA, P. SALIERES, H. MERDJI, O CHUBAR, O. GOBERT, K TAHARA, AND M E COUPRIE. **Injection of harmonics generated in gas in a free-electron laser providing intense and coherent extreme-ultraviolet light**. *Nature Physics*, **4**(4):296–300, March 2008.

[27] Z T ZHAO, D WANG, J H CHEN, Z H CHEN, H X DENG, J G DING, C FENG, Q GU, M M HUANG, T H LAN, Y B LENG, D G LI, G Q LIN, B LIU, E PRAT, X T WANG, Z S WANG, K R YE, L Y YU, H O ZHANG, J Q ZHANG, ME ZHANG, MI ZHANG, T. ZHANG, S P ZHONG, AND Q G ZHOU. **First lasing of an echo-enabled harmonic generation free-electron laser**. *Nature Photonics*, pages 1–4, May 2012.

[28] **The European x-ray free-electron laser**. *Technical Design Report, DESY*, **97**:1–26, 2006.

[29] D. H. BILDERBACK, P. ELLEAUME, AND E. WECKERT. **Review of third and next generation synchrotron light sources**. *Journal of Physics B-Atomic Molecular and Optical Physics*, **38**(9):773–797, May 2005.

[30] Z. NAJMUDIN, S. KNEIP, M S BLOOM, S. P. D. MANGLES, O. CHEKHLOV, A. E. DANGOR, A DÖPP, K. ERTEL, S. J. HAWKES, J HOLLOWAY, C. J. HOOKER, J JIANG, N C LOPES, H NAKAMURA, P. A. NORREYS, P. P. RAJEEV, C RUSSO, M. J. V. STREETER, D. R. SYMES, AND M WING. **Compact laser accelerators for X-ray phase-contrast imaging**. *Philosophical Transactions of the Royal Society A: Mathematical, Physical and Engineering Sciences*, **372**(2010), January 2014.

[31] GERARD A. MOUROU, TOSHIKI TAJIMA, AND SERGEI V. BULANOV. **Optics in the relativistic regime**. *Reviews of Modern Physics*, **78**:309–371, April 2006.

[32] J. FAURE, C. RECHATIN, A. NORLIN, A. LIFSCHITZ, Y. GLINEC, AND V. MALKA. **Controlled injection and acceleration of electrons in plasma wakefields by colliding laser pulses**. *Nature*, **444**(7120):737–739, December 2006.

[33] ANDREAS DÖPP. *Betatron radiation from laser-driven electron accelerators*. Master's thesis, RWTH Aachen, February 2012.

[34] J.D. JACKSON. **Classical Electrodynamics**, 1971.

[35] REMI LEHE. *Improvement of the quality of laser-wakefield accelerators*. PhD thesis, Ecole Polytechnique, Laboratoire d'Optique Appliquée, June 2014.

[36] W. B. MORI. **The physics of the nonlinear optics of plasmas at relativistic intensities for short-pulse lasers**. *Ieee Journal of Quantum Electronics*, **33**(11):1942–1953, November 1997.

[37] HEINRICH HORA. **Self-focusing of laser beams in a plasma by ponderomotive forces**. *Zeitschrift für Physik*, **226**(2):156–159, April 1969.

[38] G. BONNAUD, H S BRANDI, C MANUS, G MAINFRAY, AND T LEHNER. **Relativistic and ponderomotive self-focusing of a laser beam in a radially inhomogeneous plasma. II. Beyond the paraxial approximation**. *Physics of Plasmas*, **1**(4):968, 1994.

[39] HEINRICH HORA. **Theory of relativistic self-focusing of laser radiation in plasmas**. *Journal of the Optical Society of America*, **65**(8):882–5, 1975.

[40] P. SPRANGLE, C. M. TANG, AND E. ESAREY. **Relativistic Self-Focusing of Short-Pulse Radiation Beams in Plasmas** . *Ieee Transactions on Plasma Science*, **15**:1–9, April 1987.

[41] W. LU, M. TZOUFRAS, C. JOSHI, F TSUNG, W. MORI, J. VIEIRA, R. FONSECA, AND L. SILVA. **Generating multi-GeV electron bunches using single stage laser wakefield acceleration in a 3D nonlinear regime**. *Physical Review Special Topics-Accelerators and Beams*, **10**(6):061301, June 2007.

[42] C. D. DECKER, W. B. MORI, K. C. TZENG, AND T. KATSOULEAS. **Evolution of ultra-intense, short-pulse lasers in underdense plasmas**. *Physics of Plasmas*, **3**(5):2047–2056, May 1996.

[43] M. J. V. STREETER, S. KNEIP, M BLOOM, R A BENDOYRO, O. CHEKLOV, A. E. DANGOR, A DÖPP, C. HOOKER, J HOLLOWAY, J JIANG, N C LOPES, H NAKAMURA, C. A. J. PALMER, P. P. RAJEEV, D. R. SYMES, J. SCHREIBER, S. P. D. MANGLES, AND Z. NAJMUDIN. **Experimental observation of power amplification and pulse compression driven self-injection in a self-guiding laser wakefield accelerator**. *in preparation*, September 2015.

[44] D. F. GORDON, R. F. HUBBARD, J. H. COOLEY, B. HAFIZI, A. TING, AND P. SPRANGLE. **Quasimonoenergetic electrons from unphased injection into channel guided laser wakefield accelerators**. *Physical Review E*, **71**(2):026404, February 2005.

[45] W VAN DIJK, S B VAN DER GEER, M J VAN DER WIEL, AND G J H BRUSSAARD. **Parameter study of acceleration of externally injected electrons in the linear laser wakefield regime**. *Physics of Plasmas*, **15**(9):093102, 2008.

[46] T MEHRLING, J GREBENYUK, F. S. TSUNG, K FLOETTMANN, AND J. OSTERHOFF. **Transverse emittance growth in staged laser-wakefield acceleration**. *Physical Review Special Topics-Accelerators and Beams*, **15**(11):111303, November 2012.

[47] SAUL DUSHMAN. **Electron Emission from Metals as a Function of Temperature**. *Physical Review*, **21**(6):623–636, June 1923.

[48] CONYERS HERRING AND M H NICHOLS. **Thermionic Emission**. *Reviews of Modern Physics*, **21**(2):185–270, April 1949.

[49] R H FOWLER AND L NORDHEIM. **Electron Emission in Intense Electric Fields**. *Proceedings of the Royal Society A: Mathematical, Physical and Engineering Sciences*, **119**(781):173–181, May 1928.

[50] E L MURPHY AND R H GOOD. **Thermionic Emission, Field Emission, and the Transition Region**. *Physical Review*, **102**(6):1464–1473, June 1956.

[51] H HERTZ. **Ueber einen Einfluss des ultravioletten Lichtes auf die electrische Entladung**. *Annalen der Physik und Chemie*, **267**(8):983–1000, 1887.

[52] L A DUBRIDGE. **Theory of Energy Distribution of Photoelectrons**. *Physical Review*, **43**:727–741, February 1933.

[53] DAVID H DOWELL AND JOHN F SCHMERGE. **Quantum efficiency and thermal emittance of metal photocathodes**. *Physical Review Special Topics-Accelerators and Beams*, **12**(7):074201, July 2009.

[54] T PERRON, E RABEUF, E PLOUVIEZ, V SERRIERE, A PANZARELLA, AND B OGIER. **New preinjector for ESRF booster**. In *Proceedings of EPAC 2008*, pages 1–3, July 2008.

[55] D H DOWELL, R. AKRE, Y. DING, P. EMMA, J. FRISCH, S. GILEVICH, G. HAYS, P. HERING, Z. HUANG, R. IVERSON, C LIMBORG-DEPREY, H. LOOS, A. MIAHNAHRI, JOHN F SCHMERGE, J. TURNER, J. WELCH, W. WHITE, AND J. WU. **Commissioning results of the LCLS injector**. In *Proceedings of FEL 2007*, pages 1–8, March 2008.

[56] C. E. CLAYTON, M. J. EVERETT, A. LAL, D. GORDON, K. A. MARSH, AND C. JOSHI. **Acceleration and Scattering of Injected Electrons in Plasma Beat-Wave Accelerator Experiments**. *Physics of Plasmas*, **1**(5):1753–1760, November 1994.

[57] JOHN M. DAWSON. **Nonlinear Electron Oscillations in a Cold Plasma**. *Physical Review*, **113**(2):383, 1959.

[58] A.I. AKHIEZER AND R.V. POLOVIN. **Theory of Wave Motion of an Electron Plasma** . *Soviet Physics JETP*, **3**(5):696, 1956.

[59] A. MODENA, Z. NAJMUDIN, A. E. DANGOR, C. E. CLAYTON, K. A. MARSH, C. JOSHI, V. MALKA, C. B. DARROW, C. DANSON, D. NEELY, AND F. N. WALSH. **Electron Acceleration from the Breaking of Relativistic Plasma-Waves**. *Nature*, **377**(6550):606–608, October 1995.

[60] VICTOR MALKA, S. FRITZLER, E. LEFEBVRE, M-M ALEONARD, F. BURGY, J. P. CHAMBARET, J-F CHEMIN, K. KRUSHELNICK, G MALKA, AND SPD MANGLES. **Electron acceleration by a wake field forced by an intense ultrashort laser pulse**. *Science (New York, NY)*, **298**(5598):1596–1600, 2002.

[61] A. PUKHOV AND J. MEYER-TER VEHN. **Laser wake field acceleration: the highly non-linear broken-wave regime**. *Applied Physics B-Lasers and Optics*, **74**(4-5):355–361, April 2002.

[62] J. FAURE, Y. GLINEC, A. PUKHOV, S. KISELEV, S. GORDIENKO, E. LEFEBVRE, J. P. ROUSSEAU, F. BURGY, AND V. MALKA. **A laser-plasma accelerator producing monoenergetic electron beams**. *Nature*, **431**(7008):541–544, September 2004.

[63] S. P. D. MANGLES, C. D. MURPHY, Z. NAJMUDIN, A. G. R. THOMAS, J. L. COLLIER, A. E. DANGOR, E. J. DIVALL, P. S. FOSTER, J. G. GALLACHER, C. J. HOOKER, D. A. JAROSZYNSKI, A. J. LANGLEY, W. B. MORI, P. A. NORREYS, F. S. TSUNG, R. VISKUP, B. R. WALTON, AND K. KRUSHELNICK. **Monoenergetic beams of relativistic electrons from intense laser-plasma interactions**. *Nature*, **431**(7008):535–538, September 2004.

[64] C. G. R. GEDDES, C. TOTH, J. VAN TILBORG, E. ESAREY, C. B. SCHROEDER, D. BRUHWILER, C. NIETER, J. CARY, AND W. P. LEEMANS. **High-quality electron beams from a laser wakefield accelerator using plasma-channel guiding**. *Nature*, **431**(7008):538–541, September 2004.

[65] S. CORDE, A. LIFSCHITZ, G. LAMBERT, K. TA PHUOC, X. DAVOINE, R LEHE, D. DOUILLET, A. ROUSSE, V. MALKA, AND C. THAURY. **Observation of longitudinal and transverse self-injections in laser-plasma accelerators**. *Nature Communications*, **4**:1501–7, February 2013.

[66] V. MALKA. **Laser plasma accelerators**. *Physics of Plasmas*, **19**(5):055501, 2012.

[67] S. BULANOV, N. NAUMOVA, F. PEGORARO, AND J. SAKAI. **Particle injection into the wave acceleration phase due to nonlinear wake wave breaking**. *Physical Review E*, **58**:R5257–R5260, November 1998.

[68] C. G. R. GEDDES, K. NAKAMURA, G. R. PLATEAU, C. TOTH, E. CORMIER-MICHEL, E. ESAREY, C. B. SCHROEDER, J. R. CARY, AND W. P. LEEMANS. **Plasma-density-gradient injection of low absolute-momentum-spread electron bunches**. *Physical Review Letters*, **100**(21):215004, May 2008.

[69] H. Suk, N. Barov, J. B. Rosenzweig, and E. Esarey. **Plasma electron trapping and acceleration in a plasma wake field using a density transition**. *Physical Review Letters*, **86**(6):1011–1014, February 2001.

[70] K. Schmid, A. Buck, C. M. S. Sears, J M Mikhailova, R. Tautz, D. Herrmann, M. Geissler, F. Krausz, and L. Veisz. **Density-transition based electron injector for laser driven wakefield accelerators**. *Physical Review Special Topics-Accelerators and Beams*, **13**(9):091301, September 2010.

[71] A. Buck, J Wenz, J Xu, K Khrennikov, K. Schmid, M Heigoldt, J M Mikhailova, M. Geissler, B Shen, F. Krausz, S. Karsch, and L. Veisz. **Shock-Front Injector for High-Quality Laser-Plasma Acceleration**. *Physical Review Letters*, **110**(18):185006, May 2013.

[72] K P Singh. **Self-injection and acceleration of electrons during ionization of gas atoms by a short laser pulse**. *Physics of Plasmas*, **13**(4):043101, 2006.

[73] E. Oz, S. Deng, T. Katsouleas, P. Muggli, C. D. Barnes, I. Blumenfeld, F. J. Decker, P. Emma, M. J. Hogan, R. Ischebeck, R. H. Iverson, N. Kirby, P. Krejcik, C. O'Connell, R. H. Siemann, D. Walz, D. Auerbach, C. E. Clayton, C. Huang, D. K. Johnson, C. Joshi, W. Lu, K. A. Marsh, W. B. Mori, and M. Zhou. **Ionization-induced electron trapping in ultrarelativistic plasma wakes**. *Physical Review Letters*, **98**(8):084801, February 2007.

[74] M. Chen, E. Esarey, C. B. Schroeder, C. G. R. Geddes, and W. P. Leemans. **Theory of ionization-induced trapping in laser-plasma accelerators**. *Physics of Plasmas*, **19**(3):033101, 2012.

[75] C. E. Clayton, J. E. Ralph, F. Albert, R. A. Fonseca, S. H. Glenzer, C. Joshi, W. Lu, K. A. Marsh, S. F. Martins, W. B. Mori, A. Pak, F. S. Tsung, B. B. Pollock, J. S. Ross, L. O. Silva, and D. H. Froula. **Self-Guided Laser Wakefield Acceleration beyond 1 GeV Using Ionization-Induced Injection**. *Physical Review Letters*, **105**:105003, September 2010.

[76] C. McGuffey, A. G. R. Thomas, W. Schumaker, T. Matsuoka, V. Chvykov, F. J. Dollar, G. Kalintchenko, V. Yanovsky, A. Maksimchuk, K. Krushelnick, V. Yu Bychenkov, I. V. Glazyrin, and A. V. Karpeev. **Ionization Induced Trapping in a Laser Wakefield Accelerator**. *Physical Review Letters*, **104**(2):025004, 2010.

[77] X. Davoine, E. Lefebvre, C. Rechatin, J. Faure, and V. Malka. **Cold Optical Injection Producing Monoenergetic, Multi-GeV Electron Bunches**. *Physical Review Letters*, **102**(6):065001, 2009.

[78] C. Rechatin, J. Faure, A. Ben-Ismail, J. Lim, R. Fitour, A. Specka, H. Videau, A. Tafzi, F. Burgy, and V. Malka. **Controlling the Phase-Space Volume of Injected Electrons in a Laser-Plasma Accelerator**. *Physical Review Letters*, **102**(16):164801, April 2009.

[79] I. Kostyukov, E. Nerush, A. Pukhov, and V. Seredov. **Electron Self-Injection in Multidimensional Relativistic-Plasma Wake Fields**. *Physical Review Letters*, **103**(17):175003, October 2009.

[80] S. Kalmykov, S. A. Yi, V. Khudik, and G. Shvets. **Electron Self-Injection and Trapping into an Evolving Plasma Bubble**. *Physical Review Letters*, **103**(13):135004, September 2009.

[81] S. Kalmykov, A Beck, S. A. Yi, V N Khudik, M. C. Downer, E. Lefebvre, B. A. Shadwick, and D. P. Umstadter. **Electron self-injection into an evolving plasma bubble: Quasi-monoenergetic laser-plasma acceleration in the blowout regime**. *Physics of Plasmas*, **18**(5):056704, 2011.

[82] C Benedetti, C. B. Schroeder, E. Esarey, F Rossi, and W. P. Leemans. **Numerical investigation of electron self-injection in the nonlinear bubble regime**. *Physics of Plasmas*, **20**(10):103108, 2013.

[83] S. P. D. Mangles, G. Genoud, M S Bloom, M. Burza, Z. Najmudin, A. Persson, K Svensson, A. G. R. Thomas, and C. G. Wahlstrom. **Self-injection threshold in self-guided laser wakefield accelerators**. *Physical Review Special Topics-Accelerators and Beams*, **15**(1):011302, January 2012.

[84] S. Banerjee, S Y Kalmykov, N D Powers, G Golovin, V. Ramanathan, N J Cunningham, K J Brown, S. Chen, I Ghebregziabher, B. A. Shadwick, D. P. Umstadter, B M Cowan, D L Bruhwiler, A Beck, and E. Lefebvre. **Stable, tunable, quasimonoenergetic electron beams produced in a laser wakefield near the threshold for self-injection**. *Physical Review Special Topics-Accelerators and Beams*, **16**(3):031302, March 2013.

[85] Hyyong Suk, Hae June Lee, and In Soo Ko. **Generation of high-energy electrons by a femtosecond terawatt laser propagating through a sharp downward density transition**. *Journal of the Optical Society of America B*, **21**(7):1391–1396, 2004.

[86] M. C. Thompson, J. B. Rosenzweig, and H. Suk. **Plasma density transition trapping as a possible high-brightness electron beam source**. *Physical Review Special Topics-Accelerators and Beams*, **7**(1):011301, January 2004.

[87] S. Fourmaux, K. Ta Phuoc, P Lassonde, S. Corde, G Lebrun, V. Malka, A. Rousse, and J. C. Kieffer. **Quasi-monoenergetic electron beams production in a sharp density transition**. *Applied Physics Letters*, **101**(11):111106, 2012.

[88] M. Burza, A Gonoskov, K Svensson, F. Wojda, A. Persson, M Hansson, G. Genoud, M Marklund, C. G. Wahlstrom, and O. Lundh. **Laser wakefield acceleration using wire produced double density ramps**. *Physical Review Special Topics-Accelerators and Beams*, **16**(1):011301, January 2013.

[89] EMILIEN GUILLAUME. *Control of electron injection and acceleration in Laser-Wakefield Accelerators*. PhD thesis, Ecole Polytechnique, December 2015.

[90] D. BAUER, P. MULSER, A MACCHI, E CONEJERO JARQUE, AND R R E SALOMAA. **Ultrafast Ionization: TDSE Calculationsand Intense Laser Pulse–Solid Interaction**. *Laser Physics*, **9**:58–68, September 1999.

[91] ARTHUR PAK. *Injection of Tunnel Ionized Electrons into Laser-Produced Wakes*. PhD thesis, University of California, Los Angeles, August 2010.

[92] D. BAUER AND P. MULSER. **Exact field ionization rates in the barrier-suppression regime from numerical time-dependent Schrödinger-equation calculations**. *Physical Review A*, **59**:1–9, January 1999.

[93] V P KRAINOV. **Ionization rates and energy and angular distributions at the barrier-suppression ionization of complex atoms and atomic ions**. *Journal of the Optical Society of America B*, **14**(2):425–431, February 1997.

[94] X M TONG AND C D LIN. **Empirical formula for static field ionization rates of atoms and molecules by lasers in the barrier-suppression regime**. *Journal of Physics B-Atomic Molecular and Optical Physics*, **38**(15):2593–2600, July 2005.

[95] M. CHEN, E. CORMIER-MICHEL, C. G. R. GEDDES, D L BRUHWILER, L L YU, E. ESAREY, C. B. SCHROEDER, AND W. P. LEEMANS. **Numerical modeling of laser tunneling ionization in explicit particle-in-cell codes**. *Journal of Computational Physics*, **236**(C):220–228, March 2013.

[96] JEAN-PIERRE DELAHAYE. **Towards CLIC feasibility**. In *IPAC 2010*, May 2010.

[97] JAN WILHELM KOVERMANN. *Comparative studies of high-gradient RF and DC breakdowns*. PhD thesis, RWTH Aachen, 2010.

[98] W D KILPATRICK. **Criterion for vacuum sparking designed to include both rf and dc**. *Review of Scientific Instruments*, **28**(10):824–826, 1957.

[99] J W WANG AND G A LOEW. **Field emission and rf breakdown in high-gradient room-temperature linac structures**. *SLAC PUB*, **7684**, 1997.

[100] F. S. TSUNG, R. NARANG, W. B. MORI, C. JOSHI, R. A. FONSECA, AND L. O. SILVA. **Near-GeV-energy laser-wakefield acceleration of self-injected electrons in a centimeter-scale plasma channel**. *Physical Review Letters*, **93**(18):185002, October 2004.

[101] I. BLUMENFELD, C. E. CLAYTON, F. J. DECKER, M. J. HOGAN, C. K. HUANG, R. ISCHEBECK, R. IVERSON, C. JOSHI, T. KATSOULEAS, N. KIRBY, W. LU, K. A. MARSH, W. B. MORI, P. MUGGLI, E. OZ, R. H. SIEMANN, D. WALZ, AND M. M. ZHOU. **Energy doubling of 42 GeV electrons in a metre-scale plasma wakefield accelerator**. *Nature*, **445**(7129):741–744, February 2007.

[102] O. LUNDH, J. LIM, C. RECHATIN, L AMMOURA, A. BEN-ISMAIL, X. DAVOINE, G GALLOT, J P GODDET, E. LEFEBVRE, V. MALKA, AND J. FAURE. **Few femtosecond, few kiloampere electron bunch produced by a laser–plasma accelerator**. *Nature Physics*, **7**(3):219–222, January 2011.

[103] BERNHARD HIDDING. **Prospects for advanced combined laser and beam driven plasma accelerators**. In *Prospects for advanced combined laser and beam driven plasma accelerators*, September 2015.

[104] S. CORDE, C. THAURY, K. TA PHUOC, A. LIFSCHITZ, G. LAMBERT, J. FAURE, O. LUNDH, E. BENVENISTE, A. BEN-ISMAIL, L. ARANTCHUK, A. MARCINIAK, A. STORDEUR, P. BRIJESH, A. ROUSSE, A. SPECKA, AND V. MALKA. **Mapping the X-Ray Emission Region in a Laser-Plasma Accelerator**. *Physical Review Letters*, **107**:215004, November 2011.

[105] P E MASSON-LABORDE, M Z MO, A ALI, S. FOURMAUX, P LASSONDE, J. C. KIEFFER, W. ROZMUS, D. TEYCHENNE, AND R FEDOSEJEVS. **Giga-electronvolt electrons due to a transition from laser wakefield acceleration to plasma wakefield acceleration**. *Physics of Plasmas*, **21**(12):123113, December 2014.

[106] P. SPRANGLE, B. HAFIZI, J R PEÑANO, R. F. HUBBARD, A. TING, C. I. MOORE, D. F. GORDON, A. ZIGLER, D. KAGANOVICH, AND T. M. ANTONSEN. **Wakefield generation and GeV acceleration in tapered plasma channels**. *Physical Review E*, **63**(5):056405, April 2001.

[107] A. PUKHOV AND I. KOSTYUKOV. **Control of laser-wakefield acceleration by the plasma-density profile**. *Physical Review E*, **77**(2):025401–4, February 2008.

[108] W RITTERSHOFER, C. B. SCHROEDER, E. ESAREY, F J GRÜNER, AND W. P. LEEMANS. **Tapered plasma channels to phase-lock accelerating and focusing forces in laser-plasma accelerators**. *Physics of Plasmas*, **17**(6):063104, 2010.

[109] K. TA PHUOC, E. ESAREY, V. LEURENT, E. CORMIER-MICHEL, C. G. R. GEDDES, C. B. SCHROEDER, A. ROUSSE, AND W. P. LEEMANS. **Betatron radiation from density tailored plasmas**. *Physics of Plasmas*, **15**(6):063102, 2008.

[110] W. LU, C. HUANG, M. ZHOU, W. B. MORI, AND T. KATSOULEAS. **Nonlinear Theory for Relativistic Plasma Wakefields in the Blowout Regime**. *Physical Review Letters*, **96**:165002, April 2006.

[111] W. LU, C. HUANG, M. ZHOU, M. TZOUFRAS, F. S. TSUNG, W. B. MORI, AND T. KATSOULEAS. **A nonlinear theory for multidimensional relativistic plasma wave wakefields**. *Physics of Plasmas*, **13**:056709, October 2006.

[112] REMI LEHE, A. LIFSCHITZ, C. THAURY, V. MALKA, AND X. DAVOINE. **Numerical growth of emittance in simulations of laser-wakefield acceleration**. *Physical Review Special Topics-Accelerators and Beams*, **16**(2):021301, February 2013.

[113] MARTIN REISER. *Theory and Design of Charged Particle Beams*. Wiley-VCH Verlag GmbH, Weinheim, Germany, September 1994.

[114] S. FRITZLER, E. LEFEBVRE, V. MALKA, F. BURGY, A. E. DANGOR, K. KRUSHELNICK, S. P. D. MANGLES, Z. NAJMUDIN, J. P. ROUSSEAU, AND B. WALTON. **Emittance measurements of a laser-wakefield-accelerated electron beam**. *Physical Review Letters*, **92**(16):165006, April 2004.

[115] S. KNEIP, C. MCGUFFEY, J. L. MARTINS, M S BLOOM, V. CHVYKOV, F. DOLLAR, R. FONSECA, S JOLLY, G. KALINTCHENKO, K. KRUSHELNICK, A. MAKSIMCHUK, S. P. D. MANGLES, Z. NAJMUDIN, C. A. J. PALMER, K. TA PHUOC, W. SCHUMAKER, L. O. SILVA, J. VIEIRA, V. YANOVSKY, AND A. G. R. THOMAS. **Characterization of transverse beam emittance of electrons from a laser-plasma wakefield accelerator in the bubble regime using betatron x-ray radiation**. *Physical Review Special Topics-Accelerators and Beams*, **15**(2):021302, February 2012.

[116] M MIGLIORATI, A BACCI, C BENEDETTI, E CHIADRONI, M. FERRARIO, A MOSTACCI, L PALUMBO, A R ROSSI, L. SERAFINI, AND P ANTICI. **Intrinsic normalized emittance growth in laser-driven electron accelerators**. *Physical Review Special Topics-Accelerators and Beams*, **16**(1):011302, January 2013.

[117] P. CHEN, J. J. SU, T. KATSOULEAS, S. WILKS, AND J. M. DAWSON. **Plasma Focusing for High-Energy Beams**. *Plasma Science, IEEE Transactions on*, **15**(2):218–225, 1987.

[118] J. B. ROSENZWEIG AND PISIN CHEN. **Beam optics of a self-focusing plasma lens**. *Physical Review D*, **39**(7):2039–2045, April 1989.

[119] J. B. ROSENZWEIG, P SCHOESSOW, B COLE, C HO, W GAI, R KONECNY, S MTINGWA, J NOREM, M ROSING, AND J SIMPSON. **Demonstration of electron beam self-focusing in plasma wake fields**. *Physics of Fluids B-Plasma Physics*, **2**(6):1376, 1990.

[120] H. NAKANISHI, Y. YOSHIDA, T. UEDA, T KOZAWA, H. SHIBATA, K. NAKAJIMA, T. KURIHARA, N. YUGAMI, Y. NISHIDA, T. KOBAYASHI, A. ENOMOTO, T. OOGOE, H. KOBAYASHI, B S NEWBERGER, S. TAGAWA, K MIYA, AND A. OGATA. **Direct observation of plasma-lens effect**. *Physical Review Letters*, **66**(14):1870–1873, April 1991.

[121] J S T NG, P. CHEN, H BALDIS, P BOLTON, D CLINE, W CRADDOCK, C CRAWFORD, F. J. DECKER, C FIELD, Y FUKUI, V KUMAR, R. IVERSON, F KING, R E KIRBY, K. NAKAJIMA, R NOBLE, A. OGATA, P. RAIMONDI, D. WALZ, AND A. W. WEIDEMANN. **Observation of Plasma Focusing of a 28.5 GeV Positron Beam**. *Physical Review Letters*, **87**(24):244801, November 2001.

[122] G HAIRAPETIAN, P DAVIS, C. E. CLAYTON, C. JOSHI, S C HARTMAN, C. PELLEGRINI, AND T. KATSOULEAS. **Experimental demonstration of dynamic focusing of a relativistic electron bunch by an overdense plasma lens**. *Physical Review Letters*, **72**(15):2403–2406, April 1994.

[123] MARTIN REISER. *Theory and design of charged particle beams*. John Wiley & Sons, 2008.

[124] HELMUT WIEDEMANN. *Particle Accelerator Physics*. Springer International Publishing, 4 edition, February 2015.

[125] KLAUS WILLE. *The physics of particle accelerators: an introduction*. Oxford University Press, 2000.

[126] C. JOSHI, B. BLUE, C. E. CLAYTON, E. DODD, C. HUANG, K. A. MARSH, W. B. MORI, S. WANG, M. J. HOGAN, C. O'CONNELL, R. SIEMANN, D. WATZ, P. MUGGLI, T. KATSOULEAS, AND S. LEE. **High energy density plasma science with an ultrarelativistic electron beam**. *Physics of Plasmas*, **9**(5):1845, 2002.

[127] PISIN CHEN. **A possible final focusing mechanism for linear colliders**. *Particle Accelerators*, **20**:171, 1987.

[128] F BOSI, P FABBRICATORE, S FARINON, U GAMBARDELLA, R MUSENICH, R MARABOTTO, AND E PAOLONI. **Compact Superconducting High Gradient Quadrupole Magnets for the Interaction Regions of High Luminosity Colliders**. *IEEE Transactions on Applied Superconductivity*, **23**(3):4001004–4001004, August 2013.

[129] DEREK SHUMAN, ANDY FALTENS, Y KAJIYAMA, M KIREEFF-COVO, AND P SEIDL. **A Compact High Gradient Pulsed Magnetic Quadrupole**. In *Particle Accelerator Conference, 2005. PAC 2005. Proceedings of the*, pages 3771–3773. IEEE, 2005.

[130] E BOGGASCH, J JAKOBY, H WAHL, K G DIETRICH, D H H HOFFMANN, W LAUX, M ELFERS, C R HAAS, V P DUBENKOV, AND A A GOLUBEV. **z -pinch plasma lens focusing of a heavy-ion beam**. *Physical Review Letters*, **66**:1705–1708, April 1991.

[131] JOHN D. JACKSON. *Classical Electrodynamics*. Wiley, New York, 2 edition, 1990.

[132] S. KARSCH, J. OSTERHOFF, A. POPP, T. P. ROWLANDS-REES, Z. MAJOR, M. FUCHS, B. MARX, R. HORLEIN, K. SCHMID, L. VEISZ, S. BECKER, U. SCHRAMM, B. HIDDING, G. PRETZLER, D. HABS, F. GRUNER, F. KRAUSZ, AND S. M. HOOKER. **GeV-scale electron acceleration in a gas-filled capillary discharge waveguide**. *New Journal of Physics*, **9**:415, November 2007.

[133] Remi Lehe, C. Thaury, E Guillaume, A. Lifschitz, and V. Malka. **Laser-plasma lens for laser-wakefield accelerators**. *Physical Review Special Topics-Accelerators and Beams*, **17**(12):121301, December 2014.

[134] Remi Lehe, C. Thaury, A. Lifschitz, J. M. Rax, and V. Malka. **Transverse dynamics of an intense electron bunch traveling through a pre-ionized plasma**. *Physics of Plasmas*, **21**(4):043104, April 2014.

[135] R. Weingartner, M. Fuchs, A. Popp, S Raith, S. Becker, S Chou, M Heigoldt, K Khrennikov, J Wenz, T Seggebrock, B. Zeitler, Zs Major, J. Osterhoff, F. Krausz, S. Karsch, and F. Gruner. **Imaging laser-wakefield-accelerated electrons using miniature magnetic quadrupole lenses**. *Physical Review Special Topics-Accelerators and Beams*, **14**(5):052801, May 2011.

[136] Jerrold T Bushberg and John M Boone. *The essential physics of medical imaging*. Lippincott Williams & Wilkins, 2011.

[137] S Hanna. *RF Linear Accelerators for Medical and Industrial Applications*. ARTECH HOUSE, June 2012.

[138] R J Tompkins, I P Mercer, M Fettweis, C J Barnett, D R Klug, Lord G Porter, I Clark, S Jackson, P. Matousek, A W Parker, and M. Towrie. **5–20 keV laser-induced x-ray generation at 1 kHz from a liquid-jet target**. *Review of Scientific Instruments*, **69**(9):3113–3117, September 1998.

[139] Daniel H Larsson, Ulf Lundström, Ulrica K Westermark, Marie Arsenian Henriksson, Anna Burvall, and Hans M Hertz. **First application of liquid-metal-jet sources for small-animal imaging: High-resolution CT and phase-contrast tumor demarcation**. *Medical Physics*, **40**(2):021909, 2013.

[140] J. D. Watson and F. H. C. Crick. **Molecular Structure of Nucleic Acids: A Structure for Deoxyribose Nucleic Acid**. *Nature*, **171**(4356):737–738, 1953.

[141] Rosalind E Franklin and R G Gosling. **Molecular Configuration in Sodium Thymonucleate**. *Nature*, **171**(4356):740–741, April 1953.

[142] Mikael Otendal. **A compact high-brightness liquid-metal-jet X-ray source**. pages 1–75. Royal Institute of Technology, Stockholm, May 2006.

[143] Antoine Rousse, Christian Rischel, and Jean-Claude Gauthier. **Femtosecond x-ray crystallography**. *Reviews of Modern Physics*, **73**(1):17, 2001.

[144] T Anderson, I Tomov, and P Rentzepis. **Laser-driven metal photocathodes for picosecond electron and x-ray pulse generation**. *Journal of Applied Physics*, **71**(10):5161–5167, 1992.

[145] A Egbert, B Mader, B Tkachenko, C Fallnich, B N Chichkov, H Stiel, and P V Nickles. **High-repetition rate femtosecond laser-driven hard-x-ray source**. *Applied Physics Letters*, **81**(13):2328, 2002.

[146] M. M. Murnane, H. C. Kapteyn, M D Rosen, and R. W. Falcone. **Ultrafast X-ray Pulses from Laser-Produced Plasmas.** *Science*, **251**(4993):531–536, February 1991.

[147] A. Rousse, P. Audebert, J. P. Geindre, F. Fallies, J. C. Gauthier, A. Mysyrowicz, G. Grillon, and A. Antonetti. **Efficient K-Alpha-X-Ray Source from Femtosecond Laser-Produced Plasmas**. *Physical Review E*, **50**(3):2200–2207, September 1994.

[148] L. M. Chen, P Forget, S. Fourmaux, J. C. Kieffer, A. Krol, C C Chamberlain, B. X. Hou, J. Nees, and G. Mourou. **Study of hard x-ray emission from intense femtosecond Ti:sapphire laser–solid target interactions**. *Physics of Plasmas*, **11**(9):4439, 2004.

[149] R. Toth, J. C. Kieffer, S. Fourmaux, T. Ozaki, and A. Krol. **In-line phase-contrast imaging with a laser-based hard x-ray source**. *Review of Scientific Instruments*, **76**(8):083701–083701–6, 2005.

[150] J. Uhlig, W. Fullagar, J N Ullom, W B Doriese, J W Fowler, D S Swetz, N Gador, S E Canton, K Kinnunen, I J Maasilta, C D Reintsema, D A Bennett, L R Vale, G C Hilton, K D Irwin, D R Schmidt, and V. Sundstrom. **Table-Top Ultrafast X-Ray Microcalorimeter Spectrometry for Molecular Structure**. *Physical Review Letters*, **110**(13):138302, March 2013.

[151] R.D. Edwards, M A Sinclair, T J Goldsack, K. Krushelnick, F. N. Beg, E. L. Clark, A. E. Dangor, Z. Najmudin, M. Tatarakis, B. Walton, M. Zepf, K. W. D. Ledingham, I Spencer, P. A. Norreys, R. J. Clarke, R Kodama, Y. Toyama, and M. Tampo. **Characterization of a gamma-ray source based on a laser-plasma accelerator with applications to radiography**. *Applied Physics Letters*, **80**(12):2129, 2002.

[152] Y. Glinec, J. Faure, L. Le Dain, S. Darbon, T. Hosokai, J. J. Santos, E. Lefebvre, J. P. Rousseau, F. Burgy, B. Mercier, and V. Malka. **High-Resolution gamma -Ray Radiography Produced by a Laser-Plasma Driven Electron Source**. *Physical Review Letters*, **94**(2):025003, 2005.

[153] A. Ben-Ismail, O. Lundh, C. Rechatin, J. K. Lim, J. Faure, S. Corde, and V. Malka. **Compact and high-quality gamma-ray source applied to 10 micrometer-range resolution radiography**. *Applied Physics Letters*, **98**(26):264101–264101–3, 2011.

[154] A. Giulietti, N. Bourgeois, T. Ceccotti, X. Davoine, S Dobosz, P. D'Oliveira, M Galimberti, J Galy, A Gamucci, D. Giulietti, L A Gizzi, D J Hamilton, E. Lefebvre, L Labate, J. R. Marques,

P. MONOT, H POPESCU, F. REAU, G SARRI, P. TOMASSINI, AND P MARTIN. **Intense gamma-Ray Source in the Giant-Dipole-Resonance Range Driven by 10-TW Laser Pulses**. *Physical Review Letters*, **101**(10):105002, September 2008.

[155] M J BERGER. **NIST Radiation Dosimetry Data** [online].

[156] A L MEADOWCROFT, C. D. BENTLEY, AND E N STOTT. **Evaluation of the sensitivity and fading characteristics of an image plate system for x-ray diagnostics**. *Review of Scientific Instruments*, **79**(11):113102, 2008.

[157] S AGOSTINELLI. **Geant4 a simulation toolkit**. *Nuclear Instruments and Methods in Physics Research Section A - Accelerators, Spectrometers, Detectors and Associated Equipment*, **506**(3):250–303, 2003.

[158] S. CORDE, K. TA PHUOC, G. LAMBERT, R. FITOUR, V. MALKA, A. ROUSSE, A BECK, AND E. LEFEBVRE. **Femtosecond x rays from laser-plasma accelerators**. *Reviews of Modern Physics*, **85**(1):1–48, January 2013.

[159] E WIECHERT. **Elektrodynamische Elementargesetze**. *Annalen der Physik*, **309**(4):667–689, 1901.

[160] A FRIEDMAN, A GOVER, G KURIZKI, S RUSCHIN, AND A YARIV. **Spontaneous and stimulated emission from quasifree electrons**. *Reviews of Modern Physics*, **60**(2):471, 1988.

[161] GEORGE NEIL AND LIA MARINGA. **Technical approaches for high-average-power free-electron lasers**. *Reviews of Modern Physics*, **74**:685–701, July 2002.

[162] K HALBACH. **Permanent Magnet Undulators**. *Le Journal de Physique Colloques*, **44**(C1):C1–211–C1–216, February 1983.

[163] SHIGEMI SASAKI, TAIHEI SHIMADA, KEN-ICHI YANAGIDA, HIDEKI KOBAYASHI, AND YOSHIKAZU MIYAHARA. **First observation of undulator radiation from APPLE-1**. *Nuclear Instruments and Methods in Physics Research*, **347**:87–91, 1994.

[164] O CHUBAR, P. ELLEAUME, AND J CHAVANNE. **A three-dimensional magnetostatics computer code for insertion devices**. *Journal of Synchrotron Radiation*, **5**(3):481–484, 1998.

[165] H. P. SCHLENVOIGT, K. HAUPT, A. DEBUS, F. BUDDE, O. JACKEL, S. PFOTENHAUER, H. SCHWOERER, E. ROHWER, J. G. GALLACHER, E. BRUNETTI, R. P. SHANKS, S. M. WIGGINS, AND D. A. JAROSZYNSKI. **A compact synchrotron radiation source driven by a laser-plasma wakefield accelerator**. *Nature Physics*, **4**(2):130–133, February 2008.

[166] M. FUCHS, R. WEINGARTNER, A. POPP, Z. MAJOR, S. BECKER, J. OSTERHOFF, I. CORTRIE, B. ZEITLER, R. HORLEIN, G. D. TSAKIRIS, U. SCHRAMM, T. P. ROWLANDS-REES, S. M. HOOKER, D. HABS, F. KRAUSZ, S. KARSCH, AND F. GRUNER. **Laser-driven soft-X-ray undulator source**. *Nature Physics*, **5**(11):826–829, November 2009.

[167] MATTHIAS FUCHS. *Laser-driven soft-X-ray undulator source*. PhD thesis, Ludwig-Maximilians-Universität München, August 2010.

[168] STEFFEN HILLENBRAND, RALPH ASSMANN, ANKE-SUSANNE MÜLLER, OLIVER JANSEN, VITALI JUDIN, AND ALEXANDER PUKHOV. **Study of Laser Wakefield Accelerators as injectors for Synchrotron light sources**. *Nuclear Instruments and Methods in Physics Research Section A - Accelerators, Spectrometers, Detectors and Associated Equipment*, **740**(C):153–157, March 2014.

[169] F. GRUNER, S. BECKER, U. SCHRAMM, M. FUCHS, R. WEINGARTNER, D. HABS, J. MEYER-TER VEHN, M. GEISSLER, M. FERRARIO, L. SERAFINI, B. VAN DER GEER, H. BACKE, W. LAUTH, AND S. REICHE. **Design considerations for table-top, laser-based VUV and X-ray free electron lasers**. *Applied Physics B-Lasers and Optics*, **86**(3):431–435, February 2007.

[170] M E COUPRIE, C BENABDERRAHMANE, P BETINELLI, F BOUVET, A BUTEAU, L CASSINARI, J DAILLANT, J C DENARD, P EYMARD, B GAGEY, C HERBEAUX, M LABAT, B LAGARDE, A LESTRADE, A LOULERGUE, P MARCHAND, J L MARLATS, C MIRON, P MORIN, A NADJI, F POLACK, J B PRUVOST, F RIBEIRO, J P RICAUD, P ROY, T TANIKAWA, R ROUX, S BIELAWSKI, C EVAIN, C SZWAJ, G. LAMBERT, A. LIFSCHITZ, V. MALKA, R LEHE, A. ROUSSE, K. TA PHUOC, C. THAURY, G DEVANZ, M LUONG, B. CARRE, G LEBEC, L FARVACQUE, A DUBOIS, AND J. LUNING. **The LUNEX5 project in France**. *Journal of Physics: Conference Series*, **425**(7):072001, March 2013.

[171] RICHARD H MILBURN. **Electron Scattering by an Intense Polarized Photon Field**. *Physical Review Letters*, **75**, February 1963.

[172] F R ARUTYUNIAN AND V A TUMANIAN. **The Compton effect on relativistic electrons and the possibility of obtaining high energy beams**. *Physics Letters*, **4**(3):176–178, 1963.

[173] CARLO BEMPORAD, RICHARD H MILBURN, T NOBUTUKI, AND MIRCEA TOTINO. **High-Energy Photons from Compton Scattering of Light on 6. 0-GeV Electrons**. *Physical Review*, **138**(68), 1965.

[174] A D'ANGELO, O BARTALINI, V BELLINI, P LEVI SANDRI, D MORICCIANI, L NICOLETTI, AND A ZUCCHIATTI. **Generation of Compton backscattering gamma-ray beams**. *Nuclear Instruments and Methods*, **455**(1):1–6, November 2000.

[175] R. W. SCHOENLEIN, W. P. LEEMANS, A. H. CHIN, P. VOLFBEYN, T. E. GLOVER, P. BALLING, M. ZOLOTOREV, K. J. KIM, S. CHATTOPADHYAY, AND C. V. SHANK. **Femtosecond x-ray pulses at 0.4 angstrom generated**

by 90 degrees Thomson scattering: A tool for probing the structural dynamics of materials. *Science*, **274**(5285):236–238, October 1996.

[176] H. Schwoerer, B. Liesfeld, H. P. Schlenvoigt, K. U. Amthor, and R. Sauerbrey. **Thomson-Backscattered X Rays From Laser-Accelerated Electrons**. *Physical Review Letters*, **96**:014802, January 2006.

[177] K. Ta Phuoc, S. Corde, C. Thaury, V. Malka, A. Tafzi, J P Goddet, R. C. Shah, S. Sebban, and A. Rousse. **All-optical Compton gamma-ray source**. *Nature Photonics*, **6**(5):308–311, April 2012.

[178] Hai-En Tsai, Xiaoming Wang, Joseph Shaw, Zhengyan Li, Alexey V Arefiev, Xi Zhang, Rafal Zgadzaj, Watson Henderson, V. Khudik, G. Shvets, and M. C. Downer. **Compact tunable Compton x-ray source from laser-plasma accelerator and plasma mirror**. *Physics of Plasmas*, **22**:1–10, February 2015.

[179] S. Chen, N D Powers, I Ghebregziabher, C M Maharjan, C Liu, G Golovin, S. Banerjee, J. Zhang, N. Cunningham, A Moorti, S Clarke, S. Pozzi, and D. P. Umstadter. **MeV-Energy X Rays from Inverse Compton Scattering with Laser-Wakefield Accelerated Electrons**. *Physical Review Letters*, **110**(15):155003, April 2013.

[180] K Khrennikov, J Wenz, A. Buck, J Xu, M Heigoldt, L. Veisz, and S. Karsch. **Tunable All-Optical Quasimonochromatic Thomson X-Ray Source in the Nonlinear Regime**. *Physical Review Letters*, **114**:195003, May 2015.

[181] N D Powers, I Ghebregziabher, G Golovin, C Liu, S. Chen, S. Banerjee, J. Zhang, and D. P. Umstadter. **Quasi-monoenergetic and tunable X-rays from a laser-driven Compton light source**. *Nature Photonics*, pages 1–4, November 2013.

[182] G Sarri, D J Corvan, W. Schumaker, J M Cole, A Di PIazza, H Ahmed, A Harvey, C H Keitel, K. Krushelnick, S. P. D. Mangles, Z. Najmudin, D Symes, A. G. R. Thomas, M Yeung, Z Zhao, and M. Zepf. **Ultrahigh Brilliance Multi-MeV gamma-Ray Beams from Nonlinear Relativistic Thomson Scattering**. *Physical Review Letters*, **113**:224801, November 2014.

[183] Cheng Liu, Grigory Golovin, Shouyuan Chen, Jun Zhang, Baozhen Zhao, Daniel Haden, Sudeep Banerjee, Jack Silano, Hugon Karwowski, and Donald Umstadter. **Generation of 9 MeV gamma-ray by all-laser-driven Compton scattering with second-harmonic laser light**. *Optics Letters*, **39**(14):4132, 2014.

[184] I A Andriyash, R Lehe, and V. Malka. **A spectral unaveraged algorithm for free electron laser simulations**. *Journal of Computational Physics*, 2015.

[185] A. D. Debus, M. Bussmann, M Siebold, A. Jochmann, U. Schramm, T. E. Cowan, and R. Sauerbrey. **Traveling-wave Thomson scattering and optical undulators for high-yield EUV and X-ray sources**. *Applied Physics B-Lasers and Optics*, **100**(1):61–76, May 2010.

[186] Shuoqin Wang, C. Clayton, B. Blue, E. Dodd, K Marsh, W. Mori, C. Joshi, S. Lee, P. Muggli, T. Katsouleas, F Decker, M Hogan, R. Iverson, P. Raimondi, D. Walz, R. Siemann, and R. Assmann. **X-Ray Emission from Betatron Motion in a Plasma Wiggler**. *Physical Review Letters*, **88**(13), March 2002.

[187] A. Rousse, K. T. Phuoc, R. Shah, A. Pukhov, E. Lefebvre, V. Malka, S. Kiselev, F. Burgy, J. P. Rousseau, D. Umstadter, and D. Hulin. **Production of a keV x-ray beam from synchrotron radiation in relativistic laser-plasma interaction**. *Physical Review Letters*, **93**(13):135005, September 2004.

[188] K. Ta Phuoc, F. Burgy, J. P. Rousseau, V. Malka, A. Rousse, R. Shah, D. Umstadter, A. Pukhov, and S. Kiselev. **Laser based synchrotron radiation**. *Physics of Plasmas*, **12**(2):023101, February 2005.

[189] E. Esarey, B. A. Shadwick, P. Catravas, and W. P. Leemans. **Synchrotron radiation from electron beams in plasma-focusing channels**. *Physical Review E*, **65**(5):056505, May 2002.

[190] I. Kostyukov, S. Kiselev, and A. Pukhov. **X-ray generation in an ion channel**. *Physics of Plasmas*, **10**(12):4818–4828, December 2003.

[191] Michael Schnell, Alexander Sävert, Ingo Uschmann, Oliver Jansen, Malte Christoph Kaluza, and Christian Spielmann. **Characterization and application of hard x-ray betatron radiation generated by relativistic electrons from a laser-wakefield accelerator**. *Journal of Plasma Physics*, pages 1–28, April 2015.

[192] F. Albert, K. Ta Phuoc, R. Shah, S. Corde, R. Fitour, A. Tafzi, F. Burgy, D. Douillet, T. Lefrou, and A. Rousse. **Full characterization of a laser-produced keV x-ray betatron source**. *Plasma Physics and Controlled Fusion*, **50**(12):124008, November 2008.

[193] K. Ta Phuoc, R. Fitour, A. Tafzi, T. Garl, N. Artemiev, R. Shah, F. Albert, D. Boschetto, A. Rousse, D. E. Kim, A. Pukhov, V. Seredov, and I. Kostyukov. **Demonstration of the ultrafast nature of laser produced betatron radiation**. *Physics of Plasmas*, **14**(8):080701, 2007.

[194] S. Fourmaux, S. Corde, K. T. Phuoc, P M Leguay, S Payeur, P Lassonde, S Gnedyuk, G Lebrun, C Fourment, S. Sebban, A. Rousse, and J. C. Kieffer. **Demonstration of the synchrotron-type spectrum of laser-produced Betatron radiation**. *New Journal of Physics*, 2011.

[195] S. Kneip, C. McGuffey, J. L. Martins, S. F. Martins, C. Bellei, V. Chvykov, F. Dollar, R. Fonseca, C. Huntington, G. Kalintchenko, A. Maksimchuk, S. P. D. Mangles, T. Matsuoka, S. R. Nagel, C. A. J. Palmer, J. Schreiber, K. Ta Phuoc, A. G. R. Thomas, V. Yanovsky, L. O. Silva, K. Krushelnick, and Z. Najmudin. **Bright spatially coherent synchrotron X-rays from a table-top source**. *Nature Physics*, **6**(12):980–983, 2010.

[196] Kim Ta Phuoc, Sebastien Corde, Rahul Shah, Felicie Albert, Romuald Fitour, Jean-Philippe Rousseau, Fréderic Burgy, Brigitte Mercier, and Antoine Rousse. **Imaging Electron Trajectories in a Laser-Wakefield Cavity Using Betatron X-Ray Radiation**. *Physical Review Letters*, **97**:225002, November 2006.

[197] S. Corde, C. Thaury, K. Ta Phuoc, A. Lifschitz, G. Lambert, O. Lundh, P. Brijesh, L. Arantchuk, S. Sebban, A. Rousse, J. Faure, and V. Malka. **Betatron emission as a diagnostic for injection and acceleration mechanisms in laser plasma accelerators**. *Plasma Physics and Controlled Fusion*, **54**(12):124023, November 2012.

[198] Xiaoming Wang, Rafal Zgadzaj, Neil Fazel, Zhengyan Li, S. A. Yi, Xi Zhang, Watson Henderson, Y Y Chang, R Korzekwa, H E Tsai, C H Pai, H Quevedo, G. Dyer, E Gaul, M Martinez, A. C. Bernstein, T Borger, M Spinks, M Donovan, V. Khudik, G. Shvets, T. Ditmire, and M. C. Downer. **Quasi-monoenergetic laser-plasma acceleration of electrons to 2 GeV**. *Nature Communications*, **4**:1–9, 2013.

[199] K. Ta Phuoc, S. Corde, R. Fitour, R. Shah, F. Albert, J. P. Rousseau, F. Burgy, A. Rousse, V. Seredov, and A. Pukhov. **Analysis of wakefield electron orbits in plasma wiggler**. *Physics of Plasmas*, **15**(7):073106, July 2008.

[200] C. Thaury, E Guillaume, S. Corde, R Lehe, M Le Bouteiller, K. Ta Phuoc, X. Davoine, J. M. Rax, A. Rousse, and V. Malka. **Angular-Momentum Evolution in Laser-Plasma Accelerators**. *Physical Review Letters*, **111**(13):135002, September 2013.

[201] N B Delone and Vladimir P Krainov. **Tunneling and barrier-suppression ionization of atoms and ions in a laser radiation field**. *Physics-Uspekhi*, **41**(5):469–485, October 1998.

[202] B. Quesnel and P. Mora. **Theory and simulation of the interaction of ultraintense laser pulses with electrons in vacuum**. *Physical Review E*, **58**(3):3719–3732, September 1998.

[203] A Thomas, C Ridgers, S. Bulanov, B Griffin, and S. Mangles. **Strong Radiation-Damping Effects in a Gamma-Ray Source Generated by the Interaction of a High-Intensity Laser with a Wakefield-Accelerated Electron Beam**. *Physical Review X*, **2**(4), October 2012.

[204] A Variola, A Loulergue, and F Zomer. **THOMX**. Technical report, LAL / SOLEIL, January 2010.

[205] D. Strickland and G. Mourou. **Compression of Amplified Chirped Optical Pulses**. *Optics Communications*, **56**(3):219–221, December 1985.

[206] P. Tournois. **Acousto-optic programmable dispersive filter for adaptive compensation of group delay time dispersion in laser systems**. *Optics Communications*, **140**(4-6):245–249, August 1997.

[207] S. P. D. Mangles, G. Genoud, S. Kneip, M. Burza, K. Cassou, B. Cros, N. P. Dover, C. Kamperidis, Z. Najmudin, A. Persson, J. Schreiber, F. Wojda, and C. G. Wahlstrom. **Controlling the spectrum of x-rays generated in a laser-plasma accelerator by tailoring the laser wavefront**. *Applied Physics Letters*, **95**(18):181106, 2009.

[208] E Guillaume, C. Thaury, A. Lifschitz, A Döpp, K. Ta Phuoc, and V. Malka. **Effect of the Third Order Dispersion on laser pulse propagation in an underdense plasma**. October 2015.

[209] S. P. D. Mangles, A. G. R. Thomas, M. C. Kaluza, O. Lundh, F. Lindau, A. Persson, Z. Najmudin, C. G. Wahlstrom, C. D. Murphy, C. Kamperidis, K. L. Lancaster, E. Divall, and K. Krushelnick. **Effect of laser contrast ratio on electron beam stability in laser wakefield acceleration experiments**. *Plasma Physics and Controlled Fusion*, **48**(12B):B83–B90, December 2006.

[210] Michael Schnell, Maria Reuter, Maria Nicolai, Oliver Jansen, Alexander Pukhov, Malte Christoph Kaluza, and Christian Spielmann. **Optical control of hard X-ray polarization by electron injection in a laser wakefield accelerator**. *Nature Communications*, **4**:1–6, September 2013.

[211] B Beaurepaire, A Vernier, M Bocoum, F Böhle, A Jullien, J. P. Rousseau, T. Lefrou, D. Douillet, G Iaquaniello, R López-Martens, A. Lifschitz, and J. Faure. **Effect of the Laser Wave Front in a Laser-Plasma Accelerator**. *Physical Review X*, **5**(3):031012, July 2015.

[212] Karl S Kunz and Raymond J Luebbers. *The finite difference time domain method for electromagnetics*. CRC press, October 1993.

[213] John Dawson. **One-Dimensional Plasma Model**. *Physics of Fluids*, **5**(4):445–459, 1962.

[214] Xavier Davoine. *Accélération électronique par sillage laser et sources de rayonnements associées*. PhD thesis, Université de Versailles Saint-Quentin-en-Yvelines, 2009.

Acknowledgements

First of all I want to thank my Ph.D. advisor at Laboratoire d'Optique Appliquée, Kim Ta Phuoc, and my co-advisor and tutor at Universidad de Salamanca, Camilo Ruiz and Enrique Conejero, for their support and encouragement. I would also like to acknowledge the LA^{3}NET collaboration, and in particular Carsten Welsch, Luis Roso, Antoine Rousse and Victor Malka for enabling this project.

None of the results presented in this work would have been achieved without the passionate experimental team at SALLE JAUNE. Thanks to Emilien Guillaume, who shared countless hours with me in the laboratory, and to Kim Ta Phuoc and Cedric Thaury for their supervision and guidance. Furthermore, i would like to thank Fabien Tissandier and Julien Gautier for their occasional assistance, and Amar Tafzi and Jean-Phillipe Goddet for their relentless work on the laser. Agustin Lifschitz and Camilo Ruiz aided me a lot on the numerical part of the thesis, as did Remi Lehe and Igor Andriyash.

Many more people - colleagues, friends and family - have helped and kept me going over the last three years. I am afraid that any attempt to express my gratitude in a sufficient manner is condemned to fail, so i will leave it at a simple, but sincere *thank you*.